Master Thesis:
Vertical Wave Loads and Response of a Floating Fish Farm with Circular Collar

Per Christian Endresen

June 15, 2011

Abstract

In this master thesis the vertical wave loads and vertical responses of the floating collar of a circular fish farm have been investigated. The response has been investigated for a collar without the presence of mooring system and net cage. First, a linear model was used to calculate displacements, relative motion between the floater and the surface and bending stresses. The linear displacements and bending stresses in regular long crested waves were compared with a nonlinear model for the excitation forces. The nonlinear excitation forces were obtained by integrating the hydrostatic and dynamic pressures over the exact wetted surface of the floater.

Two different configurations of the floating collar were investigated; a floater with only one plastic ring and a floater with two concentric rings. The radius and the displaced mass of the two configurations were equal. The response was calculated by mode superposition. The added mass is mode dependent, and thus a modal formulation of the added mass was used. The modal resonance frequencies for one ring were higher than the modal resonance frequencies for two rings. The three first resonance frequencies for two rings, corresponding to heave, pitch and the first elastic mode, are 2.25 rad/s, 2.69 rad/s and 2.91 rad/s. The relative motion for low wave frequencies is higher for one ring than for two rings. The bending stresses are significantly higher for two rings between a wave frequency of 1.5 rad/s and 2.9 rad/s.

The linear model was used to calculate standard deviations for bending stresses in irregular waves. For low spectral peak periods the JONSWAP spectrum gave larger standard deviations for the bending stresses than the ISSC spectrum. For peak periods larger than 4.5s the ISSC spectrum gave the largest standard deviations.

For regular waves the linear and nonlinear model gave similar results for modal displacements and maximum bending stresses in the floater for small wave frequencies. At the modal resonance frequencies the nonlinear modal forces for the modes at resonance were significantly lower than the linear forces. This resulted in a reduced nonlinear response compared with linear theory at resonance. Damping was seen to only have a significant effect on the response at resonance for both the linear and nonlinear model. For some frequencies, modal excitation forces with frequencies two times, three times or higher than the incident wave frequency were observed. This induced higher frequency components in the response. The higher frequency components were close to the modal resonance frequency. Although the floater does not have forward speed, this kind of response from continueous wave loads can be associated with nonlinear springing response for ships.

Preface

The subject for this master thesis were originally presented and given by David Kristiansen at SINTEF Fisheries and Aquaculture. My supervisor has been Odd Magnus Faltinsen at Department of Marine Technology, Norwegian University of Science and Technology (NTNU). He has formulated the scope and given suggestions for which problems that should be pursued during this project. I would like to thank him for excellent guidance and motivation during the work with this master thesis. He has given me challenging assignments, continuous supervision, suggestions and encouragement, for which I am grateful.

One of the methods derived in the project carried out in autumn 2010 have been extended and used in this master thesis. I would like to thank David Kristiansen for the material and help he gave during the work with the preliminary project in 2010.

I would also like to thank Shao Yanlin at Centre for Ships and Ocean Structures (CeSOS) for providing data from BEM calculations of added mass and verification of the added mass calculations.

A special thanks goes to my friend and fellow student Jarle Havn, with whom I have had many interesting and fruitful discussions concerning the problems addressed in this thesis.

....
Per Christian Endresen

Contents

1 **Introduction** **1**

2 **Physical Problem and Calculation Method** **3**
- 2.1 Geometry, Boundaries and Axis Definitions 4
- 2.2 Assumption of Draught 4
- 2.3 Background 5
- 2.4 Matlab Code 6

3 **Velocity Potential and Added Mass** **7**
- 3.1 Velocity Potential for 1 Torus 8
  - 3.1.1 Far Field Description for Heave Motion 8
  - 3.1.2 Far Field Description for General Motion 9
  - 3.1.3 Near Field Description for Heave Motion 11
  - 3.1.4 Near Field Description for General Motion 13
  - 3.1.5 Matching of The Far Field and Near Field Velocity Potentials 14
- 3.2 Added Mass for One Torus 15
  - 3.2.1 Added Mass in Heave 15
  - 3.2.2 Vertical Added Mass for Mode n 17
- 3.3 Added Mass Two Tori 19

4 **Excitation Forces and Equations of Motion** **21**
- 4.1 Wave Potential 21
- 4.2 Wave Excitation Forces 22
- 4.3 Linear Diffraction Force 22
- 4.4 Linear Froude-Kriloff Force 23
- 4.5 Equations of Motion 24
- 4.6 Nonlinear Hydrostatic and Froude-Kriloff Forces 28
  - 4.6.1 Calculation of Nonlinear Forces 29
  - 4.6.2 Intersection Between The Water Surface and The Pipe 32
- 4.7 Equations of Motion for Nonlinear Hydrostatic and Froude Kriloff Forces 34
  - 4.7.1 Damping 34
  - 4.7.2 Discretization in the Time Domain Analysis 35
  - 4.7.3 Time Series of Linear and Nonlinear Response 36
- 4.8 Nonlinear Hydrostatic and Froude-Kriloff Forces in Irregular Sea 38
  - 4.8.1 Wave Elevation in Irregular Sea 38
  - 4.8.2 Hydrostatic and Dynamic Pressure and Equations of Motion 39

5 **Relative Motion and Bending Stress** **41**
- 5.1 Relative Vertical Motion of The Floater 41
- 5.2 Bending Stress 44
- 5.3 Standard Deviation of Bending Stresses in a Sea State 47

6 Results - Linear Analysis 51
6.1 Displacements and Relative Motion . . . 51
6.1.1 Convergence of the Transfer Function for Relative Motion . . . 51
6.1.2 Effect of Damping on the Relative Motion . . . 53
6.1.3 Comparison Between Relative Motion for 1 Torus and 2 Tori . . . 54
6.2 Bending Stress . . . 55
6.2.1 Convergence of Transfer Function for Bending Stress . . . 55
6.2.2 Effect of Damping on The Bending Stresses . . . 56
6.2.3 Comparison Between Bending Stress for 1 Torus and 2 Tori . . . 56
6.3 Maximum Bending Stress in a Sea State . . . 57
6.3.1 Effect of Damping on The Maximum Bending Stress in a Sea State . . . 58
6.3.2 Maximum Bending Stress as a Function of Position . . . 59
6.3.3 Maximum Bending Stress as a Function of Spectral Peak Period . . . 62

7 Results - Comparison Between Linear and Nonlinear Response 67
7.1 Response at Low Frequencies . . . 68
7.2 Response at Resonance . . . 70
7.3 Mode Excitation at Higher Frequencies . . . 74
7.4 Transfer Functions . . . 77
7.4.1 Displacement and Excitation Forces . . . 77
7.4.2 Bending Stresses . . . 81
7.5 Validity of Linear Wave Theory and Convergence of the Nonlinear Analysis . . . 82

8 Further Discussion, Conclusion and Suggestions for Further Work 85
8.1 Further Discussion - Error Sources . . . 85
8.2 Conclusion . . . 86
8.3 Suggestions for Further Work . . . 87

References 88

A Derivation of Chosen Expressions 91
A.1 Fourier Sum Involving Bessel Functions . . . 91

B Tables and Figures 93
B.1 Tables . . . 93
B.2 Linear Transfer Functions . . . 95
B.3 Comparison Between Linear and Nonlinear Transfer Functions . . . 96
B.3.1 1 Torus . . . 96
B.3.2 2 Tori . . . 99
B.4 Time Series . . . 102
B.4.1 1 Torus. $\omega = 1.75 rad/s$ . . . 102
B.4.2 1 Torus. $\omega = 2.0 rad/s$ . . . 104
B.4.3 1 Torus. $\omega = 2.49 rad/s$ . . . 106
B.4.4 2 Tori. $\omega = 1.2 rad/s$ . . . 108
B.4.5 2 Tori. $\omega = 1.4 rad/s$ . . . 110
B.4.6 2 Tori. $\omega = 1.5 rad/s$ . . . 112
B.4.7 2 Tori. $\omega = 1.8 rad/s$ . . . 114
B.4.8 2 Tori. $\omega = 2.25 rad/s$ . . . 116
B.4.9 2 Tori. $\omega = 2.69 rad/s$ . . . 118

List of Figures

2.1 Global coordinate system for the floating collar. To the left: one ring. To the right: two rings. R is the radius of the collar, given as the radial distance from the origin $(0,0)$ to the center line of the floater. R is then the the distance from the origin to the center line of one ring and to the midpoint between the center lines for two rings, respectively. β is the angle defining the x-coordinate on the floater given by $x = R\cos\beta$. 5
2.2 Floating fish farm with circular plastic collar consisting of two concentric rings. The photo is taken from [Faltinsen (2011)]. (Photo: SINTEF Fisheries and Aquaculture) . . . 5
2.3 Fish farm with circular plastic collar in a storm in January 2006 in Flatanger, Norway. Elastic deformations of the floater are clearly seen. The photo is taken from [Kristiansen (2010)]. (Photo: Marius Dahle Olsen) 6

3.1 Far field view of the floater. (x,y,z) is the field point and $(\xi,\eta,0)$ is a point on the floater. R is the floater radius and a is the distance to the field point from the origin. r is the distance from the field point to the position $(\xi,\eta,0)$ on the floater. 8
3.2 Near field view of the floater. $\dot{a}_0$ is the heave velocity of the torus. $\partial\phi^N/\partial r$ and $\partial\phi^N/\partial z'$ are the body boundary condition and the rigid free surface condition respectively. $\cos\theta$ is the negative z'-component of the body normal vector. c is the pipe radius. The draught of the section is c. 11
3.3 Near field view of the floater. $\dot{a}_n\cos n\beta$ is the modal vertical velocity of the torus section at the position $x = R\cos\beta$ in the global coordinate system (x,y,z). $\partial\phi^N/\partial r$ and $\partial\phi^N/\partial z'$ are the body boundary condition and the rigid free surface condition respectively. $\cos\theta$ is the negative z'-component of the body normal vector. c is the pipe radius. 13
3.4 Comparison between 3D non dimensional added mass for 1 torus calculated with slender body theory and BEM. BEM results provided by [Shao. Personal communication (2011)]. A_{33}, A_{44} and A_{55} are the 3D added mass in z-direction for heave, pitch and the first elastic mode. $M = \rho\pi^2c^2R$ is the submerged mass of the torus. c is the pipe radius and R is the radius of the torus. 18
3.5 2D non dimensional added mass for 1 torus. $a_{33}^{(n)}$ is the 2D added mass in z-direction associated with the mode shape $\cos n\beta$. $m = \rho\pi c^2/2$ is the 2D mass of the floater. c is the radius if the section. R is the radius of the floater. 19
3.6 Near field view for 2 tori. $2p$ is the horizontal center to center distance between the pipes. p is the horizontal distance between the local coordinate system (y',z') and the center of the pipes. c is the radius of the pipes. R is the radius of the torus. 19
3.7 2D non dimensional added mass for 2 tori. $a_{33}^{(n)}$ is the 2D added mass in z-direction associated with the mode shape $\cos n\beta$. $m = \rho\pi c^2$ is the 2D mass of the floater. c is the radius of the section. R is the radius of the floater. 20

4.1 Plot of the orthogonal mode $\cos n\beta$. Mode shapes for $n = 1,2,3,6,7$ and 8 are shown. The y-axis is the normalized amplitude of the modal response. The x-axis is the normalized x-coordinate on the floater referring to the global coordinate system. x is normalized by dividing with the floater radius R. 25

4.2 Undamped linear transfer functions for 1 torus. $n = 0$ is heave, $n = 1$ is pitch and $n = 2$ is the first elastic mode. $a_{n,A}$ is the motion amplitude of mode n. ζ_a is the wave amplitude and ω is the wave frequency. 27

4.3 Undamped linear transfer functions for 2 tori. $n = 0$ is heave, $n = 1$ is pitch and $n = 2$ is the first elastic mode. $a_{n,A}$ is the motion amplitude of mode n. ζ_a is the wave amplitude and ω is the wave frequency. 28

4.4 Linear hydrostatic, dynamic and total pressure underneath a wave crest and a wave trough. The wave elevation is exaggerated in order to properly show the principle. The figure is based on similar figures in [Faltinsen (1990)] and [Dean & Dalrymple (1991)]. . 30

4.5 Principle figure showing the whole floater (left) and a part of the floater defined by the coordinate β (right). Both figures are seen from the positive z-axis. The red circle on the figure of the whole floater indicates the position at which the section to the right is situated. c and R are the pipe radius and the distance from the origin to the center of the pipe, respectively. $c|\cos\beta|$ is the scaled distance in x-direction from $x = R\cos\beta$ to $x = (R - c)\cos\beta$. 31

4.6 Principle figure describing how the attachment point between the waves and the floater section is found. α_1 and θ_1 are the angles for the calculated intersection defined from negative y' and negative z'-axis respectively. Both angles are defined positive in the counter clockwise direction. w is the total vertical displacement of the section. ζ_x is the wave elevation at the center of the section. $\partial\zeta/\partial x_{(1)}$ is the wave slope at $y' = -c/2$ in the local coordinate system. $|\cos\beta|c$ is a scale factor for the wave slope from the global coordinate system (x, y, z) to the local coordinate system (y', z'). For $|w - \zeta_x| > c/2$ the horizontal distance c in the calculation of θ_1 is replace by c' from equation (4.39). . . 33

4.7 Response of the heave mode for a 2 tori configuration of the floater due to nonlinear hydrostatic and Froude-Kriloff forces. $a_{n=0}(t)$ is the time dependent response of the heave mode. $a_{n=0}(t)$ is also the time dependent Fourier coefficient in equation (4.12) for $n = 0$. The wave frequency ω is $0.5rad/s$. The wave steepness is $H/\lambda = 1/30$, giving a wave amplitude $\zeta_a = 4.11m$. $H = 2\zeta_a$ is the wave height. The modal damping level is 1.5 percent of critical damping for each mode. 37

4.8 Comparison of response of the heave mode for a 2 tori configuration of the floater for linear and nonlinear hydrostatic and Froude-Kriloff forces. $a_{n=0}(t)$ is the time dependent response of the heave mode. The wave frequency ω is $0.5rad/s$. The wave steepness $H/\lambda = 1/30$, thus giving a wave amplitude $\zeta_a = 4.11m$. $H = 2\zeta_a$ is the wave height. The modal damping level is 1.5 percent of critical damping for each mode. 37

4.9 Comparison of response of the heave mode for a 2 tori configuration of the floater for linear and nonlinear hydrostatic and Froude-Kriloff forces. $a_{n=0}(t)$ is the time dependent response of the heave mode. The wave frequency ω is $2rad/s$ The wave steepness $H/\lambda = 1/30$, thus giving a wave amplitude $\zeta_a = 0.26m$. $H = 2\zeta_a$ is the wave height. The modal damping level is 1.5 percent of critical damping for each mode. 37

5.1 RAO for maximum relative vertical motion between the floater center and the waves. $r_{a,max}$ is the relative motion. ζ_a is the wave amplitude. ω is the wave frequency. 43

5.2 RAO for maximum bending stress. $\sigma_{max}(\omega)$ is the maximum bending stress. ζ_a is the wave amplitude. ω is the wave frequency. 46

5.3 Most probable maximum normalized bending stresses in the floater. $\chi_{\sigma_{max}}$ is the most probable maximum bending stress. $H_{1/3}$ is the significant wave height. The position on the floater is given by $x = R\cos\beta$. T_p is the spectral peak period in the ISSC wave spectrum. 49

5.4 Transfer functions for the maximum bending stresses $\sigma_{max}(\omega)$ and normalized wave spectra. ω is the wave frequency. ζ_a is the wave amplitude. $H_{1/3}$ is the significant wave height. T_p is the spectral peak period. 49

6.1 Undamped transfer function for maximum relative motion with respect to wave circular frequency ω for 1 torus and 2 tori. $r_{a,max}$ is the maximum relative motion between the center line of the floater and the first order surface ζ. ζ_a is the wave amplitude. The results for a total of 7, 10 and 15 modes are compared. 52

6.2 Transfer function for maximum relative vertical motion between the floater center line and the first order surface ζ with respect to the circular wave frequency ω for 2 tori. Undamped motion and a damping level of 1 percent and 3 percent of critical damping for each mode are compared. $r_{a,max}$ is the maximum relative motion amplitude. ζ_a is the wave amplitude. $b_{33}^{(n)}$ and $b_{(33,cr)}^{(n)}$ are the vertical modal damping and vertical critical modal damping, respectively. 53

6.3 Transfer function for maximum relative vertical motion between the floater center line and the first order surface ζ with respect to the circular wave frequency ω for 1 torus and 2 tori. A damping level of 1 percent of critical damping for each mode is used. $r_{a,max}$ is the maximum relative motion amplitude. ζ_a is the wave amplitude. 54

6.4 Undamped transfer function for maximum bending stress with respect to wave circular frequency ω for 1 torus and 2 tori. σ_{max} is the maximum bending stress in the floater with respect to ω. ζ_a is the wave amplitude. The results for a total of 10, 15, 20 and 25 modes are compared. 56

6.5 Transfer function for maximum bending stress in the floater for 2 tori. The undamped response and the response for a damping level of 1 percent and 3 percent of critical damping for each mode are compared. σ_{max} is the maximum bending stress as a function of the circular wave frequency ω. ζ_a is the wave amplitude. 57

6.6 Transfer function for the maximum bending stress in the floater for 1 torus and 2 tori. σ_{max} and ω are the maximum bending stress and circular wave frequency, respectively. The 25 first modes are used, and a damping level of 1 percent of critical damping for each mode is applied. 57

6.7 Most probable maximum bending stresses around the floater in a sea state. $\chi_\sigma/H_{1/3}$ is the normalized most probable maximum bending stress as a function of the position β on the floater. σ is the standard deviation of the bending stress. $H_{1/3}$ is the significant wave height. $\beta/\pi = 0$ and $\beta/\pi = 1$ are the trailing and leading point on the floater with respect to the wave propagation direction. The waves are propagating in positive x-direction. The ISSC wave spectrum with a peak period $T_p = 8s$ is used. 59

6.8 Normalized most probable maximum bending stress for 1 torus and 2 tori plotted as a function of the position β on the floater in different sea states given by the peak period T_p. $\beta/\pi = 0$ and $\beta/\pi = 1$ are the back and front of the floater with respect to the wave propagation direction. χ_σ is the most probable maximum bending stress calculated from the standard deviation of the bending stress. $H_{1/3}$ is the significant wave height. The modal damping level is 1 percent of critical damping for each mode. The ISSC wave spectrum is used. 60

6.9 Most probable maximum bending stresses χ_σ as a function of position β on the floater for 2 tori. The stresses are normalized with the significant wave height $H_{1/3}$. Damping levels of 1, 3 and 5 percent of critical damping for each mode have been tested. The spectral peak period T_p is $3.5s$. The ISSC wave spectrum is used. 61

6.10 Normalized most probable maximum bending stress for 1 torus and 2 tori plotted as a function of the position β on the floater in different sea states given by the peak period T_p. $\beta/\pi = 0$ and $\beta/\pi = 1$ are the back and front of the floater with respect to the wave propagation direction. χ_σ is the most probable maximum bending stress calculated from the standard deviation σ of the bending stress. $H_{1/3}$ is the significant wave height. The modal damping level is 1 percent of critical damping for each mode. The ISSC wave spectrum is used. 61

6.11 Most probable normalized maximum bending stress $max(\chi_\sigma)/H_{1/3}$ as a function of spectral peak period T_p. $max(\chi_\sigma)$ is the maximum bending stress on the floater for each peak period. $H_{1/3}$ is the significant wave height. The ISSC wave spectrum is used. The results for 1 torus and 2 tori are compared. The modal damping level is 1 percent of critical damping for each mode. 62

6.12 Most probable normalized maximum bending stress $max(\chi_\sigma)/H_{1/3}$ as a function of spectral peak period T_p. $max(\chi_\sigma)$ is the maximum bending stress on the floater for each peak period. $H_{1/3}$ is the significant wave height. The ISSC wave spectrum is used. The results for 2 tori with a modal damping level of 1 percent, 3 percent and 5 percent of critical damping, respectively, are compared. 63

6.13 Most probable normalized maximum bending stress $max(\chi_\sigma)/H_{1/3}$ for 2 tori as a function of spectral peak period T_p. $max(\chi_\sigma)$ is the maximum bending stress on the floater. $H_{1/3}$ is the significant wave height. The ISSC wave spectrum is used. The modal damping level is 1 percent of critical damping. Different cross section dimensions are compared. c is the pipe radius. t_w is the wall thickness. 64

6.14 Left: Comparison of response for the ISSC and JONSWAP spectra. Damping is set to 1 percent of critical damping. The dimensions from Chapter 2 are used. Right: Dimensionless wave spectra. T_2 is the mean zero up-crossing period. $H_{1/3}$ is the significant wave height. 65

7.1 Time series of modal displacement and excitation forces for the three first modes for 1 torus for $\omega = 0.8 rad/s$. Linear and nonlinear excitation forces are compared. $a_n(t)$ and $f_{3,n}^{exc}(t)$ are the n-th time dependent Fourier coefficient and the time dependent modal force for mode n, respectively. $f_{3,n}^{exc}(t)$ are given by equation (7.1) to (7.4). The wave steepness $H/\lambda = 1/30$, giving a wave amplitude $\zeta_a = 1.61$. H and λ are the wave height and wave length. A modal damping level of 1.5 percent of modal critical damping is used. 69

7.2 Time series of modal displacement and excitation forces for the four first modes for 2 tori for heave resonance at $\omega = 2.25 rad/s$. Linear and nonlinear excitation forces are compared. $a_n(t)$ and $f_{3,n}^{exc}(t)$ are the n-th time dependent Fourier coefficient and the time dependent modal force for mode n, respectively. $f_{3,n}^{exc}(t)$ are given by equation (7.1) to (7.4). The wave steepness $H/\lambda = 1/15$, giving a wave amplitude $\zeta_a = 0.41m$. H and λ are the wave height and wave length. A modal damping level of 1.5 percent of modal critical damping is used. Note the difference between the values on the y-axes. 72

7.3 Time series of modal displacement and excitation forces for the four first modes for 2 tori for pitch resonance at $\omega = 2.69 rad/s$. Linear and nonlinear excitation forces are compared. $a_n(t)$ and $f_{3,n}^{exc}(t)$ are the n-th time dependent Fourier coefficient and the time dependent modal force for mode n, respectively. $f_{3,n}^{exc}(t)$ are given by equation (7.1) to (7.4). The wave steepness $H/\lambda = 1/15$, giving a wave amplitude $\zeta_a = 0.28m$. H and λ are the wave height and wave length. A modal damping level of 1.5 percent of modal critical damping is used. Note the difference between the values on the y-axes. 73

7.4 Comparison between linear and nonlinear modal response and excitation force for 2 tori. The results for the second elastic mode, $n = 3$, are plotted. The incident wave frequency is $\omega = 1.5 rad/s$. The wave steepness is $H/\lambda = 1/30$, giving a wave height $\zeta_a = 0.46m$. A modal damping level of 1.5 percent of critical damping for each mode is used. 75

7.5 Comparison between linear and nonlinear modal response and excitation force for 1 torus. The results for the fourth elastic mode, $n = 5$, are plotted. The incident wave frequency is $\omega = 2 rad/s$. The wave steepness is $H/\lambda = 1/20$, giving a wave height $\zeta_a = 0.39m$. A modal damping level of 2 percent of critical damping for each mode is used. 75

7.6 Comparison between linear and nonlinear modal response and excitation force for 2 tori. The results for the sixth elastic mode, $n = 7$, are plotted. The incident wave frequency is $\omega = 2.25 rad/s$, corresponding to heave resonance. The wave steepness is $H/\lambda = 1/15$, giving a wave height $\zeta_a = 0.41m$. A modal damping level of 1.5 percent of critical damping for each mode is used. 76

7.7 Transfer functions for modal response and modal excitation force for 1 torus. Linear and nonlinear response for heave and pitch, corresponding to $n = 0$ and $n = 1$, for different wave steepnesses H/λ and different damping levels are compared. ω and ζ_a are the wave frequency and wave amplitude. H and λ are the wave height and wave length. 79

7.8 Transfer functions for modal response and modal excitation force for 2 tori. Linear and nonlinear response for heave and pitch, corresponding to $n = 0$ and $n = 1$, for different wave steepnesses H/λ and different damping levels are compared. ω and ζ_a are the wave frequency and wave amplitude. H and λ are the wave height and wave length. 80

7.9 Transfer function for maximum bending stress σ_{max} in the floating collar. 1 torus and 2 tori, and the linear and nonlinear excitation force model are compared. For the nonlinear model two different damping levels, presented as a percentage of critical damping for each mode, and two different wave steepnesses H/λ are investigated. H is the wave height and λ is the wave length. ω is the wave frequency. The 20 first modes are used in the analysis for both the linear and nonlinear model. 81

B.1 Undamped linear transfer functions for 1 torus. $a_{n,A}$ is the motion amplitude of mode n. $n = 3, 4, 5$ are elastic modes. ζ_a is the wave amplitude and ω is the wave frequency. . . . 95

B.2 Undamped linear transfer functions for 2 tori. $a_{n,A}$ is the motion amplitude of mode n. $n = 3, 4, 5$ are elastic modes. ζ_a is the wave amplitude and ω is the wave frequency. . . . 95

B.3 Transfer functions for pitch and heave, given by $n = 0$ and $n = 1$, for 2 tori. n is the mode number. Undamped transfer functions and transfer functions for two different modal damping levels given as a percentage of critical damping for each mode are compared. ω is the wave frequency. $a_{n,A}$ is the modal amplitude. ζ_a is the wave amplitude. 95

B.4 Transfer functions for modal response and modal excitation force for 1 torus. Linear and nonlinear response for the two first elastic modes, corresponding to $n = 2$ and $n = 3$, for different wave steepnesses H/λ and different damping levels are compared. ω and ζ_a are the wave frequency and wave amplitude. H and λ are the wave height and wave length. 96

B.5 Transfer functions for modal response and modal excitation force for 1 torus. Linear and nonlinear response for the third and fourth elastic modes, corresponding to $n = 4$ and $n = 5$, for different wave steepnesses H/λ and different damping levels are compared. ω and ζ_a are the wave frequency and wave amplitude. H and λ are the wave height and wave length. 97

B.6 Transfer functions for modal response and modal excitation force for 1 torus. Linear and nonlinear response for the fifth and sixth elastic modes, corresponding to $n = 6$ and $n = 7$, for different wave steepnesses H/λ and different damping levels are compared. ω and ζ_a are the wave frequency and wave amplitude. H and λ are the wave height and wave length. 98

B.7 Transfer functions for modal response and modal excitation force for 2 tori. Linear and nonlinear response for the two first elastic modes, corresponding to $n = 2$ and $n = 3$, for different wave steepnesses H/λ and different damping levels are compared. ω and ζ_a are the wave frequency and wave amplitude. H and λ are the wave height and wave length. 99

B.8 Transfer functions for modal response and modal excitation force for 2 tori. Linear and nonlinear response for the third and fourth elastic modes, corresponding to $n = 4$ and $n = 5$, for different wave steepnesses H/λ and different damping levels are compared. ω and ζ_a are the wave frequency and wave amplitude. H and λ are the wave height and wave length. 100

B.9 Transfer functions for modal response and modal excitation force for 2 tori. Linear and nonlinear response for the fifth and sixth elastic modes, corresponding to $n = 6$ and $n = 7$, for different wave steepnesses H/λ and different damping levels are compared. ω and ζ_a are the wave frequency and wave amplitude. H and λ are the wave height and wave length. 101

B.10 Time series of nonlinear modal displacements for the eight first modes for 1 torus. Wave frequency $\omega = 1.75rad/s$. Wave steepness $H/\lambda = 1/15$. Wave amplitude $\zeta_a = 0.67m$. Modal damping is 3 percent of critical damping for each mode. 102

B.11 Time series of nonlinear modal excitation forces for the eight first modes for 1 torus. Wave frequency $\omega = 1.75rad/s$. Wave steepness $H/\lambda = 1/15$. Wave amplitude $\zeta_a = 0.67m$. Modal damping is 3 percent of critical damping for each mode. 103

B.12 Time series of nonlinear modal displacements for the eight first modes for 1 torus. Wave frequency $\omega = 2.0rad/s$. Wave steepness $H/\lambda = 1/20$. Wave amplitude $\zeta_a = 0.39m$. Modal damping is 2 percent of critical damping for each mode. 104

B.13 Time series of nonlinear modal excitation forces for the eight first modes for 1 torus. Wave frequency $\omega = 2.0rad/s$. Wave steepness $H/\lambda = 1/20$. Wave amplitude $\zeta_a = 0.39m$. Modal damping is 2 percent of critical damping for each mode. 105

B.14 Time series of nonlinear modal displacements for the eight first modes for 1 torus. Wave frequency $\omega = 2.49rad/s$. Wave steepness $H/\lambda = 1/30$. Wave amplitude $\zeta_a = 0.17m$. Modal damping is 1.5 percent of critical damping for each mode. 106

B.15 Time series of nonlinear modal excitation forces for the eight first modes for 1 torus. Wave frequency $\omega = 2.49rad/s$. Wave steepness $H/\lambda = 1/30$. Wave amplitude $\zeta_a = 0.17m$. Modal damping is 1.5 percent of critical damping for each mode. 107

B.16 Time series of nonlinear modal displacements for the eight first modes for 2 tori. Wave frequency $\omega = 1.2rad/s$. Wave steepness $H/\lambda = 1/30$. Wave amplitude $\zeta_a = 0.71m$. Modal damping is 1.5 percent of critical damping for each mode. 108

B.17 Time series of nonlinear modal excitation forces for the eight first modes for 2 tori. Wave frequency $\omega = 1.2rad/s$. Wave steepness $H/\lambda = 1/30$. Wave amplitude $\zeta_a = 0.71m$. Modal damping is 1.5 percent of critical damping for each mode. 109

B.18 Time series of nonlinear modal displacements for the eight first modes for 2 tori. Wave frequency $\omega = 1.4rad/s$. Wave steepness $H/\lambda = 1/15$. Wave amplitude $\zeta_a = 1.05m$. Modal damping is 3 percent of critical damping for each mode. 110

B.19 Time series of nonlinear modal excitation forces for the eight first modes for 2 tori. Wave frequency $\omega = 1.4rad/s$. Wave steepness $H/\lambda = 1/15$. Wave amplitude $\zeta_a = 1.05m$. Modal damping is 3 percent of critical damping for each mode. 111

B.20 Time series of nonlinear modal displacements for the eight first modes for 2 tori. Wave frequency $\omega = 1.5rad/s$. Wave steepness $H/\lambda = 1/30$. Wave amplitude $\zeta_a = 0.46m$. Modal damping is 1.5 percent of critical damping for each mode. 112

B.21 Time series of nonlinear modal excitation forces for the eight first modes for 2 tori. Wave frequency $\omega = 1.5rad/s$. Wave steepness $H/\lambda = 1/30$. Wave amplitude $\zeta_a = 0.46m$. Modal damping is 1.5 percent of critical damping for each mode. 113

B.22 Time series of nonlinear modal displacements for the eight first modes for 2 tori. Wave frequency $\omega = 1.8rad/s$. Wave steepness $H/\lambda = 1/30$. Wave amplitude $\zeta_a = 0.32m$. Modal damping is 1.5 percent of critical damping for each mode. 114

B.23 Time series of nonlinear modal excitation forces for the eight first modes for 2 tori. Wave frequency $\omega = 1.8 rad/s$. Wave steepness $H/\lambda = 1/30$. Wave amplitude $\zeta_a = 0.32m$. Modal damping is 1.5 percent of critical damping for each mode. 115

B.24 Time series of vertical modal displacement for the eight first modes for 2 tori for heave resonance at $\omega = 2.25 rad/s$. Response due to linear and nonlinear excitation forces are compared. $a_n(t)$ are the n-th time dependent Fourier coefficient. The wave steepness $H/\lambda = 1/15$, giving a wave amplitude $\zeta_a = 0.41$. H and λ are the wave height and wave length. A modal damping level of 1.5 percent of modal critical damping is used. Note the differences between the values on the y-axes. 116

B.25 Time series of modal excitation forces for the eight first modes for 2 tori for heave resonance at $\omega = 2.25 rad/s$. Linear and nonlinear excitation forces are compared. $f_{3,n}^{exc}(t)$ are the time dependent modal force for mode n. $f_{3,n}^{exc}(t)$ are given by equation (7.1) to (7.4). The wave steepness $H/\lambda = 1/15$, giving a wave amplitude $\zeta_a = 0.41$. H and λ are the wave height and wave length. A modal damping level of 1.5 percent of modal critical damping is used. Note the differences between the values on the y-axes. 117

B.26 Time series of vertical modal displacement for the eight first modes for 2 tori for pitch resonance at $\omega = 2.69 rad/s$. Response due to linear and nonlinear excitation forces are compared. $a_n(t)$ are the n-th time dependent Fourier coefficient. The wave steepness $H/\lambda = 1/15$, giving a wave amplitude $\zeta_a = 0.28m$. H and λ are the wave height and wave length. A modal damping level of 1.5 percent of modal critical damping is used. Note the differences between the values on the y-axes. 118

B.27 Time series of modal excitation forces for the eight first modes for 2 tori for pitch resonance at $\omega = 2.69 rad/s$. Linear and nonlinear excitation forces are compared. $f_{3,n}^{exc}(t)$ are the time dependent modal force for mode n. $f_{3,n}^{exc}(t)$ are given by equation (7.1) to (7.4). The wave steepness $H/\lambda = 1/15$, giving a wave amplitude $\zeta_a = 0.28m$. H and λ are the wave height and wave length. A modal damping level of 1.5 percent of modal critical damping is used. Note the differences between the values on the y-axes. 119

List of Tables

2.1 Dimensions for the floating collar for a one-ring and two-ring configuration, denoted 1 torus and 2 tori respectively. E, EI, I, σ_y, ρ_p are the Young modulus, bending stiffness, 2nd area moment, yield stress and plastic density, respectively. R, c, t and $2p$ are the radius of the ring, pipe radius, wall thickness and center to center distance between the pipes. 4

3.1 Values for K_n given by the integral in equation (3.15). n is the mode number. 11

4.1 Undamped and damped modal resonance frequencies for vertical motion for 1 torus and 2 tori. The modal damping level for the damped resonance frequencies is 3 percent of critical damping for each mode. ω_0 and ω_d are the undamped and damped resonance frequencies, respectively. n is the mode number. The frequencies have dimension $\mathrm{rad/s}$. 29

B.1 Comparison between the peak periods T_p for the ISSC and JONSWAP spectrum calculated from the mean zero up-crossing periods T_2. The values for T_2 and $T_{p,\mathrm{ISSC}}$ are used in Chapter 6. 93

B.2 Discrete joint frequency distribution (scatter diagram) for service restriction **R3** (coastal service), [DNV Report No. 97-0152]. The scatter diagram is constructed from theoretical parameters, and represent DNV rules for service restriction **R3** for high-speed and light crafts. T_2 and $H_{1/3}$ is the mean up-crossing period and significant wave height of the spectrum. The dimensions are seconds and meters respectively. $T_2 = 7s$ means a mean period from $6.5s$ to $7.5s$. $H_{1/3} = 2.0m$ means a significant wave height from $1.75m$ to $2.25m$. The probability of exceedence for each significant wave height is shown in the column to the right. Probability of exceedence for $H_{1/3} = 3.0m$ is calculated as $(0.5 \cdot 36 + 19 + 104 + 2)/998 = 0.053$, [Faltinsen (2005)]. Mean periods higher than $13s$ are removed from the table since there is no entries for higher periods. 94

Nomenclature

The most used symbols are listed below. Symbols not listed here will be explained when introduced. If symbols are given a different meaning than described here, this will be explained when it is introduced. When it is referred to 2D or 3D in the text this means two-dimensional and three-dimensional.

m	2D section mass for the floater
n	Integer referring to the mode number
$a_{33}^{(n)}$	2D vertical added mass for mode number n
$b_{33}^{(n)}$	2D vertical damping coefficient for mode number n
$c_{33}^{(n)}$	2D vertical restoring coefficient for mode number n
w	Vertical displacement of the floater
$\dot{w}$	Vertical velocity of the floater
$\ddot{w}$	Vertical acceleration of the floater
a_n	Vertical modal displacement. Fourier component number n.
$\dot{a}_n$	Vertical modal velocity
$\ddot{a}_n$	Vertical modal acceleration
f_3	Modal or 2D excitation force in z-direction
r	Relative motion in z-direction
σ	Bending stress
χ_σ	Most probable maximum bending stress in a sea state
ρ	Sea water density
g	Acceleration of gravity
ϕ	Velocity potential
ω	Circular wave frequency
ζ	Time and space dependent wave elevation
ζ_a	Wave amplitude
H	Wave height
λ	Wave length
$S(\omega)$	Spectral density function
$H_{1/3}$	Significant wave height
T_p	Spectral peak period
T_0	Spectral peak period
T_1	Spectral mean period
T_2	Mean zero up-crossing period
R	Radius of the floater
c	Floater pipe radius
b_w	Breadth of floater section
t	Pipe wall thickness and time. Wall thickness also referred to as t_w.
E	Young's modulus of elasticity
I	2nd area moment
β	Angle referring to the position $x = R\cos\beta$ on the floater

Chapter 1

Introduction

The scope of this master thesis is to investigate the vertical wave loads and vertical response of the floating collar of a circular fish farm. The forces and response of the floater are treated without the presence of net cage and mooring system. Since the floating collar is a slender structure and made of HDPE (high-density polyethylene) type plastic, hydroelasticity must be accounted for.

First, a linear load model will be used. The vertical displacements, relative motion between the floater and the waves, and the bending stresses will be investigated for regular linear long crested waves. Bending stresses will also be investigated in irregular long crested waves. A nonlinear model with respect to the pressure forces, found by integrating the hydrostatic and dynamic pressures over the exact wetted surface, taking elastic deformations of the floater into account, will be presented. The results in terms of vertical wave loads, displacements and bending stresses in regular waves for the nonlinear model will be compared with results obtained with the linear model.

The scope and motivation for this project is to gain knowledge and understanding of wave loads and the corresponding response of the floating collar of a circular fish farm. The floater is a flexible structure which is piercing the water surface. The study is theoretical. The starting point for the thesis is the formulation of velocity potentials and added mass presented in [Faltinsen (2011)].

In bad weather, the response of a fish farm might be violent, which in turn might damage the floater, net cage and mooring system. Structural failure of one or more of the components of a fish farm will have economic consequences due to repair costs and down time and ecologic and economic consequences if fish escape. It is therefore desirable to have a system that maintain its structural integrity in severe sea states. In this thesis, an isolated analysis of a freely floating collar will be investigated. Although this is a crude simplification and the total response of a fish farm must take all system components into account, this will give insight into the loads on the floater. In some periods the net is removed from the fish farm. The study conducted here, although the mooring system not is included in the analysis, will give general insight in the vertical excitation forces on the floating collar without the net.

Chapter 2

Physical Problem and Calculation Method

In this master thesis the vertical wave loads and vertical response of the floating collar of a circular fish farm will be investigated in linear long crested deep water waves. The effect of current is not treated. The floating collar is freely floating without the presence of mooring system, weights and net cage. Only vertical motion will be addressed. Thus, any coupling between horizontal and vertical motion will be neglected. For an operational fish farm, with mooring system, weights and net cage there will be force interaction between the nett, mooring system and the floating collar. From this statement one can draw the conclusion that one need to take all components of the system into account in order to fully understand and predict the response. In this thesis the vertical response of the floater will be separately investigated without taking horizontal deformations into account. This is done in order to simplify the problem. A linear model will be presented. A model using nonlinear hydrostatic and Froude-Kriloff forces will also be derived and the response compared with linear theory. Sometimes, the net cage is removed. In these cases there will be interesting to now how the floating collar will respond to wave loads. Although the floating collar without the net will be attached to the mooring system, this study will give insight into the loads on the floating collar. When the term response is mentioned and discussed in the text, this is always referring to the vertical response of the floater or the vertical excitation forces on the floater.

The floating collar of a circular fish farm is made of a high-density polyethylene (HDPE) type plastic. A typical HDPE type plastic has a Young's modulus of elasticity $E \approx 1000\ \mathrm{MPa}$, a yield stress $\sigma_y \approx 25\ \mathrm{MPa}$ and a density $\rho_p \approx 960\ \mathrm{kg/m^2}$. The floating collar of a circular fish farm typically consists of two concentric HDPE pipes. Typical dimensions are a ring diameter of $51\ \mathrm{m}$ and circumference of $160\ \mathrm{m}$. Fish farms with this size has typical pipe diameters from $400\ \mathrm{mm}$ to $500\ \mathrm{mm}$, and a pipe diameter to wall thickness ratio of approximately 17. The distance between the center of the pipes are $85\ \mathrm{cm}$ to $110\ \mathrm{cm}$. Floaters with only one ring exist. They are usually used for smaller fish farms. Three concentric pipes are also used, but this case will not be addressed in this work since the two ring configuration is most common for the dimensions presented above.

The dimensions used in this thesis will not be from a specific manufacturer of plastic pipes and/or collars. The dimensions will be chosen from typical values for existing collars, taken from different manufacturers. The idea is to have realistic dimensions without linking the dimensions and results to a specific company. The work in this project investigate the results for a theoretical method for force and response calculations. Results are presented for possible dimensions and material properties for the floating collar. The chosen dimensions and properties used are presented in Table 2.1. If other dimensions are used in the thesis they will be presented when used. If nothing else is stated, the dimensions in Table 2.1 are used. Both a floater with one ring and a floater configuration using two concentric rings will be addressed. For a floater with only one ring the diameter and the wall thickness of the pipe, compared with the values above, will be increased. The idea is that the two floater configurations will have the same displaced mass for the same radius R. The wall thickness is increased with the same factor as the diameter of the pipe giving the same pipe diameter to wall thickness ratio for both configurations. The factor is $\sqrt{2}$ for the dimensions presented in Table 2.1.

Parameter	Dimension	1 torus	2 tori
E	[MPa]	1000	1000
EI	[MNm^2]	3.085	1.543
σ_y	[MPa]	25	25
ρ_p	[$\mathrm{kg/m}^3$]	960	960
R	[m]	25.5	25.5
$2c$	[mm]	636	450
t	[mm]	36.2	25.6
$2p$	[cm]	-	100

Table 2.1: Dimensions for the floating collar for a one-ring and two-ring configuration, denoted 1 torus and 2 tori respectively. E, EI, I, σ_y, ρ_p are the Young modulus, bending stiffness, 2nd area moment, yield stress and plastic density, respectively. R, c, t and $2p$ are the radius of the ring, pipe radius, wall thickness and center to center distance between the pipes.

When calculating the added mass, forces and response, a sea water density $\rho = 1025\ \mathrm{kg/m}^3$ and a acceleration of gravity $g = 9.81\ \mathrm{m/s}^2$ are used. ρ is the density of sea water at approximately $18°C$ and a salinity of 3.5 percent, [Faltinsen (2005)]. This density is perhaps to low. The density for $10°C$ or $15°C$, being $1026.9\ \mathrm{kg/m}^3$ and $1025.9\ \mathrm{kg/M}^3$ for the same salinity, could have been used. The difference in the results for the different sea water densities are however small, and a density of $1025\ \mathrm{kg/m}^3$ will therefore be used.

2.1 Geometry, Boundaries and Axis Definitions

A principle figure of the global coordinate systems for a one ring (1 torus) and two ring (2 tori) configuration are shown in Figure 2.1. The local coordinate systems for 1 torus and 2 tori are shown in Figure 3.2 and 3.6 in Chapter 3. R is the radial distance from the origin to the center line of 1 torus and to the midpoint between the center lines for the pipes for 2 tori. β is the angle giving the x-coordinate on the floater $x = R\cos\beta$. This coordinate system and definition of β will be used when deriving the expressions for excitation forces and when presenting the results. The exception is Chapter 3, where a second definition of β will be used when deriving the velocity potentials for vertical motion. The new definition will be explained when used. Elsewhere, the definition of β is as explained above.

The only boundaries in the problem is the body surface and the mean free water surface. The extent of the fluid in horizontal direction goes to infinity. Deep water is assumed. That means infinite depth mathematically when deriving the velocity potentials. Incompressible non-viscous fluid is assumed.

2.2 Assumption of Draught

When deriving the velocity potential, added mass and linear excitation forces in Chapter 3 and 4, it is assumed that the draught of the floater in calm water equals the radius c of the pipe(s). This assumption is a good approximation of a real situation. But, when investigating a picture of a fish farm, Figure 2.2, it is seen that the draught is slightly less than the radius of the pipe. Whether this is true for all floating fish farms with circular plastic collar is not certain. The assumption of the draught being the radius c is still used. If it is the case that the draught is less, the results for added mass and excitation forces in this thesis might be conservative. The assumption is expected to give a good approximation since the difference in

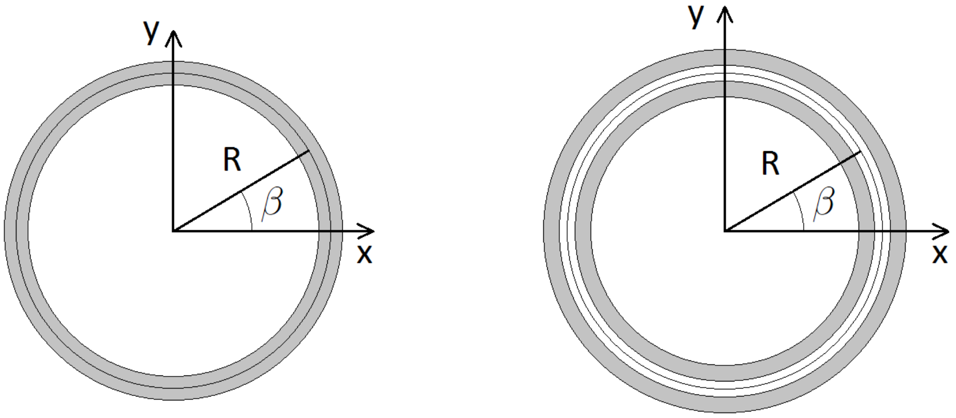

Figure 2.1: Global coordinate system for the floating collar. To the left: one ring. To the right: two rings. R is the radius of the collar, given as the radial distance from the origin $(0,0)$ to the center line of the floater. R is then the the distance from the origin to the center line of one ring and to the midpoint between the center lines for two rings, respectively. β is the angle defining the x-coordinate on the floater given by $x = R\cos\beta$.

the assumed and real draught is small. The investigation of the effect of reduced draught is not within the scope of this thesis.

Figure 2.2: Floating fish farm with circular plastic collar consisting of two concentric rings. The photo is taken from [Faltinsen (2011)]. (Photo: SINTEF Fisheries and Aquaculture)

2.3 Background

The picture in Figure 2.3 show a circular type fish farm in bad weather. The elastic deformations of the floater are clearly seen. Structural failure of one or more of the components of a fish farm will have economic and/or ecologic consequences. The equipment needs to be repaired, and fish may escape. The risk of failure is increasing in bad weather. It is therefore of interest to study the wave loads and response of the floating collar, and what maximum stresses that can be expected in a sea state. This thesis will focus on the floater response alone.

Figure 2.3: Fish farm with circular plastic collar in a storm in January 2006 in Flatanger, Norway. Elastic deformations of the floater are clearly seen. The photo is taken from [Kristiansen (2010)]. (Photo: Marius Dahle Olsen)

2.4 Matlab Code

In order to solve the task a Matlab program has been made. The code is presented in Appendix C. The program consists of several independent files or code and files containing user defined functions used by the program. A brief documentation and list of variables and used functions are given in the header of each file. Only files used for calculation of forces and responses are given in the Appendix. Files solely used for generation of figures and data post processing are not included. Two functions generating vtf-files for animation of the floater response in GLview Pro 6.5 is included.

In the theory, Chapter 3 and 4, and in the results, Chapter 6 and 7, there will be given brief physical explanations regarding the implementation of the theory in the Matlab code.

Chapter 3

Velocity Potential and Added Mass

Linear potential theory will be used to find the added mass for vertical motion of the floater. The floater is flexible and this must be taken into account when deriving the added mass. The vertical motion of the floater will be formulated as a sum of weighted orthogonal shape functions, or modes. Added mass will be mode dependent, and thus an added mass coefficient for each mode will be found. The only boundary conditions in the problem come from the body boundaries and the mean free surface. Deep water and a infinite horizontal extent of the fluid are assumed.

Since this is a three dimensional problem, three dimensional effects will effect the added mass per unit length for the floater. Thus, normal strip theory, where a 2D added mass for a heaving 2D semi-submerged circle is integrated over the floater, will not properly take the 3D effects into account. A far field and near field description of the the floater with asymptotic matching between the two must be applied in order to account for 3D effects, [Faltinsen (2011)].

In the following the velocity potential for a floater with one ring will be investigated and the added mass derived. Next, the added mass for a floater with two rings will be presented. A one ring configuration of the floater will be denoted 1 torus, while a configuration of the floater consisting of two concentric rings will be denoted 2 tori. Concentric meaning the two rings having the same midpoint. A torus is a surface of revolution generated by revolving a circle in three dimensions about an axis coplanar with the circle, [Wikipedia]. The plural form of torus is tori.

The velocity potentials for 1 torus and 2 tori and expression for added mass for 2 tori presented in this chapter are from [Faltinsen (2011)]. The presented derivation of the velocity potentials are a literature study in the subject. The work of deriving the potentials were done by Odd Magnus Faltinsen at Department of Marine Technology, Norwegian University of Science and Technology (NTNU), when writing the article given in the References as [Faltinsen (2011)].

3.1 Velocity Potential for 1 Torus

3.1.1 Far Field Description for Heave Motion

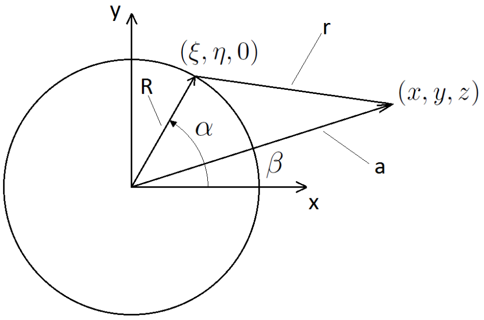

Figure 3.1: Far field view of the floater. (x, y, z) is the field point and $(\xi, \eta, 0)$ is a point on the floater. R is the floater radius and a is the distance to the field point from the origin. r is the distance from the field point to the position $(\xi, \eta, 0)$ on the floater.

Pure heave motion of the floater will now be considered. The far field view of the torus is seen in Figure 3.1. The axis system is a Cartesian system with $z = 0$ at the mean free surface. z is pointing upwards. In the far field view the details of the floater cross section and vertical displacements are not seen. (x, y, z) is the field point and $(\xi, \eta, 0)$ is a point on the floater. The field points x and y are defined by

$$\begin{aligned} x &= a\cos\beta \\ y &= a\sin\beta \end{aligned} \tag{3.1}$$

Here, a is the distance from the origin to the field point. β is the angle between the vector $\mathbf{a}$ and the x-axis defined in Figure 3.1. The coordinates $(\xi, \eta, 0)$ on the center line of the torus are

$$\begin{aligned} \xi &= R\cos\alpha \\ \eta &= R\sin\alpha \end{aligned} \tag{3.2}$$

Here, R is the radius of the floater (torus). α is the angle between the vector $\mathbf{R}$ and the x-axis. The distance r from the field point to a point on the floater is defined as

$$\begin{aligned} r &= \sqrt{(x-\xi)^2 + (y-\eta)^2 + z^2} \\ &= \sqrt{x^2 - 2xR\cos\alpha + y^2 - 2yR\sin\alpha + R^2 + z^2} \end{aligned} \tag{3.3}$$

Here, equation (3.2) is utilized. In potential theory the geometry of certain bodies can be represented by a suitable combination of sources, sinks and point dipoles within the body, [Newman (1977)]. The use of sources, sinks and dipoles can for instance in 2D represent the flow around circles, ovals, semi-infinite half-bodies, corners or flow around these objects close to a wall or the free surface. Sources and sinks are singular points where it is imagined that fluid is flowing out of or in to. The flow is uniform in all directions, [Faltinsen (1990)]. For flow exterior to the body surface a distribution of volume singularities on the surface can be used to represent the flow, [Newman (1977)]. In the far field view the details of the cross section are not seen. The effects of the motion of the torus seen from a distance can be interpreted as a volume flux with value Q. The floater can thus be represented by a source distribution on the center line of the torus. Since the details of the cross sections are hidden in the far field view and the floater is a slender structure, the center line and not the surface is used. The velocity potential for a 3D point source in a fluid at rest at infinity, from [Newman (1977)], is

$$\phi = \frac{Q}{4\pi r} = \frac{Q}{4\pi\sqrt{(x-\xi)^2 + (y-\eta)^2 + (z-\zeta)^2}} \tag{3.4}$$

Here, r is the distance from the source point. Q is the source strength. (x, y, z) and (ξ, η, ζ) are the field and source point respectively. In the far field view, $\zeta = 0$. For the case addressed here, the torus will be represented by a source distribution. The expression for the distribution is found by integrating the expression for a source point around the floater with respect to the angle α. The expression is given in equation (3.5), [Faltinsen. Personal communication (2011)].

$$\phi^F = \frac{QR}{4\pi}\int_0^{2\pi}\frac{d\alpha}{r} = \frac{QR}{4\pi}\int_0^{2\pi}\frac{d\alpha}{\sqrt{x^2 - 2xR\cos\alpha + y^2 - 2yR\sin\alpha + R^2 + z^2}} \tag{3.5}$$

Q is the density of the source distribution. The distance r from the field point to $(\xi, \eta, 0)$ is integrated around the torus with respect to α. The radial distance from the field point in equation (3.5) to the center line of the torus can be expressed as $r = \sqrt{(x - R\cos\beta)^2 + (y - R\sin\beta)^2 + z^2}$. If this and equation (3.1) are used the radial distance can be written as $r = \sqrt{(a-R)^2 + z^2}$. If these expressions are utilized and the angle $\alpha_1 = \alpha - \beta$ is introduced, equation (3.5) can be written as

$$\begin{aligned}\phi^F &= \frac{QR}{4\pi}\int_0^{2\pi}\frac{d\alpha}{\sqrt{a^2 + R^2 + z^2 - 2aR\cos(\beta - \alpha)}} \\ &= \frac{QR}{4\pi}\int_0^{2\pi}\frac{d\alpha_1}{\sqrt{r^2 + 2aR(1 - \cos\alpha_1)}}\end{aligned} \tag{3.6}$$

Solving equation (3.6) in Maple gives

$$\phi^F = \frac{QR}{\pi\sqrt{r^2 + 4aR}} K\left(2\sqrt{\frac{aR}{r^2 + 4aR}}\right) \tag{3.7}$$

Here, $K()$ is the elliptic K-function defined in Maple. A first term inner expansion of equation (3.7) around $r = 0$ in Maple will give this expression for the far field velocity potential.

$$\phi_I^F = \frac{Q}{2\pi}\ln\left(\frac{8R}{r}\right) \tag{3.8}$$

This is the same expression as in [Faltinsen (2011)] for heave.

3.1.2 Far Field Description for General Motion

The vertical motion of the floater can be expressed by a Fourier sum consisting of weighted orthogonal mode shapes defined by $\cos n\beta$, [Faltinsen. Personal communication (2011)]. n is a positive integer. The mode shapes are defined by a cosine function, since the response is assumed to be symmetric about the x-axis for waves propagating in the positive x-direction. The method of using a sum of weighted orthogonal modes in order to explain the total response of a slender flexible structure is called mode superposition. The method is used for instance in springing response calculation of ships, [Faltinsen (2005)], and response of risers in current and waves, [Larsen & Halse (1997)]. The expression for the vertical displacement is presented in Chapter 4. The vertical velocity can be expressed as

$$\dot{w} = \dot{a}_0 + \sum_{n=1}^{\infty} \dot{a}_n \cos n\beta \tag{3.9}$$

$\dot{a}_0$ is the heave velocity and $\dot{a}_n \cos n\beta$ is the vertical velocity of the n-th mode on the position β on the floater given in Chapter 2. The general far field velocity potential associated with the general mode $\cos n\beta$ can be expressed with a similar expression as the velocity potential for heave motion. The difference is that the source distribution now has the strength $Q \cos n\beta$, [Faltinsen (2011)]. The expression is

$$\phi_n^F = \frac{QR}{4\pi} \int_0^{2\pi} \frac{cos(n\alpha)}{r}\, d\alpha = \frac{QR}{4\pi} \int_0^{2\pi} \frac{cos(n\alpha) d\alpha}{\sqrt{r^2 + 2aR[1 - \cos(\alpha - \beta)]}} \tag{3.10}$$

Here, β is replaced by α according to Figure 3.1 . The distance r is equal to $\sqrt{(x-\xi)^2 + (y-\eta)^2 + z^2}$, which can be expressed as $\sqrt{r^2 + 2aR[1 - \cos(\alpha - \beta)]}$ where r is the radial distance. Similar to the derivation of the far field potential in heave, the angle $\alpha_1 = \alpha - \beta$ is introduced. The general far field potential can now be expressed as

$$\phi_n^F = \frac{QR}{4\pi} \int_0^{2\pi} \frac{cos(n\alpha_1 - n\beta) d\alpha_1}{\sqrt{r^2 + 2aR(1 - \cos\alpha_1)}} = \frac{QR}{4\pi} \cos(n\beta) \int_0^{2\pi} \frac{cos(n\alpha_1) d\alpha_1}{\sqrt{r^2 + 2aR(1 - \cos\alpha_1)}} \tag{3.11}$$

Rewriting this expression will give

$$\phi_n^F = \frac{QR}{4\pi} \cos(n\beta) \left[\int_0^{2\pi} \frac{d\alpha_1}{\sqrt{r^2 + 2aR(1 - \cos\alpha_1)}} - \int_0^{2\pi} \frac{[1 - \cos(n\alpha_1)] d\alpha_1}{\sqrt{r^2 + 2aR(1 - \cos\alpha_1)}} \right] \tag{3.12}$$

The first term on the right hand side of the equation can by expressing the term with the elliptic K-function and inner expansion around $r = 0$ be expressed as

$$\frac{Q}{2\pi} \cos(n\beta) \ln\left(\frac{8R}{r}\right) \tag{3.13}$$

The same procedure as for the far field velocity potential for heave in Section 3.1.1 is applied. A first term linear inner expansion of the second term on the right hand side of equation (3.12) is found by setting $r = 0$ and $a = R$, and performing a series expansion in Maple. The linear first term is

$$\frac{Q}{2\pi} \cos(n\beta) \frac{1}{2\sqrt{2}} \int_0^{2\pi} \frac{[1 - \cos(n\alpha_1)] d\alpha_1}{\sqrt{1 - \cos\alpha_1}} \tag{3.14}$$

$$K_n = \frac{1}{2\sqrt{2}} \int_0^{2\pi} \frac{[1 - \cos(n\alpha_1)] d\alpha_1}{\sqrt{1 - \cos\alpha_1}} \tag{3.15}$$

The results for K_n for the first 10 modes are presented in Table 3.1. The general expression for the far field velocity potential for the modes associated with $\cos n\beta$ is obtained by using the expressions in equation (3.13) and (3.14). The general far field potential for mode n is

$$\phi^F_{n,I} = \frac{Q}{2\pi}\cos(n\beta)\left[ln\left(\frac{8R}{r}\right) - K_n\right] \tag{3.16}$$

β is now referring to the x-position $x = R\cos\beta$ on the torus. By setting $n = 0$ in equation (3.16) the expression for the inner expansion of the far field potential for heave presented in equation (3.8) is found. This indicates that the far field expression for the general mode $\cos n\beta$ can be used to represent heave motion if $n = 0$. Equation (3.16) is the same expression for the general far field velocity potential as in [Faltinsen (2011)].

n	0	1	2	3	4	5	6	7	8	9
K_n	0	2.0000	2.6667	3.0667	3.3524	3.5746	3.7564	3.9103	4.0436	4.1612

Table 3.1: Values for K_n given by the integral in equation (3.15). n is the mode number.

3.1.3 Near Field Description for Heave Motion

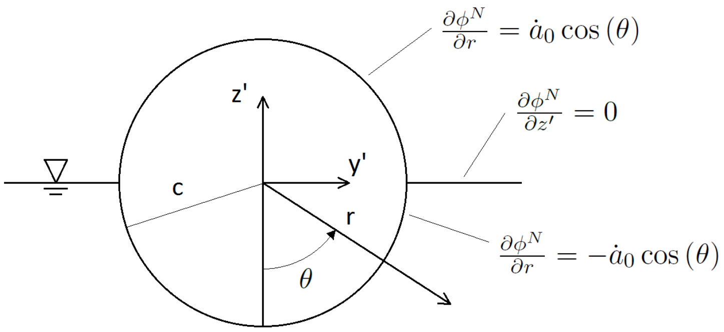

Figure 3.2: Near field view of the floater. $\dot{a}_0$ is the heave velocity of the torus. $\partial\phi^N/\partial r$ and $\partial\phi^N/\partial z'$ are the body boundary condition and the rigid free surface condition respectively. $\cos\theta$ is the negative z'-component of the body normal vector. c is the pipe radius. The draught of the section is c.

In the near field description the details of the torus cross section are seen. The draught of the section is assumed to be equal to the radius c of the section. Figure 3.2 shows the torus cross section in the near field view. A local Cartesian and a local polar coordinate system with the coordinates (y', z') and (r, θ) are defined. The relationship between the coordinate systems are $y' = r\sin\theta$ and $z' = -r\cos\theta$. θ is defined as zero at the negative z'-axis. The boundary conditions on the circle surface are

$$\frac{\partial\phi^N}{\partial r} = \begin{cases} -\dot{a}_0\cos(\theta) & \text{for } -\pi/2 < \theta < \pi/2 \\ \dot{a}_0\cos(\theta) & \text{for } \pi/2 < \theta < 3\pi/2 \end{cases} \tag{3.17}$$

$\dot{a}_0$ is the heave velocity of the floater. $\cos\theta$ is the negative z'-component of the body normal vector. The boundary conditions in equation (3.17) demand that there is no fluid flow through the boundaries of the circle. The case when the circular frequency of the forced oscillation is small and goes to zero is investigated. That is $\omega \to 0$. The rigid free surface condition presented in equation (3.18) must be satisfied.

$$\frac{\partial\phi^N}{\partial z'} = 0 \quad \text{, on the water surface at } z' = 0 \tag{3.18}$$

The linearized free surface condition for regular linear waves, $-\omega^2\phi_0 + g\partial\phi_0/\partial z = 0$ on $z = 0$, [Faltinsen (1990)], is reduced to equation (3.18) when $\omega \to 0$. ω, ϕ_0 and g are the wave frequency, wave potential and acceleration of gravity, respectively. When investigating the velocity potential of the torus cross section, incident waves are not considered. However, a heaving 2D cylindrical section piercing the free surface will generate waves. The procedure above, illustrates how a rigid free surface condition can be derived. The case investigated, when $\omega \to 0$, demands that the rigid free surface condition must be satisfied, thus no waves are generated.

The two semicircles in figure (3.2) defined by $-\pi/2 < \theta < \pi/2$ and $\pi/2 < \theta < 3\pi/2$ are assumed to have harmonic motion with opposite signs, explaining the formulation of the body boundary conditions in equation (3.17). The rigid surface condition in equation (3.18) then holds since the flow will be symmetric about the y'-axis, meaning no vertical flow at $z' = 0$. The magnitude of the heave motion for the two semicircles heaving with opposite signs is $\dot{a}_0$. In [Newman (1977)], a general expression for the velocity potential for a 2D cylinder in a uniform stream in infinite fluid is presented. This expression can also be used for fluid at rest at infinity for a cylinder with uniform or slowly varying motion. In this case harmonic oscillating motion with velocity $\dot{a}_0$. The velocity potential from [Newman (1977)] is

$$\phi = \sum_{n=1}^{\infty} \cos(n\theta) \left(A_n r^n + \frac{B_n}{r^n} \right) + A_0 + B_0 \ln(r) \tag{3.19}$$

The expression has singularities at $r = 0$ and at infinity. The expression will be used for flow exterior to the body. A_n, B_n, A_0 and B_0 are constants. r is the radial distance from the center of the section. The expression above together with a similar series with $\cos n\theta$ replaced by $\sin n\theta$ is a general solution of the problem. The expression in equation (3.19) is equivalent to expressing the complex potential by a Laurent series plus a logarithmic source term, [Newman (1977)]. The series involving $\sin n\theta$ is ruled out since the flow around the torus section for the heaving semicircles is symmetric about the z-axis. The boundary condition at infinity is $\phi \to 0$, demanding that velocities due to heave motion of the floater section is zero when $r \to \infty$, state that the term $A_n r^n$ in equation (3.19) not is a part of the solution for the problem addressed here. The term $A_0 + B_0 \ln(r)$ can be replaced by $C \ln(r/R)$, where R is the radius of the floater, since $\ln(R)$ is a constant. For a body with slowly varying velocity the potential is proportional to the velocity of the body, [Newman (1977)]. The general velocity potential for this case can now be expressed as shown in equation (3.20), [Faltinsen. Personal communication (2011)].

$$\phi^N = \dot{a}_0 \left[Cln\left(\frac{r}{R}\right) + A_0 + \sum_{n=1}^{\infty} A_n \frac{\cos n\theta}{r^n} \right] \tag{3.20}$$

C, A_0 and A_n are constants. A_0 and A_n are not the same constants as in equation (3.19). In order to determine the constants the body boundary conditions and rigig free surface condition must be satisfied. The velocity potential is differentiated with respect to the radial distance r in the local coordinate system. The expression for the differentiated potential on the body surface, given by $r = c$ is

$$\frac{\partial \phi^N}{\partial r}_{(r=c)} = \dot{a}_0 \left(\frac{C}{c} - \sum_{n=1}^{\infty} n A_n \frac{\cos n\theta}{c^{n+1}} \right) \tag{3.21}$$

The derivative of the velocity potential is now set equal to the body boundary conditions in equation (3.17) and integrated from $\theta = -\pi$ to $\theta = \pi$. The expression is as follows.

$$\dot{a}_0 \left[\int_{-\pi}^{-\pi/2} \cos\theta \, d\theta - \int_{-\pi/2}^{\pi/2} \cos\theta \, d\theta + \int_{\pi/2}^{\pi} \cos\theta \, d\theta \right] = \dot{a}_0 \int_{-\pi}^{\pi} \left(\frac{C}{c} - \sum_{n=1}^{\infty} n A_n \frac{\cos n\theta}{c^{n+1}} \right) d\theta \tag{3.22}$$

Equation (3.22) is solved with respect to C. The result is

$$C = -\frac{2c}{\pi} \tag{3.23}$$

In order to find the constant A_n the body boundary condition in equation (3.17) and the derivative of the velocity potential in equation (3.21) are multiplied with the orthogonal function $\cos m\beta$, and integrated from $\beta = -\pi$ to $\beta = \pi$. The expression and solution for A_n are presented in equation (3.24) and (3.25) respectively.

$$-\int\limits_{-\pi/2}^{\pi/2} \cos\theta \cos m\theta \; d\theta + \int\limits_{\pi/2}^{3\pi/2} \cos\theta \cos m\theta \; d\theta = \int\limits_{-\pi}^{\pi} \left[\frac{C}{c} \cos m\theta - \sum_{n=1}^{\infty} nA_n \frac{\cos n\theta}{c^{n+1}} \cos m\theta \right] d\theta \tag{3.24}$$

$$A_n = -c^{n+1} \frac{3\cos\frac{n\pi}{2} + \cos\frac{3n\pi}{2}}{n\pi(n^2-1)} \tag{3.25}$$

Since $A_n = 0$ for $n = 1, 3, 5...$ the variable m defined by $n = 2m$ is introduced. The constant A_{2m} is introduced.

$$A_{2m} = -c^{2m+1} \frac{3\cos(m\pi) + \cos(3m\pi)}{2m\pi(4m^2-1)} \tag{3.26}$$

The near field velocity potential can now be written as

$$\phi^N = \dot{a}_0 \left[-\frac{2c}{\pi} ln\left(\frac{r}{R}\right) + A_0 + \sum_{m=1}^{\infty} A_{2m} \frac{\cos 2m\theta}{r^{2m}} \right] \tag{3.27}$$

3.1.4 Near Field Description for General Motion

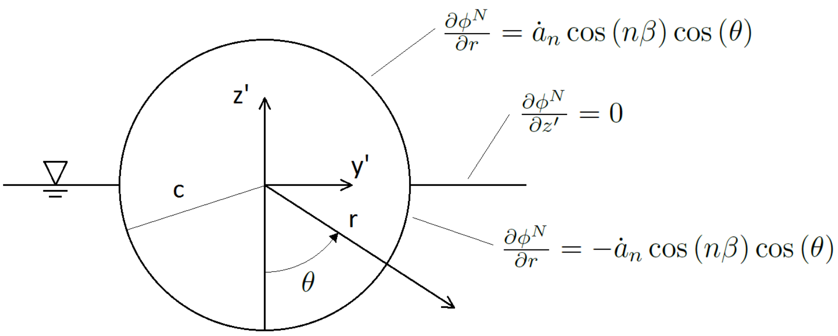

Figure 3.3: Near field view of the floater. $\dot{a}_n \cos n\beta$ is the modal vertical velocity of the torus section at the position $x = R\cos\beta$ in the global coordinate system (x, y, z). $\partial\phi^N/\partial r$ and $\partial\phi^N/\partial z'$ are the body boundary condition and the rigid free surface condition respectively. $\cos\theta$ is the negative z'-component of the body normal vector. c is the pipe radius.

The general velocity potential for the near field description for the motion mode $\cos n\beta$ has the same form as the near field velocity potential for heave presented in equation (3.20). The exception is that the velocity potential now is proportional to the general vertical velocity $\dot{a}_n \cos n\beta$ for mode n at the position β on the floater. The expression for the velocity potential is

$$\phi_n^N = \dot{a}_n \cos n\beta \left[Cln\left(\frac{r}{R}\right) + C_n + \sum_{n=0}^{\infty} A_n \frac{\cos n\theta}{r^n} \right] \tag{3.28}$$

The derivative of the near field velocity potential with respect to r for $r = c$ is

$$\frac{\partial \phi_n^N}{\partial r}_{(r=c)} = \dot{a}_n \cos n\beta \left[\frac{C}{c} - \sum_{n=0}^{\infty} n A_n \frac{\cos n\theta}{c^n} \right] \tag{3.29}$$

In order to find the constants C and A_n the body boundary conditions in equation (3.30) are introduced.

$$\frac{\partial \phi^N}{\partial r}_{(r=c)} = \begin{cases} -\dot{a}_n \cos(n\beta)\cos(\theta) & \text{for } -\pi/2 < \theta < \pi/2 \\ \dot{a}_n \cos(n\beta)\cos(\theta) & \text{for } \pi/2 < \theta < 3\pi/2 \end{cases} \tag{3.30}$$

The body boundary conditions demands that there is no fluid flow through the surface of the floater section. $\dot{a}_n \cos(n\beta)$ is the vertical velocity associated with the orthogonal mode shape $\cos n\beta$. In order to find the constant C the body boundary conditions are set equal to the derivate of the velocity potential for $r = c$. The resulting expression is integrated from $\beta = -\pi$ to $\beta = \pi$. The procedure is the same as in Section 3.1.3. The result is $C = -2c/\pi$, which is the same result obtained in equation in Section 3.1.3. The constant A_n is found by setting the body boundary condition equal to the derivate of the velocity potential with respect to r, multiplying with the orthogonal function $\cos m\beta$ and integrating from $\beta = -\pi$ to $\beta =$. The procedure for finding A_n and the result are the same as for heave motion of the floater. The constant is now denoted A_{2m}, given in equation (3.26). The general near field velocity potential for mode motion given by $\cos n\beta$ can now be written as

$$\phi_n^N = \dot{a}_n \cos n\beta \left[-\frac{2c}{\pi} ln\left(\frac{r}{R}\right) + C_n + \sum_{m=1}^{\infty} A_{2m} \frac{\cos(2m\theta)}{r^{2m}} \right] \tag{3.31}$$

3.1.5 Matching of The Far Field and Near Field Velocity Potentials

The constants A_0 and C_n in the expressions for the near field potential for heave and general vertical motion, respectively, can be found by matched asymptotic expansion of the far field and the near field velocity potentials, [Faltinsen (2011)]. The matching is performed by setting the expression for the far field potential equal to the near field potential, [Faltinsen. Personal communication (2011)]. r goes to infinity in the near field expression. This procedure demands the two potentials to be equal. The far field expression is used as close to the torus as possible, while the near field description is used as far out from the section as possible. The matching determines a constant in the near field solution, and makes the expression unique. Asymptotic matching is used since a classic 2D solution in the frequency domain of the near field expression for deep water including gravity will go to infinity when $\omega \to 0$, thus giving infinite added mass for the 2D section of the floater, [Faltinsen (2011)].

For pure heave motion, ϕ_I^F and ϕ^N, from equation (3.8) and (3.27) respectively, are demanded equal when $r \to \infty$ in the expression for ϕ^N. The result is

$$\begin{gathered} \phi_I^F = \phi^N_{(r\to\infty)} \\ \frac{Q}{2\pi}\ln 8 - \frac{Q}{2\pi}\ln\left(\frac{r}{R}\right) = \dot{a}_0 A_0 - \dot{a}_0 \frac{2c}{\pi}\ln\left(\frac{r}{R}\right) \end{gathered} \tag{3.32}$$

Here, $C = -2c/\pi$ is used. The equation is solved for $\dot{a}_0$ and A_0. The velocity is found to be $\dot{a}_0 = Q/4c$. The result for A_0 is

$$A_0 = \frac{2c}{\pi} \ln 8 \tag{3.33}$$

For the general vertical motion $\dot{a}_0 \cos n\beta$ the velocity potentials $\phi^F_{n,I}$ and ϕ^N_n, from equation (3.16) and (3.31), are demanded equal when $r \to \infty$ in ϕ^N_n. The resulting expression is

$$\begin{gathered} \phi^F_{n,I} = \phi^N_{n,(r\to\infty)} \\ \frac{Q}{2\pi} \cos n\beta \left[\ln 8 - \ln\left(\frac{r}{R}\right) - K_n \right] = \dot{a}_n \cos n\beta \left[C_n - \frac{2c}{\pi} \ln\left(\frac{r}{R}\right) \right] \end{gathered} \tag{3.34}$$

The equation is solved for $\dot{a}_n$ and C_n. The general velocity is $\dot{a}_n = Q/4c$, and the expression for C_n is

$$C_n = \frac{2c}{\pi} (\ln 8 - K_n) \tag{3.35}$$

If $n = 0$ in the expression for C_n, A_0 and C_n will be equal. The expression for the near field potential for a general vertical velocity $\dot{a}_n \cos n\beta$ inserted for the constants is

$$\phi^N_n = \dot{a}_n \cos n\beta \left\{ \frac{2c}{\pi} \left[\ln\left(\frac{8R}{r}\right) - K_n \right] - \sum_{m=1}^{\infty} c^{2m+1} \frac{3\cos(m\pi) + \cos(3m\pi)}{2m\pi(4m^2-1)} \frac{cos(2m\theta)}{r^{2m}} \right\} \tag{3.36}$$

This is the same expression for the near field solution as presented in [Faltinsen (2011)]. If heave is to be considered from this expression, $n = 0$ is used. This indicates that the velocity potential in equation (3.36) can be used for all modes $\cos n\beta$ where $n = 0, 1, 2...$

3.2 Added Mass for One Torus

3.2.1 Added Mass in Heave

The near field velocity potential for motion mode n on the surface of the torus, $r = c$, is

$$\phi^N_n = \dot{a}_n \cos(n\beta) \left\{ \frac{2c}{\pi} \left[\ln\left(\frac{8R}{c}\right) - K_n \right] - c \sum_{m=1}^{\infty} \frac{3\cos(m\pi) + \cos(3m\pi)}{2m\pi(4m^2-1)} \cos(2m\theta) \right\} \tag{3.37}$$

In order to find the 2D added mass inn heave the forces per unit length on the torus due to forced motion in heave must be found. The forcing motion is the harmonic velocity of the floater section $\dot{a}_n \cos(n\beta)$. For heave, where $n = 0$, this velocity is $\dot{a}_0$. When $n = 0$ equation (3.37) is reduced to

$$\phi^N_{n=0} = \dot{a}_0 \left[\frac{2c}{\pi} \ln\left(\frac{8R}{c}\right) - c \sum_{m=1}^{\infty} \frac{3\cos(m\pi) + \cos(3m\pi)}{2m\pi(4m^2-1)} \cos(2m\theta) \right] \tag{3.38}$$

The hydrodynamic vertical force on the torus section is found by integrating the dynamic pressure due to forced motion over the mean wetted surface of the section, [Newman (1977)]. The dynamic pressure is $-\rho\partial\phi^N_{n=0}/\partial t$. The dynamic pressure is multiplied with the section radius c and the negative z'-component, $\cos\theta$, of the body normal vector, and integrated from $\theta = -\pi/2$ to $\theta = \pi/2$. The expression and answer are shown in equation (3.39) and (3.40) respectively.

$$\begin{aligned} f_3 &= -\int\limits_{-\pi/2}^{\pi/2} p_{dyn} n_3 c \, d\theta \\ &= -\rho \int\limits_{-\pi/2}^{\pi/2} \frac{\partial\phi^N_{n=0}}{\partial t} \cos(\theta) c \, d\theta \\ &= -\rho \int\limits_{-\pi/2}^{\pi/2} \left[\frac{2c}{\pi} \ln\left(\frac{8R}{c}\right) - c\sum_{m=1}^{\infty} \frac{3\cos(m\pi) + \cos(3m\pi)}{2\pi m(4m^2-1)} \cos(2m\theta) \right] \cos(\theta) c \, d\theta \, \ddot{a}_0 \end{aligned} \tag{3.39}$$

$$f_3 = -2\rho c^2 \left[\frac{2}{\pi} \ln\left(\frac{8R}{c}\right) + \frac{3 - 4ln2}{\pi} \right] \ddot{a}_0 \tag{3.40}$$

$$\frac{3 - 4\ln 2}{\pi} = 0.072387258 \tag{3.41}$$

The result for f_3 in equation (3.40) is found by solving equation (3.39) in Maple. n_3 in equation (3.39) is the component of the body normal vector in z'-direction. Since the expression for the force due to the forced motion of the floater section can be written as $f_3 = -a^{(0)}_{33}\ddot{a}_0$, where $a^{(0)}_{33}$ is the 2D added mass in heave, [Faltinsen (1990)], the added mass for heave motion per unit length for the floater is

$$a^{(0)}_{33} = 2\rho c^2 \left[\frac{2}{\pi} \ln\left(\frac{8R}{c}\right) + \frac{3 - 4\ln 2}{\pi} \right] \tag{3.42}$$

The 3D added mass A_{33} can be found by integrating the expression for the 2D added mass in equation (3.42) around the center line of the torus, from $\beta = 0$ to $\beta = 2\pi$. Alternatively, the expression for the force per unit length in equation (3.40) can be integrated around the center line of the torus from $\beta = 0$ to $\beta = 2\pi$. It can then be used that the resulting force F_3 can be expressed as $F_3 = -A_{33}\ddot{a}_0$ in order to find the 3D added mass A_{33} due to heave motion. The expression and solution for A_{33} is

$$\begin{aligned} A_{33} &= \int\limits_{0}^{2\pi} a^{(0)}_{33} R \, d\beta \\ &= 2\pi R a^{(0)}_{33} \\ &= 4\rho\pi c^2 R \left[\frac{2}{\pi} \ln\left(\frac{8R}{c}\right) + \frac{3 - 4\ln 2}{\pi} \right] \end{aligned} \tag{3.43}$$

The non dimensional added mass A_{33}/M is found by dividing equation (3.43) with the submerged mass of the floater $M = \rho\pi^2 c^2 R$. The non dimensional added mass for heave motion is

$$\frac{A_{33}}{M} = \frac{4}{\pi} \left[\frac{2}{\pi} \ln\left(\frac{8R}{c}\right) + \frac{3 - 4\ln 2}{\pi} \right] \tag{3.44}$$

3.2.2 Vertical Added Mass for Mode n

The general expression for added mass for motion mode n can be found in the same way as explained in Section 3.2.1. Now, the near field velocity potential for vertical motion mode n in equation (3.37) must be used. The floater section is given a forced oscillation with velocity $\dot{a}_n \cos n\beta$, where β is the angle referring to the global x-coordinate for the center line of the floater. The dynamic pressure $-\rho\partial\phi_n^N/\partial t$ is found by differentiating equation (3.37) with respect to t. The dynamic pressure is multiplied with the z'-component of the negative body normal vector, $\cos\theta$, and the radius c of the section and integrated over the mean wetted surface from $\theta = -\pi/2$ to $\theta = \pi/2$. The result is the force in z-direction per unit length on the floater due to the forced motion. The expression for the force per unit length is

$$\begin{aligned} f_3 =& -\int\limits_{-\pi/2}^{\pi/2} p_{dyn} n_3 c\, d\theta \\ =& -\rho \int\limits_{-\pi/2}^{\pi/2} \frac{\partial \phi_n^N}{\partial t} \cos(\theta) c\, d\theta \\ =& -\rho \int\limits_{-\pi/2}^{\pi/2} \left[\frac{2c}{\pi} \left\{ \ln\left(\frac{8R}{c}\right) - K_n \right\} - c \sum_{m=1}^{\infty} \frac{3\cos(m\pi) + \cos(3m\pi)}{2\pi m(4m^2-1)} \cos(2m\theta) \right] \\ & \cdot \cos(\theta) c\, d\theta\, \ddot{a}_0 \cos n\beta \end{aligned} \tag{3.45}$$

n_3 is the z'-component of the body normal vector $-\cos\theta$, and K_n is defined in equation (3.15). Equation (3.45) is solved in Maple. The result for f_3 is

$$f_3 = -2\rho c^2 \left[\frac{2}{\pi} \left\{ \ln\left(\frac{8R}{c}\right) - K_n \right\} + \frac{3 - 4\ln 2}{\pi} \right] \ddot{a}_n \cos n\beta \tag{3.46}$$

The force per unit length due to forced motion can formally be expressed as $f_3 = -a_{33}^{(n)} \ddot{a}_n \cos n\beta$. $a_{33}^{(n)}$ is the added mass per unit length in z-direction associated with the vertical motion of the section $a_n \cos n\beta$ of mode number n. If this expression for f_3 is utilized the added mass in z-direction associated with mode n can be written as

$$a_{33}^{(n)} = 2\rho c^2 \left[\frac{2}{\pi} \left\{ \ln\left(\frac{8R}{c}\right) - K_n \right\} + \frac{3 - 4\ln 2}{\pi} \right] \tag{3.47}$$

The added mass in heave could also be found from this expression. If $n = 0$ in equation (3.47), $K_n = 0$, and the result is the same expression as in equation (3.42). The 3D added mass for mode n can be found by multiplying $a_{33}^{(n)}$ with $\cos^2 n\beta$ and integrating the expression around the torus from $\beta = 0$ to $\beta = 2\pi$. The expression for the 3D added mass is

$$A_{(3+n)(3+n)} = \int\limits_{0}^{2\pi} a_{33}^{(n)} R \cos^2(n\beta)\, d\beta = \begin{cases} 2\pi R a_{33}^{(0)} & \text{,for } n = 0 \\ \pi R a_{33}^{(n)} & \text{,for } n = 1, 2, 3... \end{cases} \tag{3.48}$$

By dividing with the submerged mass $M = \rho\pi^2 c^2 R$ of the torus the non dimensional 3D added mass can be expressed as

$$\frac{A_{(3+n)(3+n)}}{M} = \frac{2K}{\pi}\left[\frac{2}{\pi}\left\{\ln\left(\frac{8R}{c}\right) - K_n\right\} + \frac{3-4\ln 2}{\pi}\right], \begin{cases} K=2 & \text{,for } n=0 \\ K=1 & \text{,for } n=1,2,3... \end{cases} \tag{3.49}$$

If $n = 0$ in equation (3.49) the expression for the 3D heave added mass is obtained. The results for the non dimensional added mass calculated from equation (3.49) are compared with non dimensional added mass calculated with a BEM (Boundary Element Method) program. The added mass for heave, pitch and the first elastic mode are compared with the slender body theory presented in this chapter. The results for added mass using a BEM program where calculated and given by [Shao. Personal communication (2011)]. Figure 3.4 shows the comparison between slender body theory and BEM. The results are plotted as a function of c/R, where c and R are the section radius and the torus radius respectively. The comparison between slender body theory and BEM shows good agreement for the value of $c/R \approx 0.025$ used in this thesis for 1 torus.

The non dimensional 2D added mass results for one torus for the first six modes are presented in Figure 3.5. The results are plotted as a function of c/R. The 2D added mass is made dimensionless by dividing with the 2D mass of the section, $m = \rho\pi c^2/2$.

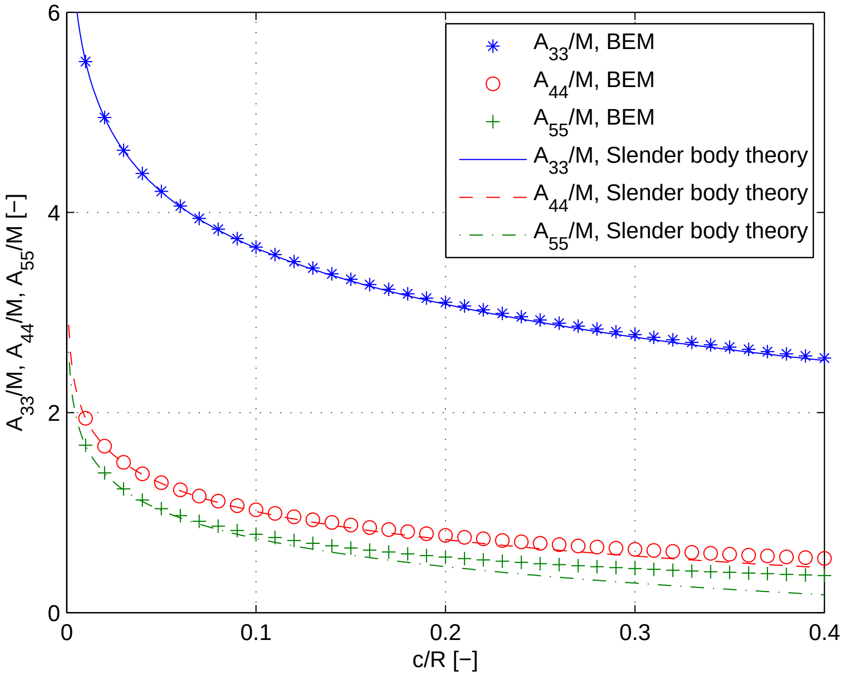

Figure 3.4: Comparison between 3D non dimensional added mass for 1 torus calculated with slender body theory and BEM. BEM results provided by [Shao. Personal communication (2011)]. A_{33}, A_{44} and A_{55} are the 3D added mass in z-direction for heave, pitch and the first elastic mode. $M = \rho\pi^2c^2R$ is the submerged mass of the torus. c is the pipe radius and R is the radius of the torus.

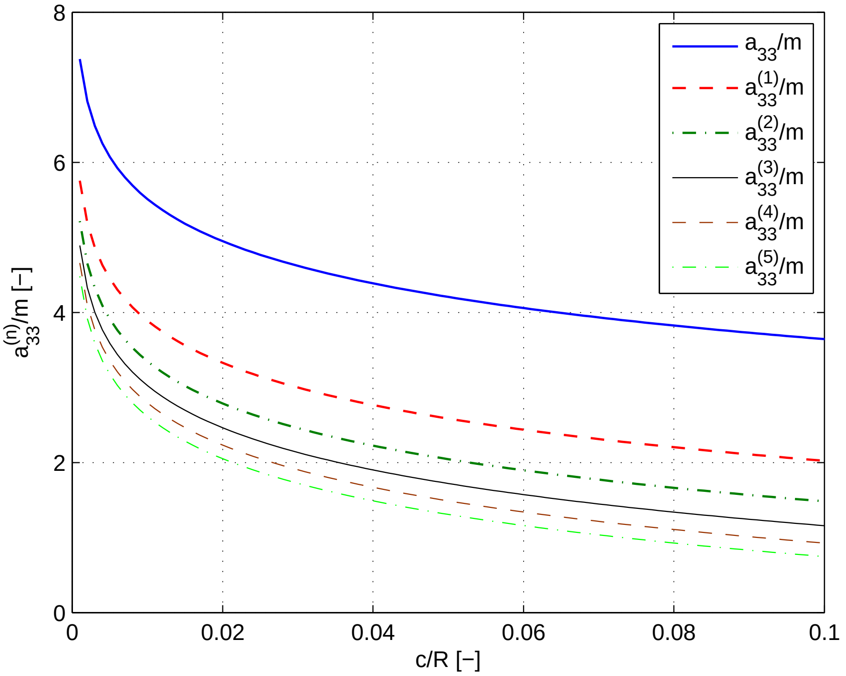

Figure 3.5: 2D non dimensional added mass for 1 torus. $a_{33}^{(n)}$ is the 2D added mass in z-direction associated with the mode shape $\cos n\beta$. $m = \rho\pi c^2/2$ is the 2D mass of the floater. c is the radius if the section. R is the radius of the floater.

3.3 Added Mass Two Tori

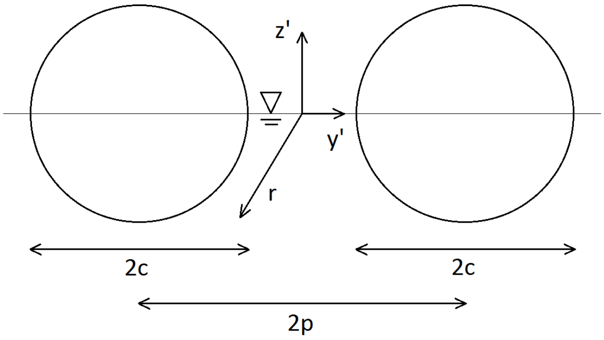

Figure 3.6: Near field view for 2 tori. $2p$ is the horizontal center to center distance between the pipes. p is the horizontal distance between the local coordinate system (y', z') and the center of the pipes. c is the radius of the pipes. R is the radius of the torus.

The near field view for 2 tori is shown in Figure 3.6. Here, $2p$ is the horizontal distance between the center of the two sections. p is the horizontal distance from the origin of the local coordinate system (y', z') to the center line of one of the pipes. The radius R of the tori is now defined as the horizontal distance from the origin of the global coordinate system (x, y, z) to the local coordinate system (y', z'). The origin of the local coordinate system is situated between the centers of the two tori sections as shown in Figure 3.6.

A near field potential for two tori is formulated with a BEM, and matching between the far field and near field expression is done in order to solve for the constants in the near field expression, [Faltinsen (2011)]. The expression for the 2D added mass given in [Faltinsen (2011)] is

$$a_{33}^{(n)} = f + \rho\frac{16c^2}{\pi}\left[\ln\left(\frac{8R}{c}\right) - K_n\right] \tag{3.50}$$

The expression for K_n is the same as presented in equation (3.15). f is given by

$$\begin{aligned}\frac{f}{\rho c^2} =& 5.74604 - 5.76835\left(\frac{2p}{c}\right) + 1.55575\left(\frac{2p^2}{c}\right)^2 \\ &- 0.21295\left(\frac{2p}{c}\right)^3 + 0.01128\left(\frac{2p}{c}\right)^4 \qquad \text{,for two tori for } 2 < \frac{2p}{c} < 6\end{aligned} \tag{3.51}$$

The non dimensional 2D added mass for 2 tori for the first six modes is plotted as a function of c/R in Figure 3.7. The 2D added mass is divided by the 2D mass $m = \rho\pi c^2$ of the floater section.

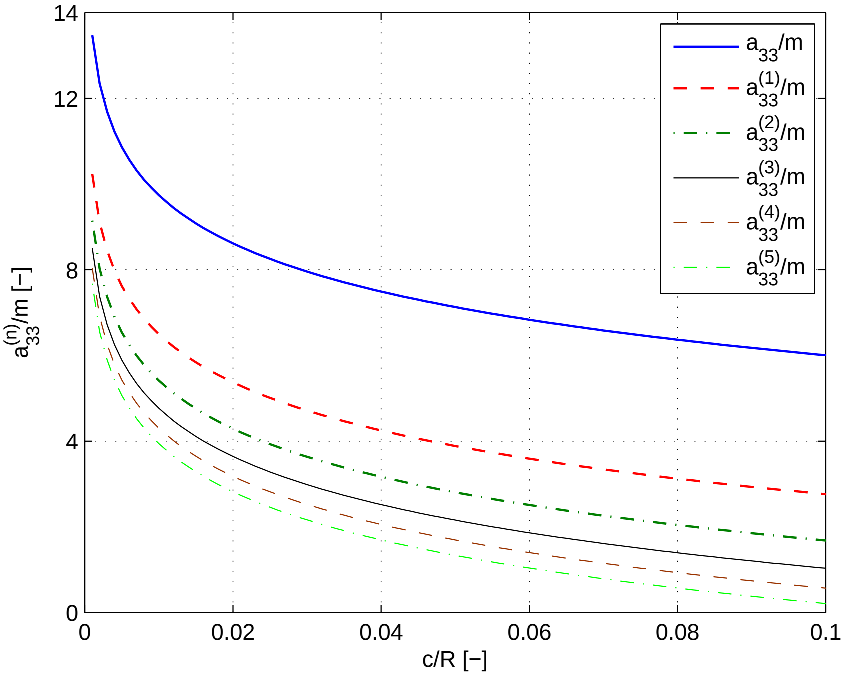

Figure 3.7: 2D non dimensional added mass for 2 tori. $a_{33}^{(n)}$ is the 2D added mass in z-direction associated with the mode shape $\cos n\beta$. $m = \rho\pi c^2$ is the 2D mass of the floater. c is the radius of the section. R is the radius of the floater.

Chapter 4

Excitation Forces and Equations of Motion

The response of the floating collar is calculated in regular long crested deep water waves. The standard deviations for the bending stresses in irregular waves will also be found. Both for regular and irregular waves linear wave theory according to [Faltinsen (1990)] is used. The initial approach is to calculate the response due to linear wave forces, [Faltinsen (1990)]. $z = 0$ is used as the z-coordinate for the linear free surface. The mean position of the floater, $z = 0$, is used when deriving the forces. The assumption of using $z = 0$ as the free surface holds for small non-steep waves where the linear free surface condition at $z = 0$ is a good approximation for the free surface at $z = \zeta$, where ζ is the wave elevation, [Faltinsen (1990)]. The approximation of using the mean position of the floater when calculating the forces will be better the longer the waves are, since the depth variation of the velocities and dynamic pressure with e^{kz} will be smaller the longer the wave are. k and z are the wave number and z-coordinate defined as zero at the mean free surface and negative downwards. The diffraction, Froude-Kriloff and hydrostatic forces are calculated according to linear theory. The damping coefficient in the equation of motion is set to a level of the critical damping. This linear damping coefficient include potential damping, skin friction, drag due to vortex shedding and structural damping of the material used in the floating collar. Although the two last contributions are nonlinear, linear damping is used as an approximation. The damping level is set sufficiently low in order to not exceed the real damping in the system. The second approach is to calculate the nonlinear time and space dependent hydrostatic and Froude-Kriloff pressure forces. That means that the time dependent position of the floater and the time dependent wave elevation must be accounted for. The hydrostatic and dynamic pressure is still calculated according to linear wave theory, but the pressure forces are found by integrating the pressures over the exact wetted surface for each time step in the analysis. This means that a numeric time integration must be applied. Although the pressures are calculated with linear wave theory this procedure will be referred to as nonlinear hydrostatic and Froude-Kriloff forces. The variation of surface elevation and response of the floater combined at various positions along the floating collar will be nonlinear. For regular linear waves the floater response due to nonlinear forces will be calculated and presented. A method for calculating the forces and response in irregular waves for nonlinear forces will be suggested, but no results will be given.

4.1 Wave Potential

The wave velocity potential according to [Faltinsen (1990)] is

$$\phi_0 = \frac{g\zeta_a}{\omega} e^{kz} cos(kx - \omega t) \tag{4.1}$$

The sign in the cosine term is shifted. ϕ_0 is the incident wave potential. g, ζ_a and k are the acceleration of gravity, wave amplitude and wave number, respectively. x, z and t are horizontal and vertical space coordinates and time. The response of the floating collar will be calculated by use of mode superposition. The 2D added mass is mode dependent. Thus, the diffraction force will be mode dependent. Since mode superposition will be used, the equations of motion will consist of N equations. N is the total number of modes. Each modal equation will have a modal mass, modal added mass, modal damping coefficient, modal restoring coefficient and modal excitation forces. It will then be most practical to express the wave forces as a Fourier sum involving Bessel functions. Therefore, it will be preferable to use the complex wave potential, [Faltinsen. Personal communication, 2011]. The expression is shown in equation (4.2).

$$\phi_0 = \frac{g\zeta_a}{\omega} e^{kz+i(kx-\omega t)} \tag{4.2}$$

Here, i is a complex number with the property $\sqrt{i} = -1$. According to linear wave theory for deep water $k = \omega^2/g$. Deep water implies $h > \lambda/2$, [Dean & Dalrymple (1991)]. h is the water depth and λ is the wave length. It is the real part of the expression that has physical meaning. This also applies for later complex expression in this text. The wave elevation is found by differentiating ϕ_0 with respect to time and inserting the expression in the dynamic linear condition $g\zeta + \partial\phi_0/\partial t = 0$ on $z = 0$, [Faltinsen (1990)]. The wave elevation ζ is then expressed as

$$\zeta = i\zeta_a e^{i(kx-\omega t)} \tag{4.3}$$

4.2 Wave Excitation Forces

The wave excitation forces are the diffraction force due to added mass and water particle acceleration and the Froude-Kriloff pressure force due to the undisturbed dynamic pressure over the wetted surface of the structure. The diffraction force will be calculated according to linear theory. The Froude-Kriloff force will first be calculated according to linear theory, where the undisturbed dynamic pressure is integrated over the mean wetted surface. The Froude-Kriloff force will next be calculated by integrating the undisturbed dynamic pressure over the exact wetted surface taking floater motion and wave elevation into account. The latter approach will give rise to nonlinear forces. Although the restoring force is not seen as a wave excitation force in the equations of motion, this force will be treated in the same way as the Froude-Kriloff force. The first approach is to calculate the restoring force according to linear theory as $-c_{33}w(\beta, t)$, where c_{33} is the linear hydrostatic restoring coefficient and $w(\beta, t)$ is the time and space dependent vertical displacement. The nonlinear restoring force is found by integrating the hydrostatic pressure over the exact wetted surface. The mass of the floater times the acceleration of gravity then need to be subtracted from the equation since this will act as a downward force. The linear forces and the corresponding linear response of the floater will be compared to the nonlinear forces and the corresponding nonlinear response in regular waves.

4.3 Linear Diffraction Force

The diffraction force can be found by solving a boundary value problem with forced oscillations and minus the vertical wave particle velocity and acceleration, [Newman (1977)]. The 2D diffraction force is then $a_z a_{33} + w b_{33}$. a_z and w are the vertical particle acceleration and velocity of the incident waves. a_{33} and b_{33} are the 2D added mass and damping terms. 2D refers to the value of the addressed term per unit length on the floater. The floater is a slender structure and will not generate a significant amount of outgoing waves. Therefor the damping coefficient is small and the diffraction force per unit length can be approximated as $a_z a_{33}$, [Faltinsen. Personal communication, 2011]. The expressions for the vertical particle acceleration of the incident waves along the center line of the floater are shown in equation (4.4) and (4.5).

$$a_z = \frac{\partial^2 \phi_0}{\partial z \partial t} = -i\omega^2 \zeta_a e^{kz+i(kx-\omega t)} \quad \text{,where } x = R\cos\beta \tag{4.4}$$

$$a_z = -i\omega^2 \zeta_a e^{kz-i\omega t} \left[J_0(kR) + \sum_{n=1}^{\infty} 2i^n J_n(kR) \cos n\beta \right] \tag{4.5}$$

$$e^{ikR\cos\beta} = J_0(kR) + \sum_{n=1}^{\infty} 2i^n J_n(kR) \cos n\beta \tag{4.6}$$

$x = R\cos\beta$ is the x-position on the floater referring to the global coordinate system. The term $e^{ikx} = e^{ikR\cos\beta}$ is expressed as a sum of Bessel functions. $J_0(kR)$ and $J_n(kR)$ are Bessel functions of the first kind with order 0 and n respectively. How equation (4.6) is derived is showed in detail in Appendix (A.1).

Since the added mass per unit length is mode dependent and the vertical water particle acceleration of the incident waves can be expressed as a Fourier sum the 2D diffraction force can be written as a Fourier sum. The expression is presented in equation (4.7).

$$f_3^D = -i\omega^2 \zeta_a \left[J_0(kR) a_{33}^{(0)} + \sum_{n=1}^{\infty} 2i^n J_n(kR) a_{33}^{(n)} \cos n\beta \right] e^{-i\omega t} \tag{4.7}$$

The z-coordinate in the expression for the the vertical acceleration, equation (4.5), is set to zero when calculating the diffraction force. $z = 0$ is the mean free surface and the mean z-coordinate of the center line of the floating ring. This approximation holds for long waves since the variation of the vertical acceleration with depth will be smaller the longer the waves are. Also, it is assumed that the pipe cross section is small compared to the wavelength. $a_{33}^{(0)}$ and $a_{33}^{(n)}$ are the 2D added mass for mode $n = 0$ and the n-th mode respectively. $n = 0$ is heave motion, $n = 1$ is pitch motion and $n = 2$ is the first elastic mode. $n = 2, 3, 4...$ are elastic modes with shape functions $\cos n\beta$.

4.4 Linear Froude-Kriloff Force

The linear Froude-Kriloff force is obtained by integrating the undisturbed dynamic pressure from the incident waves over the mean wetted surface of the floater, [Faltinsen (1990)]. The force is calculated per unit length. The expression for the dynamic pressure along the center line of the floater is

$$p_{dyn} = -\rho \frac{\partial \phi_0}{\partial t} = i\rho g \zeta_a e^{kz+i(kx-\omega t)} \quad \text{,where } x = R\cos\beta \tag{4.8}$$

The x coordinate is $R\cos\beta$, which is the horizontal position of the floater section in x-direction. The dynamic pressure is multiplied with minus the z-component of the body normal vector, the pipe radius c and integrated from $\theta = -\pi/2$ to $\theta = \pi/2$ The body normal vector in z-direction is $-\cos\theta$. θ is a angle in the local coordinate system for a given cross section of the pipe. Se Chapter 3. The derivation of the Froude-Kriloff force is shown in equations (4.9) and (4.10).

$$f_3^{FK} = -\int_{-\pi/2}^{\pi/2} p_{dyn} n_3 c \, d\theta = \int_{-\pi/2}^{\pi/2} p_{dyn} \cos{(\theta)} c \, d\theta = i\rho g b_w \zeta_a e^{i(kR\cos\beta - \omega t)} \tag{4.9}$$

$$f_3^{FK} = i\rho g b_w \zeta_a \left[J_0(kR) + \sum_{n=1}^{\infty} 2i^n J_n(kR) \cos n\beta \right] e^{-i\omega t} \tag{4.10}$$

Equation (4.10) shows the Froude-Kriloff force per unit length of the floater. n_3 is the z-component of the body normal vector pointing into the fluid and b_w is the breadth of the floater section at $z = 0$. $b_w = 2c$ for 1 torus and $b_w = 4c$ for 2 tori. c is the pipe radius. Equation (4.10) is the same expression for the Froude-Kriloff force as presented in [Faltinsen (2011)]. As the diffraction force, the Froude-Kriloff force is expressed as a Fourier sum involving Bessel functions of the first kind. Equation (4.6) is utilized. Due to the assumption of the wave length being much longer than the cross section of the floater z is set equal to zero.

4.5 Equations of Motion

The Euler beam equation can be used to model the vertical response of the floater. The restoring coefficient, wave excitation forces and forces due to added mass and damping are inserted in the equation according to Newton's second law. The beam equation is

$$m\frac{\partial^2 w(s,t)}{\partial t^2} + c_{33} w(s,t) + EI\frac{\partial^4 w(s,t)}{\partial s^4} = f_3^D(s,t) + f_3^{FK}(s,t) + f_3^{added\,mass} + f_3^{damping} \tag{4.11}$$

The vertical velocity and acceleration is $\partial w(s,t)/\partial t$ and $\partial^2 w(s,t)/\partial t^2$. The unit for each term in the equation is $\mathrm{N/m}$. The spatial coordinate s goes along the center line of the floater. For 1 torus it goes along the center of the pipe. For 2 tori it goes along the midpoint between the to pipes. For both 1 torus and 2 tori the distance from s to the origin is the floater radius R. t is time. m is the mass of the floater per unit length. m is not varying in space and is therefore a constant. c_{33} is the general 2D hydrodynamic restoring coefficient. EI is the bending stiffness. $f_3^D(s,t)$ and $f_3^{FK}(s,t)$ are the 2D diffraction and Froude-Kriloff force. $f_3^{added\,mass}$ is the 2D added mass force because of vertical acceleration of the floater section. $f_3^{damping}$ is the damping force, and contains contributions from potential damping, skin friction, vortex shedding and structural damping. c_{33} is equal to $\rho g b_w$, where $b_w = 2c$ for 1 torus and $b_w = 4c$ for a 2 tori configuration of the floating collar.

The solution for w is assumed to be a Fourier series with orthogonal shape functions defined by $\cos n\beta$, where $n = 1, 2, 3 ... \infty$. The motion will in reality only have contributions from a finite number of modes. The higher modes are assumed to give a very small contribution to the total response. The assumed solution fore w is

$$w(\beta,t) = a_0(t) + \sum_{n=1}^{\infty} a_n(t) \cos n\beta = \left(a_{0,a} + \sum_{n=1}^{\infty} a_{n,a} \cos n\beta \right) e^{-i\omega t} \tag{4.12}$$

$$\dot{w} = \dot{a}_0 + \sum_{n=1}^{\infty} \dot{a}_n \cos n\beta \tag{4.13}$$

$$\ddot{w} = \ddot{a}_0 + \sum_{n=1}^{\infty} \ddot{a}_n \cos n\beta \tag{4.14}$$

$$\frac{\partial^4 w}{\partial s^4} = \frac{1}{R^4}\frac{\partial^4 w}{\partial \beta^4} = \sum_{n=1}^{\infty} \frac{n^4}{R^4} a_n \cos n\beta \tag{4.15}$$

$a_0(t)$ and $a_n(t)$ are the time dependent Fourier coefficients. $a_{0,a}$ and $a_{n,a}$ are the amplitudes of the Fourier coefficients. The amplitudes can be complex numbers, thus taking care of the phase angle between the load and the response. Equation (4.13), (4.14) and (4.15) are the first and second derivative of w with respect to time and the fourth derivative of w with respect to s, respectively. In the last equation, it is utilized that $\partial/\partial s = \partial/(R\partial\beta)$

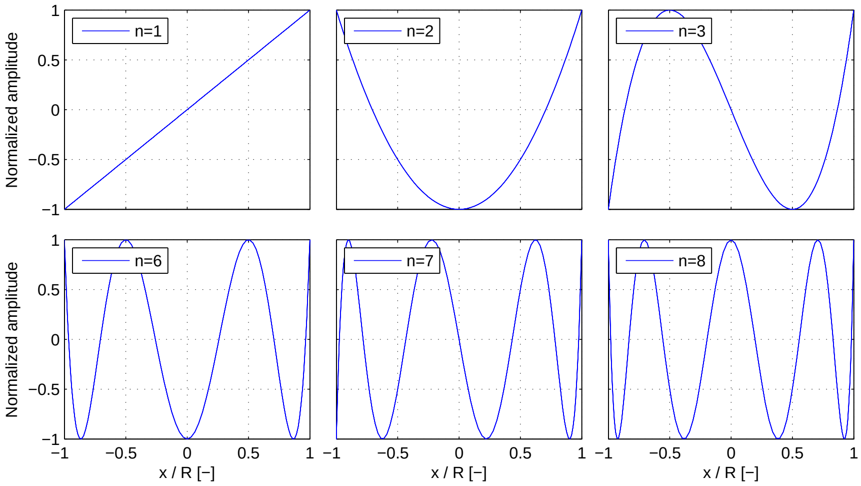

Figure 4.1: Plot of the orthogonal mode $\cos n\beta$. Mode shapes for $n = 1, 2, 3, 6, 7$ and 8 are shown. The y-axis is the normalized amplitude of the modal response. The x-axis is the normalized x-coordinate on the floater referring to the global coordinate system. x is normalized by dividing with the floater radius R.

The expressions for the derivatives of w is substituted into equation (4.11). Each term is then multiplied with the orthogonal function $\cos m\beta$, where $m = 0, 1, 2...\infty$. The resulting equation is then integrated around the center line of the floater. That means multiplying the equation with the floater radius R and integrating from $\beta = 0$ to $\beta = 2\pi$. The expression is as follows:

$$\begin{aligned}
&\int_0^{2\pi} m_{2D}\left(\ddot{a}_0 + \sum_{n=1}^{\infty} \ddot{a}_n \cos n\beta\right)\cos(m\beta)R\,d\beta \\
&+ \int_0^{2\pi} c_{33}\left(a_0 + \sum_{n=1}^{\infty} a_n \cos n\beta\right)\cos(m\beta)R\,d\beta \\
&+ \int_0^{2\pi} EI\left(\sum_{n=1}^{\infty} \frac{n^4}{R^4} a_n \cos n\beta\right)\cos(m\beta)R\,d\beta \\
&= \int_0^{2\pi}\left(f_3^D + f_3^{FK} + f_3^{added\,mass} + f_3^{damping}\right)\cos(m\beta)R\,d\beta
\end{aligned} \tag{4.16}$$

$$\int_0^{2\pi} \cos n\beta \cos m\beta \, d\beta \begin{cases} = 0 & \text{,when } n \neq m \\ \neq 0 & \text{,when } n = m \end{cases} \tag{4.17}$$

m_{2D} is the mass per unit length of the floater. Due to the property of orthogonal functions, shown in equation (4.17), a system of linear uncoupled second order differential equations emerge. In theory the number of equations will be infinite. The modal equations for the first mode, $n = 0$, and the n-th mode are shown in equation (4.18) and (4.19), respectively.

$$\left(m + a_{33}^{(0)}\right) \ddot{a}_0 + b_{33}^{(0)} \dot{a}_0 + \rho g b_w a_0 = \left(\rho g b_w - \omega^2 a_{33}^{(0)}\right) \zeta_a J_0(kR) i e^{-i\omega t} \tag{4.18}$$

$$\left(m + a_{33}^{(n)}\right) \ddot{a}_n + b_{33}^{(n)} \dot{a}_n + \left(\rho g b_w + \frac{n^4}{R^4} EI\right) a_n = \left(\rho g b_w - \omega^2 a_{33}^{(n)}\right) 2\zeta_a J_n(kR) i^{n+1} e^{-i\omega t} \tag{4.19}$$

The modal equations are found by dividing the resulting expressions in equation (4.16) with $2\pi R$ and πR for $n = 0$ and n respectively. In order to find 3D values, for instance 3D added mass $A_{(n+3)(n+3)}$, equation (4.18) and (4.19) must be multiplied with $2\pi R$ and πR. See derivation of 3D added mass in Chapter 3. In equation (4.18) and (4.19), c_{33} is substituted with $\rho g b_w$ and the expressions for f_3^D and f_3^{FK} from equation (4.7) and (4.10) are used. m is the 2D mass of the floater, and $a_{33}^{(0)}$ and $a_{33}^{(n)}$ are the modal added mass. The modal damping $b_{33}^{(0)}$ and $b_{33}^{(n)}$ is set to a level of critical damping for each mode. The differential equations are solved with respect to the modal amplitudes. By inserting the solutions for a_0 and a_n into equation (4.12) the vertical displacement is found. In order to solve the equations the solution of a_0 and a_n is assumed to be harmonic with the same circular frequency ω as the incident waves.

$$a_0 = a_{0,a} e^{-i\omega t} \tag{4.20}$$

$$a_n = a_{n,a} e^{-i\omega t} \tag{4.21}$$

The expressions for a_0 and a_n are substituted into equation (4.18) and (4.19) and the equations are solved with respect to $a_{0,a}$ and $a_{n,a}$. $a_{0,a}$ and $a_{n,a}$ are complex values taking the phase angle between the waves and the response into account. Thus, when finding the response w by inserting the expressions for a_0 and a_n into equation (4.12), the phase angle between the total response w and the waves will be accounted for. The expressions for $a_{0,a}$ and $a_{n,a}$ are:

$$a_{0,a} = \frac{\rho g b_w - \omega^2 a_{33}^{(0)}}{\rho g b_w - \omega^2 \left(m + a_{33}^{(0)}\right) - i\omega b_{33}^{(0)}} \zeta_a i J_0(kR) \tag{4.22}$$

$$a_{n,a} = \frac{\rho g b_w - \omega^2 a_{33}^{(n)}}{\rho g b_w + \frac{n^4}{R^4} EI - \omega^2 \left(m + a_{33}^{(n)}\right) - i\omega b_{33}^{(n)}} 2\zeta_a i^{n+1} J_n(kR) \tag{4.23}$$

The expressions for the linear transfer functions for each mode is found by taking the absolute value of $a_{0,a}/\zeta_a$ and $a_{n,a}/\zeta_a$. The transfer functions, giving the the normalized response amplitudes for each wave circular frequency ω are:

$$\left|\frac{a_{0,a}}{\zeta_a}\right| = \left|\frac{\rho g b_w - \omega^2 a_{33}^{(0)}}{\rho g b_w - \omega^2\left(m + a_{33}^{(0)}\right) - i\omega b_{33}^{(0)}} i J_0(kR)\right| \tag{4.24}$$

$$\left|\frac{a_{n,a}}{\zeta_a}\right| = \left|\frac{\rho g b_w - \omega^2 a_{33}^{(n)}}{\rho g b_w + \frac{n^4}{R^4} EI - \omega^2\left(m + a_{33}^{(n)}\right) - i\omega b_{33}^{(n)}} 2 i^{n+1} J_n(kR)\right| \tag{4.25}$$

The response is calculated for 1 torus and 2 tori. The response of the two cases will be different. This is due to the change in added mass between the two cases and the change in water plane area and wetted surface. The change in added mass will give a larger effective mass in the equations of motion for the 2 tori case. The diffraction forces will also increase. The increased water plane area and increased wetted surface in the 2 tori case will give a higher restoring coefficient and higher Froude-Kriloff forces. The bending stiffness EI will be reduced for the 2 tori case compared with 1 torus. The undamped resonance frequencies for the modes will decrease for 2 tori compared with 1 torus. This can qualitatively be seen from the transfer functions. The damping is low and the damped resonance frequencies will be almost identical to the undamped ones. The undamped transfer functions for the 3 first modes are shown in Figure 4.2 and 4.3. Undamped means setting $b_{33}^{(0)}$ and $b_{33}^{(n)}$ equal to zero. For the 1 torus case the pipe radius is $0.318m$. For 2 tori the pipe radius is $0.225m$. The bending stiffness EI is $3.085 \cdot 10^6 Nm^2$ and $1.543 \cdot 10^6 Nm^2$ for 1 torus and 2 tori respectively. The second area moment I is calculated as $\pi\left[c^4 - (c - t_w)^4\right]/4$, where t_w is the pipe wall thickness. The two different floater configurations are assumed to have the same displacement with the same radius R of the ring. R is set to $25.5m$. Chapter 2 gives further explanation regarding the choice of dimensions.

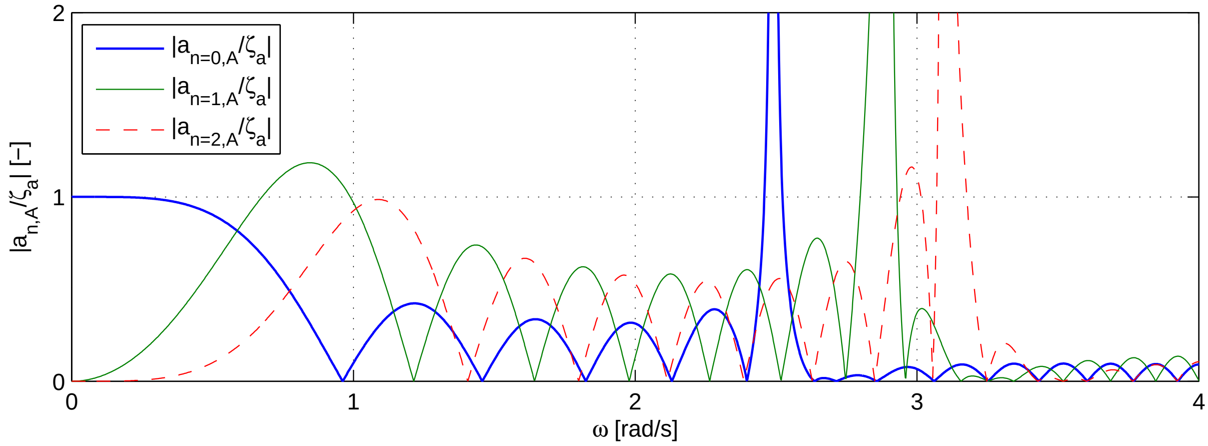

Figure 4.2: Undamped linear transfer functions for 1 torus. $n = 0$ is heave, $n = 1$ is pitch and $n = 2$ is the first elastic mode. $a_{n,A}$ is the motion amplitude of mode n. ζ_a is the wave amplitude and ω is the wave frequency.

From the transfer function graphs it can be seen that the heave motion follows the waves for long waves, that is $\omega \to 0$, which is expected. For frequencies higher than the resonance frequency for a mode, the corresponding motion amplitude is small. Between $\omega = 0$ and $\omega = \omega_0$ cancellations of the response are seen. ω_0 is the undamped resonance frequency. From equation (4.24) and (4.25) it is seen that the cancellation in the response comes for frequencies that give $J_n(kR)$ or $(\rho g b_w - \omega^2 a_{33}^{(n)})$ equal to zero, for $n = 0, 1, 2, ...$ When the total wave excitation forces integrated around the floater equals zero, the response is zero. The cancellation frequencies for the different modes are not necessarily the same. But the cancellation frequency for one mode for 1 torus is the same as the cancellation frequency for the same mode for 2 tori. This is because the variation of the wave excitation forces over the floater will be the same for 1 and 2 tori when the forces are calculated according to linear theory and the same radius R

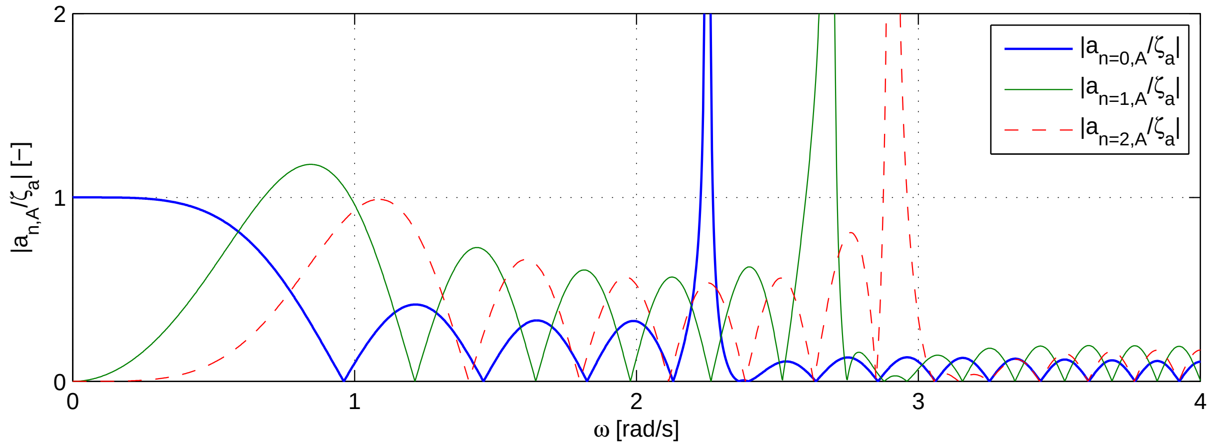

Figure 4.3: Undamped linear transfer functions for 2 tori. $n = 0$ is heave, $n = 1$ is pitch and $n = 2$ is the first elastic mode. $a_{n,A}$ is the motion amplitude of mode n. ζ_a is the wave amplitude and ω is the wave frequency.

is used. Variation is interpreted as the change with respect to space and time. The amplitudes of the force will be different for the 1 torus and 2 tori case. Although cancellations appear for the different modes, this does not mean that the total vertical response of the floater is zero. As mentioned above, the cancellation frequencies for the different modes are not necessarily the same. Since the response amplitude at a give position β on the floater is the sum of the mode amplitudes, taking phase angles between waves and response into account, multiplied with $\cos n\beta$; the response might still be significant. From Figure 4.2 and 4.3 it is observed that the resonance frequencies increase for the higher modes. When n increase ω_0 increase. This is because the modal added mass decrease when the mode number n increase. The higher modes have lower modal added mass. The undamped and damped resonance frequencies for 1 torus and 2 tori are presented in Table 4.1. The damped and undamped resonance frequencies are calculated as:

$$\omega_0 = \left[\frac{c_{33}^{(n)}}{\left(m + a_{33}^{(n)}\right)} \right]^{1/2} \tag{4.26}$$

$$\omega_0 = \left[\frac{c_{33}^{(n)}}{\left(m + a_{33}^{(n)}\right)} - \left(\frac{b_{33}^{(n)}}{2\left(m + a_{33}^{(n)}\right)} \right)^2 \right]^{1/2} \tag{4.27}$$

ω_0 and ω_d are the undamped and damped resonance frequencies, respectively. For these equations, $n = 0, 1, 2...$ $c_{33}^{(n)}$ is including both hydrostatic and structural restoring coefficients. Remember that the structural restoring coefficient for the heave mode given by $n = 0$ is zero.

4.6 Nonlinear Hydrostatic and Froude-Kriloff Forces

In Section 4.5 the linear response of the floater is found. The wave excitation forces are calculated according to linear theory. The position of the floater is fixed at the mean position when calculating the forces and long wave approximation is used, [Faltinsen (1990)]. The z-variation in the dynamic pressure is not taken into account. All coefficients are assumed linear. In this section effects of nonlinearities will be addressed. The effects of integrating the hydrostatic and undisturbed dynamic pressure over the exact wetted surface of the floater will be investigated. A procedure will be presented and some results will

n	ω_0 1 torus	ω_0 2 tori	ω_d 1 torus	ω_d 2tori
0	2.490	2.253	2.489	2.252
1	2.889	2.686	2.887	2.685
2	3.096	2.906	3.095	2.905
3	3.339	3.099	3.338	3.098
4	3.746	3.335	3.744	3.334
5	4.425	3.675	4.423	3.674
6	5.440	4.174	5.438	4.173
7	6.812	4.873	6.809	4.871
8	8.538	5.794	8.534	5.791
9	10.609	6.946	10.604	6.943

Table 4.1: Undamped and damped modal resonance frequencies for vertical motion for 1 torus and 2 tori. The modal damping level for the damped resonance frequencies is 3 percent of critical damping for each mode. ω_0 and ω_d are the undamped and damped resonance frequencies, respectively. n is the mode number. The frequencies have dimension $\mathrm{rad/s}$.

be shown and discussed. Further results and discussion are found in Chapter 7. Integrating the pressure forces over the correct wetted surface will give a more correct representation of the wave excitation forces compared with linear theory.

Added mass and damping coefficients and the diffraction force for each mode are still linear. The hydrostatic and dynamic pressure will be integrated over the exact time and space dependent wetted surface. Both the hydrostatic and dynamic pressures will be calculated according to linear theory, [Faltinsen (1990)] and [Dean & Dalrymple (1991)]. The dynamic pressure is calculated from the wave velocity potential for linear regular waves presented in equation (4.2). The formula for the hydrostatic pressure is

$$p_{hyd} = -\rho g z \tag{4.28}$$

The hydrostatic pressure are linear with respect to z, and will be negative above the mean free surface at $z = 0$ and positive underneath $z = 0$. The dynamic pressure will follow the expression in equation (4.8) for negative z values. That is underneath the mean free surface. Above $z = 0$ the z-coordinate in the expression is set to zero. That means that the dynamic pressure will be constant above $z = 0$. The idea is that the total pressure, hydrostatic and dynamic, will be equal to zero at the 1st order surface $\zeta(x, t)$. Using equation (4.28) and (4.8) this is satisfied underneath a wave crest. Underneath a wave trough this approach will give an error of 2nd order or higher. The error in the pressure is proportional to ζ_a^n where n equals 2 or higher, [Faltinsen (1990)]. Figure (4.4) indicates how the pressure is varying under a wave crest and a wave trough.

Although the hydrostatic and dynamic pressures are calculated according to linear wave theory the variation of wetted surface and floater motion combined will give rise to nonlinear wave excitation forces. Especially for short waves. Since the pressure forces are dependent on the floater motion, which in turn is dependent on the forces, the equations of motion can not be solved in the frequency domain. A direct numeric time integration procedure is needed. The method used in this thesis is a 4th order Runge-Kutta method, [Kreyszig (1999)].

4.6.1 Calculation of Nonlinear Forces

The floater is divided into sections with equal length. The length of the section is defined by the angle sector $d\beta$. The length of each section is $Rd\beta$. Between each section of the floater, at the point defined by the value of the angle β, the intersection between the 1st order free surface $\zeta(x, t)$ and the pipe cross

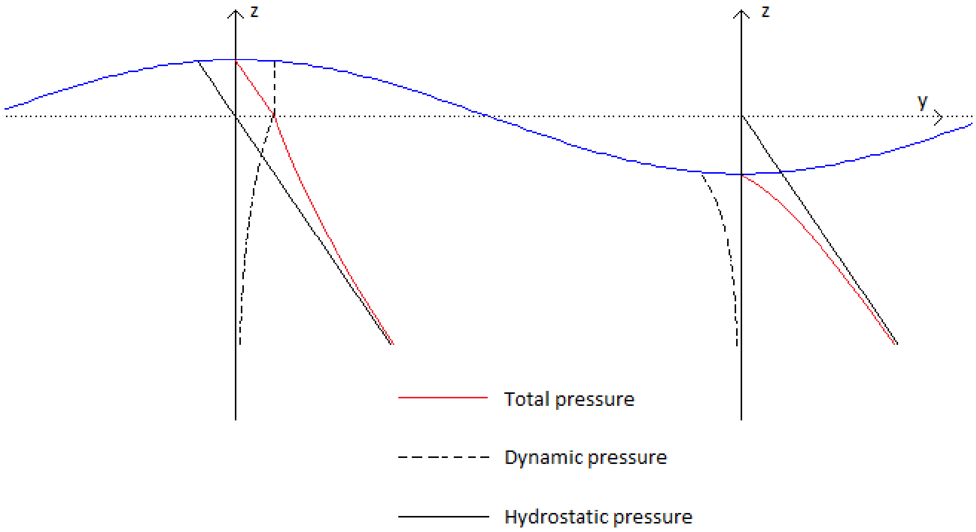

Figure 4.4: Linear hydrostatic, dynamic and total pressure underneath a wave crest and a wave trough. The wave elevation is exaggerated in order to properly show the principle. The figure is based on similar figures in [Faltinsen (1990)] and [Dean & Dalrymple (1991)].

section taking the total vertical displacement into account is found. The angles, referring to the local coordinate system for each cross section, are denoted θ_1 and θ_2. These angles describe the intersection between the water surface and the pipe cross section at β. The interval $[\theta_1, \theta_2]$ is divided into a number of elements with equal length. The hydrostatic and undisturbed dynamic pressure from the incident waves are calculated at each point in the vector $[\theta_1, \theta_2]$ between the elements on the wetted surface of the pipe. The variation of the pressure between the points are approximated as linear. The discrete function describing the pressure variation over the wetted surface are multiplied with minus the body normal vector in z-direction and integrated over the cross section from θ_1 to θ_2 using the numeric trapeze integration method. The body normal vector in z-direction is $-\cos\theta$. This gives a force per unit length on the cross section at the coordinate β. The variation of the pressure force between each point on the floater defined by $d\beta$ and β is approximated as linear. The variation of the values for the pressure forces between each point β on the floater can be interpreted as a discrete function with respect to β for each time step t in the analysis. This function is multiplied with the orthogonal function $\cos n\beta$, where n is the mode number, and integrated around the floater from $\beta = 0$ to $\beta = 2\pi$. This gives the nonlinear modal pressure force for time step t and mode number n. The procedure used to find the modal forces from the forces per unit length is similar to the method presented in equation (4.16). The results are used in the modal equations of motion in the time domain algorithm. The formulas for the hydrostatic and dynamic pressure, the pressure forces per unit length on the floater and the modal forces are shown in equation (4.29) to (4.34).

$$p_{hyd} = -\rho g z' \tag{4.29}$$

$$p_{dyn} = i\rho g \zeta_a e^{kz' + i(kx' - \omega t)} \tag{4.30}$$

$$f^{hyd}_{(3,2D)} = \int\limits_{\theta_1}^{\theta_2} p_{hyd} \cos(\theta) c \, d\theta \tag{4.31}$$

$$f^{dyn}_{(3,2D)} = \int\limits_{\theta_1}^{\theta_2} p_{dyn} \cos{(\theta)} c \, d\theta \tag{4.32}$$

$$f^{hyd}_{3,n} = \int\limits_{0}^{2\pi} f^{hyd}_{(3,2D)} \cos{(n\beta)} r \, d\beta \, , \begin{cases} ,r = R & \text{for 1 torus} \\ ,r = R - p & \text{for inner ring for 2 tori} \\ ,r = R + p & \text{for outer ring for 2 tori} \end{cases} \tag{4.33}$$

$$f^{dyn}_{3,n} = \int\limits_{0}^{2\pi} f^{dyn}_{(3,2D)} \cos{(n\beta)} r \, d\beta \, , \begin{cases} ,r = R & \text{for 1 torus} \\ ,r = R - p & \text{for inner ring for 2 tori} \\ ,r = R + p & \text{for outer ring for 2 tori} \end{cases} \tag{4.34}$$

For 1 torus the forces are integrated over the floater, one ring, using the radius R of the floater. For 2 tori the pressure forces are calculated separately for each ring. For the inner inner ring the distance $R - p$ between the pipe center and the center of the floater is used when integrating the 2D forces over the floater. For the outer ring the distance $R + p$ between the pipe center and the center of the floater is used. $2p$ is the distance between the center line of the two pipes. The x' and z'-coordinates are referring to coordinates on the floater section. The formulas are:

$$x' = R\cos\beta + c\sin\theta|\cos\beta| \tag{4.35}$$

$$z' = \begin{cases} w - c\cos\theta & \text{,for hydrostatic pressure} \\ w - c\cos\theta & \text{,for dynamic pressure if } w - c\cos\theta < 0 \\ 0 & \text{,for dynamic pressure if } w - c\cos\theta > 0 \end{cases} \tag{4.36}$$

$R\cos\beta$ is the x-position of the center of the pipe section. $c\sin\theta|\cos\beta|$ is the relative distance in x-direction from the center of the pipe to the surface of the pipe with respect to θ. The term $|\cos\beta|$ scales the radius c of the pipe with respect to the angle β on the floater. See Figure 4.5. w is the vertical displacement of the section and $c\cos\theta$ is the vertical distance between the center of the pipe section to the body surface of the pipe.

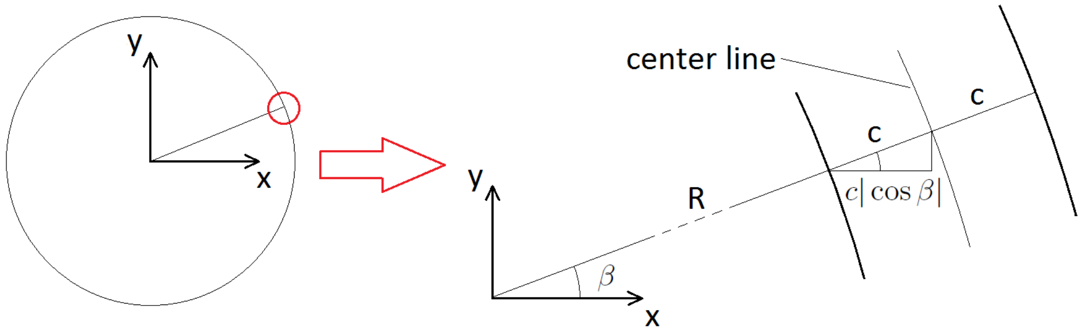

Figure 4.5: Principle figure showing the whole floater (left) and a part of the floater defined by the coordinate β (right). Both figures are seen from the positive z-axis. The red circle on the figure of the whole floater indicates the position at which the section to the right is situated. c and R are the pipe radius and the distance from the origin to the center of the pipe, respectively. $c|\cos\beta|$ is the scaled distance in x-direction from $x = R\cos\beta$ to $x = (R - c)\cos\beta$.

4.6.2 Intersection Between The Water Surface and The Pipe

The angles θ_1 and θ_2 must be found for each discrete point in the interval $\beta\epsilon[0, 2\pi]$ on the floater in order to calculate the nonlinear forces. The wave elevation at $x = R\cos\beta$ is found and denoted ζ_x. The slope of the wave at a position halfway between the center of the pipe and the respective side where the intersection point is to be found is calculated. The slopes are $(\partial\zeta/\partial x)_{(1)}$ and $(\partial\zeta/\partial x)_{(2)}$. (1) and (2) refers to the coordinates $x = R\cos\beta - c|\cos\beta|/2$ and $R\cos\beta + c|\cos\beta|/2$. Between the center of the cross section and the respective side the wave is approximated to follow the wave slope between the center and the side. The calculated wave slopes are used to calculate the attachment points θ_1 and θ_2 with respect to the local coordinate system for the cross section. The assumption that the wave profile approximately follows the slope holds for wavelengths $\lambda > 4c$. For shorter waves the change in the wave slope over the cross section is to large. This has been tested in the Matlab program by plotting the floater section against the wave elevation and the calculated attachment points between the water surface and the section. The expressions used in finding θ_1 and θ_2 are listed below. α_1 and α_2 are temporary results used in the calculation. These angles are also physical angles in the local coordinate system for the section.

$$\frac{\partial\zeta}{\partial x} = \frac{\partial}{\partial x}\left\{\zeta_a i e^{i(kx-\omega t)}\right\} = -k\zeta_a e^{i(kx-\omega t)} \tag{4.37}$$

$$\frac{\partial\zeta}{\partial x}_{(1,2)} = -k\zeta_a e^{i\left\{k\left(R\cos\beta\mp\frac{1}{2}c|\cos\beta|\right)-\omega t\right\}} \tag{4.38}$$

$$\alpha_{1,2} = \arctan\left(\frac{w-\zeta_x \pm \frac{\partial\zeta}{\partial x}_{(1,2)}|\cos\beta|c}{c'}\right), \begin{cases} c' = c & \text{when } |w-\zeta_x| < \dfrac{c}{2} \\ c' = \sqrt{c^2-(w-\zeta_x)^2} & \text{when } |w-\zeta_x| > \dfrac{c}{2} \end{cases} \tag{4.39}$$

$$\theta_1 = \begin{cases} -\pi/2+\alpha_1 & \text{,when } |w-\zeta_x| < c \\ -\pi & \text{,when } w-\zeta_x < -c \\ 0 & \text{,when } w-\zeta_x > c \end{cases} \tag{4.40}$$

$$\theta_2 = \begin{cases} \pi/2-\alpha_2 & \text{,when } |w-\zeta_x| < c \\ \pi & \text{,when } w-\zeta_x < -c \\ 0 & \text{,when } w-\zeta_x > c \end{cases} \tag{4.41}$$

The procedure presented above take into account that the floater section may be dry or completely submerged. When the section is dry θ_1 and θ_2 are set to zero, and the 2D nonlinear pressure forces for this section will be zero. When the section is completely submerged θ_1 and θ_2 are set to $-\pi$ and π respectively. The nonlinear model does not take care of impact forces or water run up on the pipe. These effects may give a change in the time history of the forces, and thus a contribution to the response. These effects are not treated in this theses.

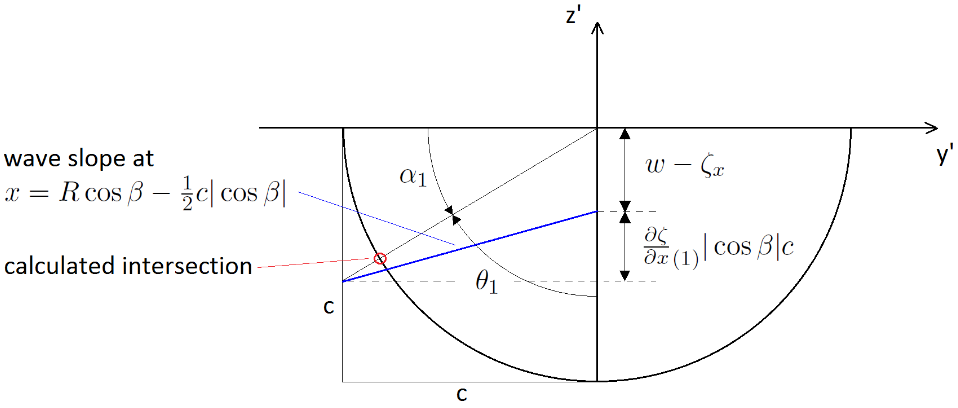

Figure 4.6: Principle figure describing how the attachment point between the waves and the floater section is found. α_1 and θ_1 are the angles for the calculated intersection defined from negative y' and negative z'-axis respectively. Both angles are defined positive in the counter clockwise direction. w is the total vertical displacement of the section. ζ_x is the wave elevation at the center of the section. $\partial\zeta/\partial x_{(1)}$ is the wave slope at $y' = -c/2$ in the local coordinate system. $|\cos\beta|c$ is a scale factor for the wave slope from the global coordinate system (x, y, z) to the local coordinate system (y', z'). For $|w - \zeta_x| > c/2$ the horizontal distance c in the calculation of θ_1 is replace by c' from equation (4.39).

4.7 Equations of Motion for Nonlinear Hydrostatic and Froude Kriloff Forces

The equations of motion used when investigating the response due to a nonlinear load model will be different from the equations used for linear loads. The starting point is still the Euler beam equation. Compared with equation (4.11) the hydrostatic restoring coefficient is replaced by the nonlinear hydrostatic force per unit length and the force per unit length due to the 2D mass of the floater. The linear Froude-Kriloff force in equation (4.10) is replaced by the pressure force per unit length on the floater because of the undisturbed dynamic pressure from the incident waves integrated over the exact wetted surface. The beam equation can now be written as:

$$m\frac{\partial^2 w}{\partial t^2} + EI\frac{\partial^4 w}{\partial s^4} = -mg + f_3^D + f_{(3,2D)}^{hyd} + f_{(3,2D)}^{dyn} + f_3^{added\,mass} + f_3^{damping} \tag{4.42}$$

In equation (4.42) $-mg$ is the 2D force due to the mass per unit length of the floater. $f_{(3,2D)}^{hyd}$ and $f_{(3,2D)}^{dyn}$ are the 2D pressure forces due to hydrostatic and dynamic pressure respectively. The same procedure as presented in Section 4.5 is used to obtain the modal equations of motion. Each term in equation (4.42) is multiplied with $\cos m\beta$ and integrated around the floater from $\beta = 0$ to $\beta = 2\pi$. m has the values $0, 1, 2, ...$ A system of uncoupled second order differential equations emerge.

$$\left(m + a_{33}^{(0)}\right)\ddot{a}_0 + b_{33}^{(0)}\dot{a}_0 = -mg - \omega^2 a_{33}^{(0)}\zeta_a J_0(kR)ie^{-i\omega t} + \frac{1}{2\pi R}f_{3,0}^{hyd} + \frac{1}{2\pi R}f_{3,0}^{dyn} \tag{4.43}$$

$$\left(m + a_{33}^{(n)}\right)\ddot{a}_n + b_{33}^{(n)}\dot{a}_n + \frac{n^4}{R^4}EIa_n = -\omega^2 a_{33}^{(n)}2\zeta_a J_n(kR)i^{n+1}e^{-i\omega t} + \frac{1}{\pi R}f_{3,n}^{hyd} + \frac{1}{\pi R}f_{3,n}^{dyn} \tag{4.44}$$

$f_{3,n}^{hyd}$ and $f_{3,n}^{hyd}$ are the modal nonlinear hydrostatic and Froude-Kriloff pressure forces presented in equation (4.33) and (4.34). For 2 tori f_3^{hyd} and f_3^{hyd} include the pressure forces for both the inner and outer ring. Thus, equation (4.33) and (4.34) must be used twice. Once using $r = R - p$ in order to calculate the forces on the inner ring, and once using $r = R + p$ in order to calculated the forces on the outer ring.

4.7.1 Damping

Damping is needed when the the nonlinear response is to be found in the time domain analysis. The damping for each mode, or modal equation is set to a level of critical damping for each mode. Damping is expressed as

$$b_{33}^{(n)} = p \cdot 2\sqrt{c_{33}^{(n)}\left(m + a_{33}^{(n)}\right)} \tag{4.45}$$

$b_{33}^{(n)}$ is the damping for each mode. $p = 0.015$ and $p = 0.03$ is most frequently used when calculating the nonlinear responses in this thesis. This corresponds to 1.5 and 3 percent of critical damping, respectively. $c_{33}^{(n)}$ is the total restoring coefficient including hydrostatic and structural restoring coefficients. The value for $c_{33}^{(n)}$ is taken from the linear model. n is the mode number having the values $0, 1, 2...$

The real damping in the system have contributions from potential damping (wave radiation), skin friction, vortex shedding and structural damping in the material used in the floater. The potential damping is assumed low since the structure is slender and wave radiation and scatter is assumed to be negligible. An attempt of approximating the potential damping by reversing the formula for exciting force amplitude given by [Newman (1962)] were made. The force amplitude per unit length is

$$|f_{3,n}| = \zeta_a \left(\frac{\rho g^2}{\omega} b_{33}^{(n)} \right)^{1/2} \tag{4.46}$$

$|f_{3,n}|$ is the amplitude of the linear excitation forces, namely diffraction and Froude-Kriloff forces. The equation were solved for $b_{33}^{(n)}$. This should in theory be the potential damping for mode n. The damping forces were small compared with the excitation forces. No effects on the linear transfer functions were observed.

Nonlinear drag due to vortex shedding could have been approximated by $f_3^{drag} = 0.5\rho C_D(2c)u|u|$, [Faltinsen (1990)], where u is the relative vertical velocity between the water particles and the floater section and $C_D = 0.2\text{KC}$ is the drag coefficient, [Bearman et al. (1984)]. KC is the Keulegan-Carpenter number. This formula demands that $KC > 2$. This is shown by experiments by [Sarpkaya (1986)]. For the floater, this criterion where not always satisfied. The drag approximation for viscous separation were therefore not used.

Consistent data for structural damping for HDPE plastic were not found. The damping is highly nonlinear. This, and the discussion of potential damping and nonlinear damping resulted in using a sufficiently low damping level to represent the combined damping effects on the system. Whether a damping level of 3 percent, which was used for the highest wave steepness in the nonlinear time domain analysis, is sufficiently low, is not certain. This was the lowest damping level that gave convergence of the time series for forces and response. Convergence will be discussed further in Chapter 7. A linear drag term due to skin friction using the shear stress, due to the viscosity of the fluid, on the surface of the floater could also have been used, [Faltinsen (1990)]. But since the contribution from other drag components were uncertain, a modal damping level set to a percentage of critical damping for each mode were chosen.

4.7.2 Discretization in the Time Domain Analysis

In order to calculate the response for nonlinear hydrostatic and Froude-Kriloff forces a time domain analysis using a fourth order Runge-Kutta method where implemented in the Matlab program. Discretization of the geometry of the ring and time must be performed. The time steps in the analysis need to be sufficiently small in order to get convergence and reliable results. The discretization of the geometry must be such that the approximation of linear variation of forces between the discrete points on the floater give good approximation of the actual forces. However, very small time increments and many discrete points on the floater will result in a long calculation time. A balance between discretization giving good results and calculation time must be found. A duration of 200s of the time series were needed in order to get convergence for all cases investigated. A time increment of 0.02s combined with the floater being divided into 600 equally sized segments from $\beta = 0$ to $\beta = 2\pi$ and the wetted surface of each section being divided into 50 equally sized segments were found to give good results. Reduced time increments and a increased number of segments beyond these values did not give any change in the results. The discretization could have been less accurate, and still produce good results. These values were chosen in order to ensure good results and convergence for all frequencies and wave steepnesses investigated. The values presented above gave good results when the 20 first modes were used in the analysis. Additional modes could have demanded increased accuracy in the discretization. 20 modes were chosen since this gave acceptable convergence for both the linear displacements, relative motion and bending stresses in the floater. Se Chapter 6. If nothing else is stated, the 20 first modes are used when obtaining the presented results for the nonlinear time domain analysis.

Additional modes added in the analysis would have increased computation time due to increased number of operations in the program and the need for a shorter time increment and smaller segments on the floater. The number of segments on the wetted surface of each section, 50, could have been reduced without compromising accuracy. But, since the forces on each segment were calculated by matrix operations in Matlab, the reduction in computation time would have been negligible. The calculation of forces around the floater and the time integration were performed by loop iterations. Increasing the discretization accuracy in terms of reduction of spacing between each angle β and reduction of time increment Δt would have increased the calculation time proportional to the product of additional segments around the floater and additional time steps in the analysis divided by the product of the original number of segments and time steps. Calculation time for one time series on a computer with two 1.3GHz processors and 4GB RAM were approximately 2 and 3 hours for 1 torus and 2 tori, respectively.

4.7.3 Time Series of Linear and Nonlinear Response

When numeric time integration is used there will be transients at the start of the time series. Therefore, it is important to run the analysis long enough for the transients to be damped out. Figure 4.7 shows a time series for the heave mode for 2 tori. The wave frequency ω is $0.5 rad/s$ and the wave amplitude ζ is $4.11m$. In Figure 4.7 the transients at the beginning of the time series are clearly seen. After approximately 150 seconds the transients have disappeared and the response is stationary.

For long waves the difference between the response due to linear forces and nonlinear forces are anticipated to be small. This is because linear theory and long wave approximation gives good results for long waves, [Faltinsen (1990)]. For shorter waves, meaning a higher wave frequency ω, it is assumed that the nonlinear response will deviate more from the linear response than for long waves. Figure 4.8 shows a time series of the heave response for 2 tori for linear and nonlinear hydrostatic and Froude-Kriloff forces. The wave circular frequency ω is $0.5 rad/s$ and the wave amplitude ζ_a is $4.11m$. This is a fairly high wave. This wave amplitude is used in order to demonstrate that linear theory gives good results compared with the results for nonlinear forces even for high waves if the waves are long. The wave steepness is $H/\lambda = 1/30$. H is the wave height. The differences in the response is small, although it is observed that the negative amplitude of the response due to nonlinear forces is smaller than the negative amplitude of the response due to linear forces. The linear response is oscillating around $z = 0$, which is expected, while the nonlinear response is oscillating around a positive z-value. The phase angle between the linear and nonlinear response and the waves is similar.

Figure 4.9 shows the response of the heave mode for a 2 tori configuration of the floater for linear and nonlinear hydrostatic and Froude-Kriloff forces. The nonlinear model has a smaller response than the linear model. The phase angles are also different. The nonlinear model are not oscillating around $z = 0$. None of the figures in this section show response for wave frequencies close to the resonance frequencies of the system. For wave frequencies close to the resonance frequency a larger deviation between linear and nonlinear forces is expected. This is treated in detail in Chapter 7.

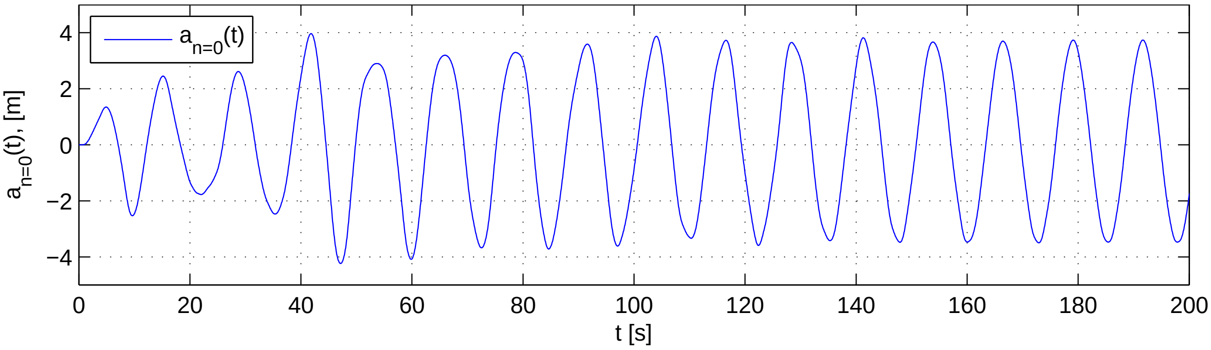

Figure 4.7: Response of the heave mode for a 2 tori configuration of the floater due to nonlinear hydrostatic and Froude-Kriloff forces. $a_{n=0}(t)$ is the time dependent response of the heave mode. $a_{n=0}(t)$ is also the time dependent Fourier coefficient in equation (4.12) for $n = 0$. The wave frequency ω is $0.5 rad/s$. The wave steepness is $H/\lambda = 1/30$, giving a wave amplitude $\zeta_a = 4.11m$. $H = 2\zeta_a$ is the wave height. The modal damping level is 1.5 percent of critical damping for each mode.

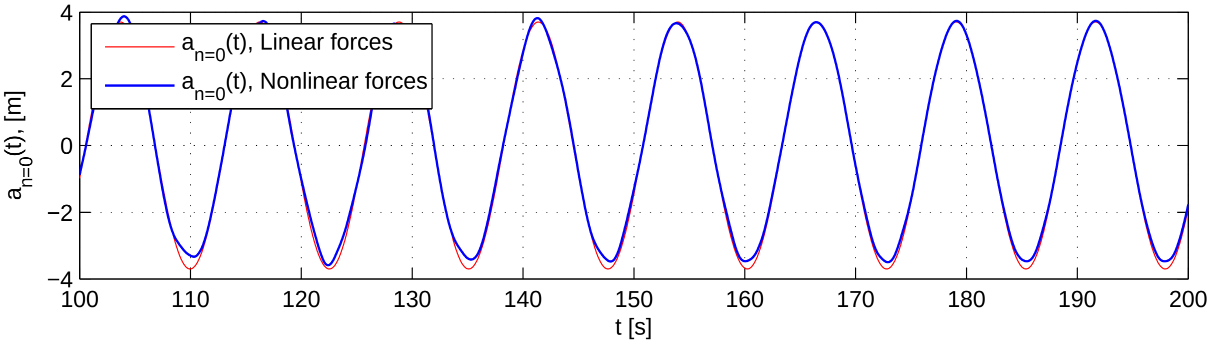

Figure 4.8: Comparison of response of the heave mode for a 2 tori configuration of the floater for linear and nonlinear hydrostatic and Froude-Kriloff forces. $a_{n=0}(t)$ is the time dependent response of the heave mode. The wave frequency ω is $0.5 rad/s$. The wave steepness $H/\lambda = 1/30$, thus giving a wave amplitude $\zeta_a = 4.11m$. $H = 2\zeta_a$ is the wave height. The modal damping level is 1.5 percent of critical damping for each mode.

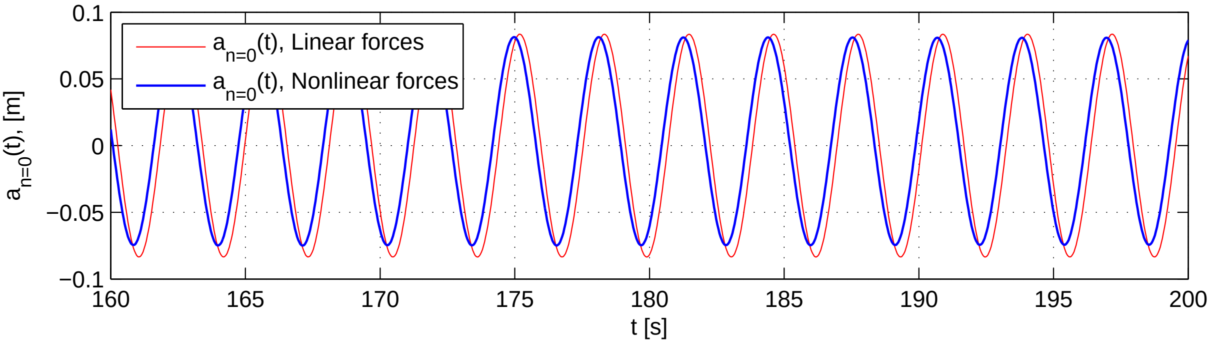

Figure 4.9: Comparison of response of the heave mode for a 2 tori configuration of the floater for linear and nonlinear hydrostatic and Froude-Kriloff forces. $a_{n=0}(t)$ is the time dependent response of the heave mode. The wave frequency ω is $2 rad/s$ The wave steepness $H/\lambda = 1/30$, thus giving a wave amplitude $\zeta_a = 0.26m$. $H = 2\zeta_a$ is the wave height. The modal damping level is 1.5 percent of critical damping for each mode.

4.8 Nonlinear Hydrostatic and Froude-Kriloff Forces in Irregular Sea

In this section a method for calculating nonlinear hydrostatic and Froude-Kriloff forces and the corresponding response in an irregular sea state will be presented. This method is a study in how the forces can be calculated. No results for the nonlinear forces in irregular long crested waves will be presented in this thesis.

4.8.1 Wave Elevation in Irregular Sea

The type of spectral density function is not specified. A known function, $S(\omega)$, is assumed. The wave elevation ζ_{an} of the frequency component ω_n and the corresponding frequency interval $\Delta\omega_n$, from [Faltinsen (2005)], is

$$\zeta_{an} = \sqrt{2S(\omega_n)\Delta\omega_n} \tag{4.47}$$

The total wave elevation $\zeta(x,t)$ at a position x and time t is the sum of the wave amplitudes for all frequency components in the wave spectrum defined by $S(\omega)$, [Faltinsen (1990)]. The wave elevation is

$$\zeta(x,t) = \sum_{n=1}^{\infty} \sqrt{2S(\omega_n)\Delta\omega_n} i e^{i(k_n x - \omega_n t - \varepsilon_n)} \tag{4.48}$$

ε_n is a random phase angle for each frequency component n in the spectrum. ε_n is a stochastic variable evenly distribution between 0 and 2π. k_n is the wave number associated with ω_n and is defined as $k_n = \omega_n^2/g$ for deep water waves.

Normally, in equation (4.48), a constant frequency interval $\Delta\omega$ is used. The wave elevation $\zeta(x,t)$ is a Fourier sum. If a constant frequency interval is used, the realization of the wave elevation with respect to time will not be a completely random process. The wave elevation from a spectrum using a constant interval $\Delta\omega$ will have a return period of $T_s = 2\pi/\Delta\omega$. This is because the longest wave represented by the sum has a period equal to T_s. The elevation of the longest wave with respect to time is considered. A fixed point in space is assumed. Each time a new wave component is added, that is n increased with 1, the component $n+1$ will have exactly one more wavelength in the time interval T_s compared with component n. The random phase angles ε_n will not change this. The wave pattern is repeated for each time period T_s. The solution is random frequency intervals $\Delta\omega_n$ for each ω_n, [Myrhaug. Personal communication (2011)]. The random frequency intervals are described by

$$\omega_{n+1} = \omega_n + c_\omega p_n \tag{4.49}$$

c_ω is a sufficiently small constant. c_ω should be the largest accepted interval between the frequencies ω_n and ω_{n+1}. p_n is a random stochastic variable evenly distribution between 0 and 1. The frequency interval $\Delta\omega_n$ can be expressed as the distance between the midpoint between ω_{n+1} and ω_n and the midpoint between ω_n and ω_{n-1}.

$$\Delta\omega_n = \frac{1}{2}(\omega_{n+1} - \omega_{n+1}) \tag{4.50}$$

When calculating the wave elevation numerically in a computer program, care must be taken at the ends of the range for ω. If $\omega_1 = 0$, the first interval can be set as $\Delta\omega_1 = \omega_2/2$. In a numeric calculation there will only exist a finite number of frequencies, and the frequency range will not go to infinity. For N frequency components, the interval for component N can be written as $\Delta_N = (\omega_N - \omega_{N-1})/2$.

A constant interval $\Delta\omega$ can be used if the value is set sufficiently small in order to prevent the return period of the wave realization for the spectrum being smaller than the desired duration of the analysis. In order to find correct stochastic values for an analysis in irregular sea, the duration must be of a certain length. This implies a small constant $\Delta\omega$. If it is desirable to decrease the needed computer calculation time, a method with random frequency intervals as presented above could be used. If the constant c_ω in equation (4.49) is sufficiently small it may not be necessary to have explicit formulations of the frequency intervals at the start and stop of the range for ω. This is because the error when integrating $S(\omega)$ over the frequency range will be small compared to the analytic result.

4.8.2 Hydrostatic and Dynamic Pressure and Equations of Motion

The hydrostatic pressure is assumed not to be affected by the wave elevation. This is according to linear wave theory, [Faltinsen (1990)]. The hydrostatic pressure is calculated by equation (4.28).

In the following, linear wave theory for deep water waves is assumed. In order to find the dynamic pressure under the waves in an irregular sea state, it is assumed that the dynamic pressure can be represented by a sum consisting of pressure contributions from each frequency ω_n and corresponding wave elevation ζ_{an} in the wave spectrum $S(\omega)$. This can be seen as a superposition of the different dynamic pressure contributions. For linear theory, superposition of the forces and responses can be applied, [Faltinsen (1990)]. The assumption of superposition is now used on the pressures. First, the n-th pressure contribution from ζ_{an} must be found. The random phase angle ε_n is included. The expression is

$$\begin{aligned} p_{dyn}(\omega_n, x, t) &= -\rho \frac{\partial \phi_{0n}(\omega_n)}{\partial t} \\ &= i\rho g \sqrt{2S(\omega_n)\Delta\omega_n} e^{k_n z + i(k_n x - \omega_n t - \varepsilon_n)} \end{aligned} \tag{4.51}$$

Here, $\phi_{0n}(\omega_n)$ is the velocity potential for wave component n in the spectrum. The wave amplitude ζ_{an} is expressed as $\sqrt{2S(\omega_n)\Delta\omega_n}$. The total dynamic pressure is obtained by adding the pressure contributions from all wave components in $S(\omega)$. The result is

$$\begin{aligned} p_{dyn}(x, t) &= i\rho g \sum_{n=1}^{\infty} p_{dyn}(\omega_n, x, t) \\ &= i\rho g \sum_{n=1}^{\infty} \sqrt{2S(\omega_n)\Delta\omega_n} e^{k_n z + i(k_n x - \omega_n t - \varepsilon_n)} \end{aligned} \tag{4.52}$$

In order to get a solution for the displacement, the forces due to nonlinear hydrostatic and Froude-Kriloff forces and the linear diffraction forces must be formulated. The instantaneous position of the floater must be considered, therefor a numeric time domain integration must be applied. The hydrostatic forces per unit length are calculated according to equation (4.31). The Froude-Kriloff forces per unit length are calculated by using equation (4.52) for the pressure and applying equation (4.32) for the forces. The linear modal diffraction forces are calculated by assuming that the contributions from the different wave components can be added. Superposition is applied. The expression for the Froude-Kriloff pressure force per unit length is

$$f_{(3,2D)}^{dyn} = \int_{\theta_1}^{\theta_2} i\rho g \sum_{n=1}^{\infty} \sqrt{2S(\omega_n)\Delta\omega_n} e^{k_n z' + i(k_n x' - \omega_n t - \varepsilon_n)} \cos\theta c \, d\theta \tag{4.53}$$

Here, x' and z' are the x and z coordinates on the wetted pipe section referring to the global coordinate system (x, y, z). θ_1 and θ_2 are the angles in the local coordinate system giving the intersection between the floater section and the 1st order surface. They are calculated by assuming that the slope of the wave elevation in an irregular sea can be expressed by the superimposed contributions from the slopes for each wave component. After the slopes are defined the method for finding θ_1 and θ_2 in Section 4.6.2 can be used. The equations of motion for the modal shape functions $\cos m\beta$ can now be formulated as

$$\begin{aligned}\left(m_{2D}+a_{33}^{(0)}\right)\ddot{a}_0+b_{33}^{(0)}\dot{a}_0=&-m_{2D}g+\frac{1}{2\pi R}\int_0^{2\pi} f_{(3,2D)}^{hyd} r\,d\beta\\&+\frac{1}{2\pi R}\int_0^{2\pi} f_{(3,2D)}^{dyn} r\,d\beta\\&-\sum_{n=1}^{\infty}\left[\omega_n^2 a_{33}^{(0)}\zeta_a J_0(k_nR)ie^{-i\omega_n t}\right]\end{aligned} \tag{4.54}$$

$$\begin{aligned}\left(m_{2D}+a_{33}^{(m)}\right)\ddot{a}_m+b_{33}^{(m)}\dot{a}_m+\frac{m^4}{R^4}EIa_m=&\frac{1}{\pi R}\int_0^{2\pi} f_{(3,2D)}^{hyd}\cos{(m\beta)}r\,d\beta\\&+\frac{1}{\pi R}\int_0^{2\pi} f_{(3,2D)}^{dyn}\cos{(m\beta)}r\,d\beta\\&-\sum_{n=1}^{\infty}\left[\omega_n^2 a_{33}^{(m)}2\zeta_a J_m(k_nR)i^{m+1}e^{-i\omega_n t}\right]\end{aligned} \tag{4.55}$$

Here, m_{2D} is the 2D mass of the floater, m is the mode number referring to the shape function $\cos m\beta$ and r is the distance from the center of the pipe to the origin of the global coordinate system (x, y, z). $r = R$ for 1 torus and $r = R \mp p$ for 2 tori. r is defined in equation (4.33) in Section 4.6.1. Equation (4.54) and (4.55) are a general formulations of the problem. When using the equations for the 2 tori case, the contributions for both rings must be included for the hydrostatic and Froude-Kriloff pressure forces.

Chapter 5

Relative Motion and Bending Stress

For a fish farm it is interesting to know the relative motion between the floater and the water surface in waves. This information will be vital in order to prevent fish escape. In this thesis only the floater without the presence of mooring system and net cage is investigated. Therefore, the effects of mooring and net cage will not be taken into account. Nevertheless, an investigation of the relative motion of the floater alone will give information about how the floater behave in waves. For a operating fish farm, the nett will be attached to the floater, and fish will be prevented from escaping even if parts of the floater are leaved completely dry for a short period of time. If parts of the floater becomes completely submerged, the net might not give a complete protection against fish escape. The net, mooring system and weights attached in order to hold the net in the preferred shape will also make the floater system behave differently compared to what is investigated in this thesis. Another aspect is the probability of structure failure of the floater or other components. A damaged floater or net might give openings in which the fish can escape. For this aspect it is important to investigate the bending stresses in the floater. Again, a complete fish farm with mooring and net cage will have different dynamic behavior than the freely floating collar investigated here. But, at certain intervals the fish cage is emptied and the netting removed. For this case it will be important to investigate the behavior of the floater in order to prevent structural damage or failure. Structural failure will have economic consequences. Structural weakening due to high loads and stresses on the floater may permanently reduce the strength of the floater, which in turn might give rise to structural failure at a later stage stage when the the net cage is reattached and housing fish. In the following the relative motion and the bending stresses for the freely floating circular collar will be investigated.

5.1 Relative Vertical Motion of The Floater

In this section the normalized vertical relative motion between the floater and the 1st order wave surface ζ will be investigated. The relative motion is normalized by dividing by the wave amplitude ζ_a. The relative motion r is calculated from the sea surface ζ to the z-coordinate of the center of the floater. Thus, the pipe radius must be subtracted from the results in order to investigate if the floater at some time and position is completely submerged or out of water. The relative motion will be investigated for both 1 torus and 2 tori in regular waves for the linear model. The relative motion is dependent on the time varying position of the floater and the wave elevation. A transfer function for the maximum relative motion on the floater will be found.

The sum of the motion for all modes, giving the total vertical displacement for each coordinate $x = R\cos\beta$ and time t must be considered. In the Matlab program only a limited number of modes will be used, starting at the first mode $n = 0$. This is because the higher modes, due to damping and structural properties, not will give significant contributions to the response. In this section a theoretical approach, that is a infinite number of nodes, will be used when deriving the expressions. The linear complex transfer function for mode n presented in Chapter 4 will now be denoted $H_0(\omega)$ and $H_n(\omega)$. The expressions are

$$H_0(\omega) = \frac{a_{0,a}}{\zeta_a} = \frac{\rho g b_w - \omega^2 a_{33}^{(0)}}{\rho g b_w - \omega^2 \left(m + a_{33}^{(0)}\right) - i\omega b_{33}^{(0)}} i J_0(kR) \tag{5.1}$$

$$H_n(\omega) = \frac{a_{n,a}}{\zeta_a} = \frac{\rho g b_w - \omega^2 a_{33}^{(n)}}{\rho g b_w + \frac{n^4}{R^4} EI - \omega^2 \left(m + a_{33}^{(n)}\right) - i\omega b_{33}^{(n)}} 2 i^{n+1} J_n(kR) \tag{5.2}$$

When it is referred to $H_n(\omega)$ in the following, this means both equation (5.1) and (5.2). When $n = 0$ equation (5.1) is used. When $n = 1, 2, 3...$ equation (5.2) is used to calculate $H_n(\omega)$. A reference to mode n will now include all values of n. That is $n = 0, 1, 2....$ This applies for all physical values and expressions presented.

The time dependent motion of mode n, or Fourier component n for the total vertical displacement can now be written as

$$a_n(t) = H_n(\omega)\zeta_a e^{-i\omega t} \tag{5.3}$$

In equation (5.3), ζ_a and ω are the wave amplitude and wave circular frequency respectively. The mode motion is harmonic with the frequency ω. The vertical displacement of mode n at $x = R\cos\beta$ and time t, denoted $w_n(\beta, t)$ can now be written as

$$w_n(\beta, t) = a_n(t)\cos n\beta = H_n(\omega)\zeta_a \cos(n\beta) e^{-i\omega t} \tag{5.4}$$

The total vertical displacement of the floater with respect to position β and time t is the sum of $w_n(\beta, t)$ over all values of n. The expression is

$$w(\beta, t) = \sum_{n=0}^{\infty} a_n(t)\cos n\beta = \sum_{n=0}^{\infty} H_n(\omega)\zeta_a \cos(n\beta) e^{-i\omega t} \tag{5.5}$$

In order to find the relative motion between the floater and the surface the wave elevation with respect to the position of the floater section and time must be known. A general expression for the wave elevation derived from the velocity potential of the incident waves is shown in Chapter 4. The expression for the wave elevation is now

$$\zeta(\beta, t) = i\zeta_a e^{ikR\cos\beta} e^{-i\omega t} \tag{5.6}$$

The relative motion can be found by subtracting the wave elevation from the total vertical displacement. The relative motion is defined as positive when the total displacement is larger than the wave elevation. The relative motion is

$$r(\beta, t) = w(\beta, t) - \zeta(\beta, t) = \zeta_a \left[\sum_{n=0}^{\infty} H_n(\omega)\cos(n\beta) - i e^{kR\cos\beta}\right] e^{-i\omega t} \tag{5.7}$$

The expression in equation (5.7) gives the relative motion for each position β and time t on the floater. In order to derive a transfer function for the relative motion the amplitude must be found. The solution of equation (5.7) is assumed to be on the form $r(\beta, t) = r_a(\beta, \omega)e^{-i\omega t}$. The transfer function is found by dividing the relative amplitude $r_a(\beta,\omega)$ by the wave amplitude and taking the absolute value of the expression. The transfer function is

$$\left|\frac{r_a(\beta,\omega)}{\zeta_a}\right| = \left|\sum_{n=0}^{\infty} H_n(\omega)\cos(n\beta) - ie^{kR\cos\beta}\right| \tag{5.8}$$

It is interesting to find the maximum relative motion between the floater and the water surface for each wave frequency. This is found by taking the maximum value of $r_a(\beta,\omega)/\zeta_a$ for each frequency ω. The formula is

$$\left|\frac{r_{a,max}(\omega)}{\zeta_a}\right| = max\left[\left|\sum_{n=0}^{\infty} H_n(\omega)\cos(n\beta) - ie^{kR\cos\beta}\right|\right] \tag{5.9}$$

max indicates the Matlab function max used in the Matlab program in order to find the maximum relative motion. max finds the maximum value of a vector or the maximum values of the the chosen dimensions in a matrix.

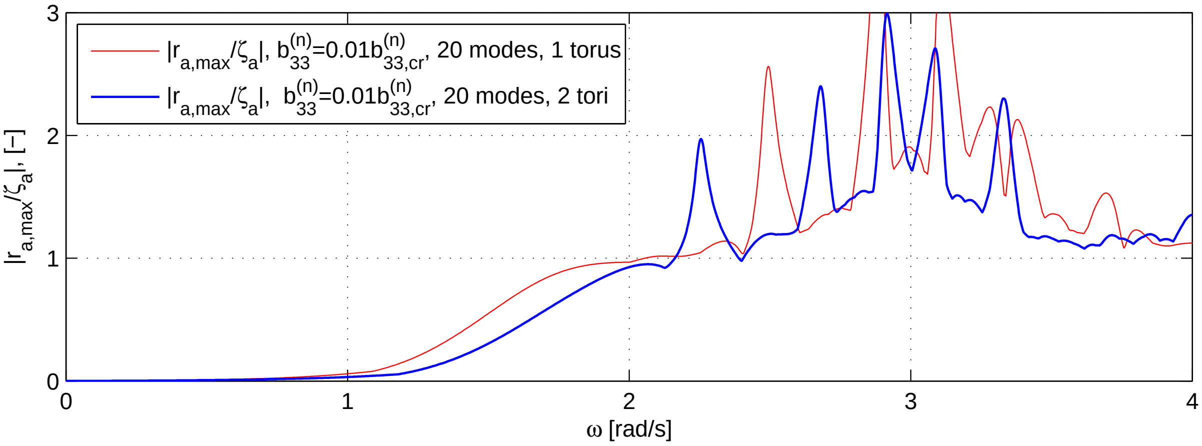

Figure 5.1: RAO for maximum relative vertical motion between the floater center and the waves. $r_{a,max}$ is the relative motion. ζ_a is the wave amplitude. ω is the wave frequency.

The normalized relative motion for 1 torus and 2 tori presented in equation (5.9) is plotted in Figure 5.1. The relative normalized motion is plotted as a function of the wave circular frequency ω. A damping level of 1% of the critical damping for each mode is applied. This is done in order to prevent the response going to infinity for the resonance frequencies. The 20 first modes are used. Anny additional modes included in the analysis will not give a visible contribution to the response. Convergence with respect to the number of modes used in the anlysis and the effect of the set damping level is addressed in Chapter 6. In Figure 5.1 the resonace frequencies of the different modes for 1 torus and 2 tori are clearly seen. It is also observed, if the resonance peaks are neglected, that the relative responses are quite similar for $\omega = 0rad/s$ to $\omega = 1rad/s$, $\omega = 2rad/s$ to $\omega = 3rad/s$ and around $\omega = 4rad/s$. The difference in response for 1 torus and 2 tori that is most consequent is between $\omega = 1rad/s$ and $\omega = 2rad/s$. Here, 1 torus has a significantly higher response than 2 tori. In general, when investigating the interval presented in Figure 5.1, the response for 1 torus is larger than for 2 tori. It is desireable to have low relative motion in terms of avoiding sections of the floater being completely submerged or completely out of water. But, a lower relative response indicates that the floater are more flexible. This might effect the stresses. Stresses will be investigated in Section 5.2.

5.2 Bending Stress

This thesis is primarily focusing on the hydrodynamic aspects of the floater. That is wave loads and vertical response. From a structural point of view it is important to investigate stresses. As a introduction to structural analysis of the floater, this section will address the bending stresses. Although a freely floating circular collar is investigated, which is a simple system compared with the complex structure of a complete fish farm, this will give insight into the structural response of the floater. For situations where the net cage is removed, the results from this investigation will be interesting. For the latter case, the mooring system will give contributions to the response. The analysis of the freely floating structure can be seen as a simplified analysis giving basic understanding of the stresses.

The HDPE pipes that are used in the floater are originally straight. They are bent into shape and welded together. This will set a certain pretension in the pipes. The pretension might be reduced over time due to the material setting in the circular shape. The effects of the pretension with respect to magnitude, deterioration, and effects on the total bending stresses will not be addressed further. It is only the vertical displacement that is considered when calculating the bending stresses. A floating collar without net cage at sea will be deformed also in the horizontal plane, and the mooring system will effect the response. The fact that the bending stresses are investigated for a freely floating collar without mooring system and net cage, and without taking horizontal motion into account, must be kept in mind when the results are discussed.

Bending stress can be derived from the bending moment in the pipes. Therefore, the bending moment will be investigated first. the general formula for bending moment according to linear beam theory, [Hibbeler (2005)], is

$$M(x,t) = -EI\frac{\partial^2 w(x,t)}{\partial x^2} \tag{5.10}$$

Equation (5.10) gives the bending moment for a straight beam with x and t as the spatial and time variable respectively. $w(x,t)$ is the vertical displacement. EI is the bending stiffness, where E and I is the E-modulus and 2nd area moment for the pipe. If the beam is curved into a circle, similar to the pipes in the floater, the expression can be written as

$$M(s,t) = -EI\frac{\partial^2 w(s,t)}{\partial s^2} \tag{5.11}$$

Here, s is the spatial coordinate going through the center line of 1 torus and along the midpoint between the center lines of the pipes for 2 tori. The 2nd derivative of the total vertical displacement $w(s,t)$ with respect to s must be found. The expression for $w(s,t)$ presented in equation (4.12) is used. n are now, and in the following expressions for coefficients, displacement, bending moment and bending stress, referring to $n = 0, 1, 2...$ This is done in order to simplify the expressions. When solving the equations presented next, either by hand calculation or by programming, care must be taken in order to make the coefficients and displacements correspond with the theory presented in Chapter 4. When finding the second derivative of the displacement the expression $\partial^2/\partial s^2 = \partial^2/R^2\partial\beta^2$ is utilized. The 2nd derivative of the vertical displacement with respect to s is

$$\frac{\partial^2 w(s,t)}{\partial s^2} = \frac{\partial^2 w(\beta,t)}{R^2\partial\beta^2} = -\frac{1}{R^2}\sum_{n=0}^{\infty} n^2 a_n(t)\cos n\beta \tag{5.12}$$

Here, $a_n(t)$ is the Fourier coefficient in the expression for the vertical displacement. The bending moment with respect to β and t is now

$$M(\beta,t) = \frac{EI}{R^2}\sum_{n=0}^{\infty} n^2 a_n(t)\cos n\beta \tag{5.13}$$

Since the Fourier coefficient $a_n(t)$ is harmonic with $e^{-i\omega t}$, the bending moment is harmonic with $e^{-i\omega t}$. The time depending bending moment and the amplitude of the bending moment can be expressed as shown in equation (5.14) and (5.15).

$$M(\beta,t) = M_A(\beta)e^{-i\omega t} = \frac{EI}{R^2}\sum_{n=0}^{\infty} n^2 a_{n,a}\cos{(n\beta)}e^{-i\omega t} \tag{5.14}$$

$$M_A(\beta) = \frac{EI}{R^2}\sum_{n=0}^{\infty} n^2 a_{n,a}\cos n\beta \tag{5.15}$$

$a_{n,a}$ is the amplitude of the Fourier coefficient in the equation for the total vertical displacement. If it is utilized that $a_{n,a} = H_n(\omega)\zeta_a$ and the bending moment is normalized by dividing by the wave amplitude we get

$$\frac{M_A(\beta)}{\zeta_a} = \frac{EI}{R^2}\sum_{n=0}^{\infty} n^2 H_n(\omega)\cos n\beta \tag{5.16}$$

$M_A(\beta)$ is the amplitude of the bending moment for the position β on the floater and a wave with circular frequency ω. The formula for the maximum bending stress σ_{max} according to linear beam theory, [Hibbeler (2005)], due to a bending moment is

$$\sigma_{max}(\beta) = \frac{M_A(\beta)}{I} r_{max} \tag{5.17}$$

$\sigma_{max}(\beta)$ is the complex amplitude, or the maximum complex bending stress with respect to β and a wave with frequency ω. I is the 2nd area moment for one pipe for 1 torus and for 2 pipes combined for 2 tori, respectively. r_{max} is the maximum radial distance from the center of the pipe to the surface of the pipe. This distance is set to the radius c of the pipe. The bending stress is normalized by dividing by the wave amplitude. The normalized maximum bending stress on a position $x = R\cos\beta$ on the floater and a wave with circular frequency ω is

$$\frac{\sigma_{max}(\beta,\omega)}{\zeta_a} = \frac{cE}{R^2}\sum_{n=0}^{\infty} n^2 H_n(\omega)\cos n\beta \tag{5.18}$$

The expression in equation (5.18) gives a complex quantity which will give the time dependent maximum normalized bending stress with respect to β and ω if multiplied with the harmonic function $e^{-i\omega t}$. In order to get the amplitude of the bending stress, the absolute value of equation (5.18) is taken. This gives the normalized amplitude of the bending stress with respect to β. For the results to be presented as a transfer function, the maximum value of equation (5.18) for each ω is found. The approach is similar to the method for finding the transfer function for the relative motion presented in Section 5.1. The expression for the normalized bending stress amplitudes and the transfer function for the bending stresses are given in equation (5.19) and (5.20).

$$\left|\frac{\sigma_{max}(\beta,\omega)}{\zeta_a}\right| = \frac{cE}{R^2}\left|\sum_{n=0}^{\infty} n^2 H_n(\omega)\cos n\beta\right| \tag{5.19}$$

$$\left|\frac{\sigma_{max}(\omega)}{\zeta_a}\right| = max\left[\frac{cE}{R^2}\left|\sum_{n=0}^{\infty} n^2 H_n(\omega)\cos n\beta\right|\right] \quad ,\text{where } \beta\epsilon[0,2\pi] \tag{5.20}$$

The expressions for bending moment and bending stress presented above will be valid for both the 1 torus and 2 tori case. For 2 tori it is important to use the 2nd area moment for the two pipes combined. This will be the same as multiplying I for one pipe with 2. Figure 5.2 shows the transfer function for the maximum bending stresses as a function of the wave circular frequency ω. The bending stresses are calculated for both 1 torus and 2 tori. A damping level of 1 percent of the critical damping for each mode is used in order to damp out infinite responses for the displacement at the resonance frequencies, which might effect the bending moments and thus the bending stresses. The 20 first modes are used in the analysis. Additional modes will not give a significant change in the bending stresses in the interval for ω presented in Figure 5.2. Convergence of the results with respect to number of modes included in the analysis and damping level will be further addressed in Chapter 6.

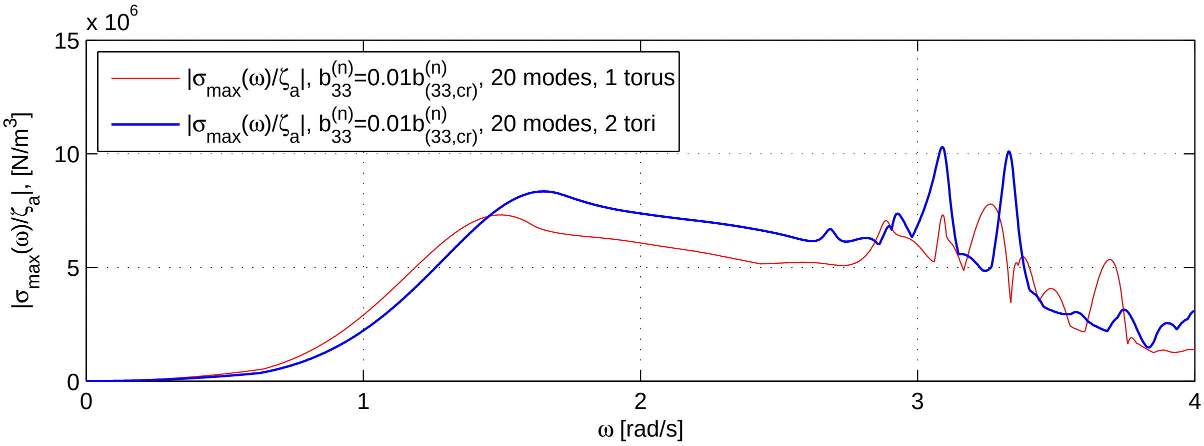

Figure 5.2: RAO for maximum bending stress. $\sigma_{max}(\omega)$ is the maximum bending stress. ζ_a is the wave amplitude. ω is the wave frequency.

From Figure 5.2 it can be observed that maximum bending stress for 2 tori is significantly higher than the maximum bending stress for 1 torus between approximately $\omega = 1.5rad/s$ and $\omega = 2.8rad/s$. From $\omega \approx 0.7rad/s$ to $\omega \approx 1.4rad/s$ the bending stress for 1 torus is larger than the bending stress for 2 tori. The results for the rest of the interval are not conclusive. The observation from Section 5.1 that the relative motion for 2 tori are smaller than the relative motion for 1 torus, and thus the 2 tori configuration being more flexible, are supported by the results in Figure 5.2. The curvature of the pipes will increase with decreasing stiffness. The bending stiffness EI for 1 torus is twice as large as the bending stiffness for 2 tori. This must not be interpreted as a conclusive result. Factors such as wave loads, restoring coefficients and damping will effect the response. Therefore, many factors contribute to the total response, and may explain that 1 torus has the largest bending moments for long waves. From equation (5.20) it is seen that the 2nd area moment I does not effect the bending stress directly. But, I is contributing to the restoring coefficient in the linear equations of motion. Since the bending stresses are calculated from the transfer functions, the property I of the cross section will effect the results.

5.3 Standard Deviation of Bending Stresses in a Sea State

The transfer function presented in equation (5.20) gives a maximum bending stress for a given circular frequency and amplitude of a regular wave. At sea the waves are irregular. Therefore, a method for predicting the most probable maximum bending stresses in a given sea state is needed. The standard deviations and the most probable maximum bending stresses in a sea state will be derived. The method will give a standard deviation for each position $x = R\cos\beta$ on the floater in the interval $\beta = 0$ to $\beta = \pi$. The response is symmetric about the x-axis due to the progagation direction of the incident waves, and it will therefore not be necessary to calculate the standard deviations for $\beta = \pi$ to $\beta = 2\pi$. The most probable maximum bending stresses are derived from the standard deviations.

The transfer function for the bending stresses are now denoted $H_\sigma(\beta, \omega)$. The expression for the absolute value of $H_\sigma(\beta, \omega)$ is

$$|H_\sigma(\beta,\omega)| = \frac{\sigma_{max}(\beta)}{\zeta_a} = \frac{cE}{R^2}\left|\sum_{n=0}^{\infty} n^2 H_n(\omega)\cos n\beta\right| \tag{5.21}$$

This function gives the bending stresses for each position on the floater β and each wave frequency ω. The next step is to find the response spectrum for the maximum bending stress due to the wave spectrum function $S(\omega)$. The response spectrum for a response given by a transfer function can be found by multiplying the absolute value of the transfer function squared with the wave spectrum, [Faltinsen (2005)]. That is when the wave spectrum represent the exciting forces. The response spectrum for the bending stresses is defined as

$$S_\sigma(\omega) = S(\omega)\,|H_\sigma(\omega,\beta)|^2 \tag{5.22}$$

The variance of the parameter a spectrum is describing, in this case the stresses, is found by taking the zeroth moment of the response spectrum, [Faltinsen (2005)]. The moment of a one sided spectrum is found by integrating the spectrum over the interval $\omega\epsilon[0,\infty]$. The variance, or standard deviation squared of the maximum bending stresses is

$$\sigma_\sigma^2 = \int_0^\infty S_\sigma(\omega)\,d\omega = \int_0^\infty S(\omega)\,|H_\sigma(\beta,\omega)|^2\,d\omega \tag{5.23}$$

The standard deviation is normalized by dividing equation (5.23) with the significant wave height squared. A normalized wave spectrum on the form $S(\omega)/H_{1/3}^2$ must then be used. $H_{1/3}$ is the significant wave height. The normalized standard deviation $\sigma_\sigma/H_{1/3}$ is expressed as

$$\left(\frac{\sigma_\sigma}{H_{1/3}}\right)^2 = \int_0^\infty \frac{S(\omega)}{H_{1/3}^2}\left(\frac{cE}{R^2}\right)^2\left|\sum_{n=0}^{\infty} n^2 H_n(\omega)\cos n\beta\right|^2\,d\omega \tag{5.24}$$

$H_n(\omega)$ is the transfer function for the vertical displacement. The expression for $H_\sigma(\beta,\omega)$ in equation (5.21) is utilized when deriving equation (5.24). A narrow banded wave process will in the following be assumed. A wave process is narrow banded if the sea surface is a narrow banded normal distributed stochastic process. The elevation of the sea surface is then described by the normal distribution, [Faltinsen (2005)]. This implies that positive and negative values of the wave elevation will be equally distributed around the mean free surface. For a narrow banded process, the Rayleigh distribution can be used for the probability density function of the maximum wave amplitudes. Given the Rayleigh distribution, an approximation for the normalized maximum response in a sea state, from [Faltinsen (2005)], is

$$\frac{\chi_\sigma}{H_{1/3}} = \frac{\sigma_\sigma}{H_{1/3}} \sqrt{2lnN} \tag{5.25}$$

χ_σ is the most probable maximum response in a sea state. N is the number of oscillations in the sea state. The assumption that the wave elevation is a stationary random process is in practice applicable for a limiting time period in the range from $1/2$ hour to 10 hours, [Faltinsen (1990)]. For a short time description of the wave elevation an approximation to the most probable maximum response is

$$\frac{\chi_\sigma}{H_{1/3}} = 4 \frac{\sigma_\sigma}{H_{1/3}} \tag{5.26}$$

In the following, a Pierson-Moskowitz (PM) type spectrum is used to represent an irregular sea state. A PM-type spectrum recommended by the 15th ITTC for a fully developed sea state is the ISSC spectrum, [Faltinsen (1990)]. The expression for the ISSC wave spectrum is

$$\frac{S(\omega)}{H_{1/3}^2} = \frac{0.11}{\omega^5} \left(\frac{2\pi}{T_1}\right)^4 exp\left[-0.44\left(\frac{2\pi}{\omega T_1}\right)^4\right] \tag{5.27}$$

Here, T_1 is the mean period defined by $T_1 = 2\pi m_0/m1$. The moment m_k is defined by the expression

$$m_k = \int_0^\infty \omega^k S(\omega)\, d\omega \tag{5.28}$$

The peak period Tp, giving the frequency $\omega_p = 2\pi/T_p$ where the spectral density function $S(\omega)$ has its maximum value is calculated as $T_p = 1.408T_2$. T_2 is defined by $T_1 = 1.086T_2$, [Faltinsen (1990)].

For a sea state with duration of 3 hours and a mean period of 10 seconds $\sqrt{2lnN} \approx 3.74$. For a duration of 6 hours and a mean period of 10 seconds $\sqrt{2lnN} \approx 3.92$. For sea states with longer duration and/or a smaller mean period, $\sqrt{2lnN}$ may be larger than 4. The expression in equation (5.26) will still give a good approximation of the most probable largest bending stress. When using equation (5.26) the duration of the sea state must be kept in mind.

The most probable normalized maximum bending stresses around the floater in a sea state defined by the ISSC wave spectrum is plotted in Figure 5.3. The peak period is 6 and 8 seconds. The results for both 1 torus and 2 tori are calculated. The damping is set to 1 percent of critical damping for each mode. The 20 first modes are used. Additional modes included will not give a contribution to the response. The maximum response for the two peak periods is seen to be largest at $\beta = \pi/2$. That is at the midpoints on the floater in the wave propagation direction. This indicates that the largest curvature in the pipes occur here. For a peak period of 6 seconds, the floater configuration with 2 tori has the highest maximum bending stress. The difference between 1 torus and 2 tori is small. For a peak period of 8 seconds, 1 tori has the largest maximum bending stress. The sea state with a peak period $T_p = 6s$ have waves with more energy for high frequencies than the sea state with $T_p = 8s$. From the transfer functions for the maximum bending stress it is seen that 2 tori generally has higher bending stresses for frequencies higher than $1.5rad/s$. For lower frequencies 1 torus has slightly higher bending stresses. The higher the peak period in a sea state is, the lower are the frequencies for the waves with the highest energy. This can be one explanation for the standard deviations for 1 torus and 2 tori.

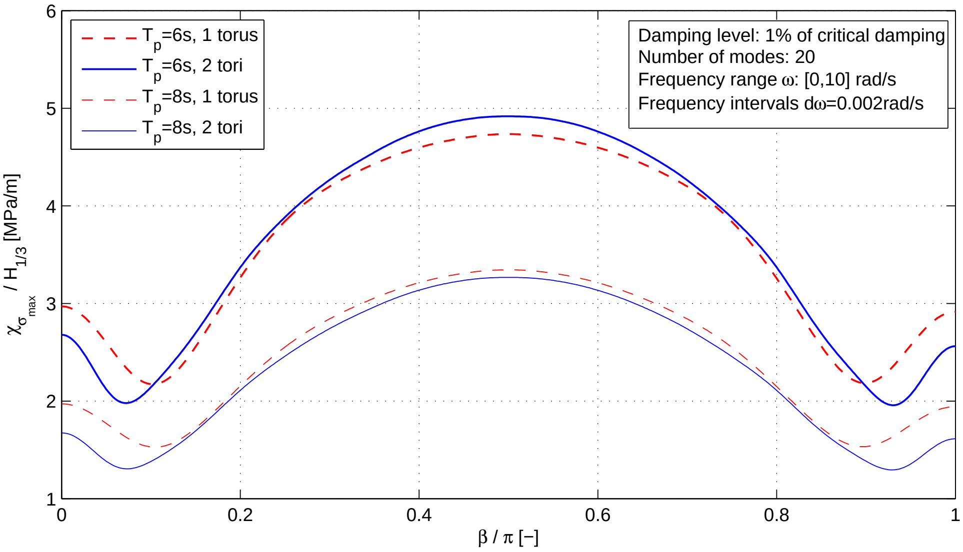

Figure 5.3: Most probable maximum normalized bending stresses in the floater. $\chi_{\sigma_{max}}$ is the most probable maximum bending stress. $H_{1/3}$ is the significant wave height. The position on the floater is given by $x = R\cos\beta$. T_p is the spectral peak period in the ISSC wave spectrum.

The plots of the transfer functions for the first three modes in Chapter 4 indicates that the higher modes need shorter waves than the lower modes in order for the corresponding mode shape to be excited. The form of the transfer functions for the modes for 1 torus and 2 tori are similar in shape, but the resonance frequencies for 2 tori are lower than the resonance frequencies for 1 torus. The transfer functions for the vertical displacement, vertical relative motion between the floater and the surface and the bending moments in Figure 4.2, 4.3, 5.1 and 5.2 respectively, give a picture of for which wave frequencies a certain response is excited. But they do not give information about which frequencies are most common in a given sea state or what the floater response will be in that sea state. In Figure 5.4 the transfer functions for the maximum bending stresses are plotted together with the normalized ISSC wave spectrum. The wave spectrum is plotted for the peak periods $T_p = 6s$ and $T_p = 8s$.

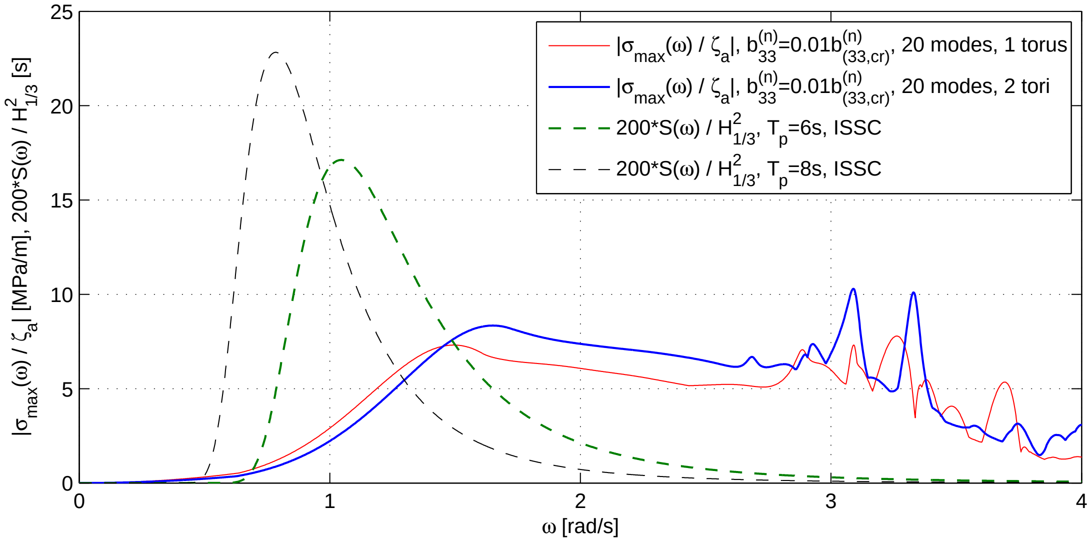

Figure 5.4: Transfer functions for the maximum bending stresses $\sigma_{max}(\omega)$ and normalized wave spectra. ω is the wave frequency. ζ_a is the wave amplitude. $H_{1/3}$ is the significant wave height. T_p is the spectral peak period.

Chapter 6

Results - Linear Analysis

6.1 Displacements and Relative Motion

The linear transfer function for maximum relative motion between the center line of the floater and the first order surface ζ were presented in Chapter 5. The transfer functions for 1 torus and 2 tori were shown in Figure 5.1. In the figure the modal damping level was 1 percent of critical damping for each mode. The 20 first modes were used. Now, convergence of the undamped transfer function with respect to the number of modes included in the analysis and the effect of damping will be presented and discussed. The effect of damping on the displacements will also be addressed. The transfer functions presented in this section are linear, and give the response due to linear coefficients and linear excitation forces. The transfer functions for relative motion give the maximum amplitude of the relative motion on the floater, but does not give information about at which positions on the floater the maximum relative response occur. The response in terms of relative motion for 1 torus and 2 tori will be compared, and the validity of the results with respect to the wave frequency ω will be duscussed.

6.1.1 Convergence of the Transfer Function for Relative Motion

The undamped transfer function for relative motion for 1 torus is plotted in Figure 6.1(a). The results for the first 7, 10 and 15 modes are compared. The first mode is always heave, given by $n = 0$ in the equations of motion. From Figure 6.1(a) it is seen that results for 7 modes deviate from the transfer functions for 10 and 15 modes between $\omega \approx 1.5rad/s$ and $\omega \approx 2.4rad/s$. For other frequencies the approximation is good for 7 modes. For frequencies higher than $4rad/s$ up to $5rad/s$, not shown in the figure, the differences in the response between 7, 10 and 15 modes are not significant. For frequencies higher than $5rad/s$ the response is chaotic due to the resonance frequencies of the higher modes. Convergence for frequencies higher than $5rad/s$ is therefore difficult to evaluate. For a frequency ω of $5rad/s$ the wave length according to linear theory, [Faltinsen (1990)], is approximately $2.46m$. For open sea conditions it is not anticipated that shorter waves than this will contain a significant amount of energy. There is a small difference in the response for 10 and 15 modes around $\omega = 2rad/s$. Any number of modes higher than 15 will not give a visible change in the response. Investigation show that 12 modes are needed for the 1 torus case in order to get convergence. A total of 30 modes have been tested. For a frequency domain analysis, the computer calculation time will be short since no iterations are needed and only one result for each frequency is needed. In a time domain analysis, for instance when the nonlinear hydrostatic and Froude-Kriloff forces are calculated, the calculation time will be long since time series of the response must be found. In the latter case it could be of interest to shorten the computer time as much as possible without compromising the results. The number of modes included if the relative motion where to be investigated in a nonlinear analysis could then be reduced to 12 or perhaps 10. In the frequency domain

10 modes give a maximum relative error of approximately 5 percent compared with 15 modes for 1 torus. The estimate for 10 modes is conservative. In order to ensure correct results a minimum of 12 modes should be included in a nonlinear analysis for 1 torus. A minimum of 15 modes will be used in order to ensure correct mathematical results. In Section 6.2.1, the bending stresses are investigated. It will be shown that more than 15 modes are needed in order to represent the stresses correctly. It must be kept in mind that Figure 6.1(a) shows the undamped relative motion. Damping will effect the results. In terms of relative motion, convergence is investigated for undamped motion. This is because it is assumed that a system without damping will have stricter requirements for convergence than a system with damping. In Figure 6.1(a) the first resonance frequencies for 1 torus are clearly seen.

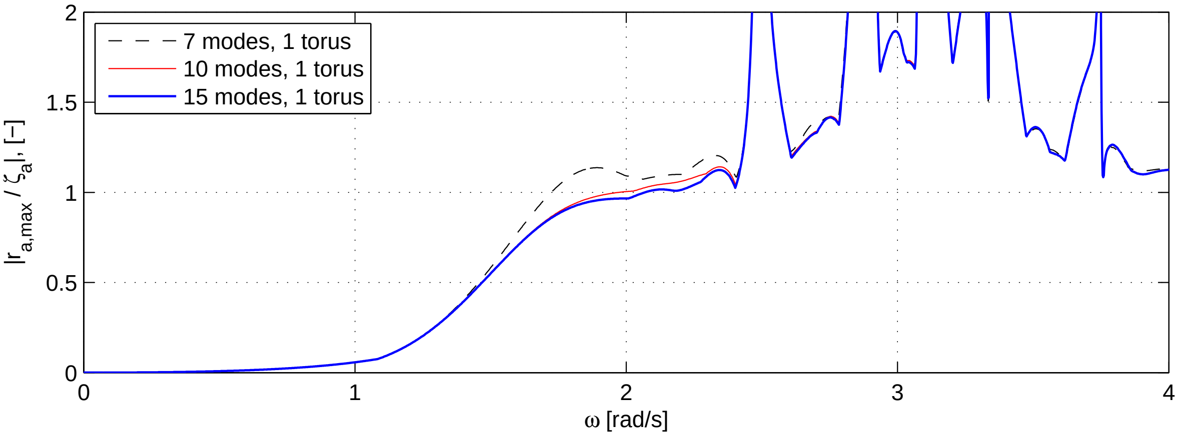

(a) Relative motion 1 torus.

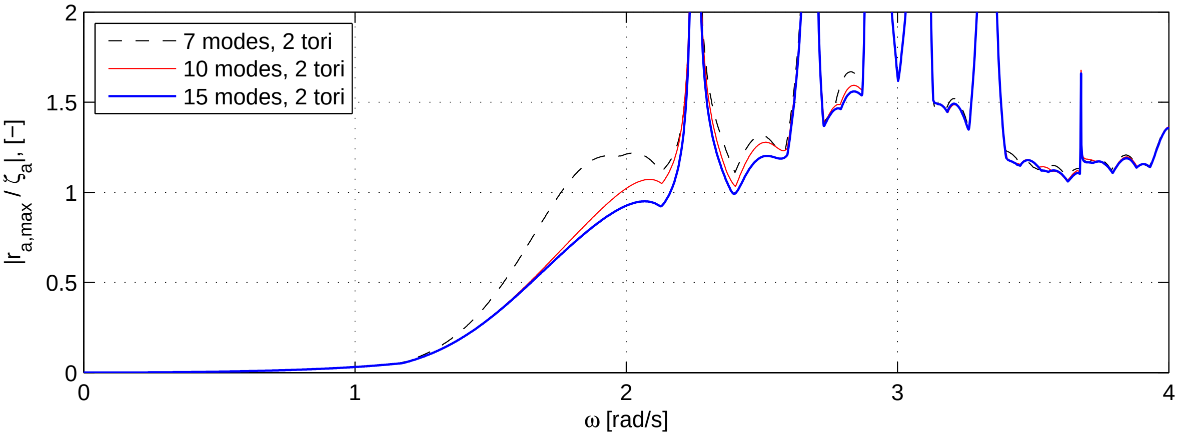

(b) Relative motion 2 tori.

Figure 6.1: Undamped transfer function for maximum relative motion with respect to wave circular frequency ω for 1 torus and 2 tori. $r_{a,max}$ is the maximum relative motion between the center line of the floater and the first order surface ζ. ζ_a is the wave amplitude. The results for a total of 7, 10 and 15 modes are compared.

Figure 6.1(b) shows the undamped transfer functions for relative motion for 2 tori. The effect of including 7, 10 and 15 modes are compared. As for 1 torus, the response for 2 tori when including the 7 first modes is to large compared with 10 and 15 modes. When additional modes are included in the analysis, the response is reduced. This is probably due to increased flexibility of the floater since the constriction on the shape of the floater is reduced. This also applies for 1 torus. Convergence of the results was reached when 13 modes were included. Additional modes included did not give a visible change in the response. The maximum number of modes tested were 30. Plots for more than 15 modes are not shown, since this will give graphs coinciding with the graph for 15 modes. The frequency range investigated is the same as for 1 torus. For 2 tori there is a larger difference between 10 and 15 modes than for 1 torus. 12 modes were also investigated. This gave, for $\omega = 2rad/s$, a relative motion smaller than for 10 modes, but larger than for 15 modes. This is expected, since the total flexibility in the system is reduced when the number of modes are reduced. The result for 12 modes and 13 modes are not included in Figure 6.1(b) due to readability. Figure 6.1(b) and the discussion above indicate that 13 modes are sufficient in order to correctly represent the relative motion for 2 tori for circular frequencies up to $5\text{rad}/s$. 15 modes are used in order to ensure that mathematical correct results are obtained. As for 1 tori, damping will effect the relative response for 2 tori.

6.1.2 Effect of Damping on the Relative Motion

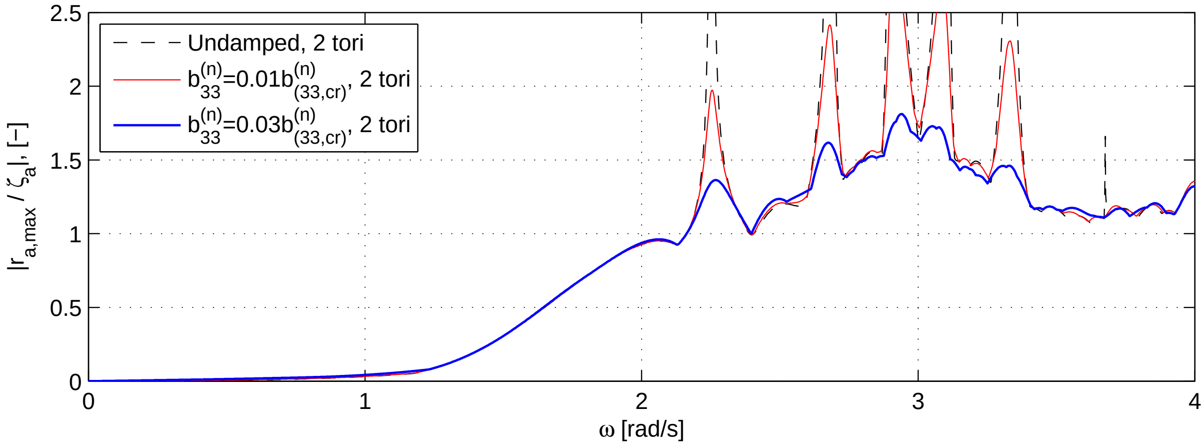

Figure 6.2: Transfer function for maximum relative vertical motion between the floater center line and the first order surface ζ with respect to the circular wave frequency ω for 2 tori. Undamped motion and a damping level of 1 percent and 3 percent of critical damping for each mode are compared. $r_{a,max}$ is the maximum relative motion amplitude. ζ_a is the wave amplitude. $b_{33}^{(n)}$ and $b_{(33,cr)}^{(n)}$ are the vertical modal damping and vertical critical modal damping, respectively.

The effects of damping on the relative motion of the 2 tori configuration of the floater is seen in Figure 6.2. The undamped transfer function and the transfer functions for a damping level of 1 percent and 3 percent of modal critical damping are plotted. The graph show that the damping levels investigated here only give a significant contribution to the response for the resonance frequencies. A small difference from the undamped case to the case with a damping of 3 percent of the critical damping is seen at $\omega \approx 1rad/s$ and $\omega \approx 2rad/s$. If the damping is increased the difference between the undamped and damped case might be larger. In this project, the damping is set sufficiently low in order to not exceed the real damping in the system. A damping level of 1.5 and 3 percent will be used for most of the cases where damping is needed. It can be mentioned that a damping level of 3 percent might be to high, but this damping level was needed in order to get convergence in the time domain analysis for the steepest waves. A high damping, being 10 percent of critical, was tested. The relative response where effected also for none-resonant frequencies for both 1 torus and 2 tori. Since a damping level of up to 3 percent only gives contribution at resonance, damping is assumed not to effect the results for convergence, with respect to the number of modes included in the analysis, presented in Section 6.1.1. Damping has a similar effect on the 1 torus case. Damping will only give contribution to the response at resonance for damping levels up to 3 percent.

In Figure B.3 in Appendix B.2 the transfer functions for heave and pitch displacement for 2 tori are shown. The undamped case and a damping level of 1.5 and 3 percent are compared. Also here it can be seen that damping only effect the response at resonance. This also applies for 1 torus and higher modes.

6.1.3 Comparison Between Relative Motion for 1 Torus and 2 Tori

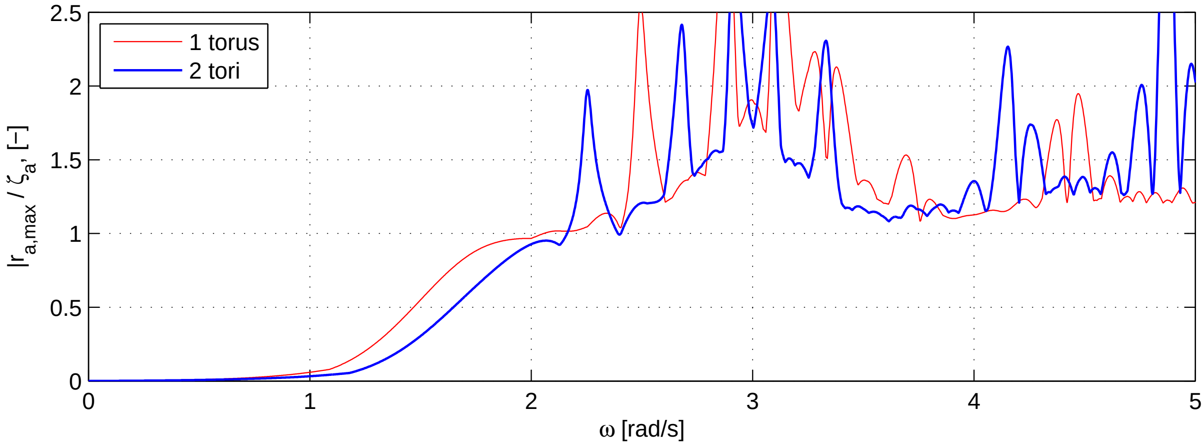

Figure 6.3: Transfer function for maximum relative vertical motion between the floater center line and the first order surface ζ with respect to the circular wave frequency ω for 1 torus and 2 tori. A damping level of 1 percent of critical damping for each mode is used. $r_{a,max}$ is the maximum relative motion amplitude. ζ_a is the wave amplitude.

In Figure 6.3, the transfer functions for maximum relative motion between the floater center line and the first order surface ζ for 1 torus and 2 tori are shown. The normalized relative motion $r_{a,max}/\zeta_a$ is plotted as a function of the wave frequency ω. The damping level for each mode is 1 percent of critical damping for each mode. The relative motion for 1 torus is generally higher than the relative motion for 2 tori in the frequency range in the figure. One reason for this can be that the bending stiffness of the floater for 1 torus is higher than the bending stiffness for the floater when it consist of 2 tori. A higher bending stiffness gives a structure that is more resistant to bending, and will therefore not follow the waves as closely as a structure with lower bending stiffness. Although the floater for 1 torus and 2 tori has the same mass per unit length, the 2 tori configuration has a significantly higher added mass, restoring and damping coefficient. The damping levels for the two cases are similar, but the increased added mass and restoring coefficient will give higher damping since a level of critical damping is used. The increased added mass for 2 tori compared with 1 torus will effect the relative motion of the floater. This could also explain the reduced relative motion. In Figure 6.3, the relative responses are plotted from $\omega = 0rad/s$ to $\omega = 5rad/s$. The velocity potentials used when deriving the added mass were formulated for the asymptotic zero frequency case, that is $\omega \rightarrow 0$. It is then evident that the added mass formulation not will be valid for high frequencies since the rigid free surface condition on which the velocity potential is based not will be satisfied. This will give uncertainties in the response calculations for high frequencies. For low frequencies the calculation of responses will give a good approximation in terms of the theory presented. The added mass for both 1 torus and 2 tori are large compared with the mass of the floater. The added mass for 1 torus and 2 tori are approximately 5 and 10 times larger than the mass of the floater. A change in the added mass will effect the response due to a change in diffraction forces and resonance frequencies. What range of frequencies that can be considered low, and thus approximately satisfy the rigid free surface condition is not investigated. The uncertainty for the response calculations for increased frequencies will therefore increase. This effect can be regarded as an error source for the results. For high frequencies, larger than $5rad/s$ the normalized relative response in figure (6.3) goes toward a value of approximately 1.25 for both 1 torus and 2 tori. In linear theory the response of a structure for high frequencies will go to zero, giving a normalized relative response equal to one. The observation that the normalized relative response is higher than one could be caused by low damping, and thus excitation of resonance frequencies for higher modes. When it is stated that the relative response goes to 1.25, it is referred to the mean lowest values of the response for high frequencies. The relative response for frequencies from $\omega = 5rad/s$ to $\omega = 10rad/s$ is not going evenly towards a given value.

The response is varying due to the resonance frequencies. 1.25 is the mean value of the local minima in the transfer functions for high frequencies. The fact that the rigid free surface condition not is satisfied for high frequencies might also be the cause for why the normalized relative motion is not going towards one.

Although damping is included in the equations of motion, the resonance frequencies for the first modes are clearly seen in Figure 6.3. Since the damping level is set low due to uncertainty in the real damping level for the floater, the responses at the resonance frequencies must not be interpreted as a conclusive result. The response will be reduced at resonance if the damping is increased. In Section 6.1.2 it was shown that a low damping level only will effect the response at resonance. It is therefore assumed that the calculated responses for frequencies lower than the first natural frequency not will be significantly altered by the real damping level for the floater.

6.2 Bending Stress

The maximum bending stresses in the floater for different wave frequencies will now be investigated. Before the bending stresses for 1 torus and 2 tori are compared, the convergence of the transfer functions for maximum bending stresses with respect to number of modes included in the analysis and the effect of damping will be investigated. The transfer function is presented in Chapter 5. The contribution from the n-th mode in the transfer function is proportional to n^2. It is therefore expected that there will be difficult to get convergence for a limited number of modes, especially when the damping is low. The transfer function give the maximum bending stress for a given wave frequency. The position on the floater for which the maximum stresses occur is not given.

6.2.1 Convergence of Transfer Function for Bending Stress

The undamped transfer functions for maximum bending stress is plotted in Figure 6.4. The results for both 1 torus and 2 tori are plotted. Figure 6.4 shows a comparison between the results when the first 10, 15, 20 and 25 modes are included in the analysis. For both 1 torus and 2 tori there are no visible change in the results when more than 25 modes are included. Additional modes do not give increased accuracy. It is also seen that 10 and 15 modes deviate from the results for 25 modes. For both 1 torus and 2 tori 10 modes give a good approximation up to $\omega \approx 1.5 rad/s$. For larger frequencies more modes are needed in order to get convergence. The result for 20 modes, for both cases, is seen to have good correspondence with the result for 25 modes in the frequency range in Figure 6.4. A small deviation is seen right before and after the first natural frequency. The deviation is larger for 1 torus than for 2 tori. When investigating the first resonance frequency in Figure 6.4(a) and 6.4(b) it is seen that these frequencies correspond to the resonance frequency of the pitch mode in the linear transfer functions for the displacements. That is when $n = 1$ in the equations of motion. This is as expected, since the heave mode, which is a rigid body mode and does not induce a moment in the floater, not will give contributions to the bending stresses. The pitch mode, which is a rigid body mode, will induce moments in the floater due to rotation. Using the 20 first modes would be sufficient in order to correctly represent the bending stresses for both 1 torus and 2 tori, since there only is a small difference between the results for 20 and 25 modes. After the first two resonance frequencies in Figure 6.4, the response is chaotic. Therefore, the matter of convergence of the results are accessed before the second natural frequency for bending stresses for both 1 torus and 2 tori. The second resonance frequency for bending stresses correspond to the resonance frequency for the first flexible mode for the displacements. A thorough investigation showed that a minimum of 22 modes and 23 modes were needed, for 1 torus and 2 tori respectively, in order to get convergence for the bending stresses in the frequency range up to the natural frequency for the first elastic mode for the displacements. If it is necessary to reduce computer calculation time, 20 modes will give good results for the bending stresses.

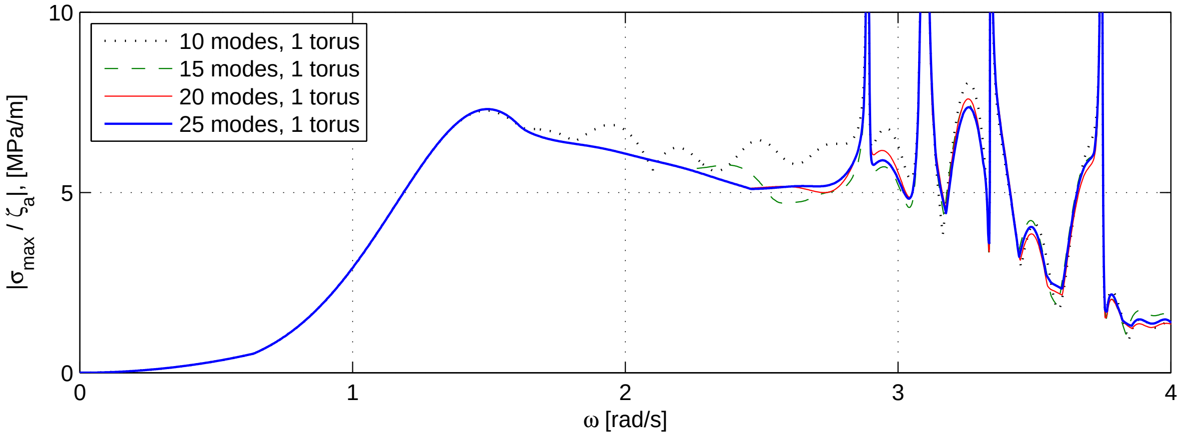

(a) Maximum bending stress 1 torus.

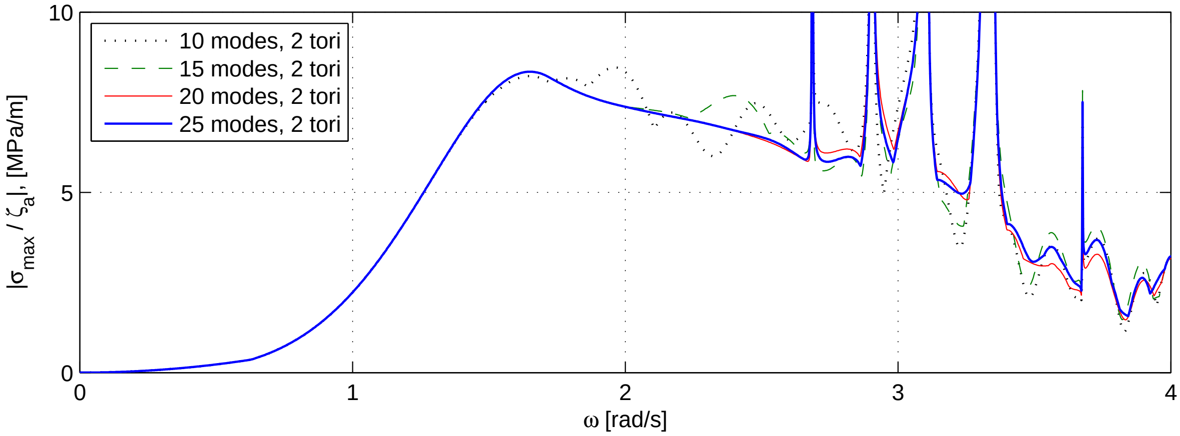

(b) Maximum bending stress 2 tori.

Figure 6.4: Undamped transfer function for maximum bending stress with respect to wave circular frequency ω for 1 torus and 2 tori. σ_{max} is the maximum bending stress in the floater with respect to ω. ζ_a is the wave amplitude. The results for a total of 10, 15, 20 and 25 modes are compared.

6.2.2 Effect of Damping on The Bending Stresses

The transfer functions for bending stresses for 2 tori for undamped motion, and a damping level of 1 percent and 3 percent of the critical modal damping are shown in Figure 6.5. In the figure it is seen that damping only give significant contribution at the resonance frequencies. Small differences between the cases are seen for frequencies between the two first natural frequencies, and before the first natural frequency. As expected, the lowest damping level gives the smallest change in response compared with the undamped case. Investigation on the effect of damping for 1 torus yields the same results as for 2 tori. A low damping level of up to 3 percent of critical damping will only effect the response at the resonance frequencies for the linear equations of motion. A damping level of 1 percent of critical damping will be applied when investigating the statistical properties of the bending stresses.

6.2.3 Comparison Between Bending Stress for 1 Torus and 2 Tori

The transfer functions for maximum bending stresses for 1 torus and 2 tori are plotted in Figure 6.6. The 25 first modes, and a damping level of 1 percent of critical damping for each modes is applied. For wave frequencies lower than approximately $1.5 rad/s$ the maximum bending stress is larger for 1 torus than for 2 tori. For frequencies higher than $1.5 rad/s$ 2 tori has in general the largest bending stresses. After

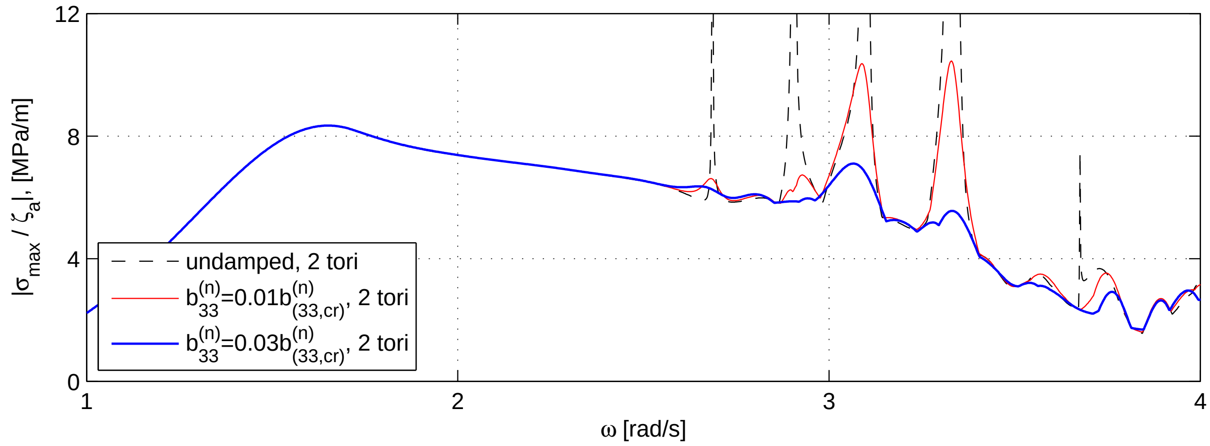

Figure 6.5: Transfer function for maximum bending stress in the floater for 2 tori. The undamped response and the response for a damping level of 1 percent and 3 percent of critical damping for each mode are compared. σ_{max} is the maximum bending stress as a function of the circular wave frequency ω. ζ_a is the wave amplitude.

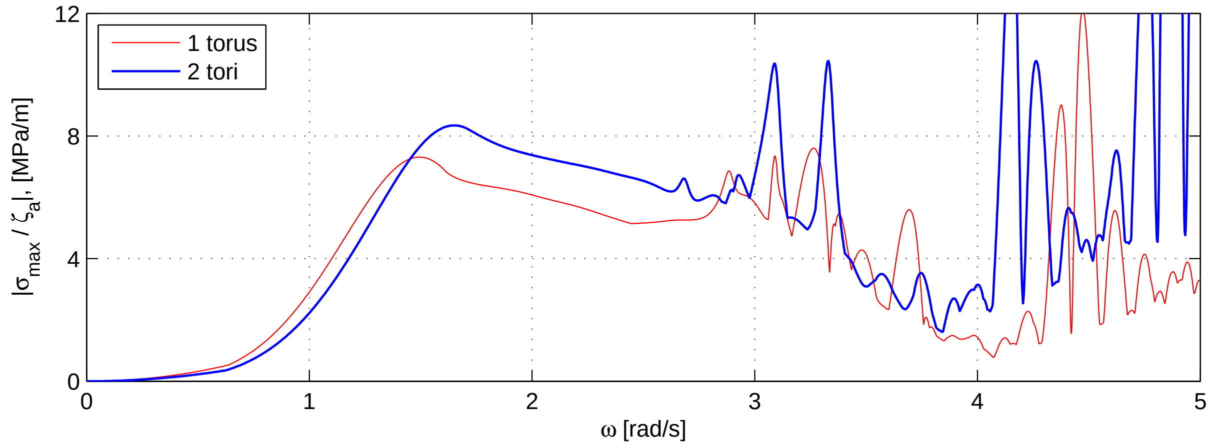

Figure 6.6: Transfer function for the maximum bending stress in the floater for 1 torus and 2 tori. σ_{max} and ω are the maximum bending stress and circular wave frequency, respectively. The 25 first modes are used, and a damping level of 1 percent of critical damping for each mode is applied.

the first resonance frequency for the bending stress, which corresponds to the resonance frequency of the pitch mode, the response is effected by resonant responses of the elastic modes. Due to the low damping level, and the fact that the real damping level is unknown, the quality of results for frequencies higher than approximately $4rad/s$ is uncertain. Another aspect, as discussed for the relative motion, is the fact that the rigid free surface condition not is satisfied for large frequencies. This is an error source for high frequencies, and the uncertainty is presumably increasing when the wave frequency is increased. After $\omega = 5rad/s$, the normalized stresses for both 1 torus and 2 tori are increasing slowly. No convergence of the results are observed.

6.3 Maximum Bending Stress in a Sea State

The transfer functions for maximum bending stress give a good picture of the magnitude of the stresses for different wave lengths and wave amplitudes. But it does not give information about the expected loads and at which position on the floater they appear in irregular sea. The most probable maximum bending stresses in the floater for different sea states will be investigated in this section. The most probable maximum bending stresses in the floater are calculated from the standard deviations of the bending stresses given in Section 5.3. The most probable maximum bending stress in a sea state is approximated as $\chi_\sigma = 4\sigma$, where σ is the standard deviation of the bending stress. The formula for the standard deviation is based on the linear transfer functions for the displacements in Section 4.5. The standard deviations are calculated for each position β on the floater from $\beta = 0$ to $\beta = \pi$. The floater motion is symmetric around the x-axis.

6.3.1 Effect of Damping on The Maximum Bending Stress in a Sea State

Before the standard deviations of the bending stresses in different sea states can be treated, the effects of damping in the linear equations of motion must be investigated. Figure 6.7 shows a comparison between the standard deviations for undamped motion and motion with a damping level set to 1 percent of the critical damping for each mode. The spectral peak period is $T_p = 8s$. The ISSC wave spectrum is used. The standard deviations are multiplied with 4 in order to get the most probable maximum bending stresses χ_σ. The stresses for the undamped case are much higher than the stresses for the damped case. Also, variation of the maximum stress with respect to β are larger for the undamped case than for the damped case. Two additional damping levels for each mode, set to 3 percent and 7 percent of the critical damping, where investigated. The response for these cases, with respect to the standard deviation, were almost identical to the response for a damping level of 1 percent. This indicates that it is important to include damping in order to get reliable results. The explanation for why damping is needed can be that the undamped transfer functions give responses going to infinity for the resonance frequencies. When the response spectrum for the stresses, equation (5.22), is integrated over all frequencies ω in order to get the standard deviations, the infinite responses for the resonance frequencies might give a contribution. The energy in the response spectrum is to high due to the infinite responses. Damping will remove energy caused by infinite response. A low damping level is set since the real damping in the system is unknown. The discussion above suggests that a higher damping level than 1 percent could be used without effecting the results for a peak period of $8s$. In Section 6.3.2 it is shown that there will be a difference in the response for low peak periods if the damping is increased.

In order to account for all frequencies in the wave spectrum, the frequency range goes from $\omega = 0 rad/s$ to $\omega = 10 rad/s$. The interval $d\omega$ in the discrete integral were set sufficiently low in order to account for the variation of the response spectrum with respect to ω. The interval were set to $0.002 rad/s$. This frequency range and frequency interval have been used in all calculations concerning irregular waves. When the upper limit of the frequency range were reduced to $5 rad/s$, for the damped case, the standard deviations were changed compared with the case where the response spectrum were integrated from $\omega = 0 rad/s$ to $\omega = 10 rad/s$. The form of the graphs were similar. The position β where the minimum standard deviations occurred were slightly changed. In general the standard deviations were reduced, but at some positions they were increased. The explanation could be that when the response spectrum is integrated over a larger frequency interval, more energy will be accounted for. Although it was a difference, this difference was small. In order to ensure graphs giving a correct picture with respect to the established mathematical formulas, the range going from $\omega = 0 rad/s$ to $\omega = 10 rad/s$ were chosen. This will ensure that all energy in the wave spectrum, with respect to the mathematical expression for the spectrum, is accounted for. Larger frequency intervals gave no change in the standard deviations. Another question is whether the mathematical expression for the wave spectrum give a correct representation of the energy for high frequencies. Over a certain frequency there might not in practice be any energy, or waves. The response from the damped transfer functions for high frequencies are small, and the energy given by the formulation of the wave spectrum are close to zero for high frequencies. The result is that the difference between the two frequency ranges above are small if damping is included in the equations of motion.

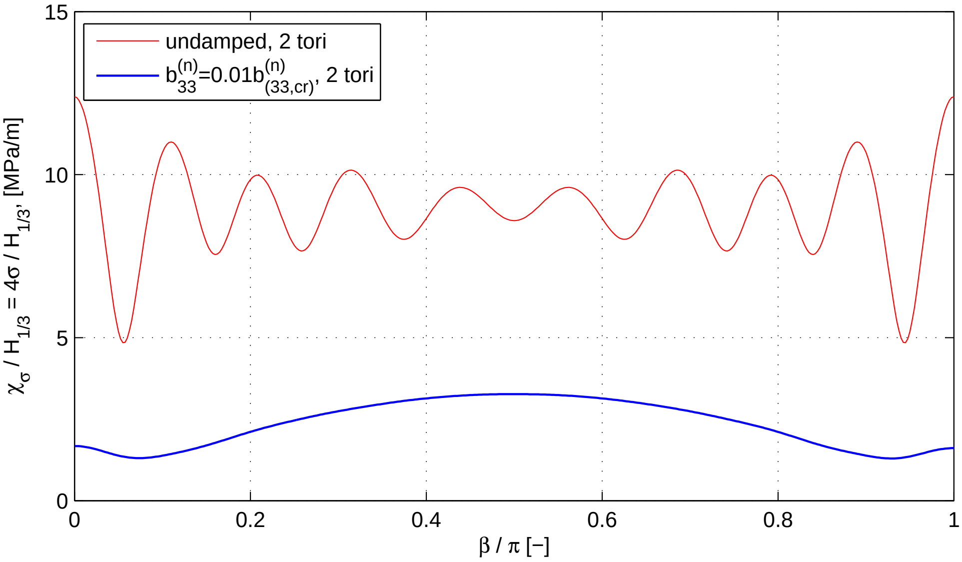

Figure 6.7: Most probable maximum bending stresses around the floater in a sea state. $\chi_\sigma/H_{1/3}$ is the normalized most probable maximum bending stress as a function of the position β on the floater. σ is the standard deviation of the bending stress. $H_{1/3}$ is the significant wave height. $\beta/\pi = 0$ and $\beta/\pi = 1$ are the trailing and leading point on the floater with respect to the wave propagation direction. The waves are propagating in positive x-direction. The ISSC wave spectrum with a peak period $T_p = 8s$ is used.

6.3.2 Maximum Bending Stress as a Function of Position

Figure 6.8 shows the most probable values for the normalized maximum bending stresses in a sea state as a function of the position β on the floater. The maximum values are calculated from the standard deviations. Figure 6.8 shows the maximum stresses for 1 torus and 2 tori for peak periods T_p being $3s$, $4s$, $5s$, $6s$ and $8s$. The ISSC wave spectrum is used. A modal damping level of 1 percent of the critical damping for each mode is applied. The floater motion is symmetric around the x-axis, and the range for β/π is therefore going from 0 to 1. However, the stresses are not symmetric around the y-axis. That is around the axis defined by $\beta = \pi/2$. The stresses are slightly larger for positive x-values compared with negative x-values. The x-coordinate is given by $x = R\cos\beta$, where R is the radius of the floater from the origin to the center line of 1 torus, or the midpoint between the center lines of the pipes for 2 tori. The difference in magnitude of the response between the positive and negative x-axis are small for high peak periods and low damping. The difference increase for low peak periods and increased damping.

In Figure 6.8, for $T_p = 6s$ and $T_p = 8s$ both 1 torus and 2 tori have maximum bending stress at $\beta = \pi/2$. This is on the position on the floater where the pipe axis is parallel to the wave propagation direction. For shorter waves, $T_p = 3s$ and $T_p = 4s$, for 2 tori and 1 torus respectively, this is not the case. The larger the peak period of the wave spectrum is, the longer are the waves with the most energy. For peak periods larger than $8s$ the point at which the maximum stresses occur is $\beta = \pi/2$ for both 1 torus and 2 tori. Figure 6.10 shows the normalized most probable maximum bending stresses for sea states with peak periods of $10s$, $12s$ and $14s$. The modal damping level is 1 percent of critical damping. For shorter peak periods than $4s$ the position for the maximum stresses move gradually to the left and right of $\beta = \pi/2$ as the peak period is reduced. There now exist two points with maximum tension on the floater. One explanation for this can be that for long waves the lower modes, heave, pitch and the first elastic modes, have the largest excitation. The first modes combined give larger curvature at the middle of the floater than at the front and back. It must be kept in mind that the heave mode does not give a contribution to the stresses. For shorter peak periods the excitation of higher modes will be higher than for long periods, and this might give larger curvature towards the front and the back of the floater with respect to the wave propagation direction. In figure 6.9 the most probable maximum bending stresses as a function of β for 2

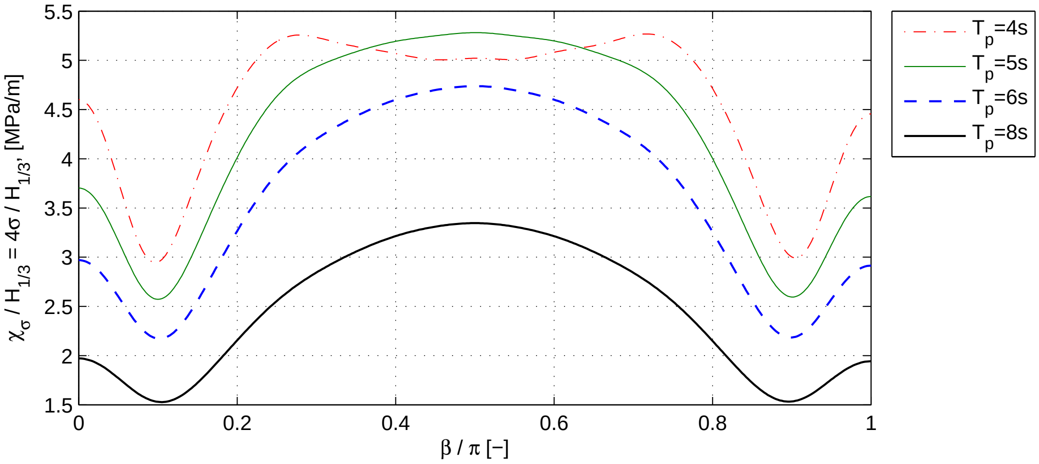

(a) Most probable maximum bending stress for 1 torus.

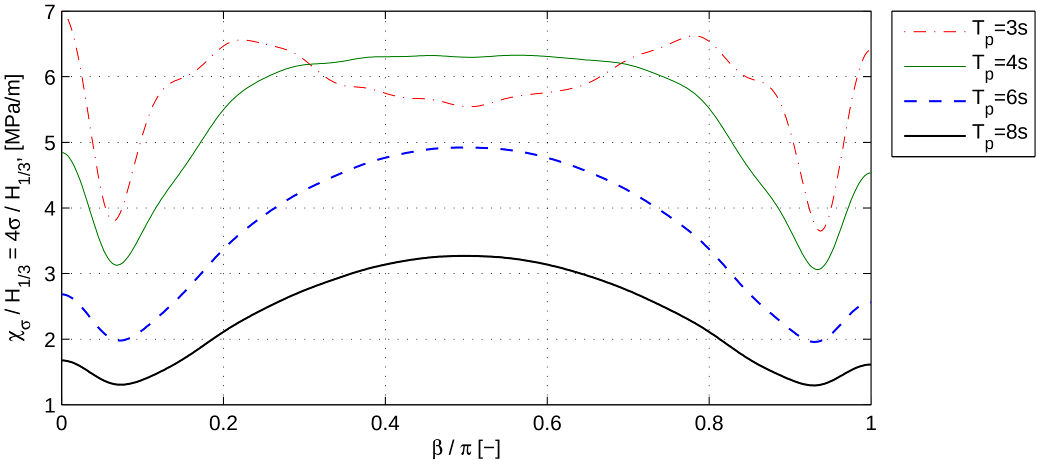

(b) Most probable maximum bending stress for 2 tori

Figure 6.8: Normalized most probable maximum bending stress for 1 torus and 2 tori plotted as a function of the position β on the floater in different sea states given by the peak period T_p. $\beta/\pi = 0$ and $\beta/\pi = 1$ are the back and front of the floater with respect to the wave propagation direction. χ_σ is the most probable maximum bending stress calculated from the standard deviation of the bending stress. $H_{1/3}$ is the significant wave height. The modal damping level is 1 percent of critical damping for each mode. The ISSC wave spectrum is used.

tori are plotted for a peak period of $3.5s$ and three different damping levels. The damping levels are 1, 3 and 5 percent of critical damping. When the damping is increased, the stresses are reduced, and the point at which the minimum stresses occur move away from the front and back end of the floater given by $\beta = \pi$ and $\beta = 0$ respectively. The reduction in stresses from a damping level of 3 percent to a damping level of 5 percent is less than the reduction in stresses between a damping level of 1 and 3 percent. The graph for a damping level of 1 percent shows resemblance with the undamped case in Figure 6.7. This indicates that for low peak periods, the set damping level will effect the response. The effect of damping for low peak periods may be due to the fact that resonant excitation of higher modes will be reduced when damping increase. In Section 6.3.3, the maximum standard deviations, represented by the the most probable maximum stresses, for different peak periods and damping levels will be compared.

The minimum bending stresses are situated towards the front and back end of the floater, for both 1 torus and 2 tori. As the peak period increase, up to $8s$, the points of minimal stress move towards the middle of the floater given by $\beta = \pi/2$. The variation of the position of the minimum stresses with respect to the variation of peak periods are small. For peak periods in the range from $10s$ to $14s$, the

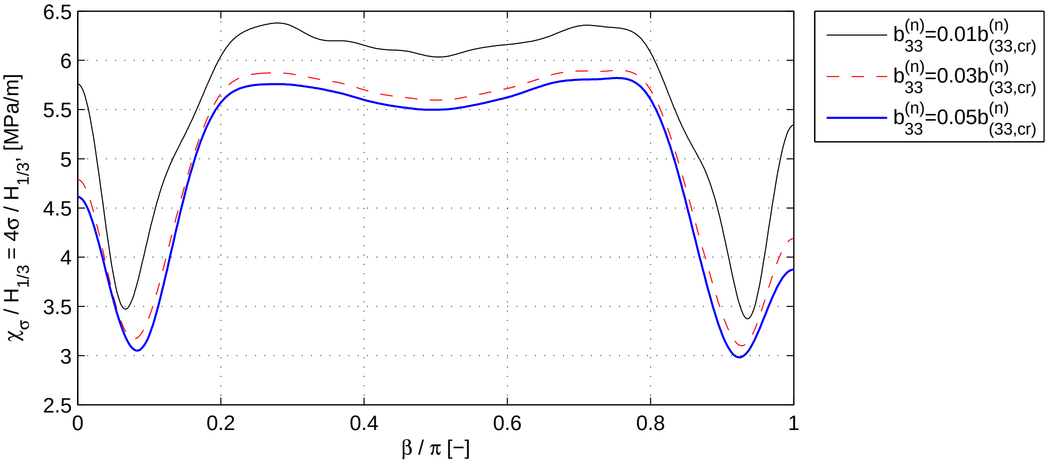

Figure 6.9: Most probable maximum bending stresses χ_σ as a function of position β on the floater for 2 tori. The stresses are normalized with the significant wave height $H_{1/3}$. Damping levels of 1, 3 and 5 percent of critical damping for each mode have been tested. The spectral peak period T_p is $3.5s$. The ISSC wave spectrum is used.

position of minimum stress is unchanged. The magnitude of the normalized stresses over the floater decrease with increasing peak period T_p. From a scatter diagram, for instance representative values for T_p and significant wave height $H_{1/3}$ for the North Sea given in [Faltinsen (1990)], it is seen that the value for the most probable significant wave height increase for increasing peak periods up to a certain value for the peak period. For higher peak periods the value for the most probable significant wave height will decrease. The results for the normalized most probable maximum stresses must therefore be used together with representative significant wave heights and peak periods for a actual location in order to get an indication of the stresses in the floater. The results for the maximum stresses are based on linear theory. For sea states with high and steep waves, nonlinear effects might have effects on the responses compared with linear theory, and thus give different results for the standard deviations. Results for nonlinear effects in irregular sea are not obtained in this thesis. However, effects on the stresses for nonlinear hydrostatic and nonlinear Froude-Kriloff forces in regular waves are investigated in Chapter 7.

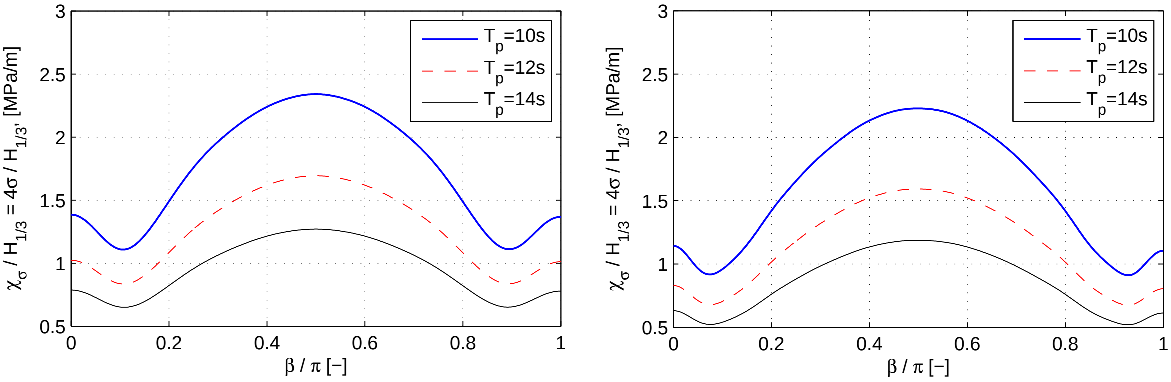

(a) Most probable maximum bending stress for 1 torus.

(b) Most probable maximum bending stress for 2 tori

Figure 6.10: Normalized most probable maximum bending stress for 1 torus and 2 tori plotted as a function of the position β on the floater in different sea states given by the peak period T_p. $\beta/\pi = 0$ and $\beta/\pi = 1$ are the back and front of the floater with respect to the wave propagation direction. χ_σ is the most probable maximum bending stress calculated from the standard deviation σ of the bending stress. $H_{1/3}$ is the significant wave height. The modal damping level is 1 percent of critical damping for each mode. The ISSC wave spectrum is used.

Sea states with two peaks in the spectral density function can also occur. These spectra have two peak periods. After a storm which induce large waves, swells might occur. These swells will travel with large velocities and might occur long distances from which they were created. Swells on a cite mixed with wind induced waves, can create a sea state which can be described by a spectrum with two peaks. The distribution of stresses around the floater for these kind of conditions might be very different from the variation given in Figure 6.8. This aspect will not be discussed further.

6.3.3 Maximum Bending Stress as a Function of Spectral Peak Period

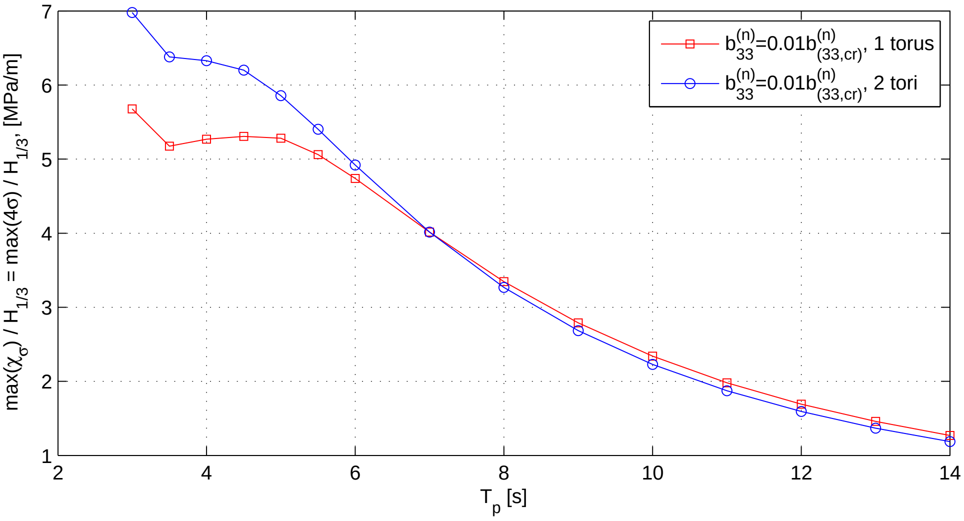

Figure 6.11: Most probable normalized maximum bending stress $max(\chi_\sigma)/H_{1/3}$ as a function of spectral peak period T_p. $max(\chi_\sigma)$ is the maximum bending stress on the floater for each peak period. $H_{1/3}$ is the significant wave height. The ISSC wave spectrum is used. The results for 1 torus and 2 tori are compared. The modal damping level is 1 percent of critical damping for each mode.

In Figure 6.11, the maximum values of the normalized most probable maximum bending stresses for peak periods from $T_p = 3s$ to $T_p = 14s$ are plotted. The results for 1 torus and 2 tori are compared. The modal damping level is 1 percent of critical damping for each mode. The figure shows that up to a peak period of $7s$, 2 tori has larger maximum stresses than 1 torus. For peak periods larger than $7s$, 1 torus has the largest maximum stresses, although the difference between 1 torus and 2 tori in this range is small. For peak periods smaller than $T_p \approx 3.5$ there is a sudden increase in the maximum stresses for both 1 torus and 2 tori. Figure 6.12 compares the maximum stresses with respect to T_p for three different damping levels. Results for 2 tori are shown. The maximum stresses are reduced with increased damping. For a damping level of 3 percent of critical damping the maximum stresses as a function of T_p are almost constant between $T_p = 3s$ and $T_p = 4s$. By increasing the damping level from 3 to 5 percent the change in response is small. For peak periods larger than approximately $6s$, the effect of increasing the damping level is small. The difference in stresses between a damping level of 1 and 3 percent for $T_p = 6s$ is approximately 1.6 percent. The dependency on damping level indicates that the maximum stresses are sensitive to the set damping level for small values of T_p. Since the real damping level in the system is unknown, the results for the lowest damping level must be considered.

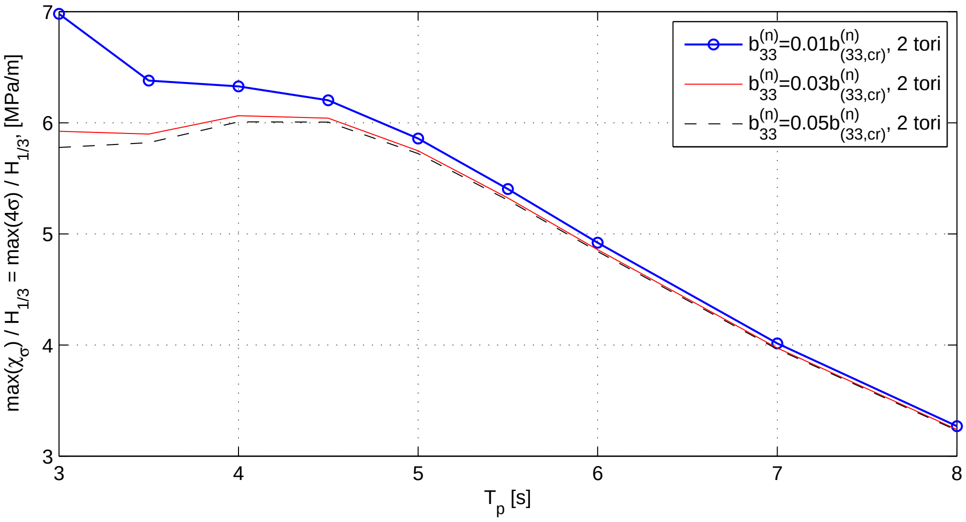

Figure 6.12: Most probable normalized maximum bending stress $max(\chi_\sigma)/H_{1/3}$ as a function of spectral peak period T_p. $max(\chi_\sigma)$ is the maximum bending stress on the floater for each peak period. $H_{1/3}$ is the significant wave height. The ISSC wave spectrum is used. The results for 2 tori with a modal damping level of 1 percent, 3 percent and 5 percent of critical damping, respectively, are compared.

Effect of Varying the Cross Section Dimension

Two different configurations of the floating collar have been investigated in this thesis. The first consisting of one ring, the second of two concentric rings. The dimension of the floater with two rings are possible dimensions of floaters existing today. The floater with one ring has been given dimensions in order to give the same submerged mass as the two ring configuration. The ratio between outer diameter and the wall thickness of the pipes has been kept similar for the 1 torus and 2 tori case. For a radius $R = 25.5m$ of the floater, the most common configuration is two rings. This gives higher torsional rigidity of the floater, partly due to the brackets used to connect the two pipes. This aspect has not been treated in this thesis.

Changing the ratio between the outer diameter and the wall thickness of the pipes will presumably have an effect on the response and thus the stresses in the floater. Since two rings are most common this has been investigated for 2 tori. Figure 6.13 shows the most probable maximum bending stresses calculated from the standard deviation as a function of the spectral peak period in a sea state. Three values of the ratio between outer diameter and wall thickness are shown. The values are 15, 17.6 and 20, where 17.6 is the value investigated in the rest of the thesis. In Figure 6.13(a) the pipe radius $c = 225mm$, while the wall thickness t_w has been changed. In Figure 6.13(b) the pipe radius has been increased to $c = 250mm$ and the wall thickness has been varied. The modal damping level is 1 percent of critical damping for each mode. The ISSC wave spectrum has been used.

From Figure 6.13 it can be seen that increased wall thickness, that is decreasing the ration between the outer diameter and the wall thickness, gives lower maximum stresses in the floater. Increasing the ratio, that is reducing the wall thickness when the pipe radius not is changed gives higher bending stresses in the floater. The effect of altering the dimensions is larger for small peak periods T_p than for large peak periods. For $T_p > 10s$ the effect of changing the ration between diameter and wall thickness is small. When comparing Figure 6.13(a) and 6.13(b) it is observed that when the submerged mass is increased, when c is increased from $225mm$ to $250mm$, and the ratio between diameter and wall thickness is unchanged and set to 17.6, the maximum stresses are reduced for $T_p < 6s$. For $T_p > 6s$ the stresses are almost similar. Note that the radius $R = 25.5m$ are kept constant in Figure 6.13.

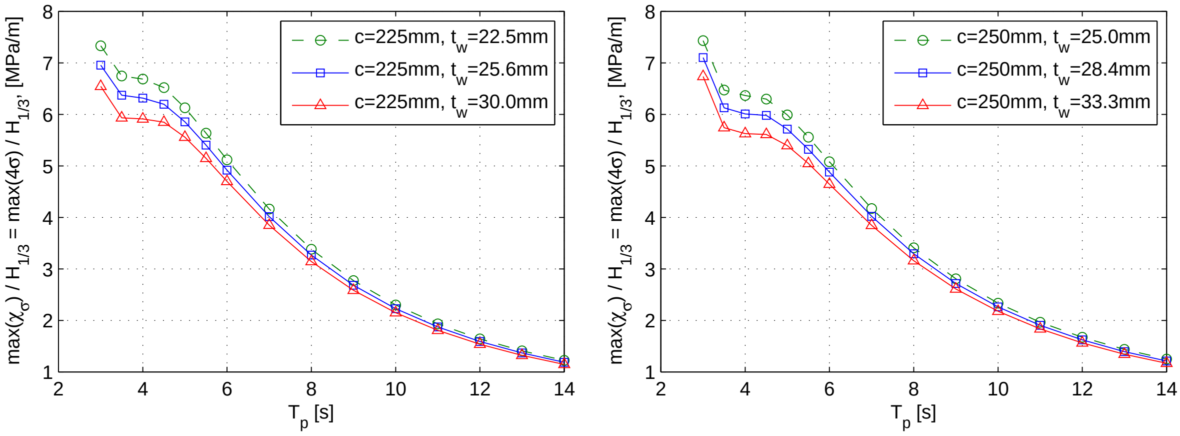

(a) Most probable normalized maximum bending stress. (b) Most probable normalized maximum bending stress.

Figure 6.13: Most probable normalized maximum bending stress $max(\chi_\sigma)/H_{1/3}$ for 2 tori as a function of spectral peak period T_p. $max(\chi_\sigma)$ is the maximum bending stress on the floater. $H_{1/3}$ is the significant wave height. The ISSC wave spectrum is used. The modal damping level is 1 percent of critical damping. Different cross section dimensions are compared. c is the pipe radius. t_w is the wall thickness.

Comparison of Response Between ISSC and JONSWAP Wave Spectrum

According to [Norwegian Standard. NS 9415.E:2009] the JONSWAP (Joint North Sea Wave Project) wave spectrum can be used for irregular sea. Guidelines for parameters in the spectrum regarding whether the waves are wind generated or consists of swells are given. Alternatively, in fjords or other partly sheltered areas, a two parameter PM (Pierson Moskowitz) type spectrum can be used. The differences in the standard deviation of the stresses calculated from the ISSC and JONSWAP spectrum will now be shown. A JONSWAP spectrum recommended by the 17th ITTC for limited fetch, [Faltinsen (2005)], is

$$\frac{S(\omega)}{H_{1/3}^2} = \frac{155}{T_1^4\omega^5} exp\left(\frac{-944}{T_1^4\omega^4}\right) 3.3^\gamma$$

where

$$\gamma = exp\left(-\left(\frac{0.191\omega T_1 - 1^2}{\sqrt{2}\sigma}\right)\right) \tag{6.1}$$

and

$$\begin{aligned} \sigma &= 0.07 \text{ for } \omega \leq 5.24/T_1 \\ &= 0.09 \text{ for } \omega > 5.24/T_1 \end{aligned}$$

T_1 is the mean period of the spectrum. The relationship between the peak period T_p and mean up-crossing period T_2 is $T_1 = 0.834T_p = 1.073T_2$, [Faltinsen (2005)]. This gives a different peak period T_p for the JONSWAP spectrum than for the ISSC spectrum for the same period T_2. The peak period T_p is often denoted T_0 in literature.

In Figure 6.14(a) and 6.14(b) the approximation for the most probable maximum stresses calculated from the standard deviation and the dimensionless ISSC and JONSWAP spectrum are plotted as a function of T_2 and the dimensionless frequency $\omega T_2/(2\pi)$. From Figure 6.14(b) it is seen that the JONSWAP spectrum has a higher and narrower peak than the ISSC spectrum. The peak period for the JONSWAP spectrum is lower than the peak period for the ISSC spectrum for the same values for T_2. Figure 6.14(a) shows the normalized most probable bending stresses in a sea state for 2 tori calculated for the ISSC and JONSWAP spectrum. For $T_2 < 4.5s$ the maximum stresses is higher for the JONSWAP spectrum than for the ISSC spectrum. For $T_2 > 4.5s$ the stresses are slightly higher for the ISSC spectrum. An explanation can be that the energy in the JONSWAP spectrum is more concentrated around the peak frequency in the spectrum, thus giving more energy for wave periods slightly lower than the peak period in the ISSC spectrum. For high frequencies, or low periods the ISSC spectrum contains more energy than the JONSWAP spectrum. For lower frequencies, or higher periods than the peak period in the ISSC spectrum, the ISSC spectrum have more energy, thus higher waves, than the JONSWAP spectrum. These observations in combination with the transfer function for the stresses, can explain the results in Figure 6.14(a). For the lowest period tested, $T_2 = 2.13s$, the stresses calculated from both spectra are similar.

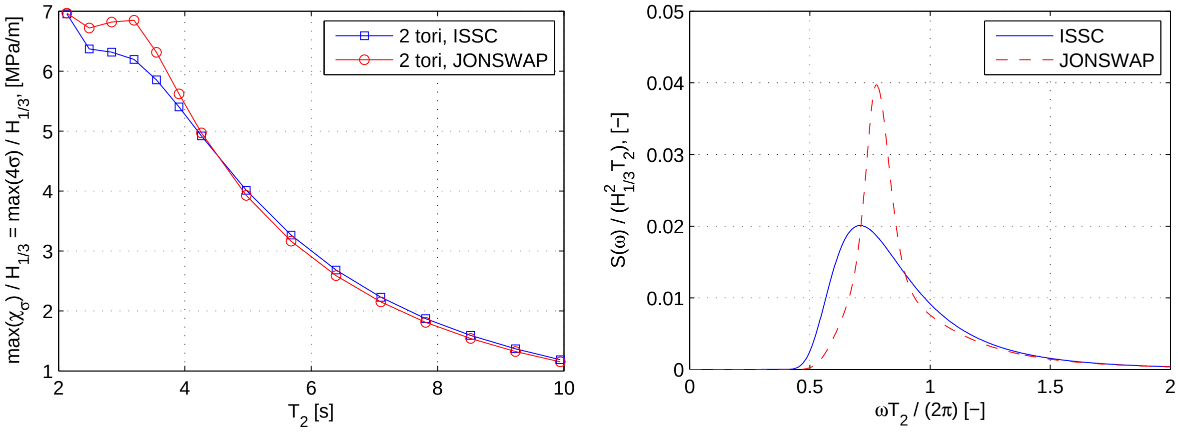

(a) Most probable normalized maximum bending stress.

(b) Dimensionless wave spectra.

Figure 6.14: Left: Comparison of response for the ISSC and JONSWAP spectra. Damping is set to 1 percent of critical damping. The dimensions from Chapter 2 are used. Right: Dimensionless wave spectra. T_2 is the mean zero up-crossing period. $H_{1/3}$ is the significant wave height.

Maximum Bending Stresses at a Location

Possible values for significant wave heights and mean periods T_2 are obtained by using the scatter digram from [DNV Report No. 97-0152] for service restriction **R3** Coastal, given in Table B.2. The scatter digram is calculated from theoretic parameters and gives service restrictions for high-speed and light crafts in coastal areas. This scatter diagram is used since it can provide data for possible weather conditions on possible locations for fish farms. $H_{1/3} = 2.5m$, corresponding to 10 percent probability of exceedence, gives $T_2 = 5s$ for the entry with the lowest period. The most probable maximum stresses $max(\chi_\sigma)$ is approximately 10 MPa for 2 tori for both the ISSC and JONSWAP spectrum. For $H_{1/3} = 2.0m$, giving a probability of exceedence of 19 percent, the entry with the lowest period has $T_2 = 4s$. This corresponds to a maximum $H_{1/3} = 2.25m$ and a minimum $T_2 = 3.5s$, giving $max(\chi_\sigma) = 14.4$ MPa and $max(\chi_\sigma) = 13.3$ MPa for JONSWAP and ISSC realization of the waves, respectively. For $H_{1/3} = 4.5$ and $T_2 = 7s$, corresponding to the a maximum significant wave height $H_{1/3} = 4.75$ and minimum period $T_2 = 6.5s$ gives $max(\chi_\sigma) \approx 11.9$ MPa for both the JONSWAP and ISSC realization. The stress calculated from the JONSWAP spectrum is slightly less than the stress calculated with the ISSC spectrum for $T_2 = 6.5s$. The probability of exceedence for this significant wave height is 0.4 percent. The yield stress for a typical HDPE type plastic used in the floating collar is $\sigma_y = 25$ MPa.

Chapter 7

Results - Comparison Between Linear and Nonlinear Response

Response for linear and nonlinear excitation forces will be compared in this chapter. Time series of Fourier coefficients of the displacements and modal excitation forces for different wave frequencies and wave steepnesses will be shown. Comparison of transfer functions for displacements, forces and maximum bending stresses in the floater for linear forces and nonlinear forces will be compared.

The Fourier coefficients can be used to find the total response on the floater at each position β and time t by using equation (4.12) in Chapter 4. In Chapter 4, the linear excitation forces are the diffraction force and the Froude-Kriloff pressure force. The linear hydrostatic restoring force is not a wave excitation force, since it is only dependent on the vertical displacement and water plane area. In this chapter, when comparing the linear and nonlinear forces, the hydrostatic restoring force will be interpreted as a wave excitation force in order to compare the linear and nonlinear modal forces and the corresponding responses. The nonlinear hydrostatic pressure force are dependent on both the vertical displacement and the instantaneous wave elevation. The hydrostatic force is thus dependent on the wave elevation, and can be interpreted as an excitation force.

The linear excitation force, including the hydrostatic restoring force, is

$$f_{3,0}^{exc} = \left[-\rho g b_w a_{0,a} + \left(\rho g b_w - \omega^2 a_{33}^{(0)}\right) \zeta_a J_0(kR) i\right] e^{-i\omega t} \tag{7.1}$$

$$f_{3,n}^{exc} = \left[-\rho g b_w a_{n,a} + \left(\rho g b_w - \omega^2 a_{33}^{(n)}\right) 2\zeta_a J_n(kR) i^{n+1}\right] e^{-i\omega t} \tag{7.2}$$

$f_{3,0}^{exc}$ and $f_{3,n}^{exc}$ are the vertical modal excitation forces for heave and the n-th mode, respectively. $a_{0,a}$ and $a_{n,a}$ are the Fourier coefficients for heave and the n-th mode. $a_{33}^{(0)}$ and $a_{33}^{(n)}$ are the modal added mass for vertical motion for heave and mode number n. b_w is the breadth of the floater section. b_w equals $2c$ and $4c$ for 1 torus and 2 tori respectively. c is the pipe radius. The nonlinear excitation forces, including the hydrostatic pressure forces can be expressed as

$$f_{3,0}^{exc} = -mg - \omega^2 a_{33}^{(0)} \zeta_a J_0(kR) i e^{-i\omega t} + \frac{1}{2\pi R} f_{3,0}^{hyd} + \frac{1}{2\pi R} f_{3,0}^{dyn} \tag{7.3}$$

$$f_{3,n}^{exc} = -\omega^2 a_{33}^{(n)} 2\zeta_a J_n(kR) i^{n+1} e^{-i\omega t} + \frac{1}{\pi R} f_{3,n}^{hyd} + \frac{1}{\pi R} f_{3,n}^{dyn} \tag{7.4}$$

Equation (7.3) and (7.4) gives the nonlinear modal excitation forces for heave and mode number n. The weight of the floater per unit length, mg is subtracted from the heave equation. This is done in order to compare the linear and nonlinear modal forces for heave. The weight per unit length is not a part of the equation of motion for $n = 1, 2, 3...$ and is therefore not a part of the equation for the modal forces for mode n. $f_{3,0}^{hyd}$, $f_{3,n}^{hyd}$, $f_{3,0}^{dyn}$ and $f_{3,n}^{dyn}$ are the modal hydrostatic forces for heave and the n-th mode and the modal dynamic pressure forces for heave and the n-th mode ,from equation (4.33) and (4.34), respectively. As seen from equation (7.1) to (7.4), the diffraction forces are linear in all equations. It is only the effect of the nonlinear hydrostatic and Froude-Kriloff forces that are investigated.

7.1 Response at Low Frequencies

For low frequencies it is expected that the nonlinear forces and corresponding response will be similar to the linear forces and linear response of the floater. When $\omega \to 0$, the heave motion follows the wave elevation and the excitation of pitch and the elastic modes goes to zero. The relative motion between the waves is small, and the nonlinear forces will not deviate much from the linear forces. In Figure 7.1, the linear and nonlinear responses and modal excitation forces for 1 tori for $\omega = 0.8 rad/s$ are shown. Heave, pitch and the first elastic mode are plotted. For $\omega = 0.8 rad/s$ the values for the transfer function for heave, pitch and the first elastic mode are 0.43, 0.54 and 1.17, respectively. The criteria for $\omega \to 0$ are not satisfied. However, the nonlinear responses for the three first modes are similar to the linear responses. The nonlinear modal excitation forces for the two first modes have the same magnitude as the linear forces, but higher frequency components in the nonlinear forces are seen. The magnitude of these components are small and does not have a significant effect on the response. The nonlinear response for the two first modes can be approximated by a function proportional to $\cos \omega t$, where ω is the wave frequency. The nonlinear response are close to linear. It is seen that the nonlinear heave response not is oscillating around $z = 0$. The nonlinear response for the first elastic mode have a small contribution from a higher frequency than the wave excitation frequency. The frequency of this component corresponds to the higher frequency component in the excitation force for the first elastic mode. The mean value of the nonlinear force for $n = 2$ corresponds to the linear force. The magnitude of the high frequency component is of the same magnitude as the linear force. The frequency is four times the wave frequency. The high frequency force component are not exciting a large high frequency response for the third mode, although a small 4ω frequency component is seen. Damping and interaction between the excitation forces and responses for all modes can be the reason for why an increased nonlinear response compared with the linear response for the first elastic mode not is seen. Higher frequency components in the modal excitation forces may give significant contributions to the response for other wave frequencies.

In Figure 7.1, the response of the three first modes are plotted. For higher modes than the first elastic mode, given by $n = 2$, the modal responses and excitation forces are an order of magnitude smaller than the responses of the three first modes. The excitation forces and modal responses have significant higher frequency components for $n > 3$. The magnitudes of the responses of the higher modes are considerably lower than the response of the three first modes, and will not give a significant contribution to the total vertical response of the floater. This can also be seen from the linear transfer functions for the six first modes, Chapter 4 and Appendix B.2. For $\omega = 0.8$, the modal response for $n = 4$ and larger is small.

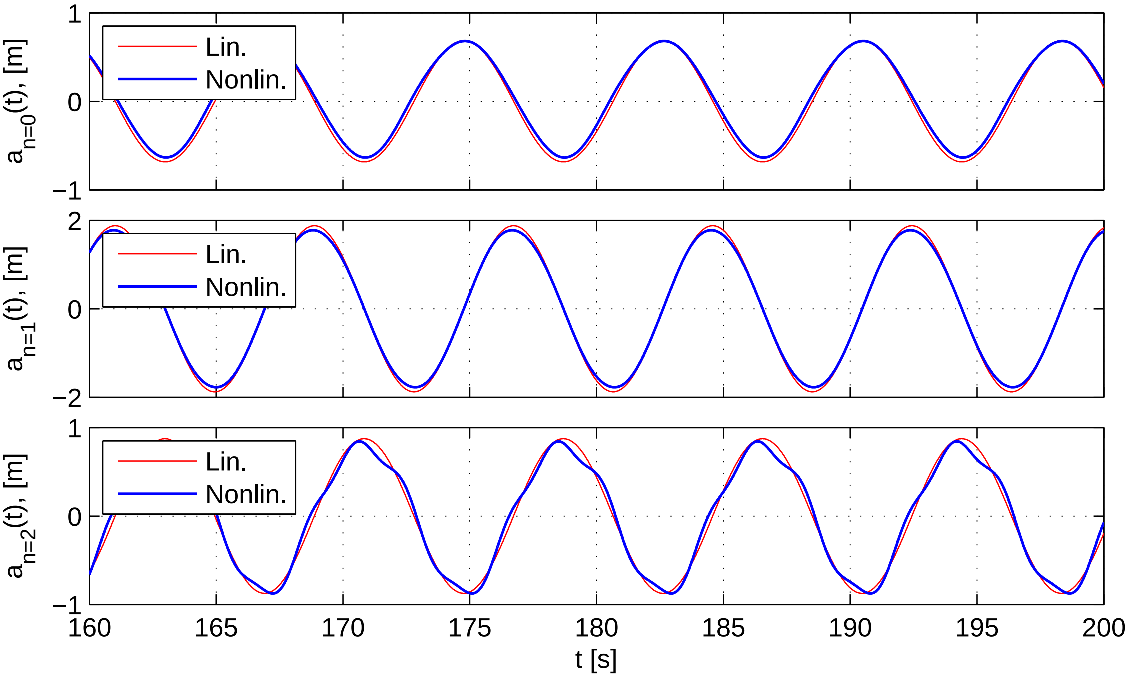

(a) Response of Fourier coefficient $a_n(t)$.

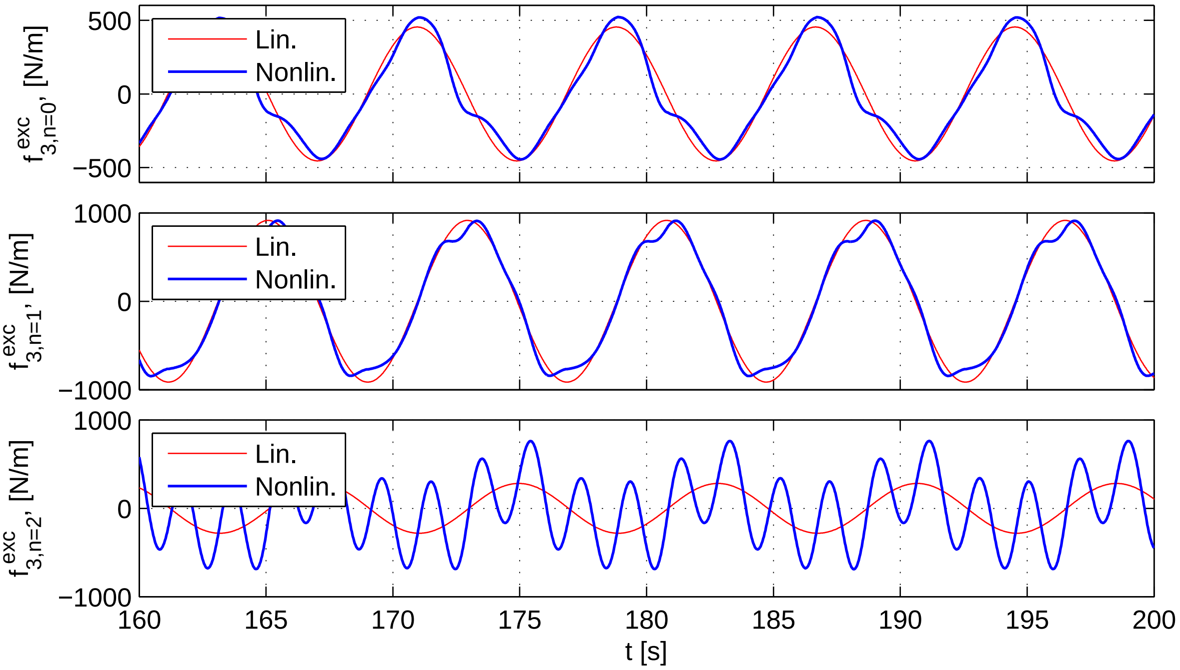

(b) Modal excitation force $f^{exc}_{3,n}(t)$.

Figure 7.1: Time series of modal displacement and excitation forces for the three first modes for 1 torus for $\omega = 0.8 rad/s$. Linear and nonlinear excitation forces are compared. $a_n(t)$ and $f^{exc}_{3,n}(t)$ are the n-th time dependent Fourier coefficient and the time dependent modal force for mode n, respectively. $f^{exc}_{3,n}(t)$ are given by equation (7.1) to (7.4). The wave steepness $H/\lambda = 1/30$, giving a wave amplitude $\zeta_a = 1.61$. H and λ are the wave height and wave length. A modal damping level of 1.5 percent of modal critical damping is used.

7.2 Response at Resonance

For the linear model, the response of a mode at resonance is significantly higher than the response of the other modes if a sufficiently small damping level is applied. In Chapter 6 it was shown for the linear model that a small damping level only will effect the response at resonance compared with undamped response. High damping will reduce the response at resonance in such a way that the resonance frequency for the mode not can be seen from the plot of the transfer function. The mathematical expression must be used. In Figure 7.2 and 7.3 linear and nonlinear response for 2 tori for heave and pitch mode resonance, respectively, are compared. The wave frequencies for heave and pitch resonance according to the linear model are $\omega = 2.25 rad/s$ and $\omega = 2.69 rad/s$. The vertical modal displacements and modal excitation forces for the four first modes are plotted. The modal damping level is set to 1.5 percent of critical damping, which for the linear model still will give a high response at resonance.

For heave resonance, Figure 7.2(a), the nonlinear heave response is significantly lower than the linear response. The magnitude is approximately 35 percent of the linear heave response, and a phase angle of approximately $\pi/2$ is seen between the two responses. The nonlinear and linear response for pitch and the first elastic mode at heave resonance are similar. The nonlinear responses are smaller than the linear responses, but the differences are small. A small shift in the phase angles are also seen. The difference between the nonlinear and linear response for the second elastic mode, $n = 3$, is larger than the difference between the nonlinear and linear responses for pitch and the first elastic mode, but the difference in magnitude is not as large as for heave. However, a large phase angle of approximately π is observed. The plot of the modal forces for heave resonance, Figure 7.2(b), explains the difference in response between the nonlinear and linear model. Similar differences in magnitudes and phase angles for the modal excitation forces as seen for the modal responses are seen. The modal heave force for the nonlinear model is significantly lower than the linear force for the heave mode. A contribution from a higher frequency component for the nonlinear excitation force for the second elastic mode is seen in Figure 7.2(b). This nonlinear effect in the modal force is giving a nonlinear effect for the corresponding modal response.

The modal response and modal excitation forces for the four first modes for pitch resonance, $\omega = 2.69 rad/s$, are plotted in Figure 7.3. As for heave resonance, the magnitude of the nonlinear response and nonlinear excitation force for the resonant mode are significantly lower than the linear response and linear force. A phase angle of approximately $\pi/2$ between the nonlinear and linear response and nonlinear and linear excitation force for pitch is also seen. The heave response and heave force are much smaller than the response and excitation force for pitch at $\omega = 2.69 rad/s$. From the linear transfer functions it can be seen that the response of a mode for a higher frequency than the resonance frequency for the mode will be small, thus explaining the low heave response for pitch resonance. For pitch resonance the nonlinear response and excitation forces for the second and third elastic mode, $n = 2$ and $n = 3$, are lower then the linear responses and excitation forces. The phase angles between the linear and nonlinear response are smaller than for pitch.

In figure 7.2 and 7.3 it is seen that the modal response and modal excitation force for the resonant mode are significantly reduced for the nonlinear model compared with the linear model. In the linear model, a wave frequency corresponding to the resonance frequency for a mode will give significant response for that mode. The magnitude of the excitation forces, calculated from linear theory, will not be effected by resonance compared with a non-resonance frequency. The linear excitation forces are dependent on the incident wave velocity potential, added mass, mean position and dimensions of the structure. The linear restoring coefficient will give large restoring forces due to large displacements at resonance. The damping is the only force that can reduce the response. If damping is low, as in this case, the response will be large. When calculating the nonlinear restoring and Froude-Kriloff forces, the hydrostatic and dynamic pressures are integrated over the exact wetted surface of the floater, thus taking the instantaneous position of each section and the instantaneous wave elevation on each section of the floater into account. When the response and relative motion of the floater with respect to the wave elevation is large the nonlinear forces will differ from the linear forces. From Figure 7.2 and 7.3 it seems that the modal force for the mode at resonance is significantly reduced when the displacement of the floater, wave elevation and exact wetted surface are accounted for. The effect of integrating the linear hydrostatic and dynamic pressures over the exact wetted surface seem to have a larger effect on the response and excitation forces at resonance than the set damping level.

The linear undamped resonance frequency of a mode is determined by the solution of $c_{33}^{(n)} + n^4 EI/R^4 - \omega^2(m + a_{33}^{(n)}) = 0$ with respect to ω. $a_{33}^{(n)}$ and $c_{33}^{(n)}$ are the modal added mass and modal hydrostatic restoring coefficients for mode n, respectively. In the nonlinear model the hydrostatic restoring force is not a function of a constant coefficient multiplied with the vertical modal displacement. The nonlinear restoring force is a function of total instantaneous displacement and instantaneous wave elevation. Thus, the restoring force is highly time dependent and nonlinear effects will occur. This may alter the resonance frequencies of the nonlinear model compared with the linear model. Also, the nonlinear restoring force will not always oscillate around zero, as the linear force. For 2 tori at $\omega = 2.69 rad/s$, $c_{33}^{(1)} \approx 9050 N/m^2$, $n^4 EI/R^4 \approx 191 N/m^2$ and $\omega^2(m + a_{33}^{(1)}) \approx 9081 N/m^2$ for pitch. This implies that the restoring coefficient has a vital contribution to the linear undamped resonance frequency. The nonlinear restoring force will differ from the linear restoring force for wave frequencies and wave amplitudes that give significant relative motion between the floater and the waves. The magnitude of the effect, or whether this has an effect on the resonance frequency at all is hard to determine, since the nonlinear restoring force is highly time dependent, and nonlinear due to the combined effect of total displacement and wave elevation around the floater. However, the difference in linear and nonlinear response is seen to be largest at resonance. This suggests that the reduction of hydrostatic and Froude-Kriloff forces combined at resonance in the nonlinear model is causing the significant reduction of the response.

In this section, the linear and nonlinear response for 2 tori for the two first resonance frequencies were investigated. Plots for the linear and nonlinear response for the two first linear resonance frequencies for 1 torus, $\omega = 2.49 rad/s$ and $\omega = 2.89 rad/s$, are shown in Appendix B.4. As for 2 tori, the nonlinear response at resonance is significantly reduced compared with the linear response due to reduction of the modal excitation forces when integrating the hydrostatic and dynamic pressure over the exact wetted surface.

Plots of the modal responses and modal excitation forces for 2 tori for the first eight modes for $\omega = 2.25 rad/s$ and $\omega = 2.69 rad/s$ is shown in Appendix B.4. For $\omega = 2.25 rad/s$ it is seen that the eight mode, $n = 7$, has a 2ω frequency component for the response and excitation force with a significant contribution to the total response. ω is the wave frequency. Modes being excited at higher frequencies than the incident wave frequency will be discussed in Section 7.3.

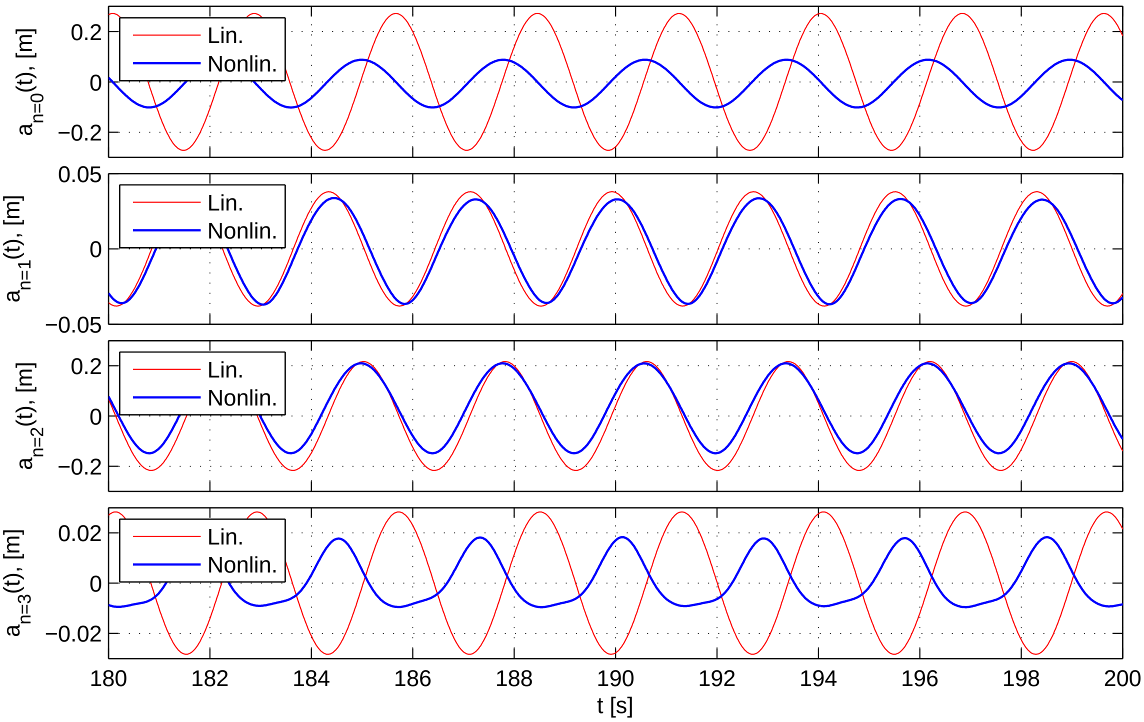

(a) Response of Fourier coefficient $a_n(t)$.

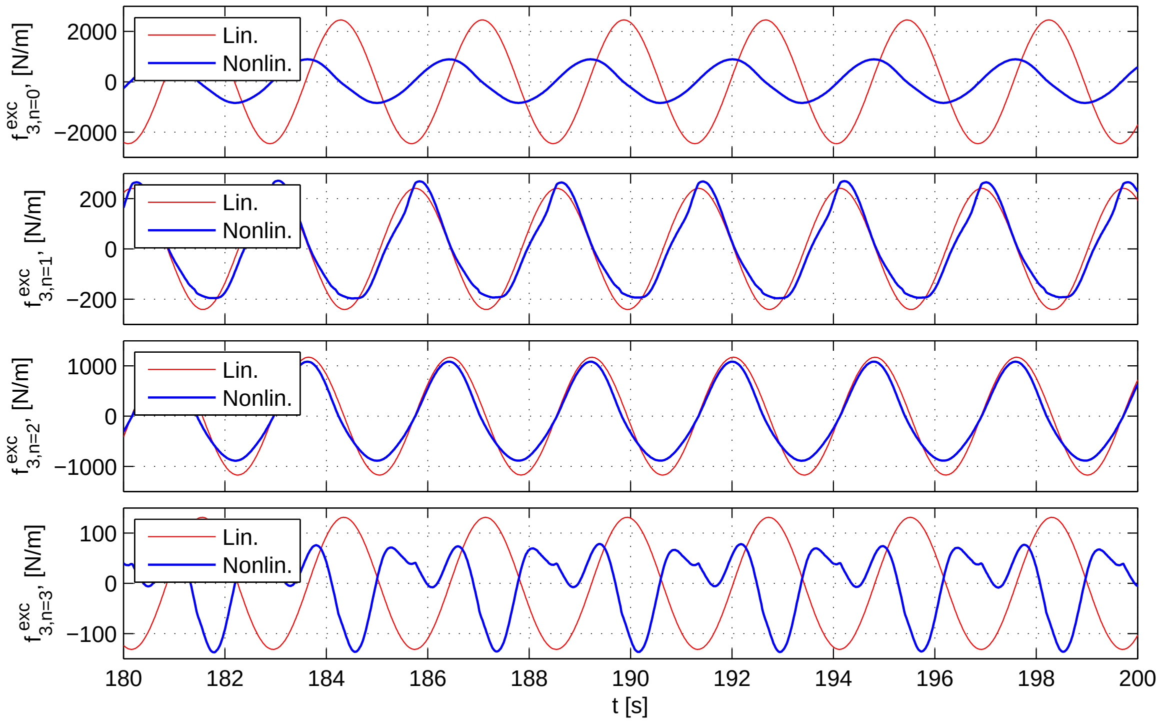

(b) Modal excitation force $f^{exc}_{3,n}(t)$.

Figure 7.2: Time series of modal displacement and excitation forces for the four first modes for 2 tori for heave resonance at $\omega = 2.25 rad/s$. Linear and nonlinear excitation forces are compared. $a_n(t)$ and $f^{exc}_{3,n}(t)$ are the n-th time dependent Fourier coefficient and the time dependent modal force for mode n, respectively. $f^{exc}_{3,n}(t)$ are given by equation (7.1) to (7.4). The wave steepness $H/\lambda = 1/15$, giving a wave amplitude $\zeta_a = 0.41m$. H and λ are the wave height and wave length. A modal damping level of 1.5 percent of modal critical damping is used. Note the difference between the values on the y-axes.

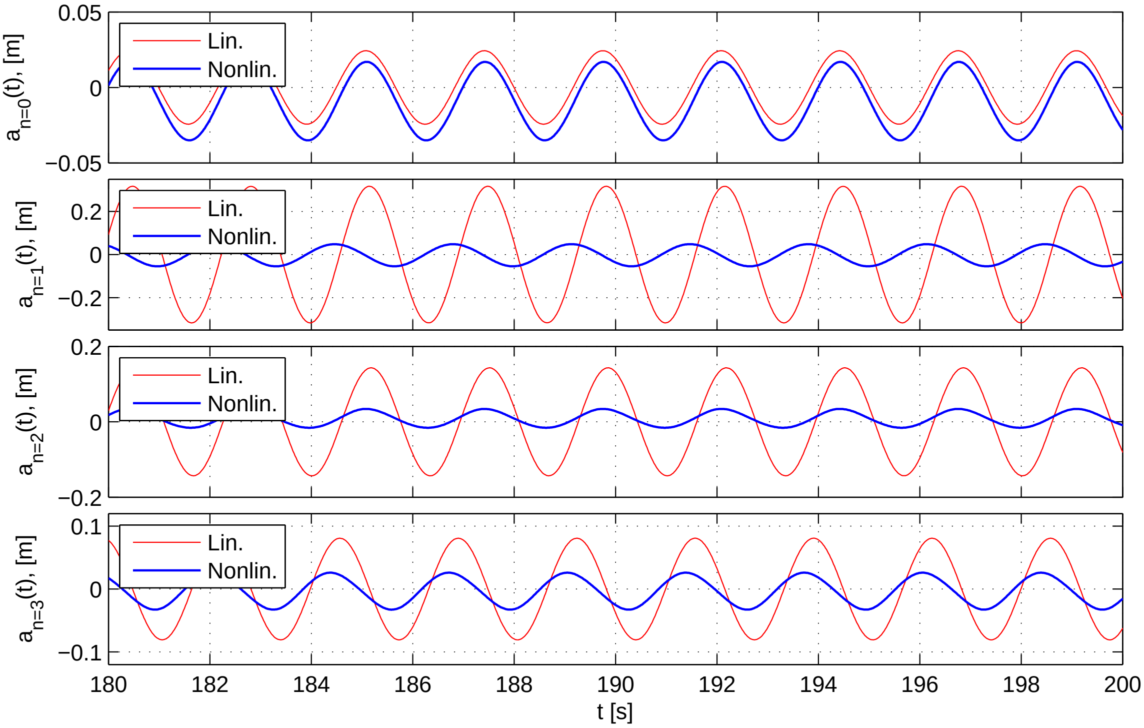

(a) Response of Fourier coefficient $a_n(t)$.

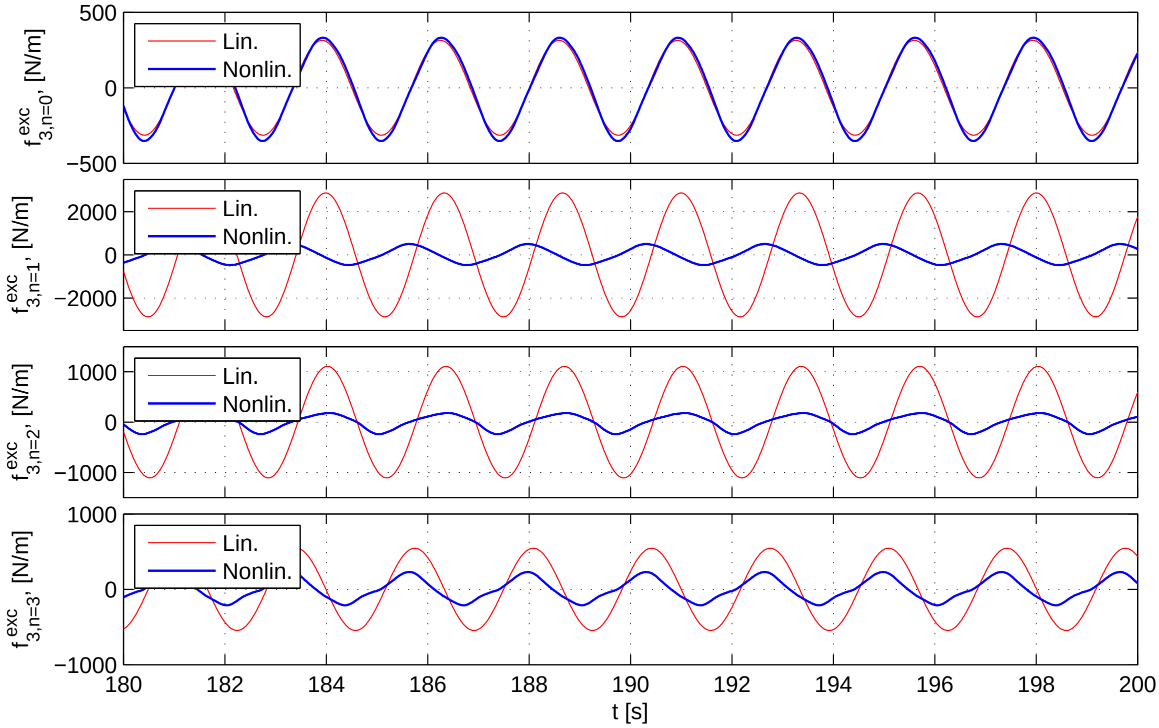

(b) Modal excitation force $f^{exc}_{3,n}(t)$.

Figure 7.3: Time series of modal displacement and excitation forces for the four first modes for 2 tori for pitch resonance at $\omega = 2.69 rad/s$. Linear and nonlinear excitation forces are compared. $a_n(t)$ and $f^{exc}_{3,n}(t)$ are the n-th time dependent Fourier coefficient and the time dependent modal force for mode n, respectively. $f^{exc}_{3,n}(t)$ are given by equation (7.1) to (7.4). The wave steepness $H/\lambda = 1/15$, giving a wave amplitude $\zeta_a = 0.28m$. H and λ are the wave height and wave length. A modal damping level of 1.5 percent of modal critical damping is used. Note the difference between the values on the y-axes.

7.3 Mode Excitation at Higher Frequencies

For some frequencies, modal responses with a higher frequency than the wave exciting frequency have been observed. The most usual is that the modal displacement and force are excited with a frequency that is two times the incident wave frequency ω. Response and force components with frequencies 3ω, 4ω and higher have also been observed. The trend is that the higher the overlaying frequency is, that is the larger m in the frequency component $m\omega$ is, where m is a positive integer, the lower is the magnitude of the modal response compared with the largest modal response for that frequency. Response will now mean both modal displacement and modal excitation force. When a mode are excited with a $m\omega$ frequency component, that does not mean that $m\omega$ is the only exciting frequency for that mode. The mode is excited with the wave frequency ω plus a frequency component with frequency equal to $m\omega$. This frequency component can either reduce or increase the modal response, or the magnitude can be unchanged. It is observed that for most cases the magnitude is increased when a $m\omega$ frequency component is present. The modal displacement containing a higher frequency component seems to be caused by, when investigating the response time series, a higher frequency component in the modal excitation force. This $m\omega$ component in the modal force can have an amplitude with the same magnitude as the frequency component for the wave frequency ω for that mode. Modal excitation forces with a $m\omega$ component that is considerably smaller than the magnitude of the wave frequency component will not excite a $m\omega$ component in the displacement of the same mode. It is not certain that a higher frequency component with a high magnitude compared with the wave frequency component in the modal force will excite a higher frequency component for the modal displacement. But the magnitude of the $m\omega$ component must be in the same order of magnitude as the wave frequency component in order to excite the modal displacement at a higher frequency.

Three different cases where a 2ω component in the response is present are shown in Figure 7.4, 7.5 and 7.6. Figure 7.4 shows the modal force and response for the second elastic mode for 2 tori for $\omega = 1.5rad/s$. The wave amplitude is $\zeta_a = 0.46m$. Figure (7.5) shows the modal force and excitation force for the fourth elastic mode for 1 torus, $\omega = 2rad/s$ and $\zeta_a = 0.39m$. The time series of the sixth elastic mode for 2 tori for heave resonance at $\omega = 2.25rad/s$ and a wave amplitude $\zeta_a = 0.41m$ is plotted in figure (7.6). Note that different wave steepnesses H/λ and different modal damping levels are used for the three cases. H and λ are the wave height and wave length, respectively. In Figure 7.4 and 7.6 the start of the time series, $t = 0s$, is seen. It is observed that the modal excitation force and response initially get their largest contribution from a component with a frequency equal to the wave frequency. A 2ω component appear and increase in magnitude when time t increase. After approximately $60s$ a stationary response is reached for both cases. In Figure 7.4 and 7.5, for $\omega = 1.5rad/s$ and $\omega = 2rad/s$ respectively, the magnitude of the nonlinear response and excitation force are larger than the linear response and excitation force. The 2ω force component seems to increase the response compared with the liner model. For $\omega = 2.25rad/s$, Figure 7.6, the magnitude of the nonlinear and linear response and excitation force is similar. The equations of motion for the linear model are uncoupled. The equations of motion for the nonlinear model are indirectly coupled since the modal excitation forces are dependent on the total displacement of the floater, thus giving coupling between the response of all modes and the modal force for a given mode.

The $m\omega$ component in the response for a wave circular frequency ω bear resemblance with nonlinear springing response of ships. For nonlinear springing response, the 2ω frequency component is most common. A mode with resonance frequency ω_N is excited by waves with encounter frequency $\omega_e = \omega_N/m$, where m is a positive integer with value 2 or higher, [Drummen (2008)]. Springing is steady state resonant elastic vibrations due to continuous wave loading, [Faltinsen (2005)]. For the floater the frequency of the $m\omega$ force component were slightly lower than the resonance frequency for the mode excited at a frequency equal to $m\omega$. Although the floater does not have forward speed, the higher frequency responses can be associated with springing.

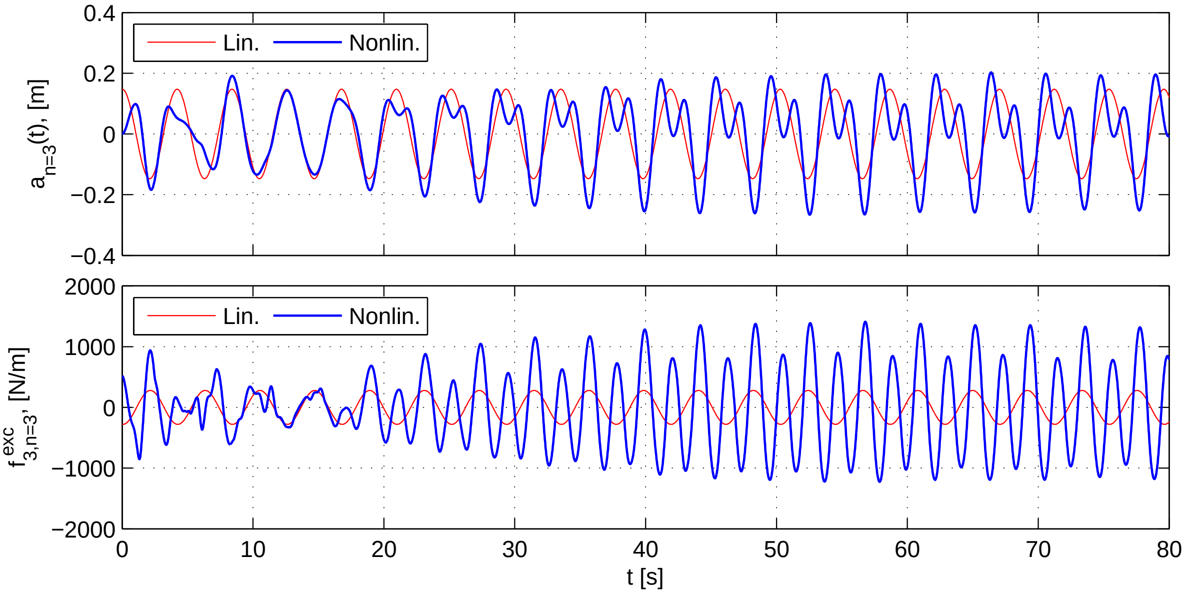

Figure 7.4: Comparison between linear and nonlinear modal response and excitation force for 2 tori. The results for the second elastic mode, $n = 3$, are plotted. The incident wave frequency is $\omega = 1.5rad/s$. The wave steepness is $H/\lambda = 1/30$, giving a wave height $\zeta_a = 0.46m$. A modal damping level of 1.5 percent of critical damping for each mode is used.

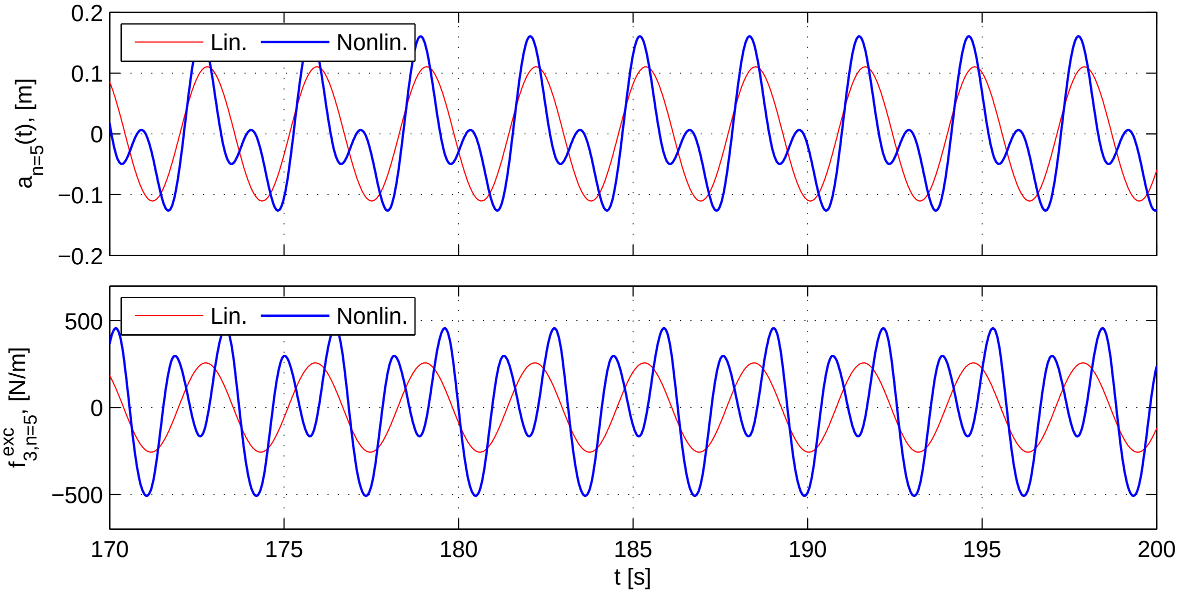

Figure 7.5: Comparison between linear and nonlinear modal response and excitation force for 1 torus. The results for the fourth elastic mode, $n = 5$, are plotted. The incident wave frequency is $\omega = 2rad/s$. The wave steepness is $H/\lambda = 1/20$, giving a wave height $\zeta_a = 0.39m$. A modal damping level of 2 percent of critical damping for each mode is used.

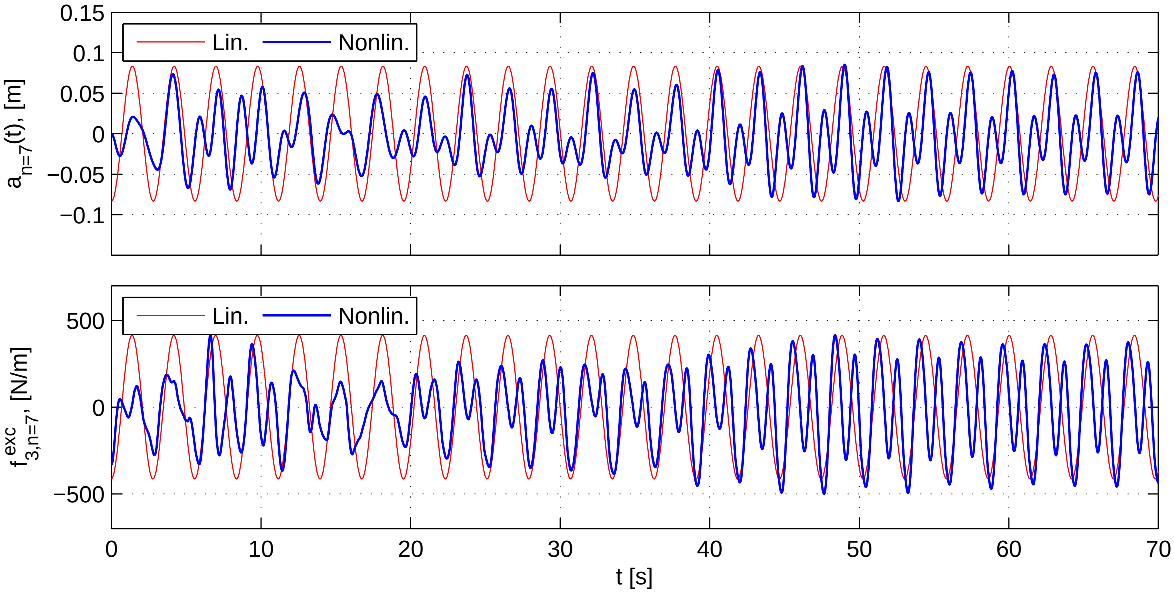

Figure 7.6: Comparison between linear and nonlinear modal response and excitation force for 2 tori. The results for the sixth elastic mode, $n = 7$, are plotted. The incident wave frequency is $\omega = 2.25 rad/s$, corresponding to heave resonance. The wave steepness is $H/\lambda = 1/15$, giving a wave height $\zeta_a = 0.41m$. A modal damping level of 1.5 percent of critical damping for each mode is used.

7.4 Transfer Functions

7.4.1 Displacement and Excitation Forces

The linear and nonlinear transfer functions for displacement and the modal excitation forces for the two first modes for 1 torus and 2 tori are shown in Figure 7.7 and 7.8, respectively. The transfer functions for the next six modes for 1 torus and 2 tori are shown in Appendix B.3.1 and B.3.2. The nonlinear force and displacement amplitudes are found by dividing the difference between the maximum and minimum values in the stationary part of the time series with the wave height H given by $H = 2\zeta_a$, where ζ_a is the wave amplitude. The linear force and displacement amplitudes are calculated directly in the frequency domain. In the nonlinear analysis computed in the time domain the response can not be evaluated by a single amplitude, since there might be a difference between the magnitude of the maximum and minimum response. The mean of the magnitudes of the positive and negative amplitudes are found in order to compare the nonlinear results with the linear results. Results for two different wave steepnesses and damping levels are investigated in the nonlinear analysis. The wave steepness is given by H/λ, where λ is the wave length.

From Figure 7.7 it is seen the nonlinear modal displacements for the two first modes for 1 torus are similar to the linear displacements up to the wave frequencies $\omega = 1.4 rad/s$. From $\omega = 1.4 rad/s$ to $\omega = 1.5 rad/s$ both the nonlinear heave and pitch responses are higher than the linear case. For $\omega = 2 rad/s$ the pitch response for the nonlinear model with a wave steepness $H/\lambda = 1/15$ is significantly higher than the pitch response for the linear model. The nonlinear modal excitation forces for frequencies up to $\omega = 1.5 rad/s$ are generally higher than the linear excitation forces. For frequencies lower than $\omega = 1.4 rad/s$ this is not inducing larger nonlinear displacements. For 2 tori, Figure 7.8, the nonlinear and linear modal displacements are similar up to $\omega = 1.5 rad/s$. For $\omega = 1.5 rad/s$ the nonlinear pitch excitation force is significantly higher than the linear force. For a wave steepness $H/\lambda = 1/15$, and $\omega = 2 rad/s$, the nonlinear heave and pitch responses are lower and higher, respectively, than the linear responses. The nonlinear excitation forces are in general higher than the linear forces for frequencies lower than $\omega = 1.5 rad/s$. As for the 1 torus case, this is not inducing larger nonlinear responses. For the undamped resonance frequencies for heave and pitch, $\omega = 2.49 rad/s$ and $\omega = 2.89 rad/s$ for 1 torus and $\omega = 2.25 rad/s$ and $\omega = 2.69 rad/s$ for 2 tori, the modal excitation forces and corresponding modal displacements are significantly lower for the nonlinear model than for the linear model.

For the six first elastic modes, transfer functions shown in Appendix B.3.1 and B.3.2, the nonlinear and linear modal displacements are almost similar for frequencies up to $\omega \approx 1.2 rad/s$ for both 1 torus and 2 tori. The nonlinear excitation forces are in general higher than the linear excitation forces up to this frequency, but as for heave and pitch this does not increase the nonlinear response compared to the linear response. The nonlinear excitation forces are in general lower than the linear excitation forces for frequencies higher than $\omega = 2 rad/s$. This also applies for heave and pitch.

A general observation for all modes up to $n = 7$, is that the nonlinear modal excitation forces are higher than the linear excitation forces for low frequencies. However, the nonlinear and linear displacements are almost similar. The reason for the nonlinear displacements not being increased compared with the linear displacements can be interaction between modes and phase angle differences between forces and displacement and between different force components, or phase angles between the modal displacements. High modal displacements for one frequency might not cause a large total motion of the floater, due to phase differences between the modal responses. For some frequencies, higher than $\omega \approx 1.2$, the excitation forces or displacements, or both, for certain modes, are smaller for the nonlinear case than for the linear case. This can be caused by $m\omega$ frequency components in the excitation forces, where $m = 2$ or larger, or be the result of large changes in the exact wetted surface of the floater, giving differences between the linear and nonlinear modal excitation forces. These effects can also give nonlinear forces and displacements larger than the forces and displacement for the linear model.

Results for two different wave steepnesses in the nonlinear analysis, $H/\lambda = 1/30$ and $H/\lambda = 1/15$, are shown in Figure 7.7 and 7.8 and in Appendix B.3.1 and B.3.2. The results are not conclusive with respect to whether the modal responses and forces will increase or decrease when the wave steepness is increased. For 1 torus $H/\lambda = 1/15$ gives an increased modal force and response at heave and pitch for the modes at resonance compared with the results for $H/\lambda = 1/30$. For 2 tori the modal forces and responses for heave and pitch resonance are decreasing when the wave steepness is increased. Increased damping is reducing the response at heave and pitch resonance for 2 tori. For 1 torus different damping levels for the same wave steepness at resonance have not been tested, and the effect of damping at resonance for 1 tori can thus not be addressed. But, it is assumed that the response will be reduced with increased damping for 1 torus, as for 2 tori. Although different damping levels for the same wave steepnesses for lower frequencies than the resonance frequencies not have been investigated, it is assumed that the low damping levels used here not will have a significant effect for non resonant frequencies. This assumption is based on the fact that a low damping level only effect the modal responses in vicinity of the resonance frequencies. The damping levels in the nonlinear analysis are generally set to 1.5 and 3 percent of critical damping for $H/\lambda = 1/30$ and $H/\lambda = 1/15$. Increased wave steepness gave, dependent on the incident wave frequency, both increased and decreased modal responses. This imply that the wave steepness has a larger effect on the response than the low damping levels used in the analysis. The damping is increased when the wave steepness is increased in order to ensure convergence of the results from the time domain analysis. The larger the wave steepness is, the larger the damping need to be in order to get reliable results in terms of convergence. The exception is resonance, where a low damping level, even for the highest wave steepness tested, was sufficient. This imply that nonlinear effects at resonance due to changes in wetted area and vertical position of the floater have larger effects on the response than the damping level. The change in modal forces and displacements when the wave steepness is increased imply that nonlinear effects are important. The larger the wave steepness is, the larger is the change in wetted area on a floater section, both with respect to time and with respect to the local attachment points between the surface and the left and right side of the floater sections for a given time step. The small differences between the linear and nonlinear displacements for low frequencies are expected, since the motion of a floating structure will follow the wave elevation when $\omega \rightarrow 0$, thus giving small relative motion between the waves and the floater and a smaller change in wetted area compared with higher frequencies.

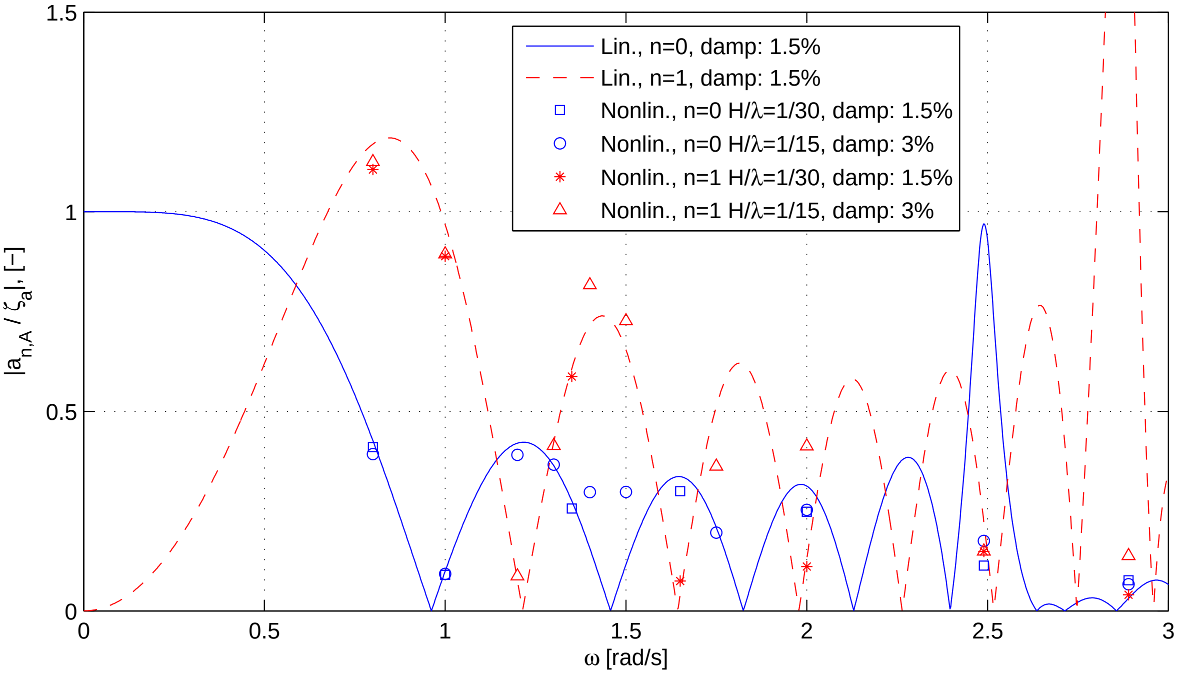

(a) Modal response.

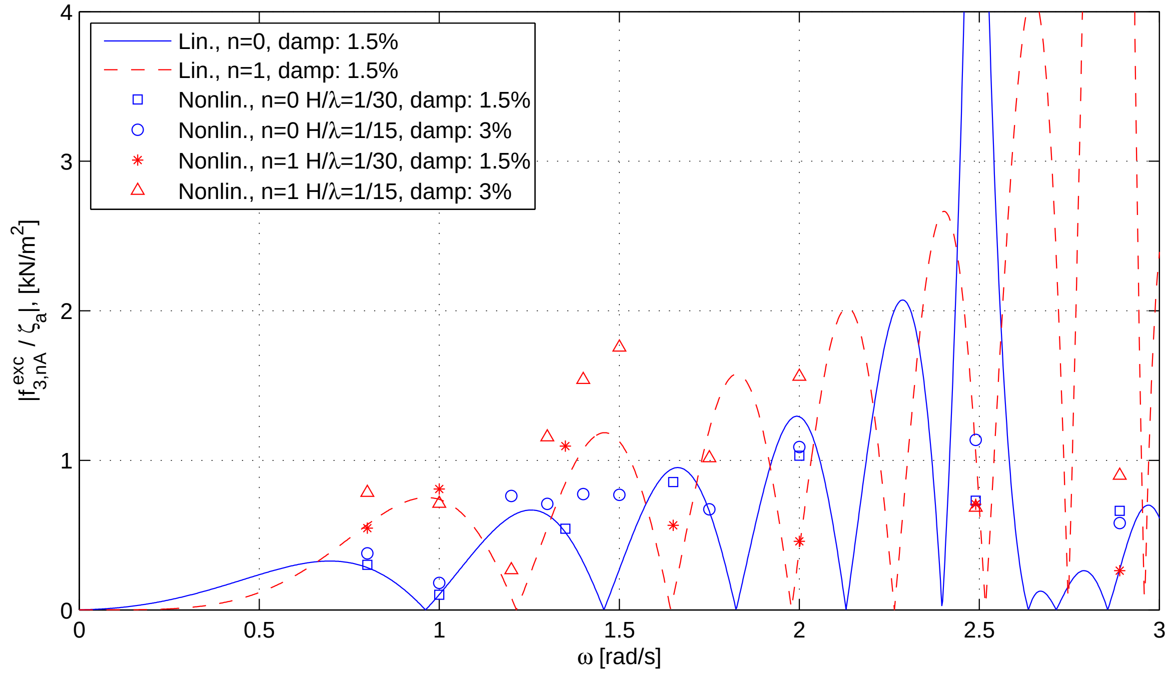

(b) Modal excitation force.

Figure 7.7: Transfer functions for modal response and modal excitation force for 1 torus. Linear and nonlinear response for heave and pitch, corresponding to $n = 0$ and $n = 1$, for different wave steepnesses H/λ and different damping levels are compared. ω and ζ_a are the wave frequency and wave amplitude. H and λ are the wave height and wave length.

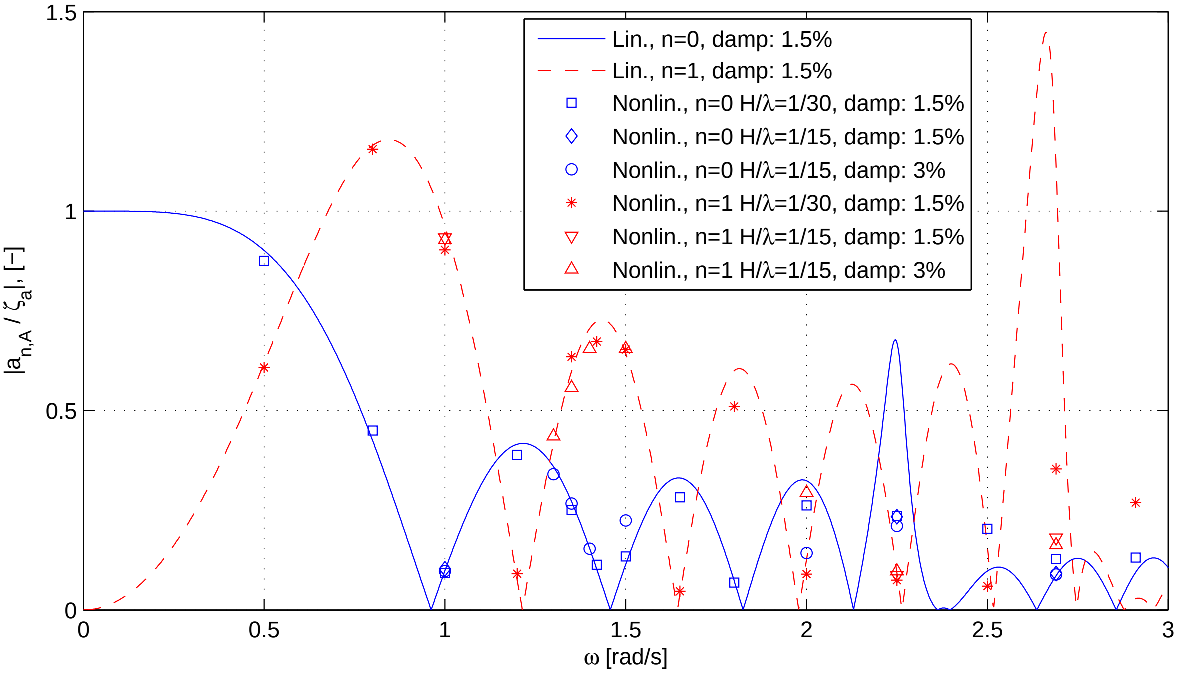

(a) Modal response.

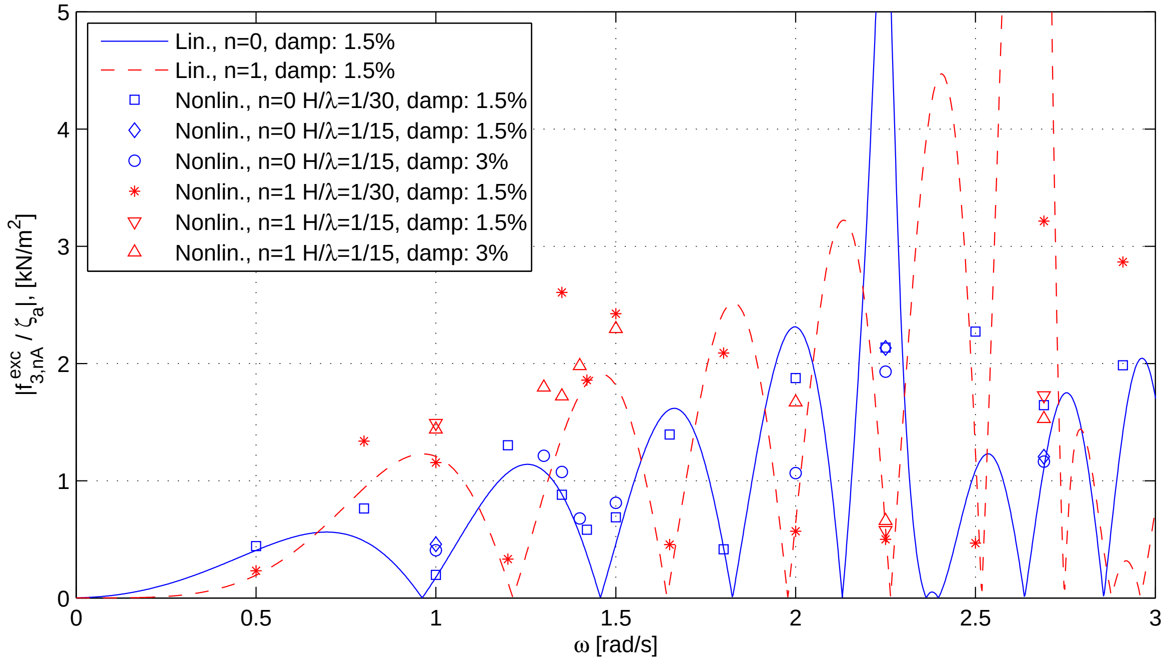

(b) Modal excitation force.

Figure 7.8: Transfer functions for modal response and modal excitation force for 2 tori. Linear and nonlinear response for heave and pitch, corresponding to $n = 0$ and $n = 1$, for different wave steepnesses H/λ and different damping levels are compared. ω and ζ_a are the wave frequency and wave amplitude. H and λ are the wave height and wave length.

7.4.2 Bending Stresses

The maximum bending stresses in the floating collar as a function of the wave frequency ω are presented in Figure 7.9. 1 torus and 2 tori, and the linear and nonlinear model are compared. For the nonlinear model two different damping levels, being a modal damping of 1.5 and 3 percent of critical damping for each mode, and two different wave steepnesses, $H/\lambda = 1/30$ and $H/\lambda = 1/15$, are shown. The transfer function for the bending stresses gives a picture of the total response of the floater, since it includes the total response of the floater in one graph. Compared with the modal transfer functions for the displacements, only the curvature of the floater, and not the displacements can be investigated from Figure 7.9. The 20 first modes, that is heave, pitch, and the 18 first elastic modes are included in the analysis. Section 6.2.1 explains why a minimum of 20 modes must be included when calculating the bending stresses.

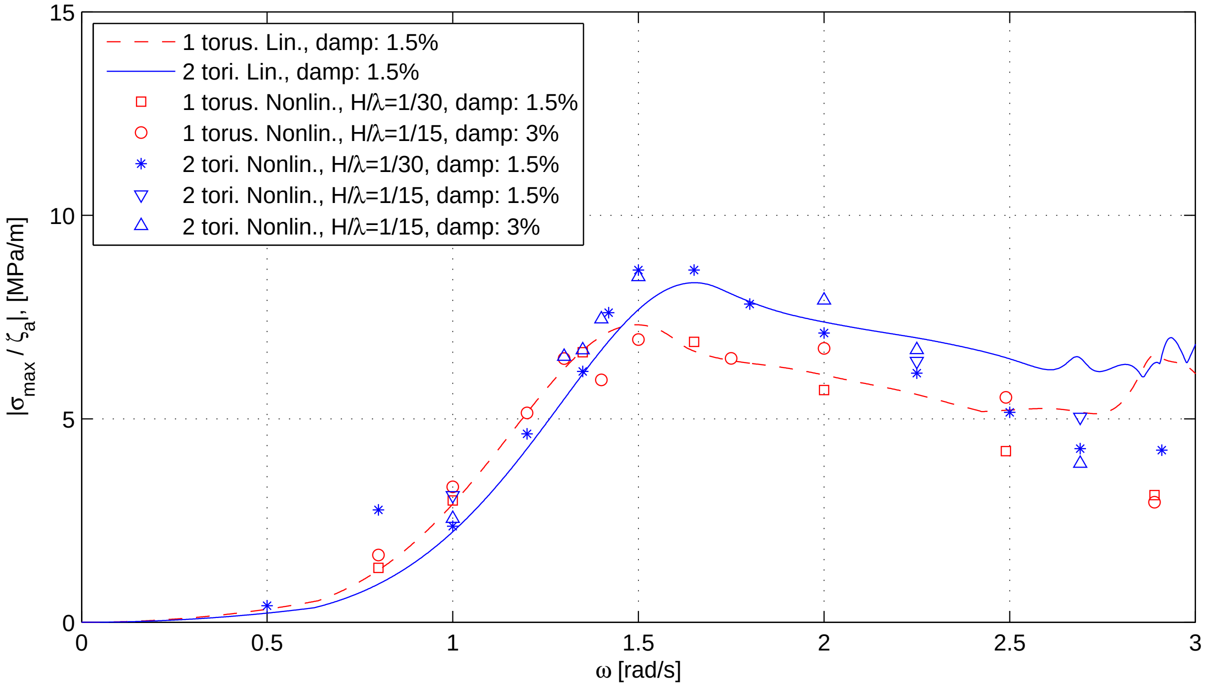

Figure 7.9: Transfer function for maximum bending stress σ_{max} in the floating collar. 1 torus and 2 tori, and the linear and nonlinear excitation force model are compared. For the nonlinear model two different damping levels, presented as a percentage of critical damping for each mode, and two different wave steepnesses H/λ are investigated. H is the wave height and λ is the wave length. ω is the wave frequency. The 20 first modes are used in the analysis for both the linear and nonlinear model.

The first resonance frequency for the transfer function for the maximum bending stresses according to the linear model are pitch resonance and resonance for the first elastic mode. This is because heave is a rigid body mode which does not induce a moment, and thus no bending stress in the floater. Pitch is a rigid body mode, but due to rotation bending moments and therefore bending stresses are induced. in Figure 7.9 the resonance frequencies for the bending stress transfer functions are not seen. This is because a low damping level has a significant effect on the bending stresses for the two first resonance frequencies. For 1 torus the nonlinear and linear bending stresses are almost similar for $\omega < 2rad/s$. The exception is $\omega = 1.4rad/s$ where the nonlinear model gives a lower maximum bending stress than the linear model. For $\omega = 2.89rad/s$, which is the resonance frequency for pitch, the nonlinear bending stress are reduced with almost 50 percent compared with the linear model. For $\omega = 2rad/s$ and $\omega = 2.49rad/s$ the bending stresses for $H/\lambda = 1/15$ are significantly higher than the bending stress for $H/\lambda = 1/30$. The bending stresses for the highest wave steepness are also higher than the linear bending stress for these two frequencies. $\omega = 2.49rad/s$ are heave resonance for 1 torus. For 2 tori the nonlinear bending stresses are higher than the linear bending stresses for $\omega < 1.75 rad/s$. For $\omega > 2 rad/s$ the nonlinear stresses are smaller than the linear stresses. At resonance for pitch and the first elastic mode, $\omega = 2.69 rad/s$ and $\omega = 2.91 rad/s$ the nonlinear stresses are significantly lower than the linear stresses. For $\omega = 0.8 rad/s$, the magnitude of the nonlinear stress for $H/\lambda = 1/30$ is more than twice the magnitude of the linear stress.

Results for the nonlinear model for both 1 torus and 2 tori show different values for the maximum stresses for the two different wave steepnesses presented in Figure 7.9. This imply that nonlinear effects due to increased variation of wetted area on the floater, with respect to both time and space, effects the motion response and thus the bending stresses in the floater. The increased damping level used for the largest wave steepness tested is used in order to ensure convergence of the nonlinear time series results. In general, increased wave steepness gives larger bending stresses for both 1 torus and 2 tori. One exception is pitch resonance for 1 torus and 2 tori where an increased wave steepness gives a reduction of the maximum stresses for a damping level of 3 percent. At resonance the reduction of the stresses can also be due to the increased damping, since damping has an effect on the response for the modal resonance frequencies. The difference in the response for the two wave steepnesses tested seem to increase with increased frequency ω. The exception is pitch resonance for 1 torus. The difference between linear and nonlinear results are also increasing with increased wave frequency. Which is expected, since the floater motion tend to follow the waves when $\omega \rightarrow 0$ in linear theory. This behavior are also expected for the nonlinear model.

7.5 Validity of Linear Wave Theory and Convergence of the Nonlinear Analysis

Linear wave theory is valid for waves with $k\zeta_a \ll 1$. $k = 2\pi/\lambda$ is the wave number. This statement will be explained later in this section. For a wave steepness $H/\lambda = 1/30$, $k\zeta_a = 0.105$. For $H/\lambda = 1/15$, $k\zeta_a = 0.209$. For a increased wave steepness $k\zeta_a$ will increase. For nonlinear excitation forces, a time domain procedure were used to find the responses for a given wave frequency and wave amplitude. When the wave steepness was increased, the modal damping level needed to be increased in order to get convergence of the time series for the response, forces and stresses. The exception were resonance, where nonlinear effects in the excitation forces had a large effect on the response. If the the wave steepness were increased further from $H/\lambda = 1/15$, the damping level needed to be increased in order to get convergence. Results for those time series are not shown since the applied damping for these cases might be significantly larger than the real damping in the system. A method with variable damping, applying high damping at the start of the time series in order to damp the transient response and reducing the damping slowly with respect to time, was tried. Still, convergence of the time series were not obtained. The problem with convergence might be caused by transient nonlinear effects due to the calculation procedure for the nonlinear forces or numerical errors in the Matlab code due to discretization. Numerical errors will be larger the higher the wave frequency is or the higher the wave steepness is. Unfortunately, there was not time to investigate and solve this problem. A procedure and Matlab code for calculating the nonlinear response in irregular sea were made. Results for nonlinear response in irregular waves are not shown and investigated since there might occur steep waves which give unphysical response due to the convergence problems. Transients will occur in irregular waves. But due to the problems with convergence for steep waves it is not possible to know whether the results are correct or not. The method for calculating nonlinear forces and responses is assumed to give good results for regular linear waves for the H/λ values presented in this chapter. This assumption is based on convergence of the time series and the fact that the nonlinear results for the displacements and stresses corresponded well with the linear results for low wave frequencies.

It can be mentioned that it is common to set the limit for breaking waves in deep water to $H/\lambda = 1/7$, referred to as the Miche criterion, [Soulsby (1997)] and [Faltinsen (2005)]. This gives $k\zeta_a = 0.449$.

The criterion for the validity of linear wave theory, $k\zeta_a \ll 1$, comes from evaluation of the momentum equation. The x-component of the momentum equation from [White (2008)] is

$$\frac{\partial u}{\partial t} + u\frac{\partial u}{\partial x} + w\frac{\partial u}{\partial z} = -\frac{1}{\rho}\frac{\partial p}{\partial x} \tag{7.5}$$

Incompressible fluid and no viscosity are assumed. u, w and p are the water particle velocities in x and z-direction and the pressure, respectively. In linear theory, for small waves, it is assumed that the convective acceleration terms $u\partial u/\partial x$ and $w\partial u/\partial z$ are small compared with the local acceleration term $\partial u/\partial t$. The convective terms are then neglected. This can be seen by by removing the convective acceleration terms from equation (7.5) and solving the equation for the dynamic pressure. The result is $p = -\rho\partial\phi_0/\partial t$ as expected for linear wave theory. ϕ_0 is the incident wave potential. $u = \partial\phi_0/\partial x$, from linear wave theory, [Faltinsen (1990)], is used. By taking the ratio between the convective and local acceleration terms and assuming deep water waves the criterion $k\zeta_a \ll 1$ is found. This indicate that the validity of linear wave theory requires a lower wave steepness than the limiting breaking criterion $H/\lambda = 1/7$.

Chapter 8

Further Discussion, Conclusion and Suggestions for Further Work

8.1 Further Discussion - Error Sources

The limiting case of $\omega \to 0$ on which the velocity potentials and the added mass is based, state that the calculated modal added mass coefficients only are valid for low frequencies were the rigid free surface condition is satisfied or approximately satisfied. What upper frequency limit that in a good way approximately satisfies the zero frequency case and thus the rigid free surface condition is not investigated. This is a subject for further work. Due to large displacements at resonance for the linear case, the resonance frequencies is assumed to be the largest possible frequency for which the rigid free surface condition is approximately satisfied. For the nonlinear case this is also dependent on the wave steepness. Possibly, the highest frequency for which the calculated values for the added mass is a good approximation of the real added mass for the floater is lower than the first resonance frequencies. The response is effected by the added mass. Thus, the quality of the results for frequencies higher than the first resonance frequencies are assumed uncertain. The error is increasing with increasing wave frequency. For very low frequencies, close to $\omega = 0$, the solution is assumed to be correct according to linear theory. For a heaving 2D semi-submerged cylinder the 2D heave added mass goes to infinity for $\omega \to 0$. For increased frequencies immediately after $\omega = 0$ the added mass is decreasing. When $\omega \to \infty$, added mass is slowly increasing, [Faltinsen (1990)]. For the floater, the added mass is not going to infinity for $\omega \to 0$ due to the asymptotic matching between the near field and far field description. For high frequencies, it is a possibility that the added mass for the floater is decreased compared with the values obtained by the zero frequency case. This will effect the response.

Vertical response of the floater is calculated without taking the mooring line forces and horizontal displacements into account. These forces and displacement will have an effect on the response. The magnitude and effect of these forces are not known. This must be kept in mind when the results in Chapter 6 and 7 are evaluated.

Damping is in this thesis set to a percentage of the critical damping, since the real damping in the system is difficult to determine correctly. The damping were set as low as possible in the nonlinear analysis in order to obtain convergence. The real damping in the system can be higher or lower than the values used in this thesis. Nonlinear damping terms are also a possibility. Investigation of the real damping for the system and the effects of nonlinear damping should in future work with this problem be addressed. Especially the effect of the structural damping of the HDPE plastic used in the floating collar. Damping in HDPE plastic is nonlinear. This can result in the higher modes having higher damping than presumed in this thesis. The effect can be that fewer modes are needed in order to describe the response of the floater than given by the linear analysis conducted in this thesis. Response means displacement, forces, relative motion and stresses.

The nonlinear analysis does not take impact forces and run-up of water on the pipe surface due to impact and sudden changes of wetted area into account. These forces may give a change in the force history, and thus change the response. Vibrations in the floater might be induced by these effects. Impact forces and run-up can possibly be found with use of for instance CFD (Computational Fluid Dynamics) software. For a large slender elastic structure in waves the calculation time would be long, and proper modeling of the physical model can be difficult and time consuming. The goal for this project, however, was to use theoretical and simplified numerical methods in order to obtain qualitatively good results.

The linear diffraction and Froude-Kriloff forces were calculating by assuming the vertical coordinate of the floater section being fixed at the mean position $z = 0$. The water particle acceleration and the dynamic pressure from the undisturbed incident waves were calculated at $z = 0$. This is an approximation that is better the longer the waves are. For shorter waves, or higher wave frequencies, this approximation is less accurate. This and the limiting zero frequency case on which the added mass calculations are based on is an error source for frequencies not close to zero. The error is presumably increasing for increasing wave frequencies.

8.2 Conclusion

The added mass calculations are based on the limiting zero frequency case. Thus, the results for both linear and nonlinear excitation forces are assumed to be a good approximation of the real response of the floater for low frequencies. For higher frequencies, and for frequencies higher than the first natural frequencies it is not certain that the theory presented in this thesis give good results. The expressions for the linear excitation forces are also assuming long waves, and the error for these calculations increase for higher wave frequencies.

The nonlinear modal response from nonlinear hydrostatic and nonlinear Froude-Kriloff forces are significantly smaller for the resonance frequencies than the linear modal response. This is due to reduction in modal excitation forces when the undisturbed hydrostatic and dynamic pressures are integrated over the exact wetted surface of the floater. A low modal damping level does only effect the responses at resonance. This applies both for the linear and nonlinear model. The effect of integrating the hydrostatic and dynamic pressures over the exact wetted surface are larger than the effect of damping. For low frequencies, theoretically $\omega \to 0$, in practice $\omega < 1rad/s$, the linear and nonlinear model gave similar results with respect to displacements. The modal forces are in general higher for the nonlinear model than the linear model for low frequencies and lower for high frequencies.

For some wave frequencies ω, $m\omega$ frequency components in the modal forces inducing $m\omega$ frequency components in the time dependent modal displacements are observed. m is a positive integer. $m = 2$ is the most common, but higher frequency components are also observed. The modes that are excited with a $m\omega$ component have a linear undamped resonance frequency slightly higher than m times the incident wave frequency ω. The nonlinear model can have small effects on the resonance frequencies due to difference in restoring forces, and the resonance frequencies for the nonlinear model can therefore be very close to the $m\omega$ frequency component in the modal excitation force. Although the floater does not have forward speed, the excitation of modes at frequencies close to their resonance frequencies for non resonant wave frequencies can be associated with nonlinear springing response for ships.

Investigation of the standard deviations and most probable maximum bending stresses in the floater according to linear theory in irregular sea showed that the response is dependent on the wave spectrum applied in the analysis. The JONSWAP and ISSC formulation were investigated. The JONSWAP spectrum gave largest standard deviations for small spectral peak periods. The ISSC spectrum gave the largest standard deviations for higher peak periods. The responses for the two formulations were similar for a peak period of approximately $4.5s$. Altering the cross section dimension on floater had largest effect on the bending stresses for low peak periods. The stresses were reduced when the ratio between the the outer diameter of the pipe and the wall thickness was reduced, meaning the bending stiffness being increased when the outer diameter were kept constant. The effect of damping on the standard deviation of the bending stress were largest for low frequencies. Increased damping gave reduction in stresses. The maximum bending stresses in a sea state were, for peak periods larger than approximately $5s$ and $4s$ for 1 torus and 2 tori, situated at the positions on the floater were the pipe axes are parallel with the wave propagation direction.

8.3 Suggestions for Further Work

The validity of the added mass calculations regarding when the rigid free surface condition not is properly satisfied, and for which frequencies the theory presented here does not give good results need to be addressed further in order to properly investigate the results obtained in this thesis. In the nonlinear model the diffraction forces were still calculated according to linear theory. Investigation of the diffraction forces for high frequencies will give a better picture of the excitation forces and responses.

Damping were estimated by a level of critical damping. In order to fully understand the dynamics of the floater, the different damping components should be investigated. Especially the structural damping in the HDPE plastic needs further investigation.

Only vertical response of the floater, without considering coupling between horizontal an vertical motion, was investigated. Horizontal deformations may effect the vertical displacements, relative motion and bending stresses in the floater. Thus, horizontal deformations and coupling between horizontal and vertical motion should be addressed. In order to fully model the floating collar without the net cage, the effects of the mooring system should be implemented in the equations. Effects of altering the floater dimensions, with respect to displacements, relative motion, bending stresses and the standard deviations of the bending stresses should also be investigated further.

The problems regarding convergence of the time series for high wave steepnesses should be investigated and hopefully fixed. The response of the floater in irregular waves due to nonlinear excitation forces can then be investigated in order to see what effects the nonlinear hydrostatic and nonlinear Froude-Kriloff forces have on the standard deviations of the stresses.

References

Abramowitz, M., & Stegun, I. A. (1972). *Handbook of Mathematical Fuctions.* Dover Publications ,Inc.

Bearman, P. W., Graham, J. M. R., Obasaju, E. D., & Drossopoulus, G. H. (1984). *The Influence of Corner Radius on the Forces Experienced by Cylindrical Bluff Bodies in Oscillatory Flows.* Appl Ocean Rec.

Dean, R. G., & Dalrymple, R. A. (1991). *Water Wave Mechanics for Engineers and Scientists.* World Scientific Publishing Co. Pte. Ltd.

Drummen, I. (2008). *Experimental and Numerical Investigation of Nonlinear Wave-Induced Load Effects in Containerships considering Hydroelasticity.* Doctoral Thesis. Department of Marine Technology, Norwegian University of Science and Technology.

Faltinsen, O. M. (1990). *Sea Loads on Ships and Offshore Structures.* Cambridge University Press.

Faltinsen, O. M. (2005). *Hydrodynamics of high-Speed Marine Vehicles.* Cambridge University Press.

Faltinsen, O. M. (2011). Hydrodynamic aspects of a floating fish farm with circular collar. *The 26th International Workshop on Water Waves and Floating Bodies (IWWFB). April 17-20. Athens, Greece.*

Hibbeler, R. C. (2005). *Mechanics of Materials.* Prentice-Hall, Inc.

Kreyszig, E. (1999). *Advanced Ingineering Mathematics.* John Wiley and Sons Inc.

Kristiansen, D. (2010). *Wave Induced Effects on Floaters of Aquaculture Plants.* Doctoral Thesis. Department of Marine Technology, Norwegian University of Science and Technology.

Larsen, C. M., & Halse, K. H. (1997). Comparison of models for vortex induced vibrations of slender marine structures. *Marine Structures. Volume 10, Issue 6, July 1997, Pages 413-441..*

Newman, J. N. (1962). *The Exciting Forces on Fixed Bodies in Waves.* Journal of Ship Res., 6, 4, 10-17.

Newman, J. N. (1977). *Marine Hydrodynamics.* The MIT Press.

Sarpkaya, T. (1986). Force on a circular cylinder in viscous oscillatory flow at low keulegan-carpenter numbers. *J. Fluid Mech., 165, 61-71.*

Soulsby, R. (1997). *Dynamics of Marine Sands.* Thomas Telford Publ., London, UK.

Walpole, Myers, Myers, & Ye (2007). *Probability & Statistics for Engineers & and Scientists.* Pearson Prentice Hall. Pearson Education, Inc.

Watson, G. N. (1952). *Theory of Bessel Functions.* Cambridge University Press.

White, F. M. (2008). *Fluid Mechanics.* McGraw-Hill Companies, Inc.

Appendix A

Derivation of Chosen Expressions

A.1 Fourier Sum Involving Bessel Functions

The Expression in equation (A.1) can be presented as a cosine Fourier sum as shown in equation (A.2). [Kreyszig (1999)]. a_0 and a_n are the first and n-th Fourier coefficients, and must not be associated with variables with similar symbols presented earlier in this thesis. $n = 1, 2, 3, ..., \infty$ and L is the half period. Since $f(\beta)$ is periodic with 2π, L is set to π. x is the variable and will be equal to β.

$$f(\beta) = e^{ikR\cos\beta} \tag{A.1}$$

$$f(x) = a_0 + \sum_{n=1}^{\infty} a_n \cos\frac{n\pi x}{L} \tag{A.2}$$

$$a_0 = \frac{1}{\pi}\int_0^{\pi} f(x)\,dx = \frac{1}{\pi}\int_0^{\pi} e^{ikR\cos\beta}\,d\beta \tag{A.3}$$

$$a_n = \frac{2}{\pi}\int_0^{\pi} f(x)\cos\frac{n\pi x}{L}\,dx = \frac{2}{\pi}\int_0^{\pi} e^{ikR\cos\beta}\cos n\beta\,d\beta \tag{A.4}$$

According to [Abramowitz & Stegun (1972)] the 0-th and n-th order Bessel functions of the first kind can be expressed by the integrals in equation (A.5) and (A.6). z and θ must not be associated with coordinates with the same variable names in the rest of the thesis. z is set to kR and θ is set to β . By comparing the expressions for the Bessel functions with the Fourier coefficients it is seen that $a_0 = J_0(kR)$ and $a_n = 2i^n J_n(kR)$. Inserting the result into equation (A.2) gives equation (A.7).

$$J_0(z) = \frac{1}{\pi}\int_0^{\pi} e^{iz\cos\theta}\,d\theta \tag{A.5}$$

$$J_n(z) = \frac{i^{-n}}{\pi}\int_0^{\pi} e^{iz\cos\theta}\cos n\theta\,d\theta \tag{A.6}$$

$$e^{ikR\cos\beta} = J_0(kR) + \sum_{n=1}^{\infty} 2i^n J_n(kR) \cos n\beta \tag{A.7}$$

Appendix B

Tables and Figures

B.1 Tables

T_2	$T_{p,\text{ISSC}}$	$T_{p,\text{JONSWAP}}$
2.13	3.00	2.74
2.49	3.50	3.20
2.84	4.00	3.66
3.20	4.50	4.11
3.55	5.00	4.57
3.91	5.50	5.03
4.26	6.00	5.48
4.97	7.00	6.40
5.68	8.00	7.31
6.39	9.00	8.22
7.10	10.00	9.14
7.81	11.00	10.05
8.52	12.00	10.97
9.23	13.00	11.88
9.94	14.00	12.79

Table B.1: Comparison between the peak periods T_p for the ISSC and JONSWAP spectrum calculated from the mean zero up-crossing periods T_2. The values for T_2 and $T_{p,\text{ISSC}}$ are used in Chapter 6.

	T_2														
$H_{1/3}$	1	2	3	4	5	6	7	8	9	10	11	12	13	Sum	Pr. exc.
0.5	0	0	15	70	104	85	50	24	10	4	1	1	0	364	0.818
1.0	0	0	1	17	51	65	49	27	12	5	2	1	0	230	0.520
1.5	0	0	0	4	24	44	43	28	13	5	2	1	0	164	0.323
2.0	0	0	0	1	9	24	30	22	12	5	2	1	0	106	0.187
2.5	0	0	0	0	3	11	18	16	9	4	1	1	0	63	0.103
3.0	0	0	0	0	1	5	10	10	6	3	1	0	0	36	0.053
3.5	0	0	0	0	0	2	5	5	4	2	1	0	0	19	0.026
4.0	0	0	0	0	0	1	2	5	2	1	1	0	0	10	0.011
4.5	0	0	0	0	0	0	1	1	1	1	0	0	0	4	0.004
5.0	0	0	0	0	0	0	0	1	1	0	0	0	0	2	0.001
5.5	0	0	0	0	0	0	0	0	0	0	0	0	0	0	-
6.0	0	0	0	0	0	0	0	0	0	0	0	0	0	0	-
Sum	0	0	16	92	192	237	208	137	70	30	11	5	0	998	

Table B.2: Discrete joint frequency distribution (scatter diagram) for service restriction **R3** (coastal service), [DNV Report No. 97-0152]. The scatter diagram is constructed from theoretical parameters, and represent DNV rules for service restriction **R3** for high-speed and light crafts. T_2 and $H_{1/3}$ is the mean up-crossing period and significant wave height of the spectrum. The dimensions are seconds and meters respectively. $T_2 = 7s$ means a mean period from $6.5s$ to $7.5s$. $H_{1/3} = 2.0m$ means a significant wave height from $1.75m$ to $2.25m$. The probability of exceedence for each significant wave height is shown in the column to the right. Probability of exceedence for $H_{1/3} = 3.0m$ is calculated as $(0.5 \cdot 36 + 19 + 104 + 2)/998 = 0.053$, [Faltinsen (2005)]. Mean periods higher than $13s$ are removed from the table since there is no entries for higher periods.

B.2 Linear Transfer Functions

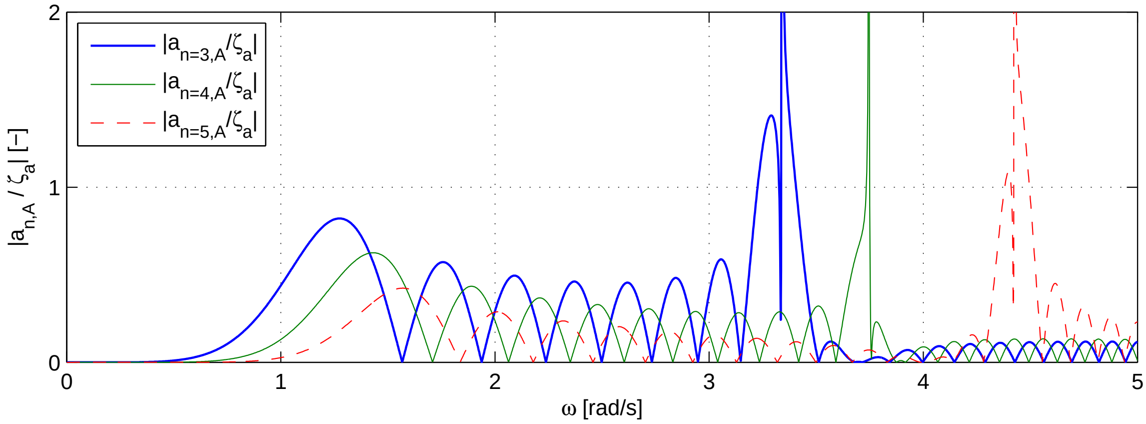

Figure B.1: Undamped linear transfer functions for 1 torus. $a_{n,A}$ is the motion amplitude of mode n. $n = 3, 4, 5$ are elastic modes. ζ_a is the wave amplitude and ω is the wave frequency.

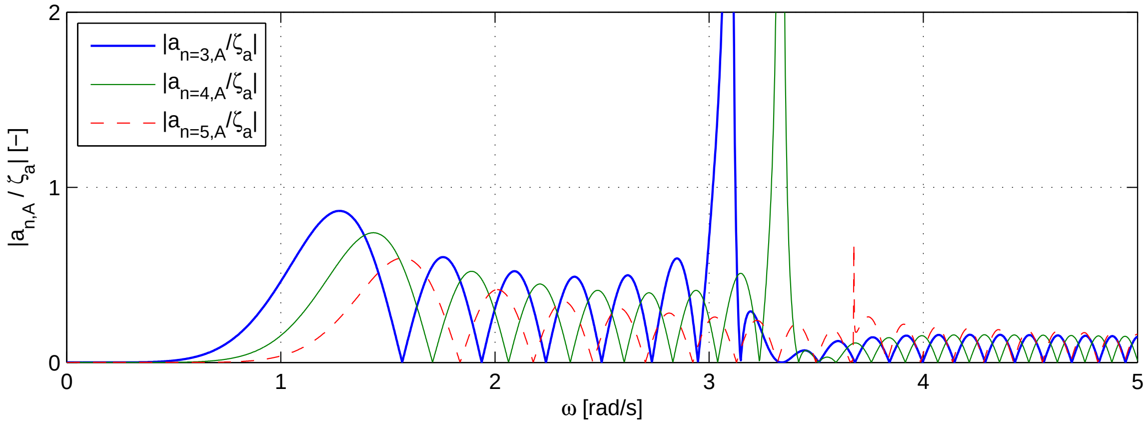

Figure B.2: Undamped linear transfer functions for 2 tori. $a_{n,A}$ is the motion amplitude of mode n. $n = 3, 4, 5$ are elastic modes. ζ_a is the wave amplitude and ω is the wave frequency.

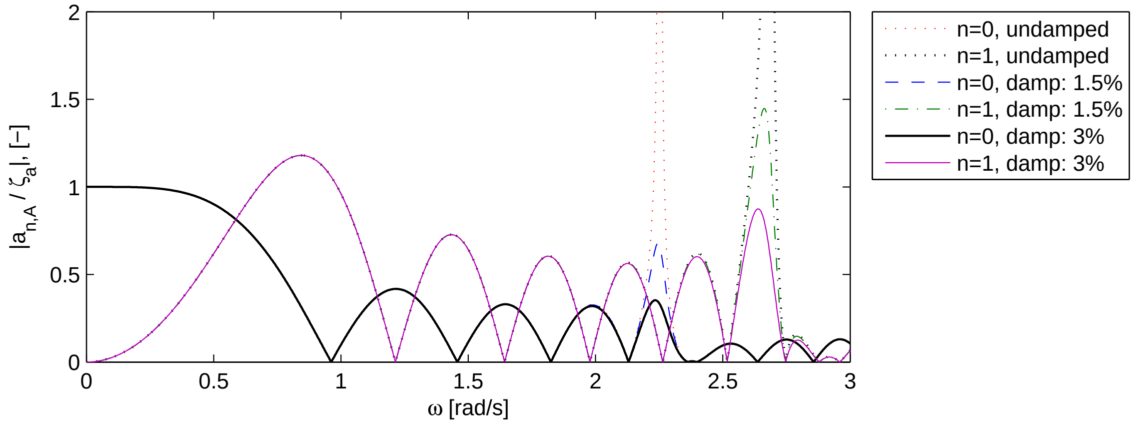

Figure B.3: Transfer functions for pitch and heave, given by $n = 0$ and $n = 1$, for 2 tori. n is the mode number. Undamped transfer functions and transfer functions for two different modal damping levels given as a percentage of critical damping for each mode are compared. ω is the wave frequency. $a_{n,A}$ is the modal amplitude. ζ_a is the wave amplitude.

B.3 Comparison Between Linear and Nonlinear Transfer Functions

B.3.1 1 Torus

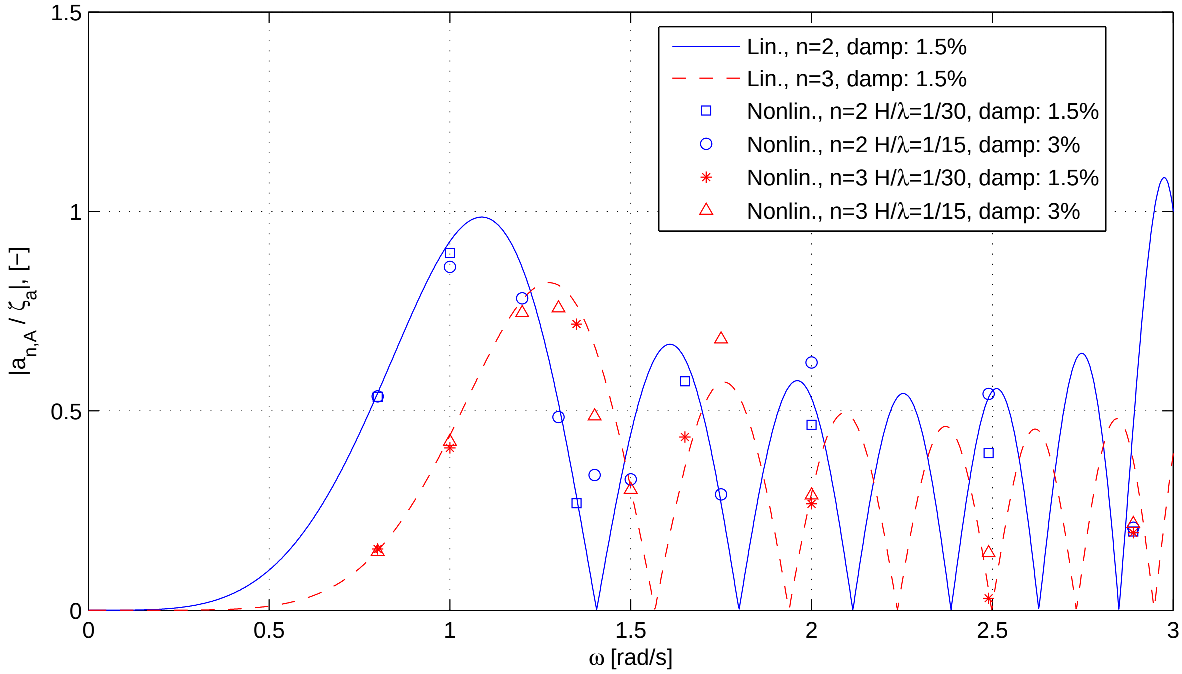

(a) Modal response.

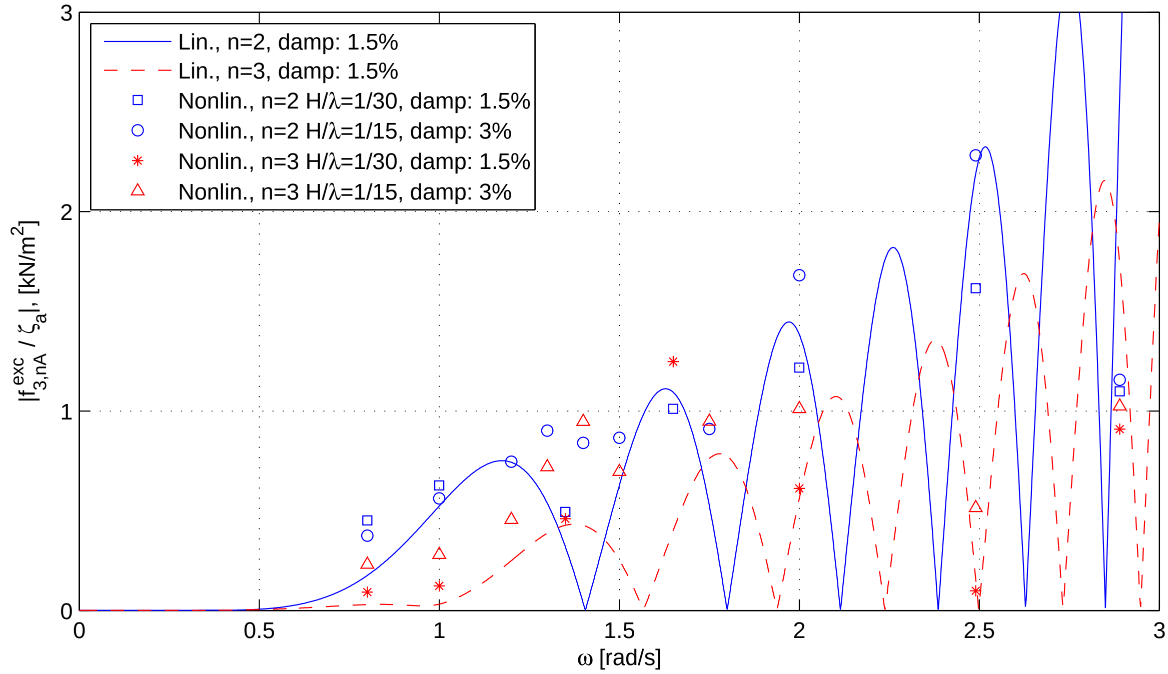

(b) Modal excitation force.

Figure B.4: Transfer functions for modal response and modal excitation force for 1 torus. Linear and nonlinear response for the two first elastic modes, corresponding to $n = 2$ and $n = 3$, for different wave steepnesses H/λ and different damping levels are compared. ω and ζ_a are the wave frequency and wave amplitude. H and λ are the wave height and wave length.

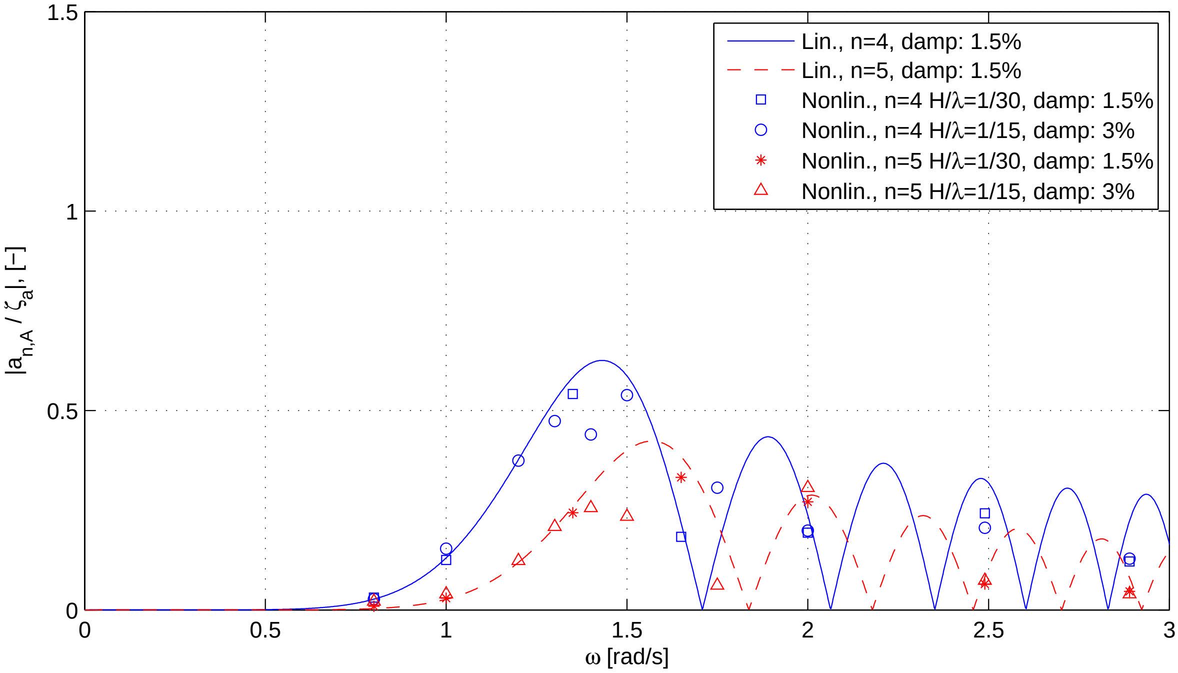

(a) Modal response.

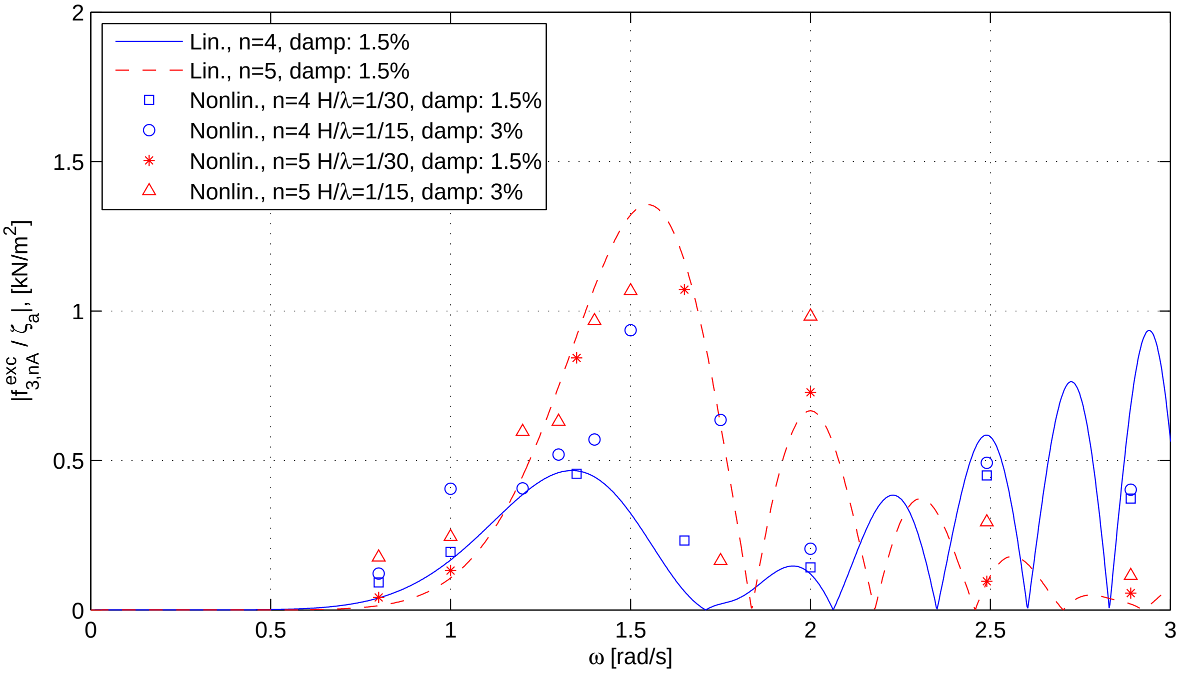

(b) Modal excitation force.

Figure B.5: Transfer functions for modal response and modal excitation force for 1 torus. Linear and nonlinear response for the third and fourth elastic modes, corresponding to $n = 4$ and $n = 5$, for different wave steepnesses H/λ and different damping levels are compared. ω and ζ_a are the wave frequency and wave amplitude. H and λ are the wave height and wave length.

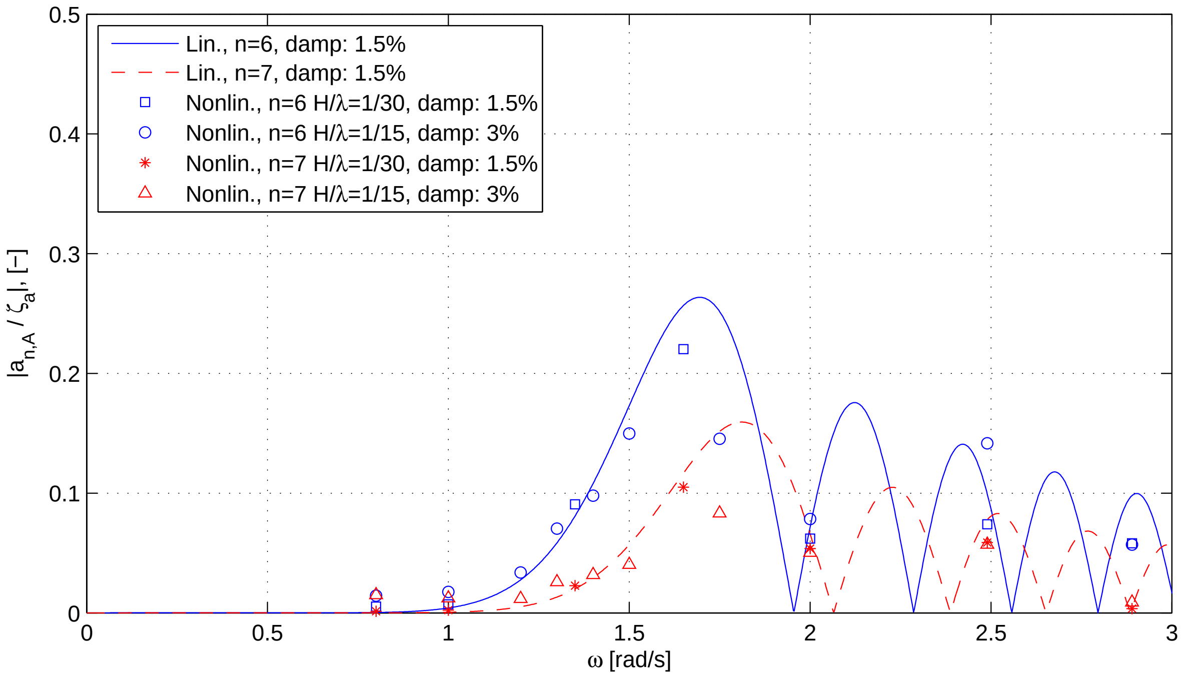

(a) Modal response.

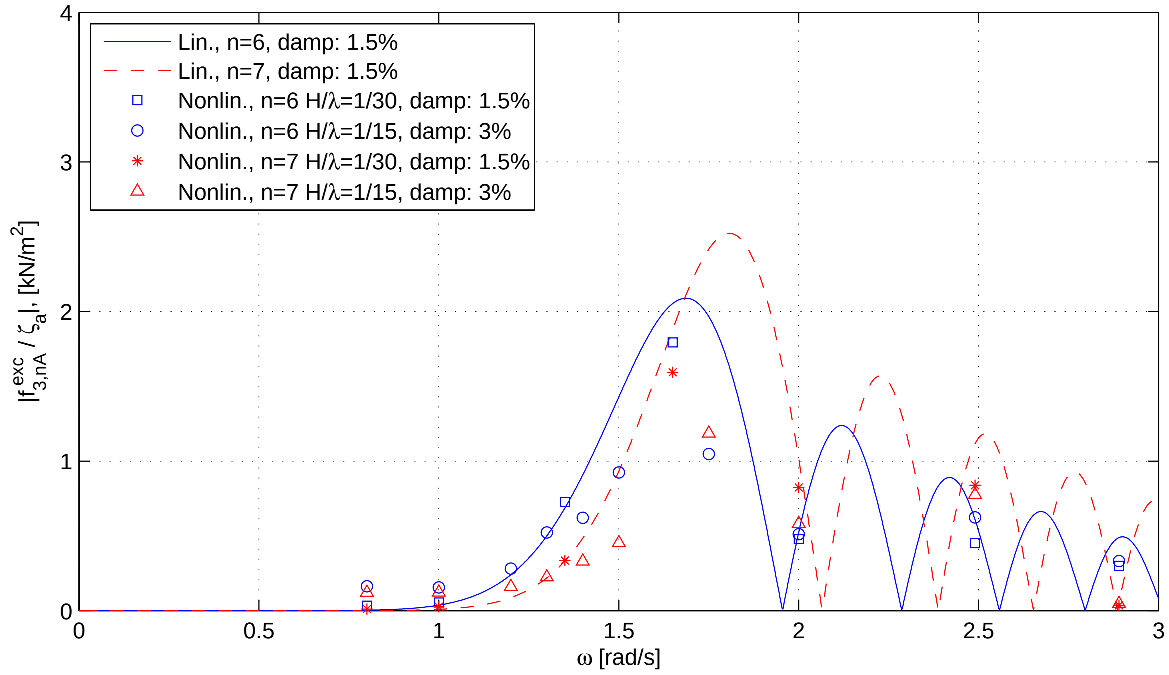

(b) Modal excitation force.

Figure B.6: Transfer functions for modal response and modal excitation force for 1 torus. Linear and nonlinear response for the fifth and sixth elastic modes, corresponding to $n = 6$ and $n = 7$, for different wave steepnesses H/λ and different damping levels are compared. ω and ζ_a are the wave frequency and wave amplitude. H and λ are the wave height and wave length.

B.3.2 2 Tori

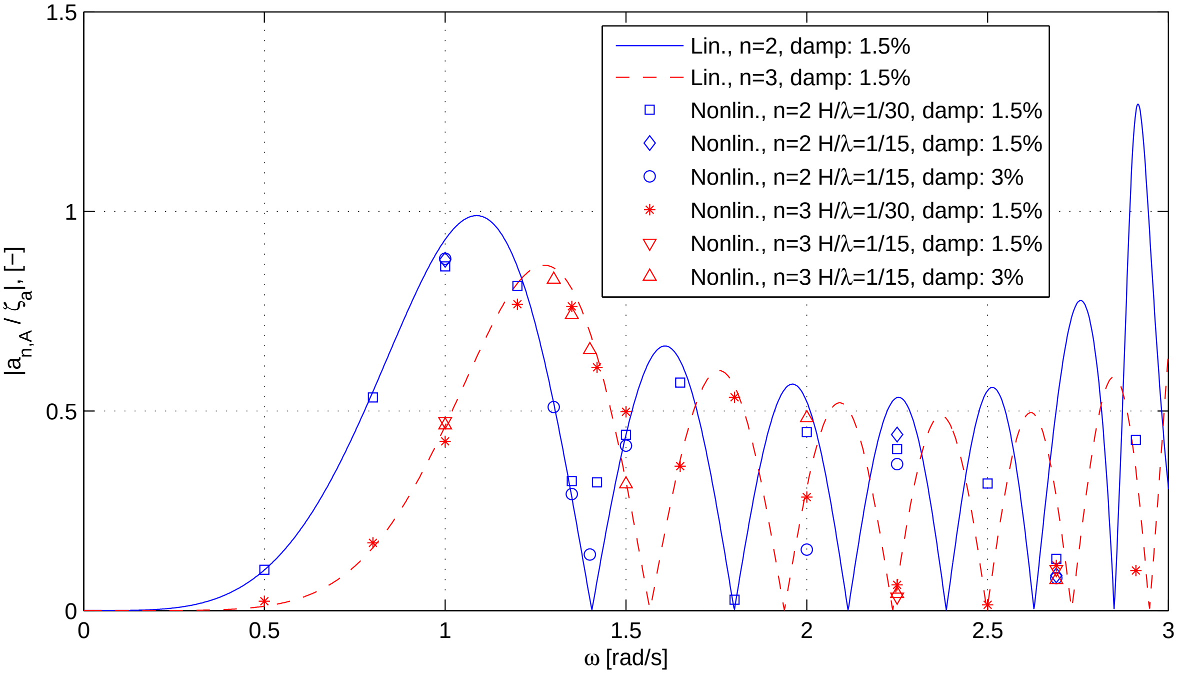

(a) Modal response.

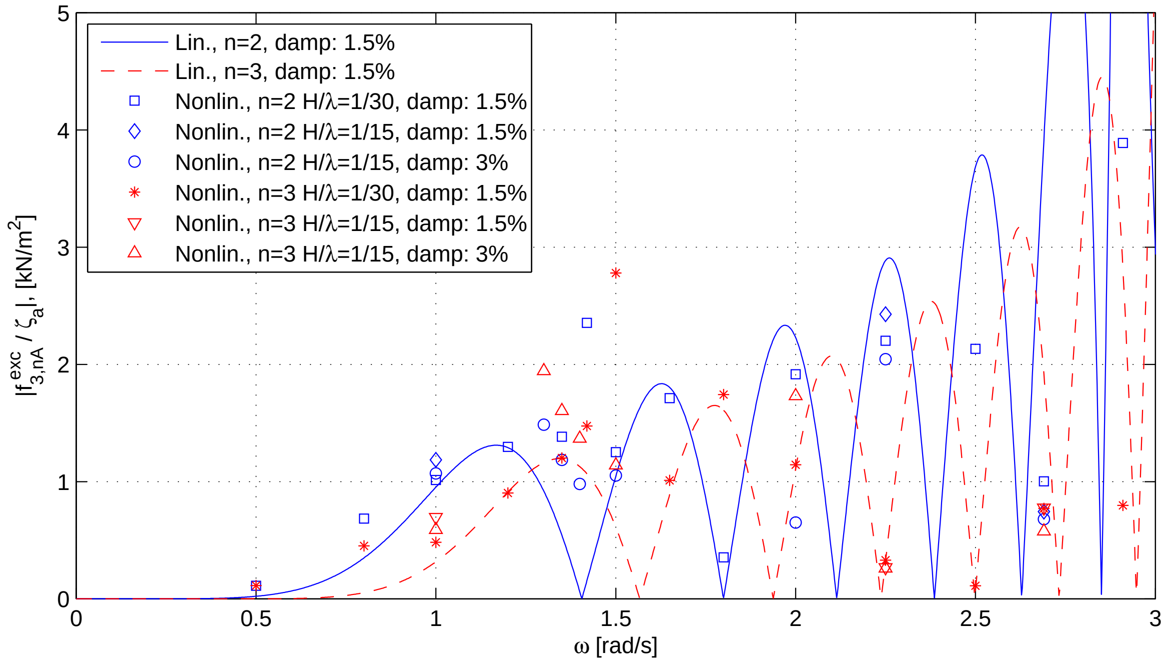

(b) Modal excitation force.

Figure B.7: Transfer functions for modal response and modal excitation force for 2 tori. Linear and nonlinear response for the two first elastic modes, corresponding to $n = 2$ and $n = 3$, for different wave steepnesses H/λ and different damping levels are compared. ω and ζ_a are the wave frequency and wave amplitude. H and λ are the wave height and wave length.

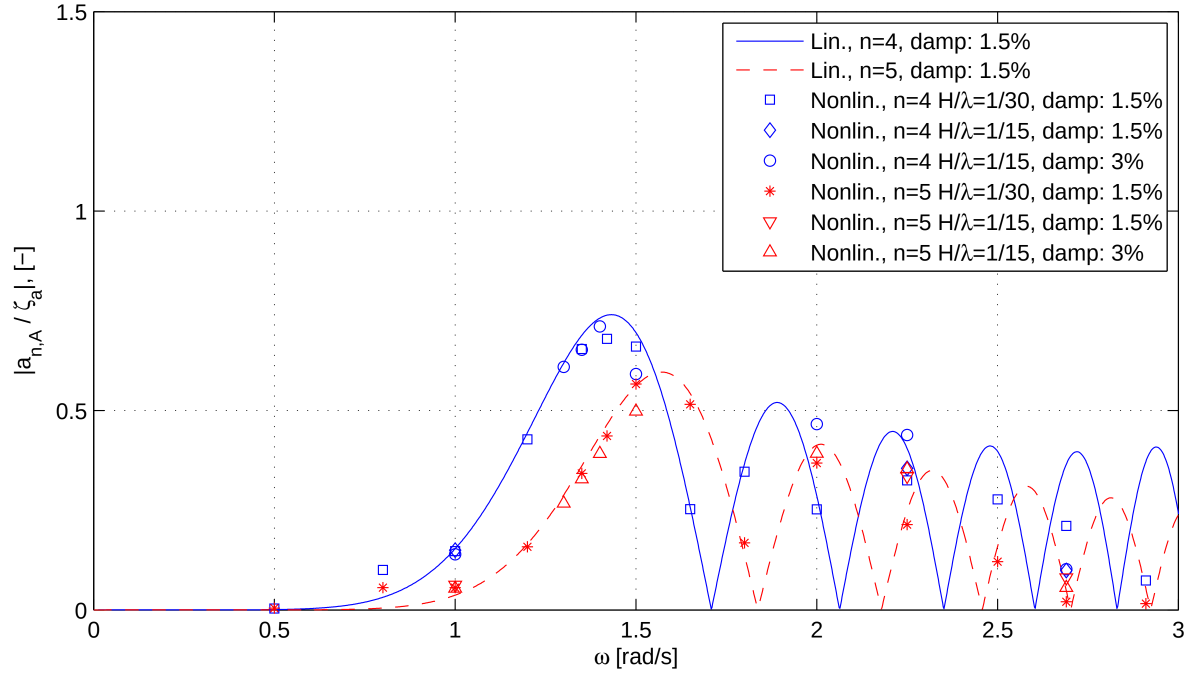

(a) Modal response.

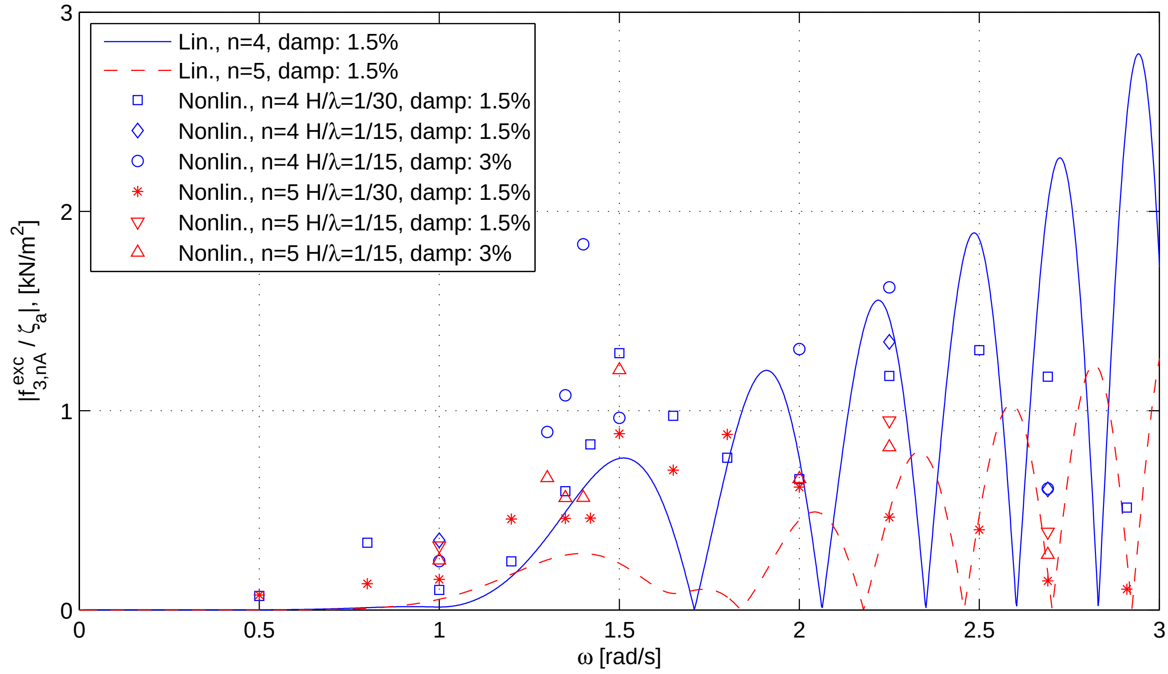

(b) Modal excitation force.

Figure B.8: Transfer functions for modal response and modal excitation force for 2 tori. Linear and nonlinear response for the third and fourth elastic modes, corresponding to $n = 4$ and $n = 5$, for different wave steepnesses H/λ and different damping levels are compared. ω and ζ_a are the wave frequency and wave amplitude. H and λ are the wave height and wave length.

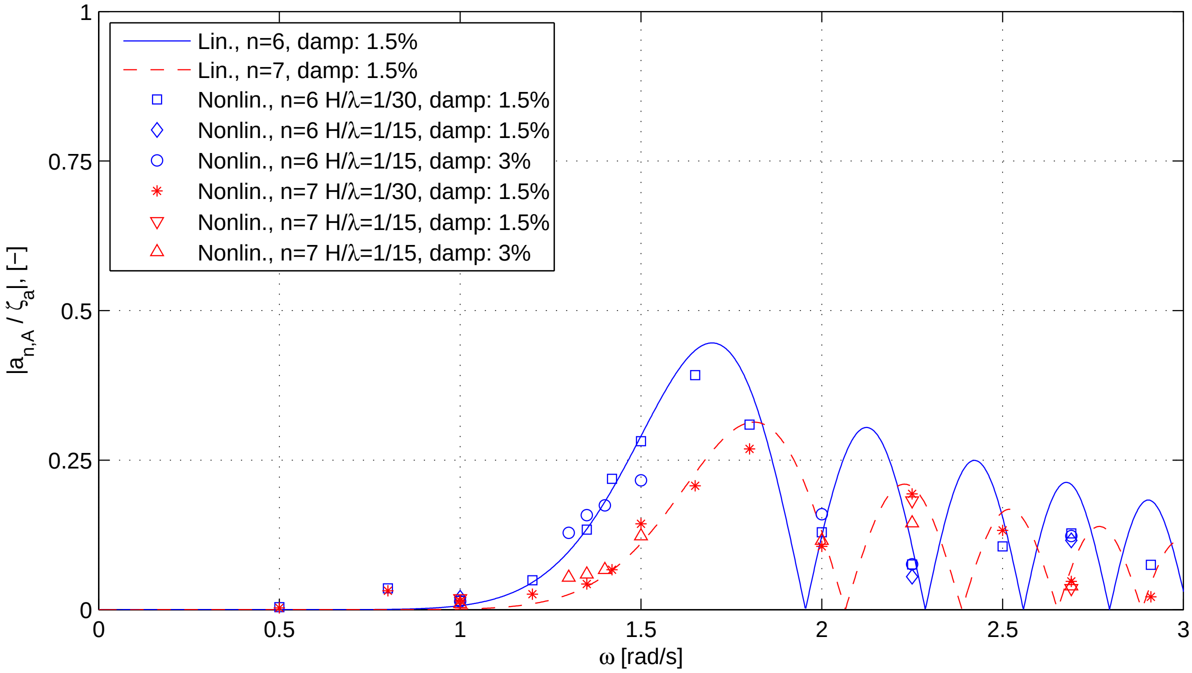

(a) Modal response.

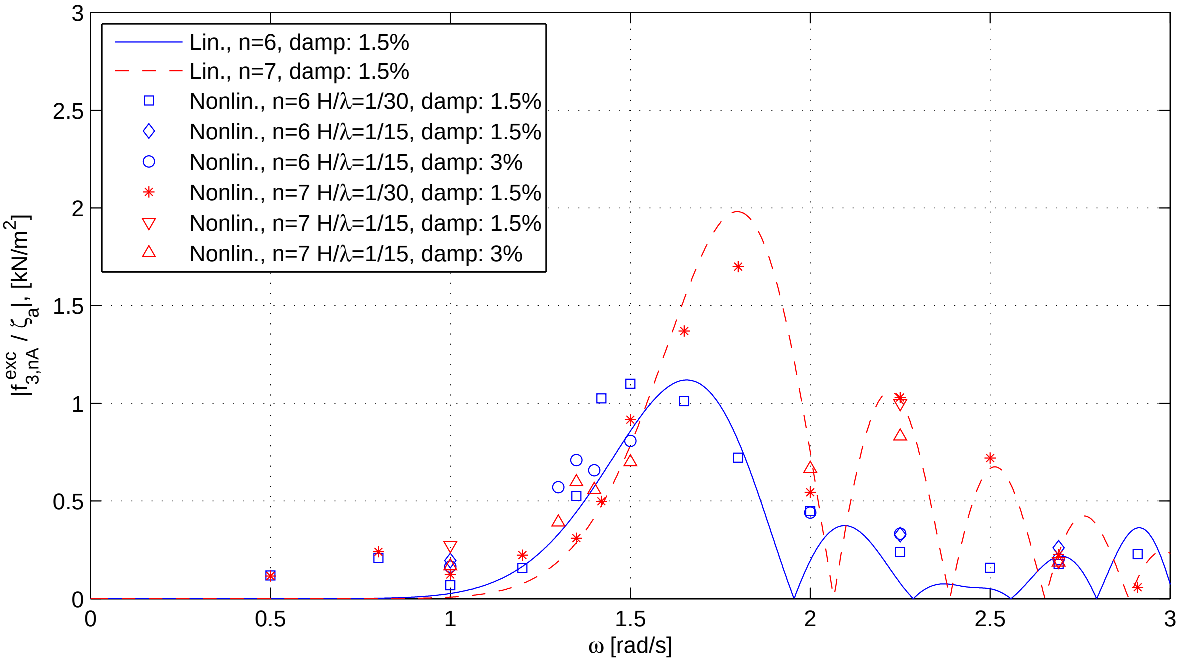

(b) Modal excitation force.

Figure B.9: Transfer functions for modal response and modal excitation force for 2 tori. Linear and nonlinear response for the fifth and sixth elastic modes, corresponding to $n = 6$ and $n = 7$, for different wave steepnesses H/λ and different damping levels are compared. ω and ζ_a are the wave frequency and wave amplitude. H and λ are the wave height and wave length.

B.4 Time Series

B.4.1 1 Torus. $\omega = 1.75 rad/s$

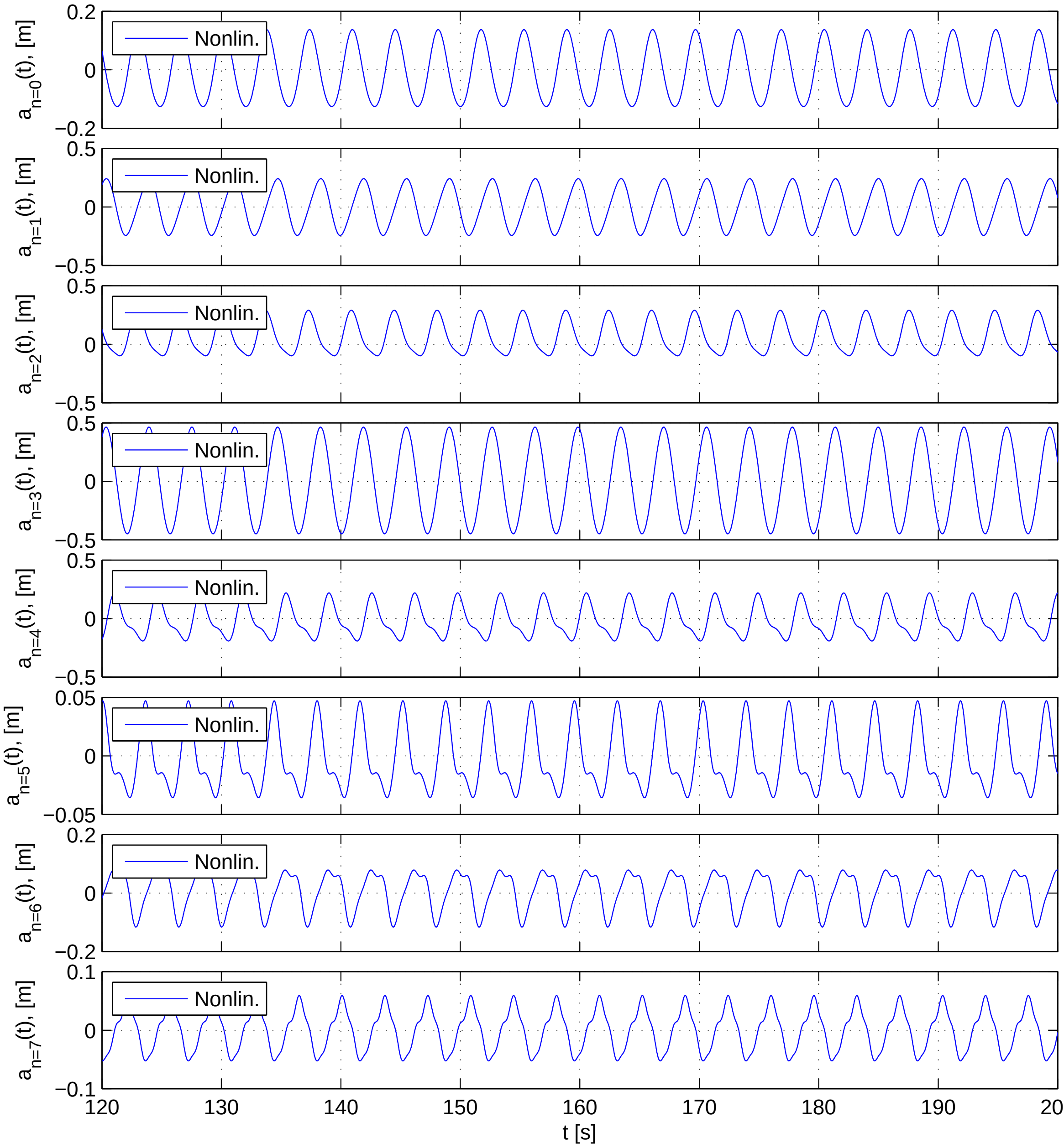

Figure B.10: Time series of nonlinear modal displacements for the eight first modes for 1 torus. Wave frequency $\omega = 1.75 rad/s$. Wave steepness $H/\lambda = 1/15$. Wave amplitude $\zeta_a = 0.67m$. Modal damping is 3 percent of critical damping for each mode.

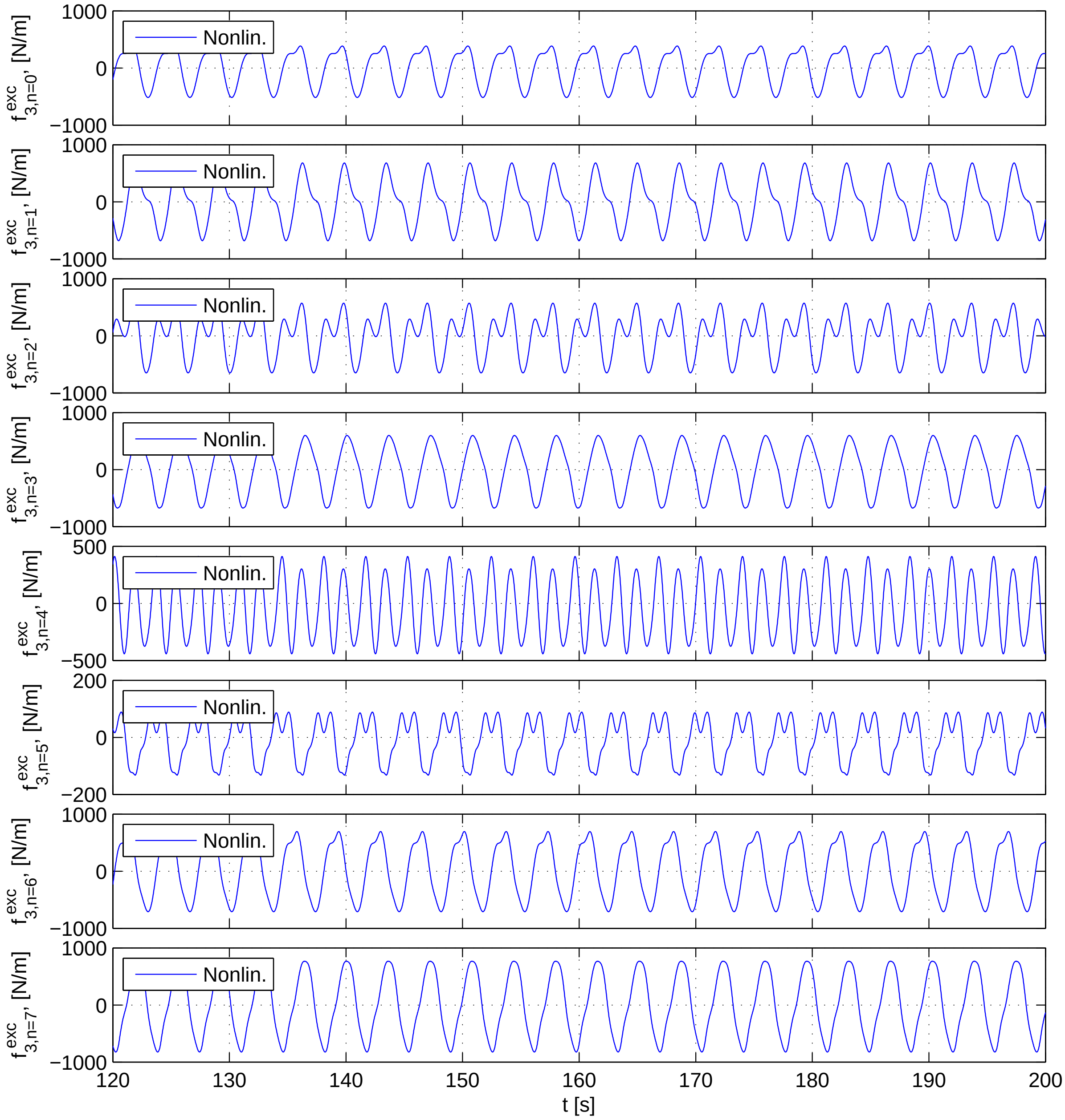

Figure B.11: Time series of nonlinear modal excitation forces for the eight first modes for 1 torus. Wave frequency $\omega = 1.75 rad/s$. Wave steepness $H/\lambda = 1/15$. Wave amplitude $\zeta_a = 0.67m$. Modal damping is 3 percent of critical damping for each mode.

B.4.2 1 Torus. $\omega = 2.0 rad/s$

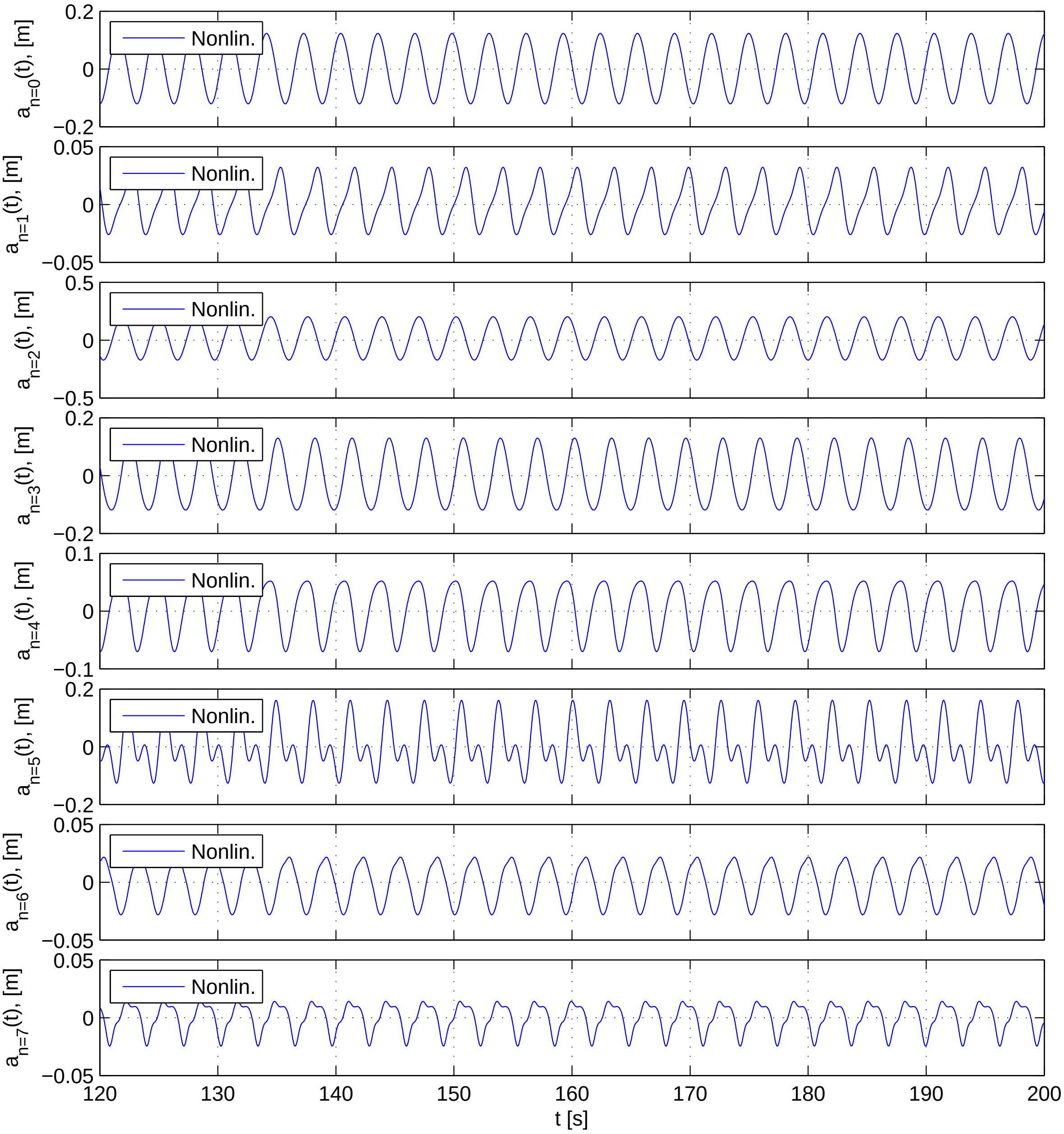

Figure B.12: Time series of nonlinear modal displacements for the eight first modes for 1 torus. Wave frequency $\omega = 2.0 rad/s$. Wave steepness $H/\lambda = 1/20$. Wave amplitude $\zeta_a = 0.39m$. Modal damping is 2 percent of critical damping for each mode.

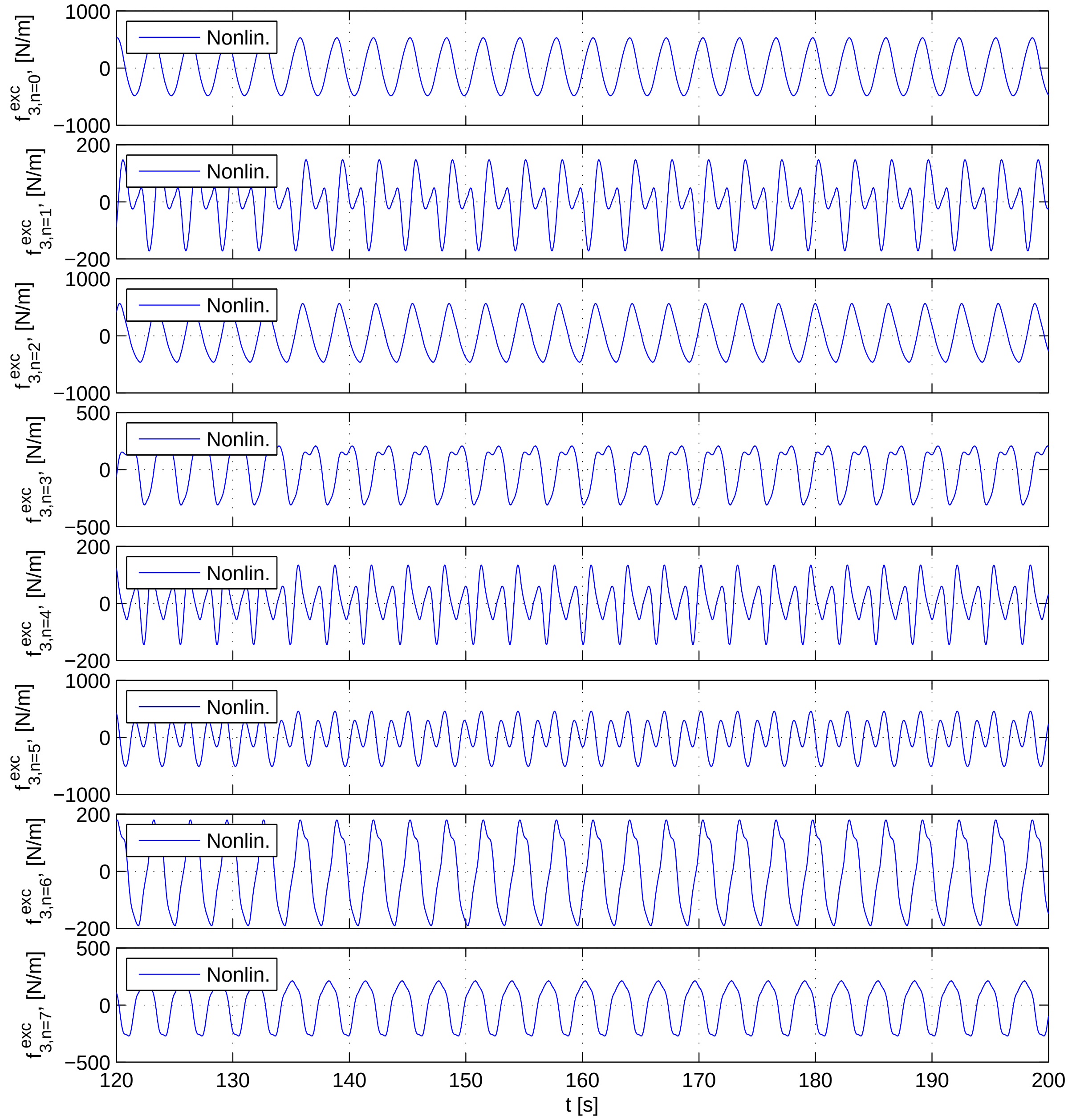

Figure B.13: Time series of nonlinear modal excitation forces for the eight first modes for 1 torus. Wave frequency $\omega = 2.0rad/s$. Wave steepness $H/\lambda = 1/20$. Wave amplitude $\zeta_a = 0.39m$. Modal damping is 2 percent of critical damping for each mode.

B.4.3 1 Torus. $\omega = 2.49 rad/s$

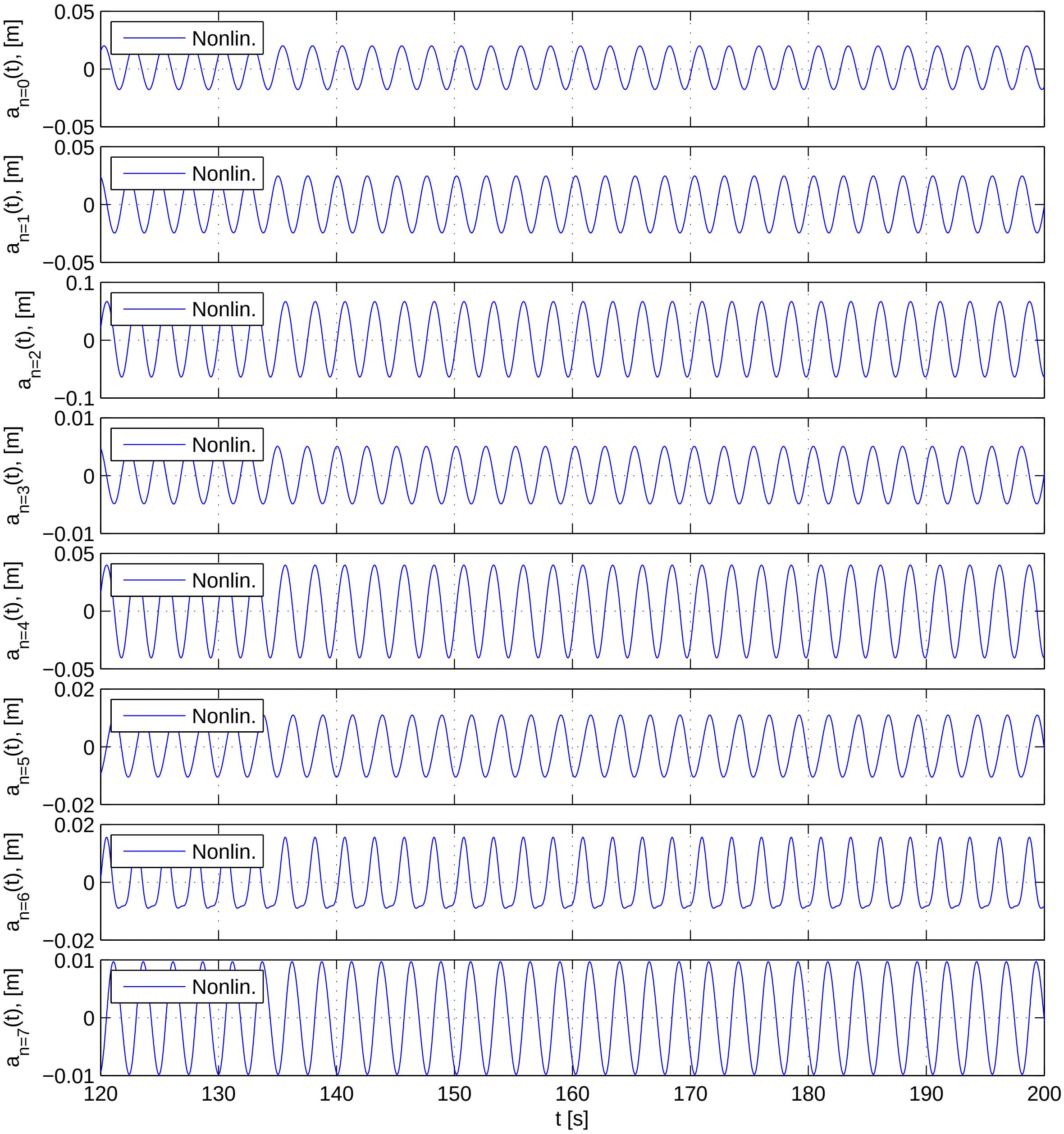

Figure B.14: Time series of nonlinear modal displacements for the eight first modes for 1 torus. Wave frequency $\omega = 2.49 rad/s$. Wave steepness $H/\lambda = 1/30$. Wave amplitude $\zeta_a = 0.17 m$. Modal damping is 1.5 percent of critical damping for each mode.

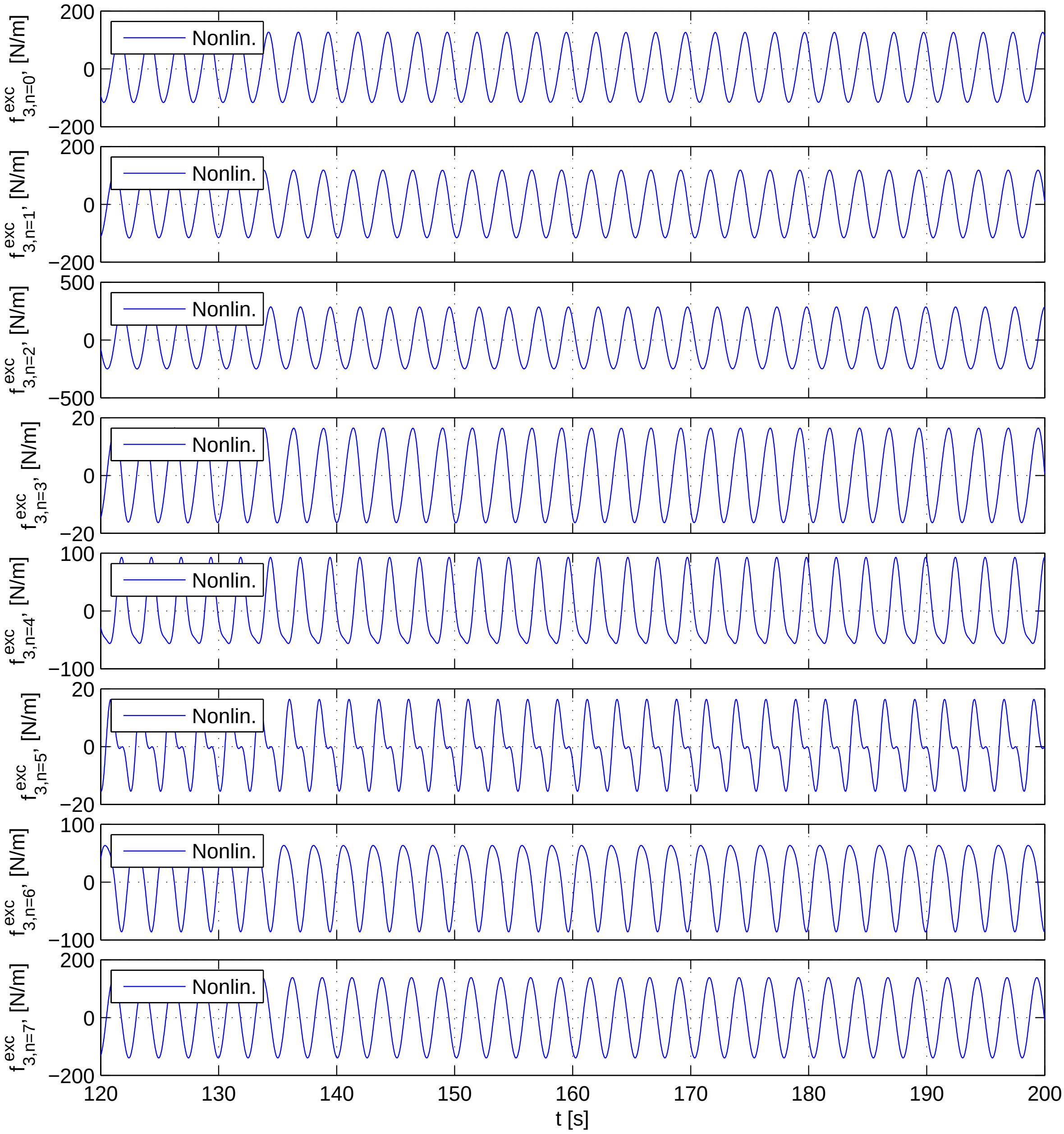

Figure B.15: Time series of nonlinear modal excitation forces for the eight first modes for 1 torus. Wave frequency $\omega = 2.49rad/s$. Wave steepness $H/\lambda = 1/30$. Wave amplitude $\zeta_a = 0.17m$. Modal damping is 1.5 percent of critical damping for each mode.

B.4.4 2 Tori. $\omega = 1.2rad/s$

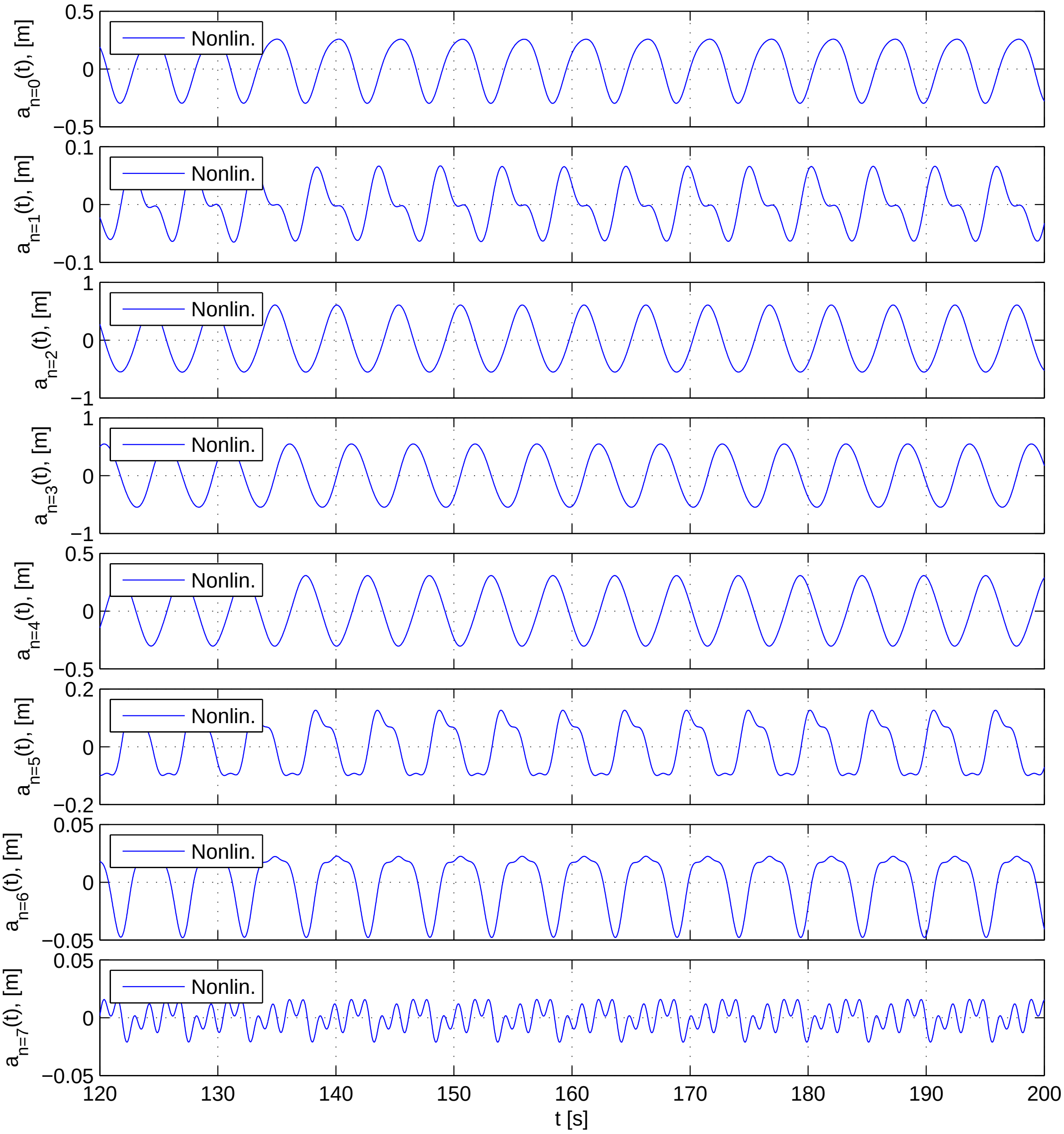

Figure B.16: Time series of nonlinear modal displacements for the eight first modes for 2 tori. Wave frequency $\omega = 1.2rad/s$. Wave steepness $H/\lambda = 1/30$. Wave amplitude $\zeta_a = 0.71m$. Modal damping is 1.5 percent of critical damping for each mode.

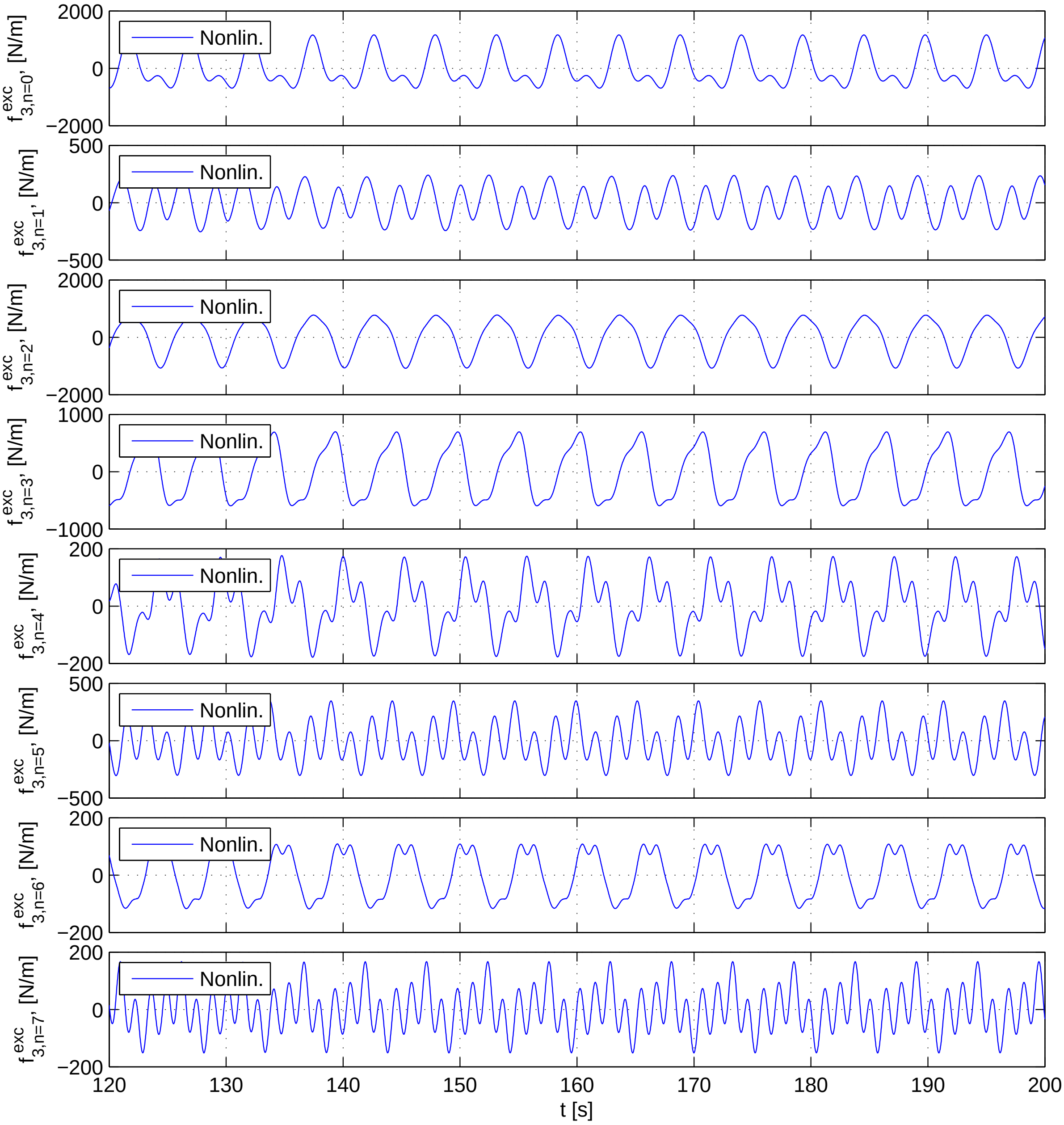

Figure B.17: Time series of nonlinear modal excitation forces for the eight first modes for 2 tori. Wave frequency $\omega = 1.2rad/s$. Wave steepness $H/\lambda = 1/30$. Wave amplitude $\zeta_a = 0.71m$. Modal damping is 1.5 percent of critical damping for each mode.

B.4.5 2 Tori. $\omega = 1.4 rad/s$

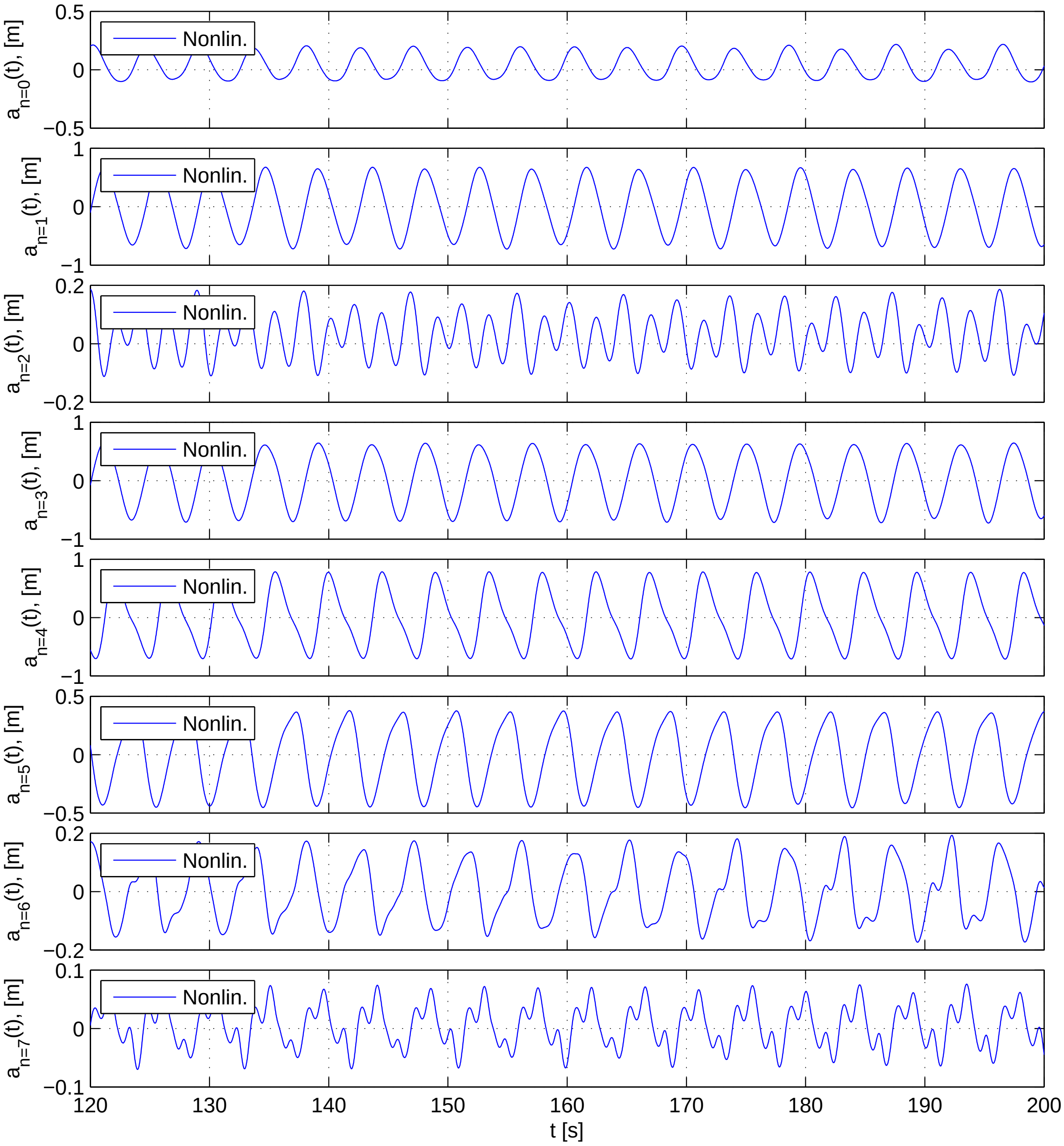

Figure B.18: Time series of nonlinear modal displacements for the eight first modes for 2 tori. Wave frequency $\omega = 1.4 rad/s$. Wave steepness $H/\lambda = 1/15$. Wave amplitude $\zeta_a = 1.05m$. Modal damping is 3 percent of critical damping for each mode.

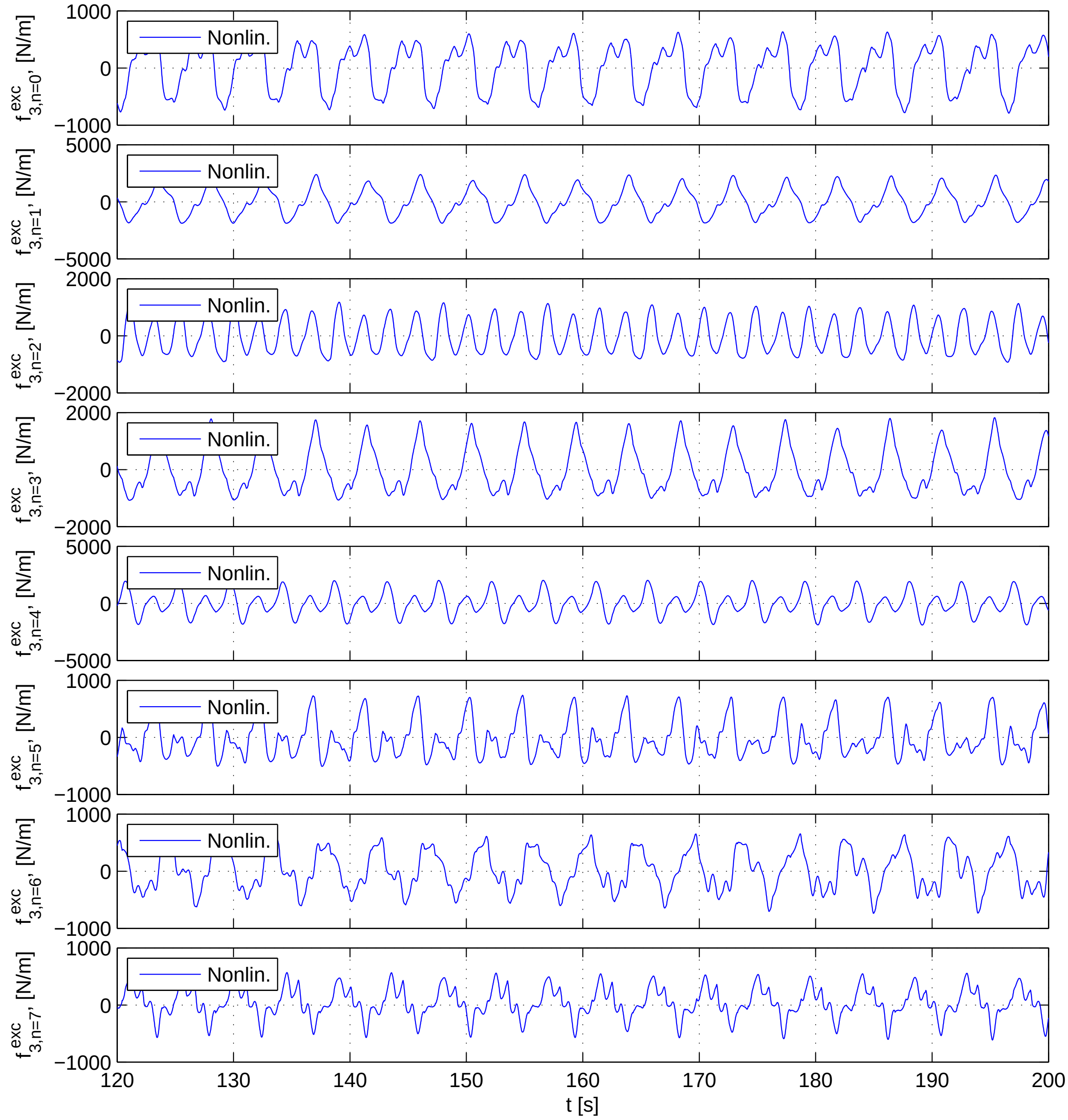

Figure B.19: Time series of nonlinear modal excitation forces for the eight first modes for 2 tori. Wave frequency $\omega = 1.4 rad/s$. Wave steepness $H/\lambda = 1/15$. Wave amplitude $\zeta_a = 1.05m$. Modal damping is 3 percent of critical damping for each mode.

B.4.6 2 Tori. $\omega = 1.5 rad/s$

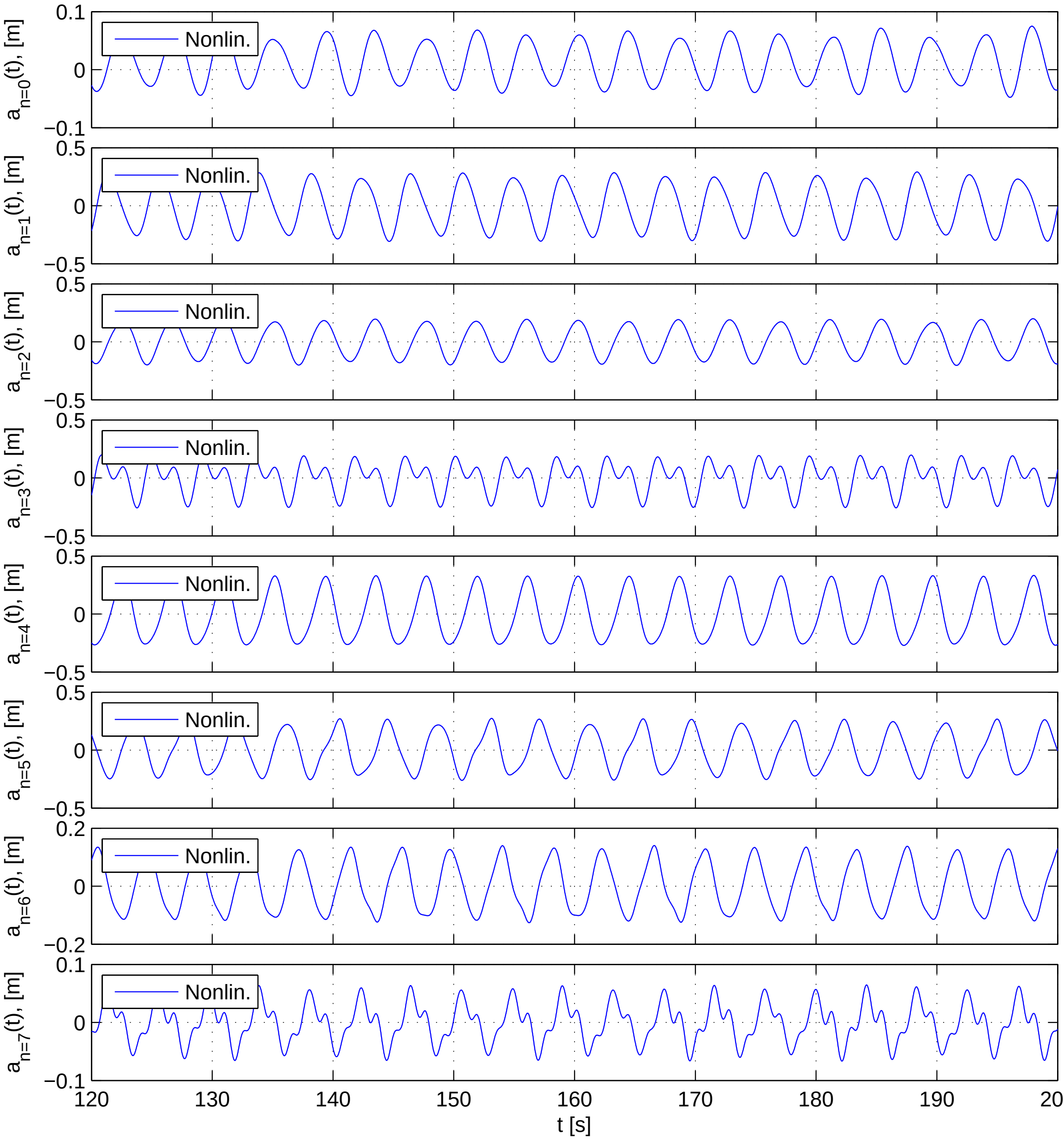

Figure B.20: Time series of nonlinear modal displacements for the eight first modes for 2 tori. Wave frequency $\omega = 1.5 rad/s$. Wave steepness $H/\lambda = 1/30$. Wave amplitude $\zeta_a = 0.46m$. Modal damping is 1.5 percent of critical damping for each mode.

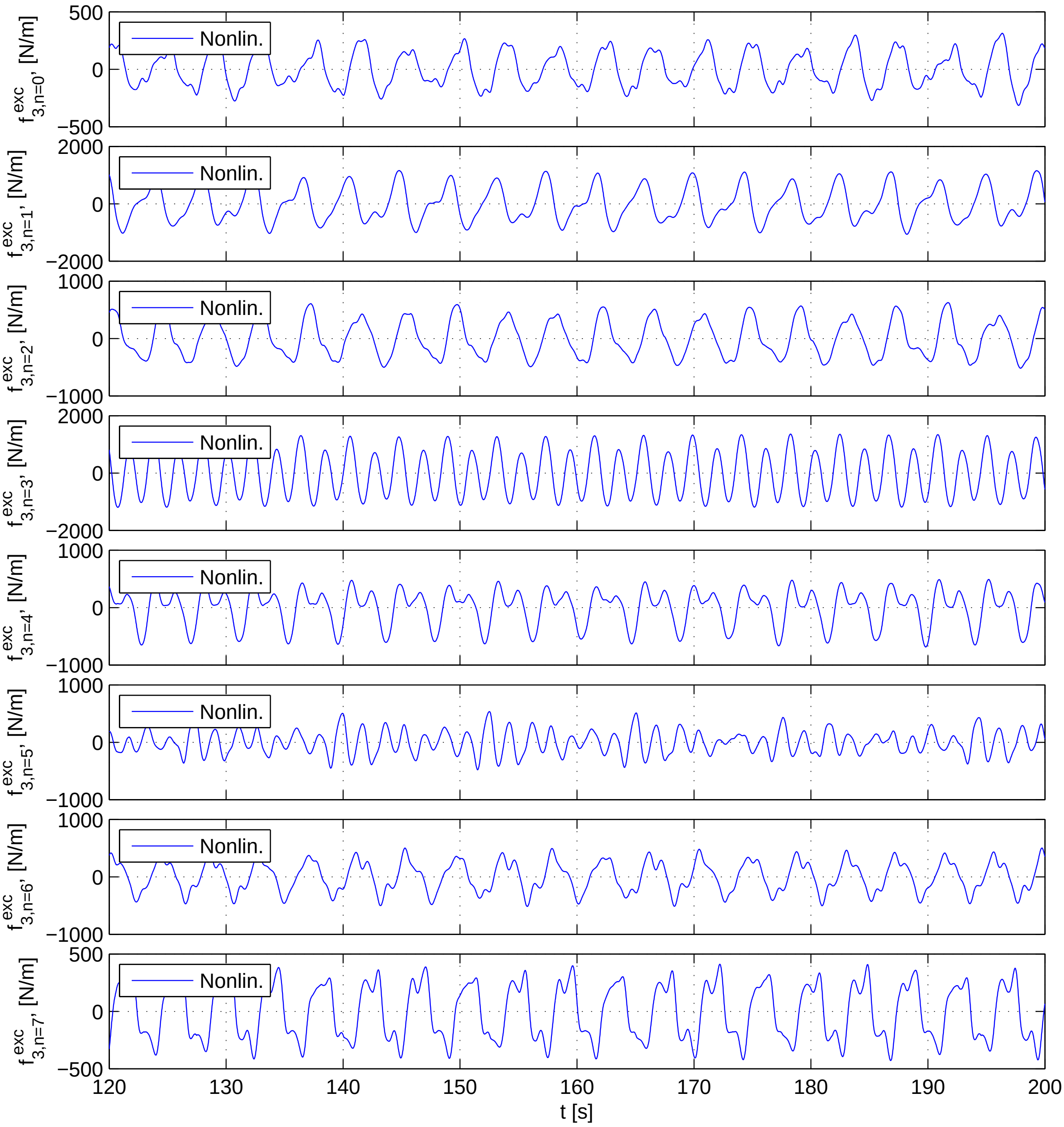

Figure B.21: Time series of nonlinear modal excitation forces for the eight first modes for 2 tori. Wave frequency $\omega = 1.5 rad/s$. Wave steepness $H/\lambda = 1/30$. Wave amplitude $\zeta_a = 0.46m$. Modal damping is 1.5 percent of critical damping for each mode.

B.4.7 2 Tori. $\omega = 1.8 rad/s$

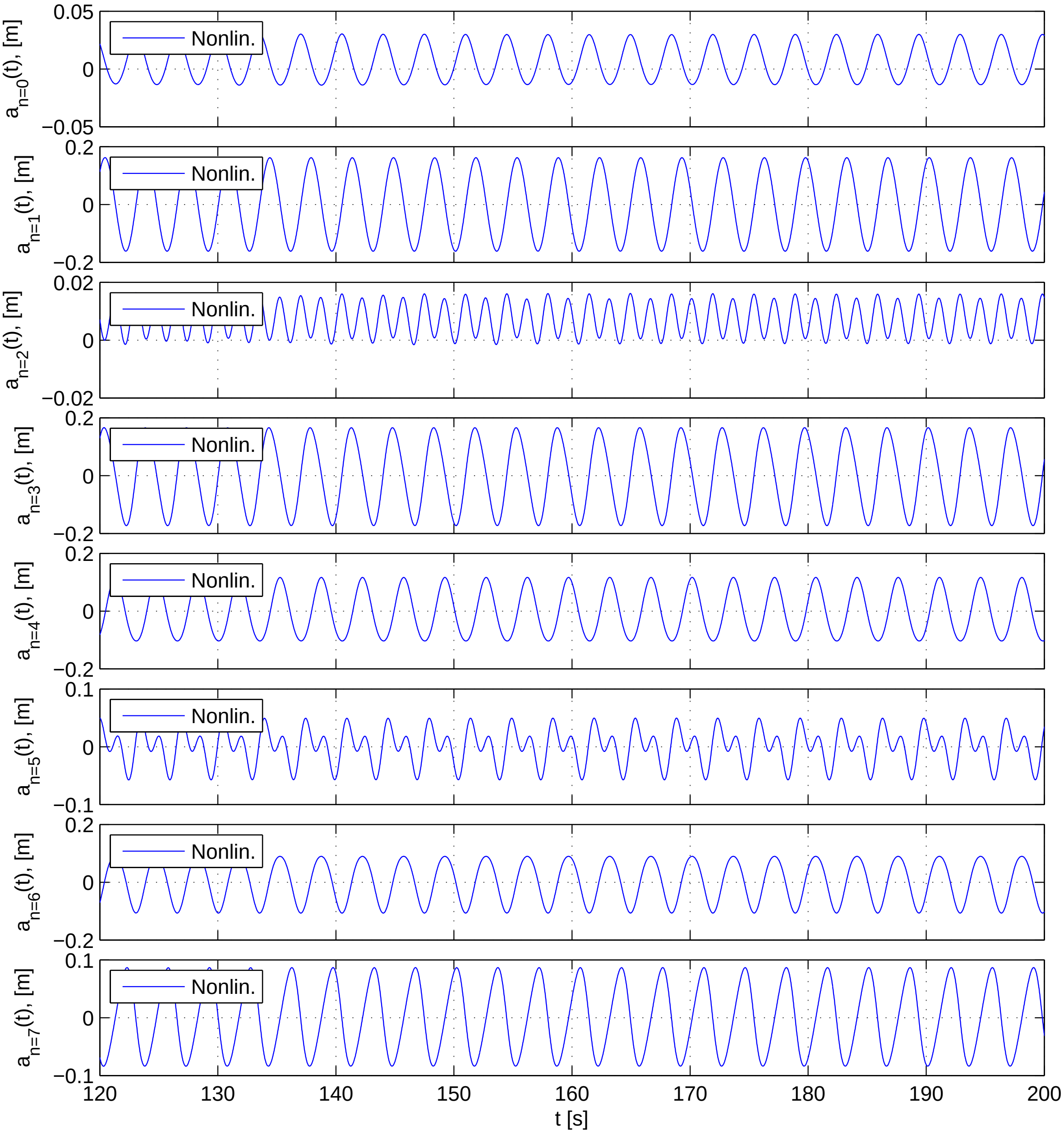

Figure B.22: Time series of nonlinear modal displacements for the eight first modes for 2 tori. Wave frequency $\omega = 1.8 rad/s$. Wave steepness $H/\lambda = 1/30$. Wave amplitude $\zeta_a = 0.32 m$. Modal damping is 1.5 percent of critical damping for each mode.

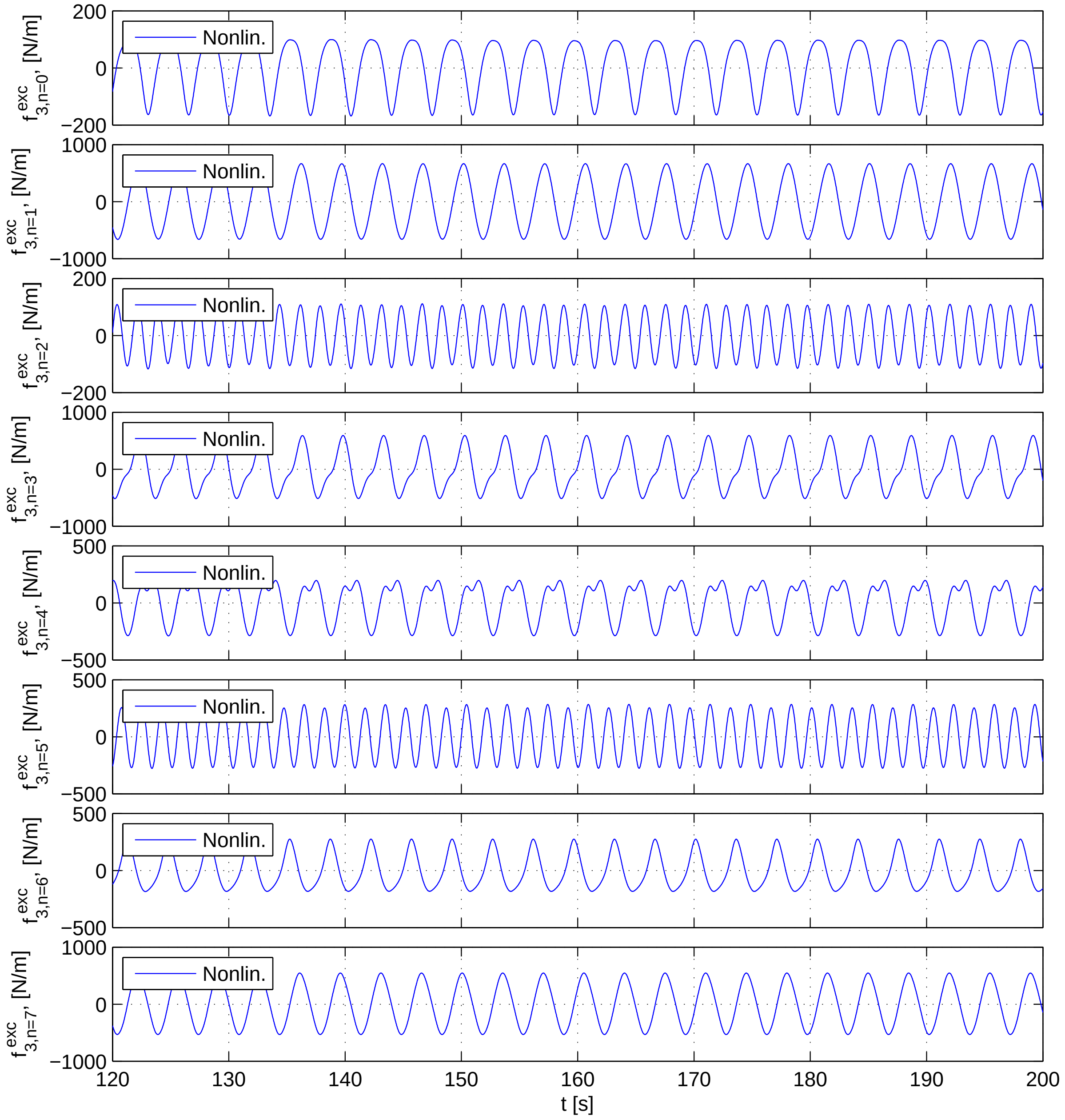

Figure B.23: Time series of nonlinear modal excitation forces for the eight first modes for 2 tori. Wave frequency $\omega = 1.8rad/s$. Wave steepness $H/\lambda = 1/30$. Wave amplitude $\zeta_a = 0.32m$. Modal damping is 1.5 percent of critical damping for each mode.

B.4.8 2 Tori. $\omega = 2.25 rad/s$

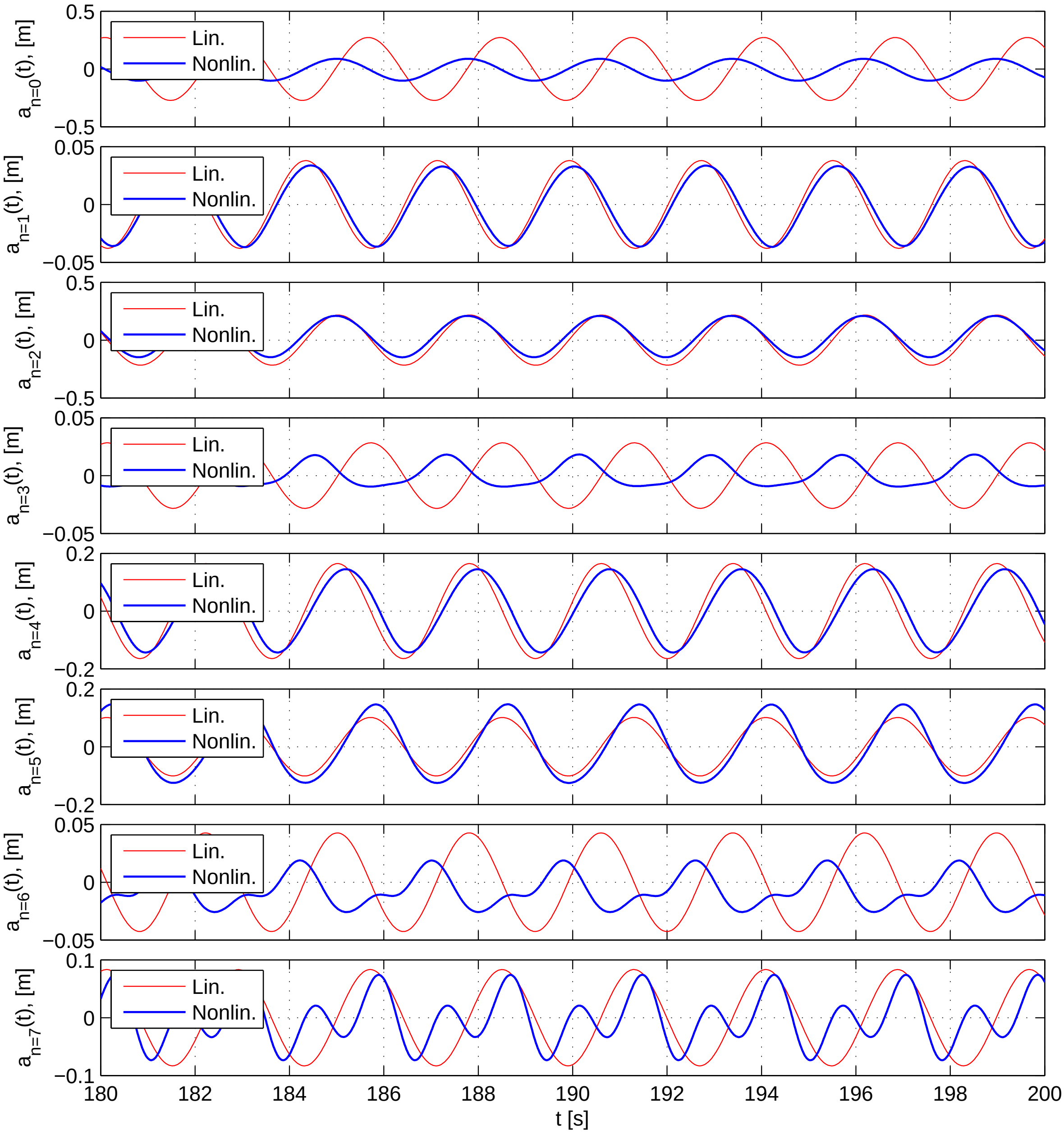

Figure B.24: Time series of vertical modal displacement for the eight first modes for 2 tori for heave resonance at $\omega = 2.25 rad/s$. Response due to linear and nonlinear excitation forces are compared. $a_n(t)$ are the n-th time dependent Fourier coefficient. The wave steepness $H/\lambda = 1/15$, giving a wave amplitude $\zeta_a = 0.41$. H and λ are the wave height and wave length. A modal damping level of 1.5 percent of modal critical damping is used. Note the differences between the values on the y-axes.

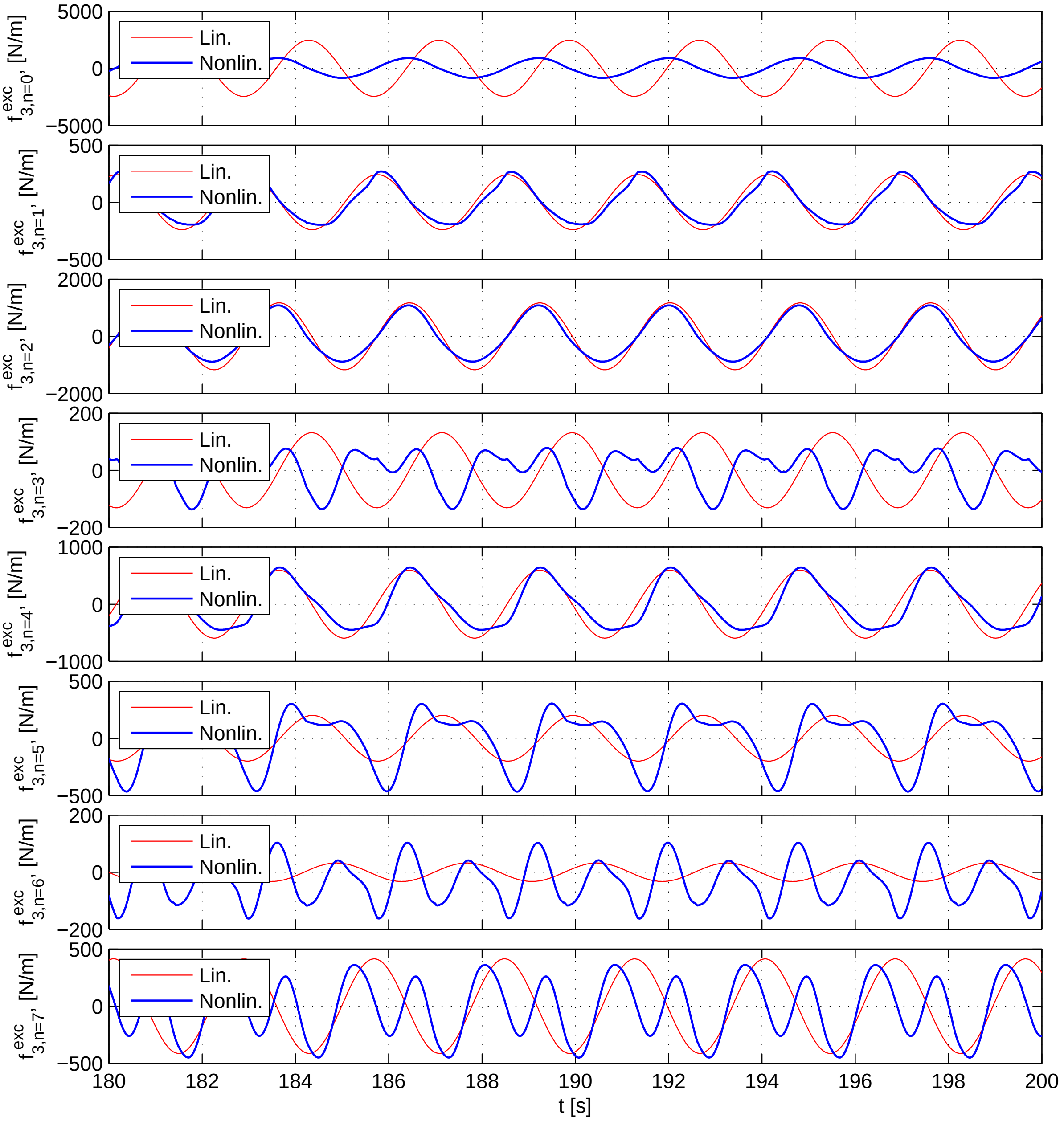

Figure B.25: Time series of modal excitation forces for the eight first modes for 2 tori for heave resonance at $\omega = 2.25 rad/s$. Linear and nonlinear excitation forces are compared. $f^{exc}_{3,n}(t)$ are the time dependent modal force for mode n. $f^{exc}_{3,n}(t)$ are given by equation (7.1) to (7.4). The wave steepness $H/\lambda = 1/15$, giving a wave amplitude $\zeta_a = 0.41$. H and λ are the wave height and wave length. A modal damping level of 1.5 percent of modal critical damping is used. Note the differences between the values on the y-axes.

B.4.9 2 Tori. $\omega = 2.69 rad/s$

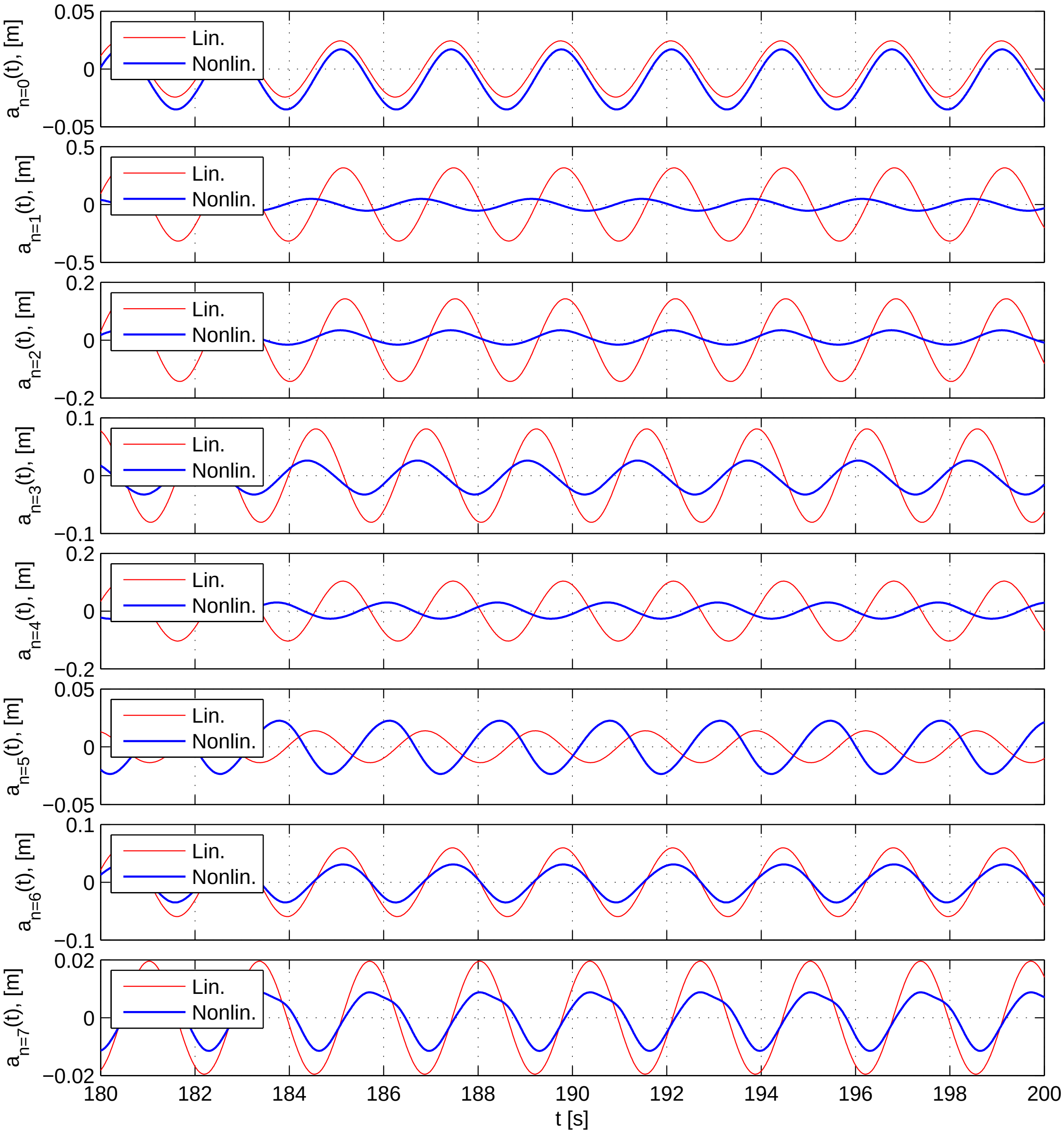

Figure B.26: Time series of vertical modal displacement for the eight first modes for 2 tori for pitch resonance at $\omega = 2.69 rad/s$. Response due to linear and nonlinear excitation forces are compared. $a_n(t)$ are the n-th time dependent Fourier coefficient. The wave steepness $H/\lambda = 1/15$, giving a wave amplitude $\zeta_a = 0.28m$. H and λ are the wave height and wave length. A modal damping level of 1.5 percent of modal critical damping is used. Note the differences between the values on the y-axes.

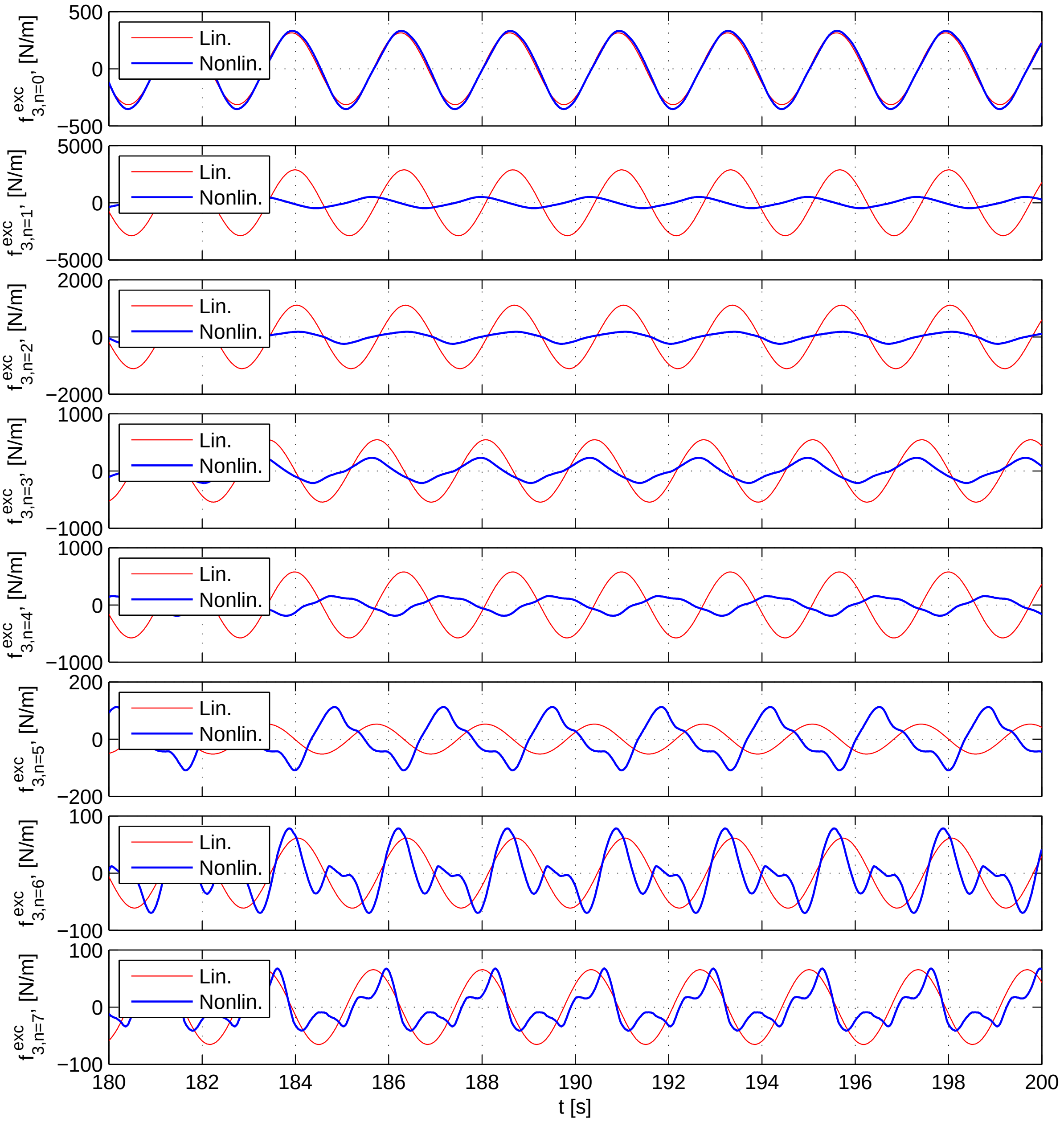

Figure B.27: Time series of modal excitation forces for the eight first modes for 2 tori for pitch resonance at $\omega = 2.69 rad/s$. Linear and nonlinear excitation forces are compared. $f^{exc}_{3,n}(t)$ are the time dependent modal force for mode n. $f^{exc}_{3,n}(t)$ are given by equation (7.1) to (7.4). The wave steepness $H/\lambda = 1/15$, giving a wave amplitude $\zeta_a = 0.28m$. H and λ are the wave height and wave length. A modal damping level of 1.5 percent of modal critical damping is used. Note the differences between the values on the y-axes.